Mitochondria: Hubs of hypoxia-tolerance in naked mole-rats

By Hang Cheng

Thesis submitted to the University of Ottawa in partial fulfillment of the requirements for the Doctorate in Philosophy degree in Biology

Department of Biology
Faculty of Science
University of Ottawa

Abstract

Most adult mammals are highly sensitive to reduced oxygen availability; however, some species have evolved to live in hypoxic environments. Naked mole-rats (NMRs, *Heterocephalus glaber*) are among the most hypoxia-tolerant mammals and rapidly reduce whole animal oxygen consumption (>80% in 3% O_2) during hypoxia, presumably by downregulating numerous cellular functions across multiple tissues. Mitochondria are cellular oxygen sensors, major consumers of oxygen, and regulators of numerous cellular signalling pathways, and thus likely play key roles in cellular responses to hypoxia. However, little is known about the specific mechanisms and pathways that mitochondria regulate in NMRs, nor about how these roles vary between tissues with divergent metabolic demands in hypoxia. Of particular interest are mechanisms that regulate mitochondrial oxidative phosphorylation (OXPHOS) function, and reactive oxygen species (ROS) and Ca^{2+} homeostasis, since ATP deficits, and ROS and Ca^{2+} dysregulation are central to hypoxic/ischemic cell death in hypoxia-intolerant mammalian cells. Therefore, the goal of my thesis is to uncover mechanisms via which mitochondria regulate OXPHOS, ROS, and Ca^{2+}, and the impact of these mechanisms on hypoxia/ischemia tolerance in NMR interscapular brown adipose tissue (iBAT), brain, and skeletal muscle. These tissues were chosen because 1) thermoregulation is a major energy drain in small rodents and decreased thermoregulation is a common strategy to save energy during hypometabolism in such species, 2) maintenance of brain function is both energetically expensive but also obligatory in all animals, and 3) NMRs remain physically active in hypoxia, and therefore require the maintenance of skeletal muscle function. Based on the divergent energy demands and sensitivity to hypoxia of these tissues, we expected to find highly divergent tissue-specific regulation at the mitochondrial level. Using multiple approaches, including high-resolution respirometry, optical fluorescence measurements, western

blot, qPCR, and transmission electron microscopy, our integrated findings revealed numerous novel responses in each of these tissues that help to explain the remarkable tolerance to hypoxic/ischemic stress in NMRs. Specifically:

1) In hypoxia, iBAT mitochondria significantly suppress respiration (by 45-70%) and rate of Ca^{2+} uptake. These functional changes were accompanied by rapid reductions in the expression of OXPHOS and UCP1 proteins, which was likely mediated by mitochondrial membrane remodeling, including the activation of mitochondrial fission and inhibition of apoptosis.
2) NMR brain mitochondria have a very high capacity to buffer Ca^{2+}. Elevated mitochondrial Ca^{2+} suppresses the O_2 consumption rate without compromising membrane integrity in NMRs but not in mice. The mechanism underlying this enhanced capacity likely involves the occurrence of larger and more interconnected mitochondrial networks in NMR brain. As a result, NMR brain is better able to regulate redox state, minimize excitotoxity (i.e., glutamate, Ca^{2+}), and retain OXPHOS function under *in vitro* ischemia than mouse brain.
3) Skeletal muscle mitochondria exhibit a mild decrease in OXPHOS function but reduce mitochondrial superoxide ($O_2^{\cdot -}$) emission in acute and chronic hypoxia, which may support continuous exercise in intermittent hypoxic burrow systems in nature.

Overall, these results suggested that NMR mitochondria play key roles in maintaining essential functions (e.g., brain function, physical activity), and also suppressing non-essential functions (e.g., thermogenesis) in a tissue-specific fashion to minimize the O_2 consumption and hypoxia-induced cell damage.

Acknowledgements

To the people who have been supporting me all the way.

Guo Cheng and Wenjun Shi, who woke up the truth, goodness, and beauty again deep in my mind.

Liping Cheng and Hejin Cheng, who brought me to a village the first and only.

Dr. Matthew Edward Malin Pamenter, the boss but more than a boss.

Dr. Daniel Munro and pre-Dr. Liam Eaton, colleagues, and friends.

Dr. Baptiste Lacoste, Dr. Diane Lagace, and Dr. Mary-Ellen Harper, mentors in academia.

Dr. Graham R. Scott, Dr. Kenneth B. Storey, Dr. Mary-Ellen Harper, and Dr. Michael G. Jonz, provided valuable comments that greatly benefited this thesis.

“And I'd just like to say, I thank God that you're here with me” -- Ronald Michael Pope.

Contents

List of abbreviations

16S	16S mitochondrial ribosomal RNA
aCSF	artificial cerebral spinal fluid
ADP	adenosine diphosphate
AIF	apoptosis inducing factor
AKT	serine/threonine protein kinase
AMPK	AMP-activated protein kinase
AMPK	AMP-activated protein kinase
ANOVA	analysis of variance
ANT	ADP/ATP carrier protein
ATP	adenosine triphosphate
AU	auranofin
AUR	Amplex UltraRed
B2M	beta-2-microglobulin
BAT	brown adipose tissue
Bcl-2	B-cell lymphoma 2
BNIP3	BCL-2/adenovirus E1B 19 kDa protein-interacting protein 3
CASP3	caspase3
CCCP	carbonyl cyanide m-chlorophenyl hydrazine
CJ	cristae junction
CM	cristae membrane
CS	citrate synthase
Ct	threshold cycle
DNA	deoxyribonucleic acid
Drp1	dynamin-1-like protein
Drp1	Dynamin-related protein 1
ER	endoplasmic reticulum
ETC	electron transport chain
Fis1	mitochondrial fission 1 protein
FLRT	Forward Looking Infrared
FUNDC1	BCL-2-interacting protein 3-like and FUN14 domain-containing 1
GDP	guanosine diphosphate
GTPases	guanosine triphosphates
Gpx	peroxidase
h	hour
H_2O_2	hydrogen peroxide
HBSS	Hanks' Balanced Salt Solution
HIF	hypoxia-inducible factor
Htra2/Omi	Serine protease HTRA2
I/R	ischemia/reperfusion
IBM	inner boundary membrane
IC_{50}	half-maximal inhibitory concentration
IMM	inner mitochondrial membrane

IMS	intermembrane space
IP3R	inositol trisphosphate receptor
KAR	kainate receptor
K_{off}	Ca^{2+}-binding Calcium green 5-N decay rate
LC3(B)	microtubule-associated proteins 1A/1B light chain 3B
MCU	mitochondrial calcium uniporter
Mff	mitochondrial fission factor
Mfn1	mitofusin 1
Mfn2	mitofusin 2
MICOS	mitochondrial contact site and Cristae Organizing System
MICU1	mitochondrial Ca^{2+}uptake 1
MIEF1&2	mitochondrial dynamics proteins
mPTP	mitochondrial permeability transition pore
mRyR	mitochondrial ryanodine receptor
mtDNA	mitochondrial NDA
mTOR	mammalian target of rapamycin
NAD+	Nicotinamide adenine dinucleotide phosphate
NADPH	Nicotinamide adenine dinucleotide phosphate (reduced)
nDNA	nuclear DNA
NF-κB	nuclear factor kappa B
NHE	sodium/hydrogen exchangers
NIX(BNIP3L)	BCL2/adenovirus E1B 19 kDa protein-interacting protein 3-like
NMDAR	N-methyl-D-aspartate receptor
NMR	Naked mole-rat
Nrf2	nuclear factor erythroid-2-related factor-2
$O_2^{\cdot -}$	superoxide
OGD	oxygen glucose deprivation
OMM	outer mitochondrial membrane
OPA1	optic atrophy 1
OXPHOS	oxidative phosphorylation
p53	tumor protein p53
p62	ubiquitin-binding protein P62
PAD	peptidylarginine deiminase
PARKIN	parkin RBR E3 ubiquitin protein ligase
PINK1	PTEN-induced kinase 1
PKC	protein kinase C
PMF	proton motive force
Prx	peroxiredoxin
PTM	post translational modification
qPCR	quantitative polymerase chain reaction
RAB7A	Ras-related protein Rab-7a
RaM	rapid mode of uptake
RCR	respiratory control rate
Rh-123	Rhodamine-123

RIPA	radio-Immunoprecipitation Assay
ROS	reactive oxygen species
RyR	ryanodine receptors
SBEM	block face electron microscopy
SEM	standard error of mean
SOD	superoxide dismutase
SQOR	sulfide:quinone oxidoreductase
SUIT	substrate-uncoupler-inhibitor titration
T_a	ambient temperature
T_b	body temperature
TBC1D15	TBC1 Domain Family Member 15
TCA	tricarboxylic acid
TEM	transmission electron microscopy
TMPD	N,N,N',N'-tetramethyl-p-phenylenediamine
UCP	uncoupling protein
UPS	ubiquitin-proteasome system
α-KGDH	alpha-ketoglutarate dehydrogenase
$\Delta\psi_m$	mitochondrial membrane potential

List of figures and tables

Figures

Tables

Supplementary Information

Framework and Highlights

This thesis contains a **General Introduction** (**Chapter 1**) discussing mitochondrial function and the role of mitochondria in responding to acute hypoxia. Therein, I also introduce NMRs as an emerging model of hypoxia/ischemia tolerance, whose ability to adapt to hypoxia may be due in part to their capacity to modify mitochondrial function in response to hypoxic stress in a tissue-specific fashion. I then explore this framework in three tissues which have distinct functional requirements in hypoxia, and in which I expected to find divergent changes in mitochondrial function and control of cellular pathways. Specifically:

Thermoregulation is a major energy drain in small rodents and non-shivering thermogenesis, mediated by brown fat mitochondria, may be decreased to save energy in hypoxia in small rodents. NMRs reduce body temperature (T_b) to ambient temperature (T_a) in hypoxia; therefore, in **Chapter 2**, I explore how NMR brown fat mitochondria are regulated in hypoxia *in vitro* and *in vivo.* I discovered that OXPHOS function is carefully reduced and that there is a rapid and robust downregulation of key thermogenic and metabolic proteins that are associated with mitochondrial membrane dynamics in hypoxic brown fat tissue. As a result, brown fat energy demands decrease and non-shivering thermogenesis ceases in hypoxia, providing key energy savings during hypoxia.

Like thermogenesis in brown fat, brain function is a major energy drain in small rodents; however, unlike thermoregulation, brain function is obligatory and must be maintained during hypoxia. It is already known that OXPHOS is downregulated in NMR brain mitochondria during hypoxia and so in **Chapter 3**, I evaluate neuroprotective mechanisms that support brain function in hypoxic NMRs. Specifically, I explore how the unique ultrastructure of NMR brain mitochondria supports a remarkably high Ca^{2+} buffering capacity relative to hypoxia-intolerant mouse brain, which enables the maintenance of respiratory function and prevents cell death in hypoxic NMR brain. Building upon this and previous work in hypoxic NMR brain, I then confirm in **Chapter 4** that NMR brain mitochondria are very tolerant to *in vitro* ischemia compared to mouse brain mitochondria, and thereby develop a new *in vitro* model in which to study how mitochondria contribute to hypoxia/ischemia tolerance in NMR brain.

Unlike brown fat and brain, skeletal muscle is relatively hypoxia-tolerant and regularly experiences periods of metabolic hypoxia during exercise. In adapting to environmental hypoxia, muscle is often deprioritized relative to O_2-sensitive tissues such as brain. However, NMRs remain active during prolonged periods of environmental hypoxia, suggesting that skeletal muscle function is sustained. Therefore, in **Chapter 5**, I explore how muscle mitochondria function changes with acute and prolonged hypoxia, to better understand the capacity of skeletal muscle to sustain exercise during acute and chronic hypoxia exposures in NMRs. Surprisingly, I find that skeletal muscle mitochondrial metabolism and mitochondrial function are barely impacted by hypoxia exposure, which would support sustained exercise in hypoxia but at the expense of maintaining high O_2 consumption by skeletal muscle in hypoxia.

Finally, in **Chapter 6**, I provide a systemic evaluation of the interplay between mitochondrial function across tissues in NMRs, and of their impact on hypoxia-tolerance in this fascinating species.

1 General introduction to hypoxia and hypoxia-tolerant animals

1.1 Hypoxia and pathologies related to low-O_2 stress

Hypoxia is a condition of reduced O_2 availability, at either the tissue or environmental level. Within tissues, hypoxia is usually defined as a state in which there is not enough O_2 to maintain cellular energy homeostasis. Such an imbalance may arise due to insufficient O_2 availability or supply, or excessive O_2 consumption, and tissue/cellular hypoxia is a common component of numerous diseases and pathologies (Hoppeler & Vogt, 2001; Peers et al., 2009; Thornton et al., 2017). Environmental hypoxia is usually defined relative to O_2 availability at sea level. As such, any environment in which O_2 availability is below ~ 21% may be considered hypoxic. There are many such hypoxic environments, including high-altitude niches (Lui et al., 2015), and densely populated or sealed underground burrows (Roper et al., 2001; Shams et al., 2005). Depending on the physiological or environmental cause, hypoxia can vary in duration from acute to chronic, or occur intermittently, while the intensity of hypoxia can be mild to severe.

Although there have been many studies of the impact of hypoxia on physiology, there is often confusion regarding the use of the terms "hypoxia" and "normoxia", due to the range of oxygenation at various steps along the O_2 transport cascade and the species-specific definition of what constitutes hypoxia to a given animal. For example, the O_2 level in "healthy" human tissues varies, e.g., from 1.1% in skin (superficial region) to 13.2% in arterial blood, and averages about 5%O_2 (Carreau et al., 2011). Thus, *ex vivo* experiments using cells or tissues in standard laboratory conditions near sea level (wherein ambient O_2 approaches 21%) are quite hyperoxic relative to the *in vivo* milieu. Furthermore, beyond O_2 gradients in a healthy animals and various environments, Therefore, for the purposes of my thesis, I define hypoxia as a level of ambient O_2 that is not sufficient to meet an organisms' metabolic demands, and for which physiological responses or adaptations are required.

Most widely studied laboratory animal models are intolerant of hypoxia, including mice (*Mus musculus*), rats (*Rattus rattus*), and most other adult mammals. However, several species, such as diving birds and mammals, experience acute hypoxia in their day to day lives (Allen & Vazquez-Medina, 2019; Bryan & Jones, 1980; Butler & Stephenson, 1988), while species that live at high altitude or in underground burrows may experience chronic or intermittent hypoxia (Dawson et al., 2018; Ivy et al., 2020; Lauren, 1995; Logan et al., 2020; Storz et al., 2019), respectively. Indeed, O_2 is naturally limited in many environments, such as at high altitude, in deep ocean habitats, and in subterranean tunnels (Semenza, 2007a). Species that live in these environments usually exhibit a remarkable suite of adaptations to hypoxia. For example, many specialists that exercise in hypoxic conditions are capable of increasing O_2 storage capacity in blood (Cabanac et al., 1999; Snyder, 1983), muscle (O'Brien et al., 1992; Polasek & Davis, 2001), and lungs (Lenfant et al., 1970; Tenney & Remmers, 1963; Widmer et al., 1997). However, increasing O_2 transport alone is not sufficient to sustain activity in prolonged hypoxia and often requires significant periods of rest to reset O_2 stores after intense exercise with limited O_2. Thus, species that experience longer-term or more regular but intermittent hypoxia often achieve a state of hypometabolism, which is perhaps the most critical strategy for coping with hypoxia (Hochachka, 2000). This concept is that animals reduce their O_2 consumptions and restrict hypoxic cell damages through a hypometabolic state, which requires careful coordination among probably all organs.

When considering the impact of hypoxia on physiology, it is important to consider the varying needs of different organs for O_2 and their sensitivity to periods of hypoxia. In this thesis, I focus upon the impacts of hypoxia on three major tissues with very different O_2 demands and sensitivities to hypoxia: BAT, which requires large amounts of O_2 to support non-shivering thermogenesis to maintain T_b in small mammals (Foster & Frydman, 1978; Orava et al., 2011), brain, which is almost exclusively dependent on ATP generated through mitochondrial OXPHOS (Siesjö, 1978), and is thus highly sensitive to O_2 availability (Thornton et al., 2017), and skeletal muscle, which regularly experiences exercise-induced and localized hypoxia and is thus relatively hypoxia-tolerant (Sahlin et al., 1987). This thesis examines mitochondrial adaptations to acute hypoxia in each of these organs.

1.2 Cellular oxygen sensing

Hypoxia can induce molecular changes to cellular components such as proteins within minutes and induce transcriptional change within a few hours (Dang & Myers, 2015; Semenza, 2011a). However, there is currently no clear consensus regarding the central underlying cellular mechanisms of oxygen sensing that initiate these responses. It can be argued that systemic hypoxia sensing occurs primarily via central and peripheral chemoreceptors, membrane-bound potassium channels, and sensors located in arterial mitochondria (Lahiri et al., 1995; Prabhakar & Overholt, 2000).

Cellular and genetic sensors of O_2 levels are stimulated both acutely and chronically by a change in O_2 availability. These sensors have been broadly studied and include a large number of molecules that enhance O_2 uptake and delivery (Bruick, 2003; Giaccia et al., 2004), and/or play important roles in mitochondria-related responses to hypoxia (Dang & Myers, 2015; Semenza, 2011a). For example, hypoxia inducible transcription factor-1 (HIF-1) senses hypoxia in the cell through a process that involves suppression of HIF-prolyl hydroxylase activity, which leads to the accumulation of HIF-1α (Kallio et al., 1997). As a result, when O_2 decreases, HIF-α binds to HIF-β to form a HIF complex that regulates hypoxia-related gene expression (Semenza, 2001). Other mechanisms, such as O_2-sensitive ion channels control a variety of cellular functions during hypoxia (Shimoda & Polak, 2011). It is likely that numerous components of most cells and some organelles are O_2-sensitive and thus that myriad systems and pathways can detect and respond to hypoxia. One of the most prominent detectors of O_2 are mitochondria, which are the primary hub of aerobic energy production.

1.3 Mitochondrial function in hypoxia

Mitochondria are major consumers of O_2 in the cell, wherein molecular O_2 is the final acceptor of electrons delivered by NADH and flavoproteins in the process of mitochondrial ATP production (Fuhrmann & Brune, 2017; Lenaz & Genova, 2010). Thus, mitochondrial energetics are tightly coordinated with O_2 availability. In addition to ATP production, hypoxia alters mitochondrial ROS and Ca^{2+} management, and mitochondrial membrane dynamics (Silverman, 1993; Waypa & Schumacker, 2010), while severe hypoxia may trigger mitochondrial-dependent apoptosis cell death (Wang & Youle, 2009).

Science's fascination with mitochondria spans more than 130 years. Mitochondria were first documented as bioblasts in 1890 (Altmann, 1890); in 1898, they were named mitochondria (Benda, 1898). Gradually, mitochondrial genetic inheritance (Payne, 1909), energy metabolism (Chance & Williams, 1955; Kingsbury, 1912), fission and fusion (Lewis & Lewis, 1915), Ca^{2+} uptake (Carafoli et al., 1966), and mitophagy (selective autophagy of mitochondria) (Kissova et al., 2004; Lemasters, 2005) were discovered. Along the way, it has become abundantly clear that mitochondrial function is central to many key processes within a cell.

1.3.1. Mitochondrial energetics. In mammals, up to 98% of O_2 consumption is related to OXPHOS, a process that occurs in the respiratory chain of mitochondria in the inner mitochondrial membrane (IMM) (Bennett et al., 2022; Silver & Erecinska, 1998). This respiratory chain is composed of five multi-subunit complexes, which are complex I (NADH–ubiquinone oxidoreductase), complex II (succinate dehydrogenase), complex III (ubiquinol–cytochrome c oxidoreductase), complex IV (cytochrome c oxidase) and complex V (ATP synthase), all of which are located in IMM invaginations termed 'cristae' (Zick et al., 2009). Coupled with electron transport function of respiratory complexes, the proton motive force (PMF) is a main component of mitochondrial membrane potential ($\Delta\psi_m$) and drives ATP synthesis. Electron transport pathways along respiratory complexes have been well studied (Guo et al., 2018; Letts & Sazanov, 2017); the state of electron transport is regulated by multiple mechanisms that are associated with cell fate, including activities and abundance of respiratory enzymes, cofactor levels (e.g. NAD^+/NADH, Ca^{2+}), and the most critical variable: O_2 availability (Bennett et al., 2022).

Mitochondria can enhance OXPHOS capacity at higher O_2 concentrations, whereas hypoxia depresses mitochondrial respiratory function and even reduces mitochondrial density in hypoxia-tolerant cells (Campian et al., 2004; Chiu et al., 2019; Zhang et al., 2008). For example, the function of OXPHOS components may be reduced under hypoxia, including reductions of citrate synthase (CS) activity and mitochondrial complex I content (Baracca et al., 2010; Baracca et al., 2007). In other cases, hypoxic cells adaptatively reduce O_2-expensive processes of phosphorylation to improve efficiency (Semenza, 2007b). In most adult mammals, it is apparent that mitochondrial ATP production may not satisfy cellular ATP consumption when the O_2 level is reduced below a certain level, *i.e.*, in hypoxia/ischemia, which can lead to the failure of ATP-dependent ion gradients, membrane potential depolarization, and consequential cell death (Knickerbocker & Lutz, 2001).

1.3.2. Mitochondrial redox regulation. Beyond regulation of energy production, mitochondria play key roles in the modulation of several second messenger systems, including ROS homeostasis. The term ROS refers to variety of molecules and free radicals, primary $O_2^{\bullet-}$, which is the precursor of most cellular ROS, including hydroxyl radicals ($HO^{\bullet}$), and hydrogen peroxide (H_2O_2) (Zorov et al., 2014). Mitochondrial ROS production was demonstrated for the first time in 1971 (Loschen et al., 1971), and mitochondria are now recognized as containing many of the major cellular sites of ROS production within complexes I, II, and III (Boveris & Chance, 1973; Mazat et al., 2020). The occurrence of complex I-produced ROS was initially debated under physiological conditions (Grivennikova & Vinogradov, 2006); however, numerous studies reported that defects of complex I are associated with mitochondrial disorders and serve as major sources of mitochondrial ROS generation (Abramov et al., 2007; Kushnareva et al., 2002; Maklashina et al., 2002; Perry et al., 1982; Smeitink et al., 2001). Complex II is not considered a major source for the production of ROS in resting conditions, partially because succinate in tissues is too low (~ μM) to produce significant amounts of ROS (Raha & Robinson, 2001). However, under hypoxia/ischemia, the tissue succinate level rises as much as 10-fold, which triggers reverse electron transport from complex II to complex I and results in substantial ROS production (Benzi et al., 1982; Chouchani et al., 2014; Wiesner et al., 1988). ROS production from complex III is complicated due to electron transport from complex I and II (Liu et al., 2010; Liu et al., 2002; Malinska et al., 2010; Muller et al., 2008).

Physiologically, ROS balance is well maintained and ROS are important cellular signals that initiate and/or participate in diverse cellular events through downstream signalling pathways and/or mitochondrial dynamics (Droge, 2002). Within the mitochondrial matrix, $O_2^{\bullet -}$ could be enzymatically converted to H_2O_2 by superoxide dismutase (SOD) (Palma et al., 2020). H_2O_2 can be reduced to water by peroxiredoxin (Prx) and glutathione peroxidase (Gpx). Both Prx and Gpx can transfer their redox state to thioredoxins and glutathione respectively, and then recycled back to a reduced cycle through utilizing electrons from NADPH coupled with mitochondrial respiration (Rhee et al., 2005). Mitochondria-independent ROS regulation, including antioxidants (vitamins C and E), and catalase, also play important roles in maintaining cellular homeostasis and preventing oxidative stress, but are beyond the scope of this thesis (Z. Liu et al., 2018; Salvi et al., 2007).

On the other hand, defects in ROS management can result in oxidant-induced cell damage, cell death, and even whole organ failure (Kozlov et al., 2011). For example, excessive $O_2^{\bullet -}$ and H_2O_2 may undergo Fenton chemistry with iron (Fe^{2+}) to form $HO^{\bullet}$, which causes cellular damage due to its highly reactive (Wardman & Candeias, 1996). Thus, mitochondrial ROS are important redox signaling molecules in both healthy physiological and pathophysiological processes (Andreyev et al., 2005; Finkel, 2012; Hamanaka & Chandel, 2010). Mitochondrial ROS are often central to hypoxic signalling cascades, including post-transcriptional and epigenetic regulators, kinases, and Ca^{2+} signals, among others. ROS also play a key role in regulating hypoxia-inducible factor (HIF) (Kietzmann & Gorlach, 2005; Pan et al., 2007). Many other transcription factors are ROS targets, including nuclear factor kappa B (NF-κB) and nuclear factor erythroid-2-related factor-2 (Nrf2), etc. (Kohlgruber et al., 2017). The direct or indirect ROS-dependent regulation of kinases is complex and may include post translational modifications (PTMs). For example, protein kinase C (PKC) activity is enhanced by tyrosine kinase Lck phosphorylation due to H_2O_2 (a member of the ROS family) (Konishi et al., 2001). ROS production and cytosolic Ca^{2+} homeostasis are also closely linked, which may affect ER-Ca^{2+} stress (Ramming et al., 2014), and mitochondrial-dependent apoptosis (Ferri & Kroemer, 2001). Together, regulation of various cellular targets by ROS is clearly crucial for adaptation to hypoxic environments, but also for the progression of hypoxia-linked diseases and pathologies like ischemia, inflammation, and cancer.

1.3.3. Mitochondrial Ca^{2+} handling. Coupling of mitochondrial matrix and cytosolic Ca^{2+} concentrations [Ca^{2+}] is critical to the regulation of OXPHOS and cellular signalling activities (Gellerich et al., 2010). Hypoxic conditions may cause decreased ER [Ca^{2+}] and increased mitochondrial and cytosolic [Ca^{2+}] (Chipurupalli et al., 2019; Mekahli et al., 2011). One of the primary mitochondrial means of buffering Ca^{2+} influx is via uptake of Ca^{2+} into the matrix of mitochondria through the mitochondrial calcium uniporter (MCU) complex (Lim et al., 2021). Hypoxic Ca^{2+} overload within the cytosol results in large-scale Ca^{2+} uptake into the mitochondria but this buffering capacity is finite and excessive Ca^{2+} accumulation within the mitochondrial matrix disturbs respiratory complex activity and disrupts mitochondrial membranes (Joza et al., 2001; Kroemer et al., 2007; Lim et al., 2021; Polster & Fiskum, 2004). These impacts also result in ROS overproduction. Importantly, it has become increasingly clear that hypoxic Ca^{2+} overload is critical to the opening of the mitochondrial permeability transition pore (mPTP) (Bernardi & Petronilli, 1996; Gunter et al., 1994; Kinnally et al., 2011; Zoratti & Szabo, 1995), which typically results from mitochondrial damage and subsequently induces cell death via mitochondria-mediated apoptotic pathways (Khaspekov et al., 1999; Matsumoto et al., 1999). Thus, mitochondrial Ca^{2+} regulation is clearly important for cell survival under hypoxic stress.

1.3.4. Mitochondrial dynamics. Along those lines, hypoxia alters mitochondrial fusion, fission, and mitophagy, which are referred to collectively as mitochondrial quality control or mitochondrial (membrane) dynamics (Eisner et al., 2018; Galluzzi et al., 2012). Mitochondria are highly dynamic organelles that are constantly undergoing fission and fusion, to maintain their size, shape, and cellular location (Pekkurnaz & Wang, 2022; Pickles et al., 2018). Although it is still under investigation, mitochondrial fusion could allow communication of mitochondrial matrix component (*i.e.*, mitochondrial DNA (mtDNA) and proteins) and enhancement of OXPHOS capacity (Mishra & Chan, 2016; Pickles et al., 2018). In normoxia, mitochondria produce ATP through OXPHOS in tubular networks (Friedman & Nunnari, 2014). During hypoxia, single mitochondrion appear due to fission, and even trigger mitophagy through selective autophagy pathways, all to help maintain mitochondrial integrity, Ca^{2+} buffering, and ROS concentration, as well as to reduce OXPHOS activity (Fuhrmann & Brune, 2017; Giacomello et al., 2020; Tilokani et al., 2018; S. Wang et al., 2022). For example, hypoxic fusion of mitochondria and enhanced network formation promotes protective effects and is associated with cell survival and proliferation (Archacka et al., 2021; Rambold et al., 2011). Interestingly, hypoxia-induced mitochondrial fission will trigger cell death in some cell types (Ong et al., 2010; Zhang et al., 2018), but could be a strategy of survival during hypoxia in others (Han et al., 2019; Parra et al., 2017).

Overall, mitochondrial function is tightly coupled to the dynamics of mitochondrial networks through complicated processes. Additionally, mitochondrial dynamics are regulated by not only cellular metabolism (which may be supressed during hypoxia), but also as downstream targets for cellular responses and adaptations that are associated with cellular signalling messengers and events, such as ROS-induced transcriptional processing and Ca^{2+} signalling. Thus, mitochondrial function and dynamics interact extensively with hypoxic conditions via various pathways.

1.4 The impact of hypoxia on BAT

Hypoxia can trigger adipose tissue dysfunction, including ROS (Zhang et al., 2011) and Ca^{2+} stress (Al-Anazi et al., 2018), and adipocyte death (Ye, 2009). Adipose tissue indirectly regulates systemic metabolism and plays critical roles in the development of metabolic diseases, such as ischemic stroke (Haley et al., 2017) and obesity (Cinti, 2006). When body fat content exceeds > 20% of body mass, adipose tissue hypoxia may occur and induce mitochondrial oxidative stress, inflammatory responses, and adipocyte death in adipose tissue (Ye, 2009; Zhang et al., 2011).

Beyond pathological effects of hypoxia, adipose tissue, and particularly BAT, is essential for non-shivering thermogenesis and cold acclimation-recruited norepinephrine-regulated thermogenesis in mammals, which involves oxidation of lipid and glucose fuels in mitochondria (Cannon & Nedergaard, 2004). BAT uses large amounts of O_2 for non-shivering thermogenesis to maintain T_b in mammals, and particularly small mammals (Foster & Frydman, 1978), and is therefore an O_2- and energetically-expensive process. For example, blood perfusion to BAT doubles in human during cold acclimation (Orava et al., 2011) and this tissue combusts large amounts of lipids and glucose (Cannon & Nedergaard, 2004), in addition, BAT is responsible for more than half of total non-shivering thermogenesis in rats acclimated to the cold (Foster & Frydman, 1978).

In hypoxia, most small animals reduce T_b to suppress metabolic demand and provide energy savings (Frappell et al., 1992; Tattersall et al., 2002). This can be achieved in many ways.

First, behavioural selection of lower temperatures may support reduced T_b in hypoxia and has been reported in hypoxic mice and rats to reduce T_b (Gordon & Fogelson, 1991). Other physiological responses, such as facilitating heat loss and the transfer of core body heat to the periphery, occurs in other rodents (Mortola & Feher, 1998; Tattersall & Milsom, 2003).

BAT is responsible for non-shivering thermogenesis through its thermogenic uncoupling protein1 (UCP1), and plays an important role in maintaining T_b, particularly in small heterothermic and homeothermic animals (Cannon & Nedergaard, 2004). In hypoxia or other hypometabolic conditions, many small mammals reduce T_b by suppressing non-shivering thermogenesis to preserve O_2 availability (Madden & Morrison, 2005; Mortola et al., 1999; Mortola & Naso, 1997; Tattersall & Milsom, 2009). For example, changes in the amount of BAT and the total mitochondrial content within BAT contribute to maintaining T_b in ground squirrels during hibernation and cold acclimation (Ballinger & Andrews, 2018; Barger et al., 2006; Milner et al., 1989). Similarly, a handful of studies report that acute hypoxia may interfere with BAT function (Martinez et al., 2010; Martinez et al., 2008); however, no studies have explored how BAT mitochondria contributes to T_b reduction in mammals experiencing acute or intermittent hypoxia.

The mechanisms via which non-shivering thermogenesis is regulated in hypoxia are complex and under active investigation. For example, in mice, several studies have demonstrated that hypoxia stimulates the expression and secretion of adipokines, enhances glucose uptake and elevates glycolysis in adipose tissue, and reduces BAT thermogenic capacity (Basse et al., 2017; Trayhurn & Alomar, 2015; Trayhurn et al., 2008). Furthermore, deletion of HIF2α, a transcription factor that senses O_2, may result in adipose tissue dysfunction, including insulin resistance, and dysfunction of mitochondrial UCP1 expression, resulting in a reduced thermogenic response to cold exposure (Garcia-Martin et al., 2016). Conversely, mechanisms of BAT regulation have received minimal attention in hypoxia-tolerant species and have not been explored in NMRs.

1.5 The impact of hypoxia on brain

Like adipose tissue, brain has a high metabolic demand and requires significant O_2 to function; however, brain is also particularly sensitive to hypoxia and most mammalian brains are rapidly and severely damaged when O_2 is limited for even a very short duration. Specifically, most adult mammals suffer brain damage and dysfunction after just a few minutes of hypoxia, resulting from reductions of ATP availability due to the impairment of aerobic metabolism, and the resulting inability to sustain ATP-dependent processes, such as ion pumping to generate neuronal membrane potential (Katsura et al., 1994). As neuronal membrane ion gradients run down, brain cells exhibit excitotoxicity, which is triggered initially by glutamate accumulation and involves Ca^{2+} and ROS imbalances (Lai et al., 2014). Downstream of this, hypoxia activates a wide range of cell death pathways, including autophagy, apoptosis, and necrosis, all of which are implicated in neuronal loss, which drives deficits in physical function during and following hypoxic or ischemic challenges to brain (Perez-Pinzon et al., 2012; Sekerdag et al., 2018; Thornton et al., 2017; Zarruk et al., 2018). Thus, although the severity, type, exposure duration, and frequency of hypoxia may vary, it is well-established that hypoxia is a critical factor in many neurological pathologies and diseases in hypoxia-intolerant mammals (Burtscher et al., 2021).

For example, hypoxia is a critical component of ischemic stroke, which accounts for larger than 80% of stroke cases (Virani et al., 2020). Ischemic stroke is associated with reduction/prevention of cerebral arterial blood flow due to clotting or obstruction in blood vessels, which reduces O_2 delivery to the affected area, resulting in hypoxia-ischemia brain damage.

Ischemic stroke is one of the leading causes of disability and is associated with long-term poor functional and clinical outcomes, such as lost function of memory and learning, and speech problems (Ferdinand & Roffe, 2016; Powers, 2020). Similarly, physical functions, such as motor speed and precision, may be negatively affected at altitude (hypobaric hypoxia) compared to sea level performance (Hornbein et al., 1989). Moreover, acute and chronic hypoxia can impair cognitive functions, including attention, and learning and memory in rodents and humans (Deguil et al., 2016; Turner et al., 2015; X. Wang et al., 2022). Additionally, cerebral hypoxia is a contributing factor to the detrimental impacts of many neurodegenerative diseases, including Alzheimer's disease and Parkinson's disease (Peers et al., 2009). For example, hypoxia arising from cardiovascular and respiratory disorders is associated with Alzheimer's disease through vessel damage (Kalback et al., 2004; Skoog & Gustafson, 2006). Similarly, exacerbation of respiratory failure is associated with subnormal sensitivity to hypoxia in Parkinson's disease patients (Onodera et al., 2000).

On the other hand, hypoxia-tolerant mammals can survive periods of hypoxic exposure without apparent brain damage and may employ multiple approaches to protect brain from low O_2 stress. For example, arctic ground squirrels decrease ventilation during hypoxia (7% O_2) (Ma et al., 2009), but their brain remains well oxygenated with no evidence of cellular stress, neuronal pathology, or oxidative modification during hypoxia (around 10% O_2) (Ma et al., 2005). Indeed, this tolerance extends beyond hypoxia to cerebral ischemia from asphyxia and cardiac arrest (Dave et al., 2006). The mechanisms underlying this tolerance are complex, and include OXPHOS-independent energy supply (Larson et al., 2014), which remains under investigation. Similarly, Brandt's voles do not have significant learning deficits or neuronal loss (Li et al., 2021) or apoptotic cell damage (X. J. Li et al., 2022) following hypoxic stress (5-10% O_2 for 6-48 h). On the other hand, hypoxia acclimation significantly changes (either enhances or reduces) their antioxidant responses on the molecular level, and these changes vary across tissues (*e.g.*, brain, liver, and kidney) (Shi et al., 2022). 13-lined ground squirrels can tolerant 4.5% O_2 more than 1 h (D'Alecy et al., 1990), partially due to a higher antioxidative capacity through sulfide:quinone oxidoreductase (SQOR) activity in brain (also in liver and heart) (Marutani et al., 2021). Thus, studies of adaptive mechanisms that mitigate the deleterious impact of hypoxia on the brains of hypoxia-tolerant species indicate that there are many potential neuroprotective mechanisms that can ameliorate the deleterious effects of environmental or systemic hypoxia in brain. Clearly studying these mechanisms in different hypoxia-tolerant species may be fruitful in advancing our understanding of how to protect mammal brain against low O_2 stress.

1.6 The impact of hypoxia on skeletal muscle

Skeletal muscle is the largest organ in the body for supporting physical activity (Pedersen, 2013). During exercise, skeletal muscle is a major O2 consumer in the body. For example, blood flow to exercising muscle increases > 30-fold (Bangsbo & Hellsten, 1998), and O_2 uptake can reach up to 350 mL min^{-1} kg^{-1} in active muscle (Bangsbo, 2000). As a result, skeletal muscle often experiences localized and acute hypoxia when exercising because O_2 supply cannot be sustained to match the metabolic demands of contracting muscle beyond a certain intensity of physical activity (Joyner & Casey, 2015). This exercise-induced local hypoxia is compounded when superimposed on hypoxia in animals that live and/or exercise in hypoxic environments (Hoppeler et al., 2003; Lundby et al., 2009). Indeed, beyond exercise, hypoxia in skeletal muscle may arise due to life in high altitude conditions or pathologies incorporating hypoxia (*e.g.*, diseases of the cardio-respiratory system associated with reduced arterial O_2 saturation (Chaillou, 2018)). In either case, and because of regular exposure to hypoxia in a normal physiological context when exercising, skeletal muscle is relatively tolerant to hypoxic conditions. However, although skeletal muscle experiences hypoxia regularly and is somewhat hypoxia-tolerant relative to other tissues, it may still exhibit damage during low O_2 stress. For example, ROS formation can lead to oxidative damage in hypoxic skeletal muscle during and after exercise (Bailey et al., 2004; Kerksick & Zuhl, 2015; Steinbacher & Eckl, 2015). This ROS imbalance is primarily due to low levels O_2 availability (Richardson et al., 1995), and related changes in redox state (Clanton, 2007; Sahlin et al., 1987).

The impact of hypoxia on skeletal muscle has been extensively investigated, including effects on the structure, metabolism, and function of skeletal muscle (Breen et al., 2008; Shortt et al., 2013; Slot et al., 2016). A general conclusion is that muscle composition and function following training in acute hypoxia, when not too severe, are similar but not identical to in normoxia (Bailey et al., 2000; Hoppeler & Vogt, 2001; Melissa et al., 1997). However, changes in muscle composition and function following hypoxic exposure depend on the training conditions and the fitness of the individuals, and often occur with repeated or prolonged exposure. For instance, hypoxic training (hypobaric hypoxia corresponding to an altitude of 2,300 m for 4 weeks; 3–4 training sessions of 30 min per day) significantly improves time to fatigue, and increases CS activity and myoglobin concentration (Terrados et al., 1990). Similarly, training under moderate normobaric hypoxic conditions (13.5% O_2, 8 weeks; 3 training sessions of 30 min per day) significantly enhances muscle CS activity when compared to training under normoxic conditions (Melissa et al., 1997). However, hypoxic training may not significantly change skeletal muscle structure and function beyond changes induced by normoxic training (Lundby et al., 2009). For example, some studies suggest that there is no difference in myoglobin concentration, muscle fiber composition, capillarity, or CS activity following hypoxia training (hypobaric hypoxia corresponding to an altitude of 2,500 m for 8 weeks, 1 training sessions of 15 min every two days) (Masuda et al., 2001).

Chronic hypoxia may induce various adaptive responses in skeletal muscle, including enhanced enzyme activity and function (Jackson et al., 1987; Reynafarje, 1962). On the other hand, several studies suggest that decreases in fiber size and muscle atrophy might be a direct consequence of chronic hypoxia exposure (Hoppeler et al., 1990; Kayser, 1992; MacDougall et al., 1991). At the cellular level (in C2C12 skeletal muscle cells), *in vitro* hypoxia may promote muscle differentiation and hypertrophy by increasing the expression of related proteins (*e.g.*, myogenin, mammalian target of rapamycin (mTOR), and ribosomal protein S6 kinase beta-1) (Sakushima et al., 2020). Additionally, hypoxic training may increase mitochondrial density (Vogt et al., 2001), and improve mitochondrial coupling between energy utilization and production sites, but may not alter mitochondrial function (Ponsot et al., 2006). Increases in mitochondrial density and respiratory efficiency might result in increased mitochondrial enzyme activity in some cases, and physiologically provide a tighter integration between ATP demand, supply, and antioxidative capacity under hypoxia (*i.e.*, exercise-induced muscle hypoxia). In hypoxia-tolerant mammals, chronic or lifelong exposure to hypoxia may impact skeletal muscle. For example, deer mice (*Peromyscus maniculatus*) skeletal muscle has a unique phenotype that contributes to their hypoxia-tolerance, *e.g.*, enhanced mitochondrial respiratory capacity and O_2 affinity (Dawson & Scott, 2022; Nikel et al., 2018).

In addition, skeletal muscle is the source of shivering thermogenesis, which is the most effective way of heat production in cold conditions (Stocks et al., 2004). Unfortunately, very few studies have examined hypoxia-mediated changes in shivering thermogenesis, although a recent study in humans suggested that the combination of cold and hypoxia expedited the onset of shivering, possibly due to a faster cooling rate in hypometabolic conditions (Arnold et al., 2021).

In summary, environmental hypoxia and training in hypoxia likely enhances muscle function and therefore hypoxia tolerance, but the impact of such training is highly variable depending on the duration of training and hypoxia, the depth of hypoxia exposure, and the muscle and species under study. Broadly, the cellular and molecular changes underlying these effects warrants further study and these putative adaptations have received particularly minimal attention in hypoxia-tolerant species that experience chronic or intermittent hypoxia in nature.

1.7 Adaptations supporting hypoxia-tolerance in NMRs

In addition to those discussed above, there are numerous species that have received considerable study as model organisms of hypoxia-tolerance. Perhaps one of the most well-studied hypoxia-tolerant small mammal model organisms are NMRs, which are the primary subject of my thesis. NMRs are among the most hypoxia-tolerant mammals identified. Notably, the O_2 concentration in NMR burrows has not been well-characterized, however, it is reasonable to speculate that variable hypoxia should be exist due to large numbers of individuals respiring in a confined area (Buffenstein et al., 2022; Holtze et al., 2018; Šumbera et al., 2006). Nonetheless, in a laboratory setting NMRs can tolerate minutes of anoxia (Park et al., 2017), hours at 3% O_2 (Pamenter et al., 2018), and weeks at 8-10% O_2 (Chung et al., 2016). Moreover, NMRs can maintain physical activity and consciousness in anoxia for 100 s, and then recover within 4-6 min, whereas mice die from the same treatment (Hartung & Cottrell, 1987; Ilacqua et al., 2017).

In support of this tolerance, NMRs have a low resting metabolic rate (O'Connor et al., 2002), and like many other hypoxia-tolerant animals (Frappell et al., 1992), they drastically supress

O_2 consumption as a key defense strategy to cope with hypoxia. For example, during acute hypoxia (4 h, 3% O_2), the whole animal metabolic rate of NMRs is depressed >85% (Pamenter et al., 2018). On the other hand, NMRs maintain basic physiological functions during hypoxia, including physical activity such as movement and work (*e.g.*, digging) within their environment, albeit at a reduced level. This ability is partially supported by a high O_2 affinity for hemoglobin (Johansen et al., 1976), but there is also considerable emerging evidence that NMRs employ tissue-specific responses to adapt to hypoxia and prioritize the function of some tissues over others (and even some regions within a given tissue) when O_2 is limited (Pamenter, 2022).

1.7.1. Thermoregulatory adaptations to hypoxia in NMRs There were two reported mechanisms of maintaining T_b in NMRs, ectothermic mechanisms of huddling (S. Yahav & R. Buffenstein, 1991) and endothermic heat-generating mechanisms using BAT (Daly et al., 1997) for non-shivering thermogenesis (Hislop & Buffenstein, 1994). Recently, shivering and BAT-dependent non-shivering thermogenesis were proposed to contribute to the maintenance of T_b at low T_a (20°C) in NMRs (Oiwa et al., 2020). NMRs are mammals with relatively low T_b and basal metabolic rate relative to other small mammals (e.g., mouse and rat) that live in an environment with relatively variable T_a (< 25 °C to > 45 °C) (Holtze et al., 2018). Under hypoxia conditions, NMRs reduce T_b to near ambient levels (Ilacqua et al., 2017; Kirby et al., 2018; Pamenter et al., 2019a), and this change is not due to mechanisms of evaporative cooling or vasodilation (Vandewint et al., 2019). Thus, it is highly possible that NMR may suppress non-shivering thermogenesis to reduce T_b in hypoxia. Indeed, we recently noticed that rapidly turn off non-shivering thermogenesis in brown fat tissue within 1 h of 7% O_2 exposure (Sebaa & Harper, 2020). However, the underlying mechanisms are unclear.

1.7.2. Adaptation to hypoxia in NMR brain Consistent with whole animal O_2 consumption repression, NMR brain mitochondrial respiratory capacity also exhibits an equal depression *in vitro* (Pamenter et al., 2018). Also in brain, Na^+/K^+ ATPase activity is regionally regulated, and overall activity is reduced during *in vivo* acute hypoxia ((3% O_2 for 4 h; (Farhat et al., 2021) and see Chapter 3). Notably, ATP concentration in NMR brain does not change during acute hypoxia, indicating that a new energetic balance is achieved, but creatine phosphate is > 2-fold higher (Pamenter et al., 2019a), which suggests that there may be other sources of ATP production aside from mitochondrial OXPHOS. Recently, next-generation sequencing indicated that *in vivo* acute hypoxia (7% O_2 for 4 h) coordinates anaerobic glycolytic fuel sources and induces anaerobic glycolysis in NMR brain, while also suppressing energy expensive processes, such as *de novo* protein translation and cellular proliferation (Hadj-Moussa et al., 2021b). Several additional pathways may help conserve O_2 and ATP in hypoxic NMR brain, such as reducing protein biosynthesis regulated by the Akt/mTOR pathway (Al-Attar et al., 2020), suppressing ATP-dependent heat shock proteins (Nguyen et al., 2019), modifications of glycolysis and immune function via the peptidylarginine deiminase (PAD) family (Pamenter et al., 2019b), and microRNA-mediated changes to various metabolic pathways (Hadj-Moussa et al., 2021b).

Importantly, there is no evidence of brain damage in NMR brain during acute or chronic hypoxia exposure. For example, hypoxic NMR brain exhibits minimal changes in DNA, RNA, and protein oxidation, but instead upregulates antioxidant capacity (Hadj-Moussa et al., 2022). In hypoxic NMR brain, HIF1α-induced downstream proteins involved in neuroprotection, cell-cycle arrest, and the promotion of antiapoptotic functions are widely upregulated (Hawkins et al., 2019).

Finally, hypoxia-mediated alterations in Akt/mTOR pathway may also inhibit hypoxia-induced apoptosis in NMR brain (Al-Attar et al., 2020).

Importantly, whereas key cellular messaging systems are deleteriously deranged by hypoxia/ischemia in hypoxia-intolerant mouse brain (see above), these systems are largely kept in homeostasis in NMR brain. For example, *in vitro* hypoxia or ischemia do not induce any changes in neuronal nitric oxide (NO) (Wang et al., 2020) or ROS in NMR brain (Eaton et al., 2022). NO is a form of reactive nitrogen species that can induce excessive nitrosative stress in hypoxic/ischemic brain (Ridnour et al., 2004), and, in conjunction with other ROS, results in hypoxic oxidative stress (Lubos et al., 2008). In addition, NMR neurons maintain synaptic transmission under severe *in vitro* hypoxia and even recover from 30 min anoxia (Larson & Park, 2009),

Similarly, Ca^{2+}, which is a key cellular second messenger but also triggers hyperexcitability, hypoxic/ischemic NO bursts (Peeters-Scholte et al., 2002), and increased ROS (Gorlach et al., 2015) in the brain of hypoxia-intolerant species, is better maintained in NMR brain. For example, less Ca^{2+} influx occurs in NMR brain neurons than mouse neurons during *in vitr*o hypoxia (Peterson et al., 2012a). The mechanisms of how hypoxic NMR brain restrict elevation of cytosolic [Ca^{2+}] is largely unclear, but is perhaps partially due to relatively high expression of neonatal N-methyl-D-aspartate receptor (NMDAR) GluN2D subunits (Peterson et al., 2012b), a glutamate receptor which permits lower rates of glutamate-induced Ca^{2+} influx (Dingledine et al., 1999).

1.7.3. Adaptations to hypoxia in NMR skeletal muscle reduce but do not cease physical activity (including time spent active and movement velocity) when acutely exposed to hypoxia (Ilacqua et al., 2017). This means that likely reduce O_2 consumption by suppressing physical activity, but how the energetic balance of skeletal muscle is impacted by hypoxia in remains unclear. A key mechanism for modulating cellular energetics is the AMP-activated protein kinase (AMPK) pathway, which is a regulator that regulates energy production through glucose uptake and fat oxidation when glycogen levels are low (Long & Zierath, 2006). It is notable that AMPK function is inhibited in hypoxic NMR muscle (Hadj-Moussa et al., 2021a). In addition, the Akt/mTOR pathway is suppressed in hypoxic muscle (Al-Attar et al., 2020), which would support energy preservation. Indeed, glucose and ATP concentration re not reduced but creatine phosphate accumulates in hypoxic skeletal muscle (Pamenter et al., 2019a). Together, it is reasonable to speculate that hypoxic NMR skeletal muscle might suppress glucose uptake from blood to preserve O_2 consumption, and instead use other sources of energy, such as anaerobic metabolism, to maintain physical activities. This warrants further study.

Beyond functional regulation of muscle activity in hypoxia, it is also notable that oxidative damage is a common consequence of hypoxia in muscle. However, minimal oxidative stress damage occurs in hypoxic NMR muscle (Hadj-Moussa et al., 2022). In addition, H_2O_2 consumption rates are around two-fold greater in NMR skeletal muscle than mouse (Munro et al., 2019). These findings suggest that NMR skeletal muscle may be regulated in some fashion in hypoxia. As major O_2 consumers and ROS generators, mitochondria and how mitochondrial functions are changed in hypoxic NMR skeletal muscle warrants further study.

1.8 Study hypothesis and significance

The main objective of this thesis is to explore mitochondria-related mechanisms of hypoxia-tolerance in NMR brown adipose, brain, and muscle tissues. As discussed in the previous sections, various tissues may have divergent responses to hypoxia due to their physiological functions, while mitochondria have tissue-specific variations of energy metabolism (Kappler et al., 2019), mtDNA density (Herbers et al., 2019), enzyme activity (Karahalil et al., 2002), ROS production (Panov et al., 2007), Ca^{2+} management (Patron et al., 2019), and responses to stresses (Holmstrom et al., 2012; Pacheu-Grau et al., 2018).

1.8.1. BAT. Recently, functional BAT was reported in NMRs, which contributes to the maintenance of T_b (Oiwa et al., 2020). The primary regulator of non-shivering thermogenesis in BAT is UCP1, which induces a proton leak to generate heat (Bertholet & Kirichok, 2022). Thus, we became interested in how BAT mitochondria are involved in this hypoxia-induced heat reduction. **We hypothesized that** the respiratory function of NMR BAT would be downregulated in hypoxia. We further hypothesized that this downregulation would be mediated by changes in mitochondrial membrane dynamics that initiate hypoxic responses and regulate UCP1 and respiration chain protein expression or function. **We predicted that** 1) hypoxic mitochondria should have active fission and/or mitophagy, which in turn would 2) suppress mitochondrial respiration due to functional protein degradation but 3) increase mitochondrial oxidative stress due membrane damage.

1.8.2. Brain. Suppression of *in vitro* mitochondrial function during hypoxia occurs in NMR brain (Pamenter et al., 2018), which was proposed to be a mechanism of conserving O_2 and reducing energy demands to tolerate hypoxia. Like BAT, no study has assessed how NMR brain mitochondrial dynamics change in hypoxia, or what regulates mitochondrial metabolic suppression in hypoxic NMR brain. **We hypothesized that** NMR brain mitochondria may have different membrane dynamics relative to a hypoxia-intolerance rodent, i.e., mouse. **We predicted**

that 1) hypoxic NMR brain mitochondria will have no or reduced damage during *in vivo* hypoxia, and 2) improved Ca^{2+} management relative to mouse brain under the same conditions. As a result, 3) NMR brain mitochondria may have better resistance to ischemia stress than mouse.

1.8.3. Muscle. NMRs reduce O_2 consumption and physical activity in hypoxia but stay somewhat active and can recover activity within one hour (Houlahan et al., 2018; Ilacqua et al., 2017; Pamenter et al., 2019a). Thus, **we hypothesized that** NMR skeletal muscle mitochondrial respiratory function should exhibit minimal changes during acute hypoxia. **We predicted that** skeletal muscle mitochondria will 1) not alter OXPHOS capacity to support sustained activity under hypoxia and reoxygenation but will instead 2) regulate ROS production to prevent or reduce oxidative stress damage. In addition, we predicted that 3) NMR skeletal muscle mitochondria will maintain a stable respiratory capacity under chronic hypoxia (Buffenstein et al., 2022).

To test my hypotheses, I examined mitochondrial respiratory function between normoxic and hypoxic conditions, including O_2 consumption capacity, and H_2O_2 emission (an indirect method of assessing net $O_2^{\cdot -}$ production, which provides insight into mitochondrial electron transport regulation). In addition, I evaluated mitochondrial Ca^{2+} uptake capacity, and how extra-mitochondrial Ca^{2+} affects $\Delta\psi_m$ and OXPHOS function. In addition, I studied adaptive changes in mitochondrial dynamics in acute hypoxia *in vivo*. Specifically, I evaluated mitochondrial membrane dynamic protein changes and morphological changes in normoxic and hypoxic mitochondria.

These assessments were performed across brown adipose, brain, and muscle tissues. Multiple methods were applied according to the specific responses of each tissue, and the extent and durations of hypoxia (O_2 availability) was chosen to reveal responses specific to each tissue and species. Overall, we did not report ground-breaking mechanisms in every tissue, however, we provided a comprehensive picture of hypoxia-tolerant strategies at the mitochondrial level among multiple tissues in NMRs. Notably, whereas some of the mechanisms we describe are like those reported in other animals (e.g., mitochondrial respiration suppression), others are reported for the first time in any species in this thesis, (*e.g.*, very rapid changes of UCP1 density in BAT, unique means of mitochondrial Ca^{2+} management in brain, and the first report of mitochondrial nanotunnel systems in the brain of any species). In addition, we include a case study of hypoxia/ischemia brain damage in NMRs *in vitro*, which supports the hypothesis that mechanisms that are neuroprotective against natural environmental hypoxia also confer protection against clinically relevant ischemic stresses in this species.

2 NMR intrascapular BAT function in hypoxia: heat production, mitochondrial dynamics, and mitochondrial respiration

Part of the data from this chapter are published in:

Cheng, H., Sebaa, R., Malholtra, N., Lacoste, B., El Hankouri, Z., Kirby, A., Bennett, N. C., van Jaarsveld, B., Hart, D. W., Tattersall, G. J., Harper, M. E., & Pamenter, M. E. (2021). Naked mole-rat brown fat thermogenesis is diminished during hypoxia through a rapid decrease in UCP1. *Nature communications*, *12*(1), 6801. https://doi.org/10.1038/s41467-021-27170-2

Statement of contribution:

Rajaa Sebaa completed 1/3 of the western blot replicates in Fig 2.5 C&D.

Baptiste Lacoste analyzed the electron microscopy data in Fig 2.6.

Alexia Kirby, Glenn Tattersall, and Nikita Malholtra conducted the FLIR imaging experiments in SF. 2.1-2.3.

Ziyad El Hankouri conducted the immunohistochemistry experiments and analysis in SF. 2.4.

Matthew Pamenter, Mary-Ellen Harper, and Glenn Tattersall conceived of the study; Mary-Ellen Harper, Rajaa Sebaa, and I collected tissue for western blot and immunohistochemistry assays; Matthew Pamenter wrote the manuscript in published article.

I conducted the remainder of the work for this publication.

We would like to thank Drs. S. Kelly Sears and Jeannie Mui from the Facility for Electron Microscopy Research at McGill University for TEM services and Dr. Ryan Russell, University of Ottawa, for expert advice on electron micrograph analyses. We would also like to thank Dr. Michael Downey and Alix Denoncourt, University of Ottawa, for their assistance with co-immunoprecipitation experiments.

2.1 Introduction

The primary mechanism of cold-induced thermogenesis in small mammals is UCP1-mediated mitochondrial uncoupling in BAT (i.e., non-shivering thermogenesis). There is no agreement on the exact mechanisms of action of UCP1 function (Nedergaard & Cannon, 2018); however, the net outcome of UCP1 activity corresponds to proton transport (Nedergaard et al., 2001). This means that protons that were pumped out of the mitochondria matrix by the electron transport chain (ETC) can re-enter mitochondria, and mitochondrial respiration (O_2 consumption and electron transport) can therefore proceed uncoupled from and ATP-synthesis (Argyropoulos & Harper, 2002; Nedergaard et al., 2001). As a result, the $\Delta\psi_m$ is dissipated and the resulting futile cycle of proton pumping to regenerate this gradient results in increased heat generation due to the innate inefficiency of this biological process, which produces heat as a waste biproduct. In inactivated adipose tissue, UCP1 is inhibited by a purine nucleotide di- or triphosphate on the cytoplasmic side (Nicholls, 1976), and typically, GDP is applied to isolated mitochondria to inhibit UCP1 in experimental conditions (Nedergaard & Cannon, 2018). Mechanisms of UCP1 activation and its control still remain to be clarified, but may include an increased ADP/ATP ratio (Xie et al., 2017), and/or fatty acids (Shabalina et al., 2004).

Cold-induced thermogenesis is among the most energy-intensive processes in small mammals, e.g. around 60% of total cardiac output is directed to BAT depots in cold-acclimated rats (Foster & Frydman, 1978). NMRs expend considerable energy to thermoregulate outside of their thermoneutral zone and several studies have reported their ability to maintain T_b well above T_a in a range of temperatures (T_b -T_a differential ranging from 0.0 to >13.0°C in animals exposed to T_as ranging from 37-10°C) (Buffenstein & Yahav, 1991; Daly et al., 1997; Mcnab, 1966;

Withers & Jarvis, 1980; Shlomo Yahav & Rochelle Buffenstein, 1991). In addition, huddled NMRs consumed less O_2 than individuals to maintain the same T_b (Withers & Jarvis, 1980).

Mammals, including humans, employ thermoregulatory strategies to reduce T_b and facilitate reduced metabolic demand in hypoxia (Frappell et al., 1992; Kottke et al., 1948; Mortola, 1993; Steiner & Branco, 2002). For example, animals may move to colder environments in hypoxia to gain antipyretic energy savings, decrease their T_b set point, and/or shut off thermogenic behaviours such as shivering and non-shivering thermogenesis as described in previous chapter (Ballinger & Andrews, 2018; Gordon & Fogelson, 1991; Milner et al., 1989; Mortola & Feher, 1998; Tattersall & Milsom, 2003). Intriguingly, earlier studies in our lab demonstrated that NMRs also reduce their T_b in hypoxia. Specifically, NMRs significantly reduce T_b during hypoxia independent to T_a (Ilacqua et al., 2017; Kirby et al., 2018), and the extent of T_b reduction is negatively related to environmental O_2 from 9-3% (Pamenter et al., 2019a). However, NMRs prefer a warmer environment, even if in hypoxia and at the expense of potential energy savings. For example, they choose warmer (38°C) but not colder (20°C) chambers during a hypoxic episode (Kirby et al., 2018). Importantly, hypoxic NMRs significantly reduce time spent active, movement speed, and huddling behaviours in hypoxia, although these changes are minor or absent in grouped animals (Houlahan et al., 2018). In addition, inhibiting radiative and evaporative cooling strategies does not alter the hypoxic change in T_b (Vandewint et al., 2019). Therefore, NMRs do not employ behavioural or vascular strategies in support heat loss in hypoxia.

Although a previous study suggested that NMRs are poikilothermic, more recent work has demonstrated that NMRs express functional BAT and are more accurately labelled as heterotherms (Oiwa et al., 2020). Recently, it was demonstrated that acute hypoxia (1 h of 7% O_2 exposure) diminishes interscapular thermogenesis in NMRs (SF. 2.1), via a mechanism by which thermogenic and metabolic proteins in iBAT may be downregulated during hypoxia (Sebaa & Harper, 2020). Specifically, hypoxic (1 h of 7% O_2 exposure) NMRs decrease iBAT thermogenesis at temperatures near or below thermoneutrality, mediated by a significant reduction in iBAT levels of UCP1 and OXPHOS proteins (Sebaa & Harper, 2020).

Based on these studies, we posited that hypoxic NMR iBAT mitochondria might selectively suppress functional O_2 consumption and the proteins related to non-shivering thermogenesis and mitochondrial respiratory function (i.e., UCP1 and OXPHOS proteins) through unknown mechanisms. We suspected that the ubiquitin-proteasome system (UPS) might lead to the rapid degradation of thermogenic proteins, however, no directly evidence was found (Sebaa & Harper, 2020). Another mechanism that had not been tested is mitophagy, a type of mitochondrial dynamic that is involved in the regulation of BAT mitochondrial homeostasis in mouse, and which impacts BAT heat production, mitochondrial O_2 consumption, ROS flux, and Ca^{2+} management (Kazak et al., 2017; Ko et al., 2021; Lu et al., 2018; Moore et al., 2022).

Due to the significant reductions of thermogenesis in hypoxic NMRs, **we hypothesized** that iBAT mitochondrial function would be changed in hypoxia and predicted that O_2 consumption and also mitochondrial functions including ROS homeostasis and Ca^{2+} management, may also be altered. W**e also hypothesized that** mitochondrial dynamics participate in the reductions of thermogenic proteins. To test these hypotheses, we assessed mitochondrial respiration, H_2O_2 emission, and Ca^{2+} buffering *in vitro* and also measured changes protein expression and mitochondrial morphology following *in vivo* hypoxia using western blots and transmission electron microscopy (TEM), respectively.

2.2 Methods

2.2.1 Ethics approval

NMRs were group-housed in interconnected multi-cage systems at 30°C and 21% O_2 in 50% humidity with a 12L:12D light cycle. Animals were fed fresh tubers, vegetables, and fruit, and Pronutro cereal supplement *ad libitum*. Animals were not fasted prior to experimental trials. All experimental procedures were approved by the University of Ottawa Animal Care Committee in accordance with the Animals for Research Act and by the Canadian Council on Animal Care. Non-breeding (subordinate) NMRs do not undergo sexual development or express sexual hormones and thus we did not take sex into consideration when evaluating our results (Holmes et al., 2009).

2.2.2 In vivo acute hypoxia treatments

Subordinate NMRs (adult, 1-2 years old) were exposed to one of four treatment conditions: normoxia (21% O_2, balance N_2), acute hypoxia (4 h, 5%; or 1 h, 3 h, or 4 h in 7% O_2, balance N_2), or hypoxia followed by reoxygenation (4 h in 7% O_2 followed by 21% O_2, balance N_2). Animals were not provided with food during the hypoxic treatment periods.

2.2.3 Collection and analysis of thermographic data

FLIR thermal images were captured directly to radiometric video files using an infrared thermal imaging camera (Make: FLIR, Model: SC 660, Teledyne FLIR, LLC, Wilsonville, OR, USA) connected to a computerized acquisition program (Thermacam Researcher Pro v 2.9, Teledyne FLIR). Images were captured every 10 s throughout the experimental period. Image analysis was as described previously (Greenberg et al., 2012; McCafferty et al., 2013). Briefly, emissivity was assumed to be 0.96, air temperature and reflected environment temperatures were set to 20, 30, or 36 °C, as appropriate, relative humidity set to 50%, the object distance set to 0.35 m, and the transmittance of the Germanium IR window set to 0.95 (determined empirically). Image analysis was conducted by a blinded researcher using images taken every fifth minute during the experimental period, and by drawing regions of interest over the interscapular and hind back regions. Average temperatures across the entire drawing regions of interest were extracted and quantified. Data were corrected using the Thermimage package V3.0 in R. Body temperature measurements. Body temperature was measured using a handheld RFID reader that scanned individual naked mole-rats instrumented with subcutaneous RFID microchips (Destron Fearing, Dallas, TX) every 10 min, with microchip implantation and validation described previously (Kirby et al., 2018).

2.2.4 Tissue collection for molecular biology assessments

Immediately following treatment, animals were sacrificed by cervical dislocation followed by immediate decapitation. iBAT was rapidly dissected on ice and snap-frozen and stored at −80 °C until it was used for the western blot, qPCR, and enzymes activity analysis.

2.2.5 iBAT Mitochondrial isolation

Whole experiment was performance at 4°C or on ice. Isolated mitochondria were used immediately for assessment of respiration and Ca^{2+} titration; and aliquots were frozen at −80°C for subsequent enzyme assays.

iBAT (~200 mg) was rapidly dissected on ice following cervical dislocation and decapitation, minced using scissors and then gently homogenized using a glass mortar with a Teflon pestle (10 strokes) in 2 ml homogenization buffer (250 mM sucrose, 1 mM EGTA, 10 mM HEPES, 1mg/ml BSA, pH 7.4) (McFarlane et al., 2017). Homogenization was then centrifuged for 10 min at 5,000 g. Top fat layer was discarded followed by resuspended pellet in ice-cold homogenization buffer and centrifuged for 5 min at 600 g. Supernatant was transferred to a clean, ice-cold tube, and then centrifuged at 5,000 g for 5 min. Discard clear supernatant and the mitochondria were resuspended in ice-cold Tris solution (~200 µl, KCl 105 mM, Tris-HCl 50 mM, pH 7.1).

2.2.6 Isolated iBAT mitochondrial respiration and H_2O_2 emission

Rates of O_2 consumption and H_2O_2 emission were monitored simultaneously using an Oroboros O2k (Oroboros, Innsbruck, Austria) equipped with a fluorescence detection module mounted with the appropriate excitation and emission filters for the fluorescent probe Amplex UltraRed (AUR), as described previously (Cheng, Munro, et al., 2021). Briefly, AUR (10 µM), SOD (10 IU/ml), and horseradish peroxidase (2 IU/ml) were added to 2 ml respiration medium containing (in mM): KCl 120, HEPES 20, KH_2PO_4 20, $MgCl_2$ 2.5, EGTA 1, and BSA 0.045; pH 7.2, followed by isolated mitochondria (~20 µg protein/ml, biuret method), and held at 32°C. An O_2 range of 200 µM to 80 µM in the air-saturated medium was maintained during the whole measurement (Makrecka-Kuka et al., 2015).

Baseline values for O_2 consumption and H_2O_2 production were measured following addition of mitochondria to chambers without effectors. Substrate-uncoupler-inhibitor titration (SUIT) protocols were sequentially performed as indicated below.

SUIT1 evaluated mitochondrial respiration through the pyruvate dehydrogenase complex pathway, and outer-mitochondrial membrane integrity. The following components were added sequentially: pyruvate/malate to induce UCP1-dependent respiration by carbohydrates from complex I, GDP to block UCP1-dependent respiration, ADP to induce OXPHOS respiration from complex I, cytochrome c to assess outer-mitochondrial membrane damage.

SUIT2 evaluated mitochondrial respiration through the fatty acid oxidation pathway and complexes I–II maximal capacity. The following components were added sequentially: octanoylcarnitine/malate induce UCP1-dependent reparation by fatty acid, GDP to block UCP1-dependent respiration, ADP to induce OXPHOS respiration, pyruvate and glutamate to induce maximal OXPHOS respiration from complex I, succinate to induce maximal OXPHOS respiration from complexes I&II, CCCP to induce maximal electron transport capacity from complexes I&II.

SUIT3 evaluated mitochondrial respiration through the succinate dehydrogenase complex pathway and complex IV maximal capacity. The following components were added sequentially: succinate to induce UCP1-dependent respiration by carbohydrates from complex II, GDP to block UCP1-induced respiration, rotenone to block complex I, ADP to induce OXPHOS respiration from complex II, antimycin A followed by ascorbate/TMPD to induce maximal complex IV capacity.

Table 2.1 Substrates for mitochondrial SUIT protocols

Substrates	Abbreviation	Working concentration
Malate	M	2 mM
Pyruvate	P	5 mM
Succinate	S	10 mM
Octanoylcarnitine	Oct	0.5 mM
Ascorbate	ASC	2 mM
TMPD	TMPD	0.5 mM
Cytochrome *c*	CytC	10 µM
ADP	D	1 mM
GDP	G	1 mM
CCCP	U/CCCP	0.5 or1 µM steps to max responses
Antimycin A	AA	2.5 µM
Rotenone	R	0.5 µM

Saturating concentrations were determined in pilot experiments (data not shown). Preparation of all substrates were as per (Fontana-Ayoub et al., 2016).

In other experiments, rates of fluorescent product (resorufin) formation were converted to micromoles of H_2O_2 based on a three-point standard curve conducted with isolated mitochondria alone and by direct addition of 0.1 µM H_2O_2 twice to the chamber.

2.2.7 Ca^{2+} uptake experiment

Ca2+ uptake by isolated iBAT mitochondria (~20 µg protein/ml, biuret method) was estimated with the Ca^{2+} sensitive Calcium green 5-N fluorescent dye using an Oroboros and methods modified from (Spinazzi et al., 2019) at physiological temperatures (32°C). Ca^{2+} titrations were measured in an EGTA free medium (in mM: KCl 120, HEPES 20, KH_2PO_4 20, $MgCl_2$ 2.5, NaCl 5, and BSA 0.03, 1 µM Calcium green 5-N; pH 7.2). Substrates combinations including 10 mM glutamate, 5 mM pyruvate, 5 mM malate, 1 mM GDP, 1 mM ADP, and individual experiments were performed using different substrate combinations (including glutamate/pyruvate/malate/GDP/ADP (UCP1-independent), glutamate/pyruvate/malate, glutamate/pyruvate/malate/ADP (UCP1-dependent), glutamate/pyruvate/malate/GDP (membrane potential dependent)). Following 5-10 mins equilibration, mitochondria were exposed to Ca^{2+} titrations (20 µM per bolus, with 5 mins following the first injection and 2 min following each subsequent injection), and fluorescence reductions represented mitochondrial Ca^{2+} uptake. mPTP opening was detected as a fluorescence increase and the overall titrated Ca^{2+} represented as maximal Ca^{2+} resistance capacity. Ca^{2+} uptake rates were calculated within first 5 mins of fluorescence reducing using "One phase decay-equation" in GraphPad Prism 9 (GraphPad Prism, La Jolla, CA, USA).

2.2.8 Na^+/K^+-ATPase activity measurement

Frozen tissue was weighed (~50 mg) and homogenized on ice with a sonicator in a 4:1 SEI:SEID buffer (SEI: 250 mM sucrose, 10 mM EDTA, 42 mM imidazole, pH 7.3; SEID: 100 mL SEI + 0.5 g sodium deoxycholate). Homogenates were then centrifuged at 10,000x *g* for 5 min at 4ºC, top fat layer was discarded, and the resulting supernatant was directly used in the assay.

Na^+/K^+-ATPase activity was measured using commercial Na^+/K^+-ATPase activity assay kit (Elabscience, Cat # E-BC-K539-M), ATPase activity was expressed as nmol P_i $mg^{-1}{}_{protein}$ min^{-1} where protein content was quantified by performing a Biuret test.

2.2.9 CS enzyme analysis

CS enzyme activity was measured using a method modified from (Farhat et al., 2020). Briefly, 50 mg of tissue was weighed and homogenized on ice in 1 ml of extraction solution (20 mM Tris-HCl, 1 mM EDTA, and 0.1% (v/v) Triton X-100, pH 7.2). Homogenates were then centrifuged at 4°C at 10,000g for 10 min, top fat layer was discarded, and the supernatant was immediately used to assay CS activity. The CS activity was measured in assay buffer (50 mM Tris-HCl, 0.5 mM oxaloacetate, 0.1 mM acetyl CoA, 0.2 mM 5,5′-dithiobis-(2-nitrobenzoic acid) (DTNB), pH 8.1) as the increase in the slope of the absorbance at 412 nm during 5 min (Alp et al., 1976), and was determined at 32°C using a Spectra Max Plus384 Absorbance Microplate Reader (Molecular Devices, Sunnyvale, CA). Concentrations used in the assay were saturating and not inhibitory, as determined from preliminary experiments. Substrate-free controls were run simultaneously to determine background activity. Enzyme activity was normalized to total soluble protein, which was quantified with a Biuret test.

2.2.10 qPCR for mitochondrial DNA quantification

Tissues were homogenized using a glass tissue grinder (PYREX, CAT# 77241) at 50 mg wet weight/ml in lysis Solution (25 mM NaOH, 0.2 mM EDTA), then incubated at 95°C for 30 min, followed by centrifugation at 10,000 rpm for 5 min at 4°C. Top fat layer was discarded, and the supernatant was then collected and mixed with an equal volume of 40 mM Tris-HCl (Truett et al., 2000). DNA concentrations ere quantified using a NanoDrop Spectrophotometer (ND-1000, Thermofisher Scientific, Napean, ON, CAN). The relative mtDNA/nDNA ratios were measured by qPCR using a Rotor-Gene Q (Qiagen Inc., Montreal, QC, CAN), with a reaction medium containing 5 µl qPCR SYBR Green Mix (A600A; Promega, Madison, WI, USA), 0.1 µM primer (Primers are listed in Table 7.1), 2 µl DNA (optimal dilutions were determined previously), and H_2O; total volume 10 µl). The copy number of mtDNA was calculated using the following formula (Quiros et al., 2017):

a) $\Delta Ct = Ct\ (\text{nDNA gene}) - Ct\ (\text{mtDNA gene})$

b) Copies of mtDNA = $2 \times 2^{\Delta\Delta Ct}$

c) Relative mtDNA content = mtDNA treatment/mtDNA normoxic

Table 2.2 List of primers for mtDNA quantification.

Species	Target	Sequence (5' to 3')
NMR	16S mitochondrial ribosomal RNA	GTACCGCAAGGGAAAGATGAAAG
		TAGCTCGTTTGGTTTCGGGGTT
	beta 2-microglobulin	GCCAAACTACTTGAACTGCTATG
		GTCCAGTCCTTGCTGAAAGA

2.2.11 Western blot

iBAT tissue was homogenized by sonication (20 times, 1s/time) at 100 mg/ml (W/V) in radio-Immunoprecipitation Assay (RIPA) buffer with protease inhibitors and phosphatase inhibitors. The homogenate was spun at 12,000*g* for 10 min at 4 °C. The supernatant was kept for protein concentration measurements using the Biuret assay and followed by SDS-PAGE. First, 10–50 µg of protein was loaded per lane onto a 12 or15% SDS-polyacrylamide gel, which in turn was run for 1–1.5 h at 130 V. The separated proteins were then transferred to a nitrocellulose membrane for 1 hr at 100 V. Successful transfer was determined by Ponceau S staining. Membranes were then incubated with 5% bovine serum albumin for 60 min to block non-specific binding sites. Levels of specific proteins were determined using the antibodies listed in Table 7.2. Quantification was performed using ImageJ software (V1.53j, NIH, Bethesda, MD).

Table 2.3 List of antibodies.

Target	Vendor	Cat #
AIF	Abcam	ab32516
BAX	Santa Cruz	SC-526
Bcl2	Santa Cruz	sc-492
BNIP3	Abclonal	A19593
Caspase-3	Abclonal	A0214
Drp1	Abclonal	A2586
Drp1-S616	Abclonal	AP0849
Drp1-S637	CST	4867
Fis1	Abclonal	A19666
LC3B	Abclonal	A19665
MFF	Abclonal	A4874
MFN1	Abclonal	A9880
NIX	Abclonal	A6283
MFN2	Abclonal	A19678
OPA1	Abclonal	A9833
OXPHOS rodent cocktail	Abcam	ab110413
p53	CST	2524
p62	Abclonal	A11483
Parkin	Abclonal	A0968
Pink1	Abclonal	A7131
RAB7A	Abclonal	A12784
TBC1D15	Abclonal	A10593
TOM20	Abclonal	A19403
ubiquitin	Abcam	ab7780
UCP1	Sigma	U6382
UCP3	Abcam	ab3477
Rabbit IgG (secondary)	Thermofisher	31458
Mouse IgG (secondary)	Thermofisher	A16017

Polyclonal antibodies were diluted at 1 µg/ml in 3-5% BSA, monoclonal antibodies were diluted at 0.5 µg/ml in 3-5% BSA, Secondary antibodies were diluted at 0.1 µg/ml in 3-5% BSA.

2.2.12 TEM

Immediately following in vivo treatments (section 2.2.2), animals were anesthetized with ketamine (200 mg/kg) + xylazine (10 mg/kg) and then rapidly returned to their treatment condition until they had lost consciousness, to minimize reoxygenation of hypoxic animals. Animals were then perfusion-fixed via cardiac puncture using 2% formaldehyde and 2.5% glutaraldehyde. Following fixation, iBAT was dissected and further fixed overnight at 4°C in 2.5% glutaraldehyde in 0.15 M sodium cacodylate buffer, pH 7.4, and washed three times with washing buffer. Samples were post-fixed with 1% aqueous OsO_4 + 1.5% aqueous potassium ferrocyanide for 2 h and washed three times with washing buffer. Specimens were dehydrated in a graded ethanol-dH2O from 30%, 50%, 70%, 80%, 90%, to 100% ethanol. The samples were infiltrated with a graded Epon-ethanol series (1:1, 3:1), embedded in 100% Epon and then polymerized in an oven at 60°C for 48 h. Ultra-thin sections (90–100 nm thick) were prepared from the polymerized blocks with a Diatome diamond knife using a Leica Microsystems EM UC7 ultramicrotome (Leica Biosystems, Buffalo Grove, IL, USA), transferred onto 200-mesh copper grids, and stained with 4% uranyl acetate for 6 min and Reynold’s lead for 5 min. The TEM grids were imaged by a FEI Tecnai G2 Spirit 120 kV TEM equipped with a Gatan Ultrascan 4000 CCD Camera Model 895. The proprietary Digital Micrograph 16-bit images (DM3) were converted to unsigned 8-bit TIFF images. Image analysis was performed blinded and using ImageJ (NIH) on micrographs obtained at 9000X (9k) or 19,000X (19k) magnifications. Metrics quantified included (i) total mitochondrial area normalized to cytoplasm area (%) from 9k micrographs, (ii) maximal length (mm) of individual mitochondria average from 19k micrograph, as well as (iii) average cristae number (1/mm2) and total length (mm/mm2) normalized to mitochondrial area from 19k micrographs. All metrics were quantified manually from scaled micrographs, using tools of Polygon and Freehand

Selections (mitochondrial and cytoplasmic area; cristae length) or Straight Line (mitochondrial max length), followed by the Measure function. We would like to thank Drs. S. Kelly Sears and Jeannie Mui from the Facility for Electron Microscopy Research at McGill University for TEM services and Dr. Ryan Russell, University of Ottawa, for expert advice on electron micrograph analyses.

2.2.13 IHC

Immediately following in vivo treatments (section 2.2.2), iBAT was dissected, cleaned to remove any white adipose, muscle or connective tissues, and then fixed in 10% formalin overnight. iBAT was then ethanol dehydrated and stored in 70% ethanol prior to paraffin embedding. Embedded tissue was sectioned to the largest surface area. IHC staining was performed on 5 µm sections using the Leica Bond™ system using a modification of protocol F that eliminates the post primary step when using rabbit antibodies on rodent tissue. Sections were pretreated using sodium citrate buffer (pH 6.0, epitope retrieval solution 1) for 20 min. The sections were then incubated using a 1:1000 dilution of rabbit UCP-1 for 30 min at room temperature and detected using an HRP conjugated compact polymer system. Slides were then stained using DAB as the chromogen, counterstained with hematoxylin, mounted and cover slipped.

After staining, Mirax Viewer Image software (version 1.6) was used to analyze the sections in a ZEISS-MIRAX Midi Slide scanning system (Zeiss Microimaging, Oberkochen, Germany, and 3DTech, Budapest, Hungary) and digital images were acquired at 20x magnification. Images were extracted using Aperio ImageScope software (version 12.3.3; Leica Biosystems), and were then processed using Zeiss software ZEN 3.2 (Zen Lite; Carl Zeiss Canada Ltd, Toronto, Canada).

For lipid droplet analysis of hematoxylin and eosin (H&E)-stained sections, regions of interests were carefully selected in each image using the rectangular selective tool bar in the ZEN

3.2 software, making sure to avoid blood vessels and edges of the tissue. All the regions of interests were converted to a TIFF format. Then, images were analyzed using FIJI (ImageJ version 1.53j; NIH) by a blinded researcher. The range thresholding applied across all replicate images in all conditions was 200–255 and the range of lipid droplet area analyzed was between 1 and 1000 μm^2. The scale of each image processed was calibrated by adding a scale according to the regions of interest analyzed. Finally, the total lipid droplet area of each image was measured, and a percent lipid area was calculated using FIJI (Parlee et al., 2014).

For UCP-1 cell count analysis, DAB-stained images were converted into TIFF format and then analyzed using FIJI by a blinded reviewer. For each replicate, two sections of 2000 × 2000 pixels were randomly taken and analyzed by manual counting of DAB-positive cells. This count was then divided by the total number of cells in each section to obtain the percentage of UCP-1-positive cells.

2.2.14 Statistical analysis

All statistical analyses were performed using GraphPad Prism 9 (GraphPad Prism, La Jolla, CA, USA). Data were analyzed using two-tailed t-tests (Fig. 2.3C); unpaired multiple t-tests with two-stage step-up calculations (SF 2.5); multiple t tests followed by Welch t-test (Fig. 2.3A&B); one-way ANOVA with Dunnett multiple comparison (Fig. 2.5&2.6, SF 2.4), or Tukey (Fig. 2.7-2.9) post-tests; two-way ANOVAs followed by with a Sidak (Fig. 2.1, 2.2, Table 2.1), Dunnett (Fig. 2.4), or Tukey (SF 2.1-2.3) multiple comparisons tests. Significance was determined with a level of $p < 0.05$ unless otherwise indicated in results, and all data are expressed as the mean ± SEM.

2.3 Results

O_2 consumption and H_2O_2 efflux are suppressed in hypoxic iBAT mitochondria. Interscapular heat production is rapidly suppressed during acute hypoxia in NMRs, suggesting that BAT mitochondrial function is altered in hypoxia (Ikeda & Yamada, 2020). Therefore, we tested mitochondrial respiration and ROS production following *in vivo* hypoxia (5% O_2, 4 h). We found that iBAT mitochondria significantly reduced O_2 consumption ($F_{1,8} = 34.72$, $p = 0.0004$, Fig. 2.1A; $F_{1,8} = 17.80$, $p = 0.0029$, Fig. 2.1B; $F_{1,8} = 31.11$, $p = 0.0005$, Fig. 2.1C) and H_2O_2 efflux ($F_{1,8} = 16.38$, $p = 0.0037$, Fig. 2.1D; $F_{1,8} = 13.97$, $p = 0.0029$, Fig. 2.1E; $F_{1,8} = 48.80$, $p = 0.0001$, Fig. 2.1F) (Fig. 2.1 & Table 2.1). Furthermore, UPC-1 induced (without GDP) and ADP-induced (with GDP and ADP) O_2 consumption were both suppressed ~ 45%-65% (Fig. 2.1A-C). Mitochondrial H_2O_2 efflux was reduced ~ 45% (Fig. 2.1D-F), but the increase in succinate-induced (without GDP) H_2O_2 efflux was lesser (~20%, $p = 0.8207$). Conversely, electron leak (H_2O_2 efflux/O_2 consumption) changed variably depending on mitochondrial electron transport pathways (Fig. 2.1G-I). Specifically, a significant increase occurred when GDP was applied during pyruvate- (~85%, from 1.08 ± 0.09 to 2.01 ± 0.33, $p = 0.009$, Fig. 2.1G), and octanoylcarnitine- (~ 65%, from 0.98 ± 0.15 to 1.62 ± 0.15, $p < 0.0001$, Fig. 2.1H) fuelled respiration. However, leakage (with GDP) was significantly lower during succinate-induced respiration (~27%, from 3.12 ± 0.27 to 2.28 ± 0.31, $p = 0.0091$, Fig. 2.1I), but then increased following the addition of rotenone (complex I inhibitor, by ~ 120%, from 0.61 ± 0.27 to 1.34 ± 0.22, $p = 0.0283$, Fig. 2.1I).

ETC reprograming in acute iBAT mitochondria. Mitochondrial ATP generation is driven by the ETC (Sokolova et al., 2019). Thus, we analysed the relative changes between OXPHOS function and ETC capacity. We found that O_2 consumption with each substrate was significantly reduced when normalized to either complex I-II electron transport ($F_{1, 8} = 66.75$, $p < 0.0001$, Fig. 2.2A) or complex IV capacity ($F_{1, 8} = 14.55$, $p = 0.0051$, Fig. 2.2B). Although both leak and OXPHOS respiration were reduced (Fig. 2.1A-F & Table 2.4), respiratory control ratios (RCRs, calculated as the quotient of OXPHOS capacity to leak respiration (with the UCP inhibitor, GDP), increased significantly (~63%-89%, Fig. 2.3A). We also noticed the proportions of uncoupled (UCP1-induced) O_2 consumption had no impact on pyruvate (~6% increase, p = 0.1347, Fig. 2.3B) or octanoylcarnitine pathways (~ 3% increase, p = 0.4750, Fig. 2.3B), but significantly increased flux through the succinate pathway (~39% increase, $p = 0.0024$, Fig. 2.3B). Another notable change was observed for outer-mitochondrial membrane integrity, where a slight but significant increase of cytochrome c-mediated O_2 consumption was found in hypoxic iBAT mitochondria (~ 5% increase, $p = 0.0086$, Fig. 2.3C).

Acute hypoxia inhibited mitochondrial Ca^{2+} uptake rate but did not affect Ca^{2+} resistance capacity. In mouse, low [Ca^{2+}] (half-maximal around 0.1 μM) is essential for heat production in BAT mitochondria (de Meis et al., 2010); however, the reduction of UCP1 and respiratory chain proteins sensitizes mitochondrial Ca^{2+} buffering (Kazak et al., 2017). In addition, mitochondrial Ca^{2+} buffering is involved in thermogenic regulation and adiponectin secretion (Al-Anazi et al., 2018; Connolly & Nedergaard, 1988). Therefore, we tested the impact of hypoxia on the Ca2+-buffering capacity of NMR iBAT mitochondria. We found that the extra-mitochondria Ca^{2+} resistance of isolated iBAT mitochondria was enhanced by ADP addition (~100% enhanced, Fig. 2.4A, SF. 2.6E), but were not affected by either hypoxia acclimation or UCP1 inhibition (with GDP). However, the Ca^{2+} uptake rate (Ca^{2+}-binding Calcium green 5-N decay rate, K_{off}) was significantly decreased by ~50-60% in hypoxic mitochondria with all substrates (Fig. 2.4B, SF. 2.6A-D).

iBAT UCP1 and OXPHOS proteins are degraded under hypoxia, and more so during prolonged* in vivo *hypoxia. To understand the mechanism underlying the rapid change in interscapular thermogenesis and reduction of hypoxic mitochondrial respiration, we held NMRs in normoxia or for 1 or 3 hrs in acute hypoxia (7% O_2) at 30 °C, and then sacrificed animals and rapidly dissected iBAT. We then examined the expression of thermogenic UCP1 and UCP3 proteins as well as that of mitochondrial OXPHOS complexes I–V. We found that, following 1 and 3 hrs of acute hypoxia, UCP1 protein expression decreased by 58–62% relative to normoxic controls (Fig. 2.5A, B; $F_{2,33} = 10.96$, $p = 0.0002$, $n = 19$, 11, and 6 biologically independent replicates for normoxia and 1 and 3 h hypoxia, respectively). UCP3 protein expression tended to decrease with progressive hypoxia, but this change did not reach significance (Fig. 2.5A, B; $F_{2,15} = 2.06$, $p = 0.162$, $n = 6$ biologically independent replicates each).

We next analyzed the number of UCP1-expressing cells in iBAT samples using immunohistochemical approaches and found that the percent of cells expressing UCP1 decreased by ~ 9% at 3 hrs of hypoxia but was unchanged after 1 hr of hypoxia (SF. 2.4; $F_{2,19} = 3.684$, $p = 0.0442$, $n = 12$, 11, and 11 biologically independent replicates for normoxia and 1 and 3 h hypoxia, respectively). In addition, the expression of mitochondrial ETC complexes I–IV proteins decreased by 37–63% in 1 and 3 hrs hypoxia (Fig. 2.5C, D; $F_{4,165} = 60.90$, $p < 0.0001$, $n = 19$, 11, and 6 biologically independent replicates for normoxia and 1 and 3 hrs hypoxia, respectively), while the expression of the F_1F_o-ATPase (complex V) decreased after 3 hrs ($p = 0.0032$), but not 1 hr of hypoxia exposure ($p = 0.6012$; Fig. 2.5C, D). We also examined lipid droplet area within the cytoplasm of NMR iBAT samples, but the variability in this analysis was large and no significant changes were observed (SF. 2.4E-H; $F_{2,31} = 0.85$, $p = 0.1461$; $n = 12$, 11, and 11 biologically independent replicates for normoxia and 1 and 3 h hypoxia, respectively).

Mild "degradation" and morphological changes of iBAT mitochondria under hypoxia. Our observation of rapid changes in iBAT mitochondrial protein expression prompted further investigation of the underlying mechanisms. Since UCP1, the ETC complexes, and the F_1F_o-ATPase are all situated within the mitochondrial inner membrane (Busiello et al., 2015; Kuhlbrandt, 2015), we next examined changes in mitochondrial ultrastructure and cristae morphology in iBAT from NMRs exposed to hypoxia *in vivo*. Using immunoblotting, we measured changes in the expression of TOM20, which is located in the mitochondrial outer membrane, as a marker of mitochondrial content. Expression of TOM20 exhibited a decreasing trend with progressive hypoxia and was significantly reduced by 3 hrs of hypoxia (Fig. 2.6A, B; $F_{2,15} = 3.98$, $p = 0.0428$; $n = 6$ biologically independent replicates each). Consistently, we noticed a significant reduction of mtDNA, but no significant change in CS activity in hypoxic iBAT (7% O_2 for 4 h) (SF. 2.5).

This change in TOM20 protein and mtDNA prompted further investigation of mitochondrial ultrastructure. We next used TEM to examine iBAT mitochondria from NMRs treated in normoxia, 1 or 4 h hypoxia, or 4 h of hypoxia with 1 hr of recovery in normoxia. We found that iBAT from normoxic NMRs contained abundant mitochondria with dense cristae and intact inner membranes. Conversely, mitochondria in iBAT from hypoxic NMRs displayed significant morphological alterations. After 1 hr of hypoxia, total mitochondrial area was significantly decreased compared with normoxic conditions, consistent with the observed decrease in TOM20; and subsets of mitochondria were more tortuous and had sparser cristae (Fig. 2.6). Following 4 h of hypoxia, we measured a significant decrease in cristae length and number (Fig. 2.6E). After recovery, all structural indices were comparable to normoxic conditions, except average cristae number, which failed to fully recover (Fig. 2.6). There were also degradative, lysosome-like vacuoles between iBAT mitochondria from hypoxic NMRs (Fig.2.2D, red arrow). Next, we performed blinded qualitative analysis of mitochondria ultrastructure and cristae morphology ($n = 22$–42 technical replicates from four biological replicates per treatment; Fig. 2.6G-J). We found that, during hypoxia, mitochondrial area (as a % of the cytoplasm; $F_{3,110} = 19.01, p < 0.0001$), cristae length ($F_{3,104} = 23.53, p < 0.0001$), and cristae number ($F_{3,109} = 14.20, p < 0.0001$) were all decreased in hypoxia, whereas mitochondrial length was unchanged ($F_{3,134} = 0.77, p = 0.5155$). Notably, these ultrastructural changes were all partially or completely reversed within 1 hr of recovery in normoxia.

Mitochondrial membrane dynamics are involved in mitochondria morphological changes. It was suggested that the reduction of mitochondrial proteins is due to ubiquitination and proteasomal degradation in hypoxic NMR iBAT (Sebaa & Harper, 2020). However, no such relationship was found because UCP1 and ubiquitin did not co-immunoprecipitate. As we could not find a direct link between UCP1 and ubiquitin, we investigated other potential protein degradation mechanisms, such as mitophagy. Specifically, we used immunoblotting to explore changes in key activators of mitophagy, including parkin, PINK1, p62, FUNDC1, Nix, BNIP3, TBC1D15, RAB7A, and LC3-I and II proteins in iBAT following 1 or 3 hrs of *in vivo* hypoxia. There were no increases in the expression of any of these proteins in hypoxia, except for LC3-II, which increased ~50% after 3 hrs of hypoxia ($F_{2,12} = 4.14, p = 0.0441$; Fig. 2.7; $n = 6$–12 biologically independent replicates for each treatment condition). In addition, the expression of BNIP3 decreased 42–53% with progressive hypoxia ($F_{2,15} = 6.16$, $p = 0.0111$). This change may be related to the role of this protein in regulating apoptosis, instead of in mitophagy (see below) (Zhang & Ney, 2009).

Changes in mitochondrial size and shape are often mediated by mitochondrial fission or fusion and so we next examined the expression of key mediators of these processes in NMR iBAT (Fig. 2.8; $n = 6$-12 biologically independent replicates each). We found that progressive hypoxia increased phosphorylation of DRP1 at serine 616 (DRP-S616; ~2.25-fold increase; $F_{2,15} = 4.492$, $p = 0.0296$) and upregulated the expression of FIS1 by 243% at 3 hrs of hypoxia ($F_{2,33} = 23.83$, $p < 0.0001$), indicating the occurrence of fission in iBAT mitochondria with acute *in vivo* hypoxia. Conversely, canonical mediators of fusion, including OPA1, and MFN1 and MFN2 were unchanged.

Cellular apoptosis can occur in conjunction with mitophagy and autophagy and/or mitochondrial fission events and so we also examined activation of apoptosis pathways (Fig. 3.5; $n = 6$ biologically independent replicates each). Intriguingly, we found that key activators of apoptosis were downregulated during acute *in vivo* hypoxia, including p53 (by 38% and 63% at 1 and 3 hrs hypoxia, respectively; $F_{2,15} = 6.087$, $p = 0.0116$) and caspase 3 (by 83 and 90% in 1 and 3 hrs hypoxia, respectively; $F_{2,15} = 24.64$, $p < 0.0001$), and BNIP3 (Fig. 2.7, see above), while BAX and Bcl-2 remained unchanged. The apoptotic indicator AIF was also unchanged by hypoxia.

2.4 Figures and tables

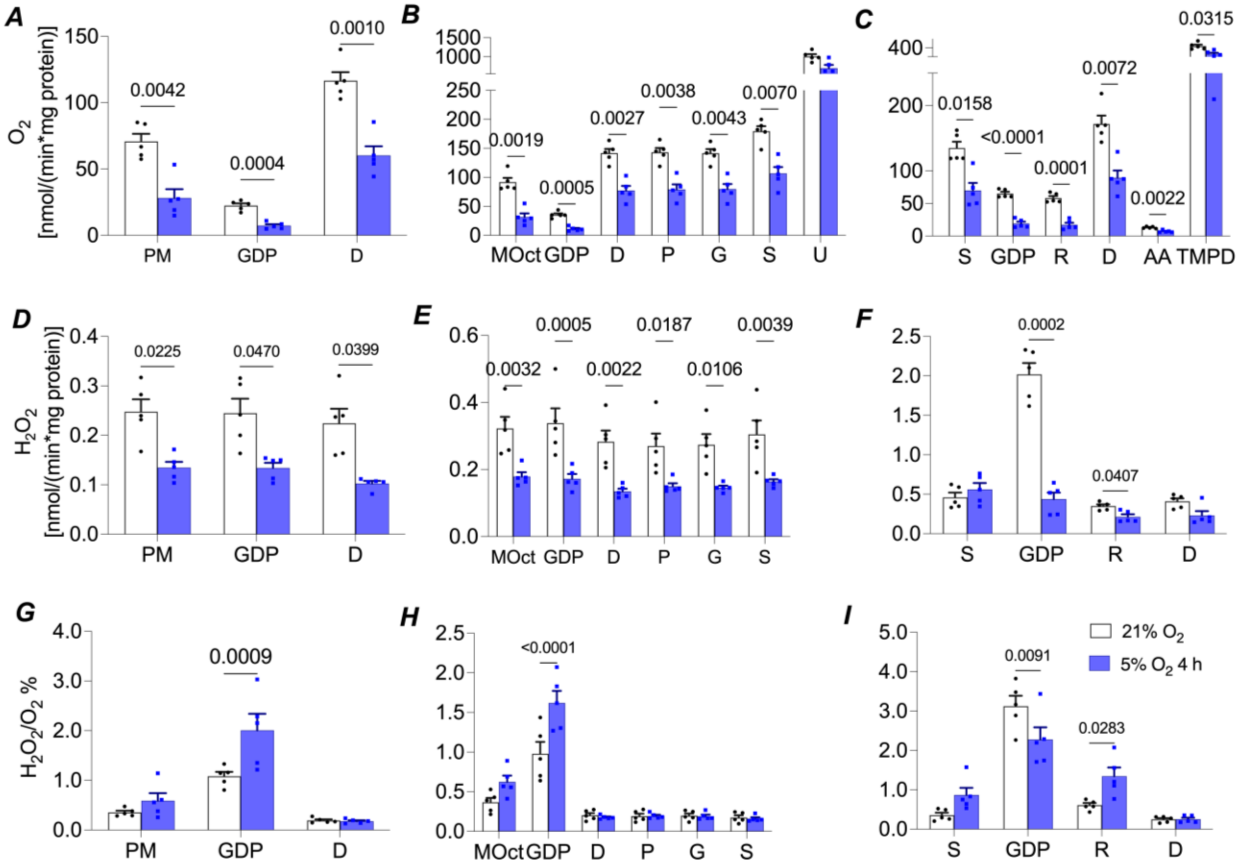

Figure 2.1 Hypoxia decreases mitochondrial respiration, coupling, and H_2O_2 production in NMR iBAT.

Summaries of **(A)** pyruvate-, **(B)** octanoylcarnitine-, and **(C)** succinate-induced O_2 consumption; **(D)** pyruvate-, **(E)** octanoylcarnitine-, and **(F)** succinate-induced H_2O_2 production; **and (G)** pyruvate-, **(H)** octanoylcarnitine-, and **(I)** succinate-induced electron leakage (H_2O_2/O_2) from iBAT mitochondria isolated from NMRs treated for 4 h in *in vivo* normoxia or acute hypoxia (5% O_2). Substrates were added sequentially in the order indicated on the x-axis for each graph. Abbreviations: P, pyruvate; M, malate; GDP, guanosine diphosphate; D, ADP; Oct, octanoylcarnitine; G, glutamate; S, succinate; R, rotenone; AA, Antimycin A; TMPD, ascorbate + N,N,N,N-tetramethyl-p-phenylenediamine; U, carbonyl cyanide *m*-chlorophenyl hydrazine, $n = 5$ biologically independent samples. Data are presented as means ± SEM. Significant differences ($*p < 0.05$ normoxia *vs.* hypoxia) were determined by two-way ANOVAs followed by Sidak multiple comparison tests.

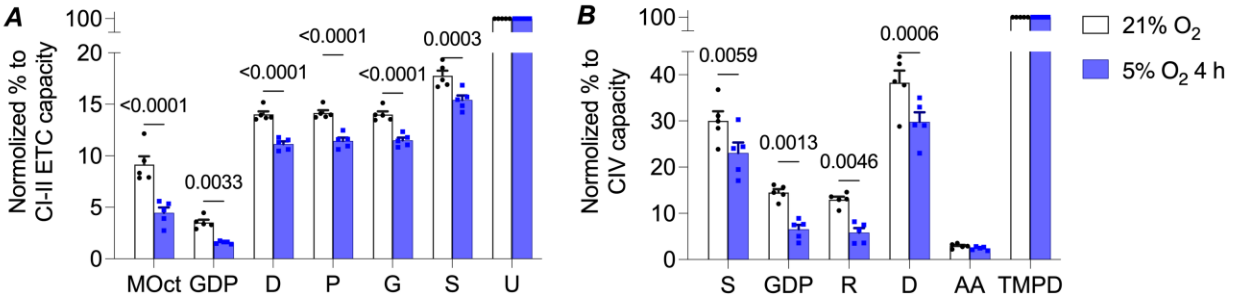

Figure 2.2 Mitochondrial respiration from iBAT of normoxic and hypoxic NMRs.

Summaries of complex I-II fuelled O_2 consumption normalized to **(A)** electron transport capacity (from 2.1B), and **(B)** complex IV capacity (from 2.1C). Substrates were added sequentially in the order indicated on the x-axis for each graph. Abbreviations: M, malate; Oct, octanoylcarnitine; GDP, guanosine diphosphate; D, ADP; P, pyruvate; G, glutamate; S, succinate; R, rotenone; AA, Antimycin A; TMPD, ascorbate + N,N,N,N-tetramethyl-p-phenylenediamine, $n = 5$ biologically independent samples. Data are presented as means ± SEM. Significant differences ($*p < 0.05$ normoxia *vs.* hypoxia) were determined using two-way ANOVAs followed by with a Sidak multiple comparisons test.

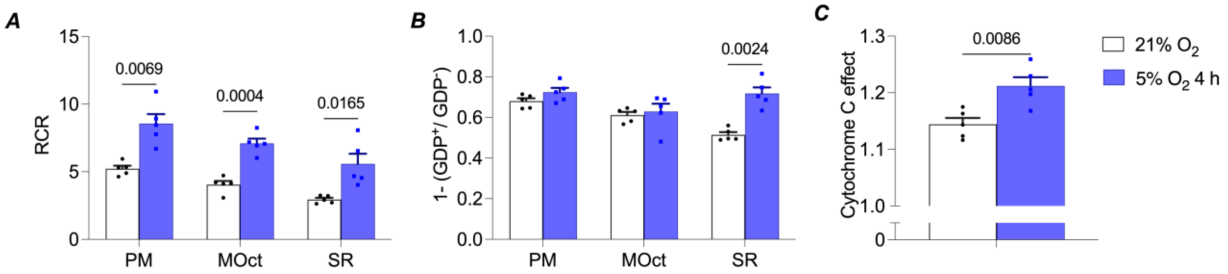

Figure 2.3 Mitochondrial coupling efficiency and outer-membrane damage in iBAT following acute *in vivo* hypoxia.

Summaries of **(A)** RCRs (evaluated as the quotient of OXPHOS capacity to GDP-induced leak respiration); mitochondria were stimulated with pyruvate/malate (PM), malate-octanoylcarnitine (MOct), or succinate/rotenone (SR); **(B)** UCP1-uncoupled O_2 consumption (proportion of UCP1-induced leak respiration, 1-(GDP^+/GDP^-)); and **(C)** outer-mitochondrial damage presented as the ratio of change in O_2 consumption following cytochrome c addition. $n = 5$ biologically independent samples. Data are presented as means ± SEM. Significant differences (*$p < 0.05$ normoxia *vs.* hypoxia) were determined by multiple t tests (Welch t-test) (A&B), and two-tails t-test (C).

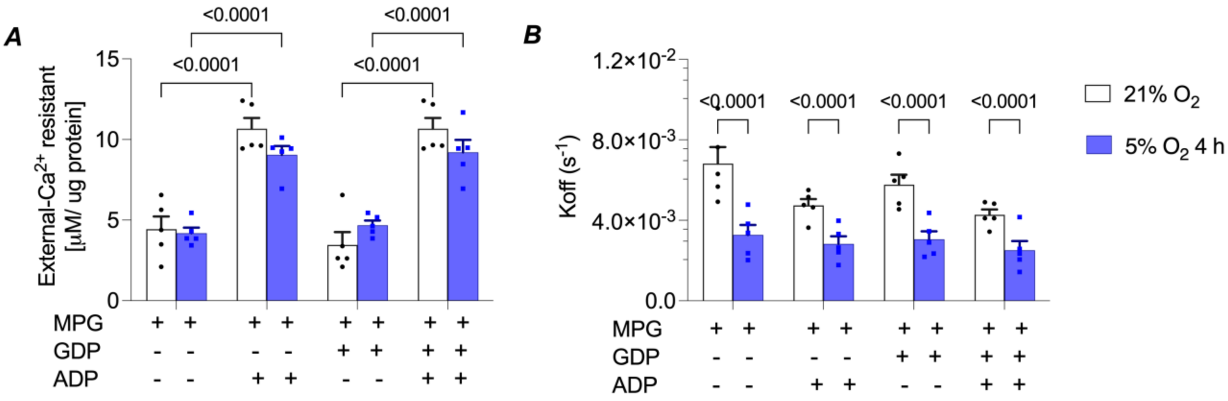

Figure 2.4 Extra-mitochondrial Ca^{2+} resistance and Ca^{2+} uptake rates of isolated iBAT mitochondria.

Summaries of **(A)** Extra-mitochondrial Ca^{2+} resistance and **(B)** Ca^{2+} uptake rates (Koff) in the first five min following $CaCl_2$ injection (SF 2.6E). Each bar represents individual experiments with substrates indicated below the figures. Abbreviations: +, presence; -, absence; MPG, malate/pyruvate/ glutamate; GDP, guanosine diphosphate; D, ADP, *n* = 5 biologically independent samples. Data are presented as means ± SEM. Significant differences ($*p < 0.05$ normoxia *vs.* hypoxia) were determined by two-way ANOVAs followed by a Tukey multiple comparisons test.

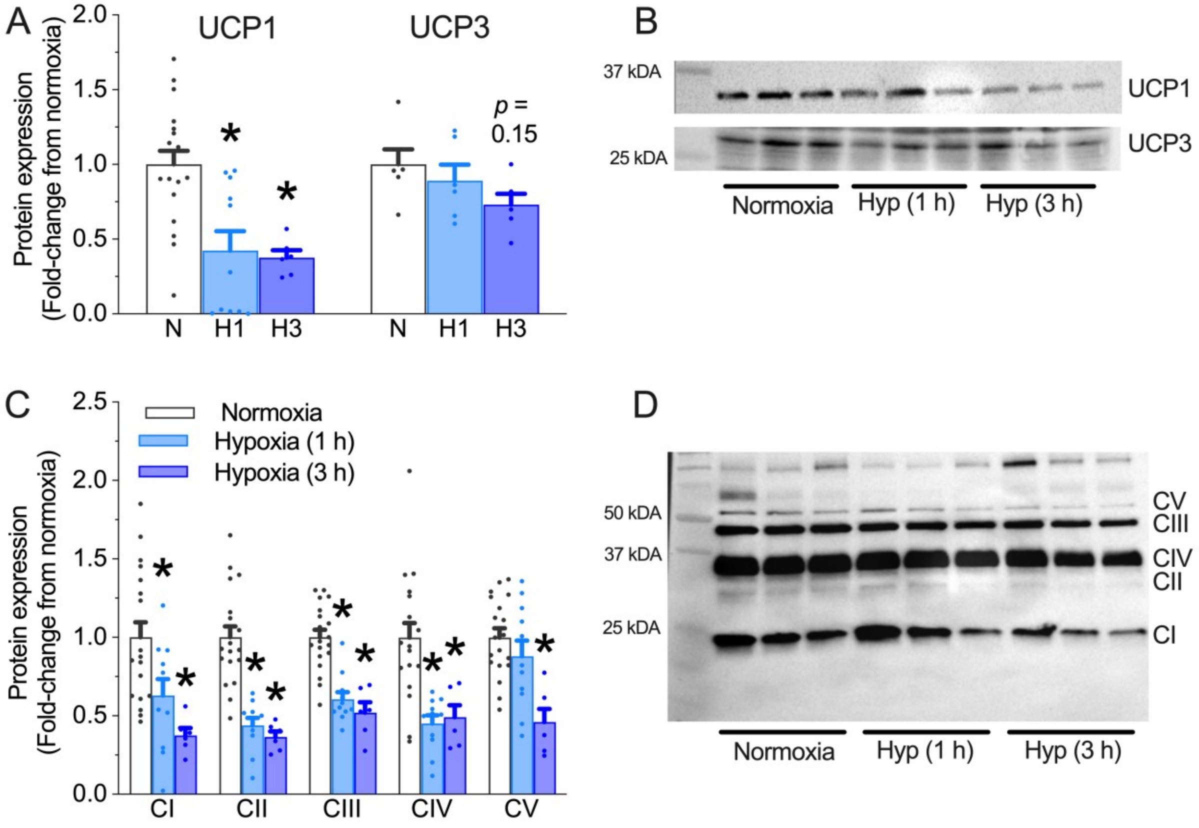

Figure 2.5 Thermogenic and oxidative phosphorylation protein expression decreases in acute hypoxia.

(A) Summary of UCP1 and UCP3 expression in iBAT from NMRs treated in normoxia (21% O_2, clear bars; $n = 18$ and 6 biologically independent samples for UCP1 and UCP3, respectively), or 1 or 3 hrs of hypoxia (7% O_2, light and dark blue bars, respectively; $n = 11$ and 6 biologically independent samples for UCP1 and 6 for each time point for UCP3). (**B**) Western blot images of UCP1 and UCP3 protein bands from (A). **(C)** Summary of ETC complexes I–IV (CI–CIV) and F_1F_o-ATPase (CV) protein expression in iBAT from NMRs treated as in (A). **(D)** Western blot image of ETC complexes I–IV and F_1F_o-ATPase protein bands. Data are mean ± SEM. Asterisks indicate significant difference from normoxic controls (one-way ANOVA with Dunnett's multiple comparisons test; $F_{2,33} = 10.96$, $p = 0.0002$ for UCP1; $F_{4,165} = 60.90$, $p < 0.0001$ for ETC proteins; $p > 0.05$ for other proteins). Additional abbreviations: N – normoxia, H1 – 1 hr hypoxia, H3 – 3 hrs hypoxia.

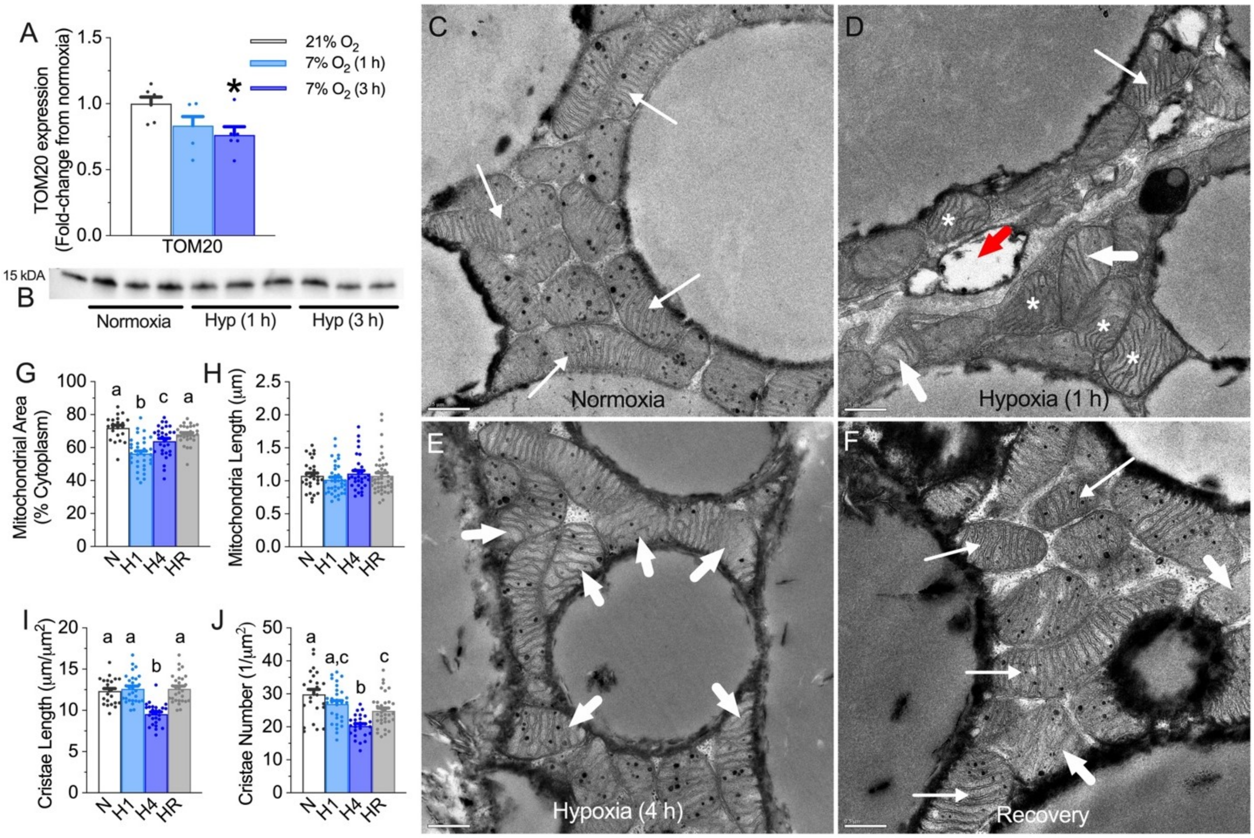

Figure 2.6 Mitochondrial and cristae density is reduced in acute hypoxia.

(A) Summary of translocase of outer membrane 20 (TOM20) protein expression in iBAT homogenates from NMRs held at 30 °C in normoxia (21% O_2, clear bars; *n* = 6 biologically independent samples) or after 1 or 3 hrs of hypoxia (7% O_2, light and dark blue bars, respectively; *n* = 6 biologically independent samples). **(B)** Western blot image of TOM20 protein bands. **(C–F)** Representative electron micrographs of iBAT from NMRs held at 30 °C in normoxia (C), 1 hr hypoxia (D), 4 h hypoxia (E), or 4 h of hypoxia with 1 hr recovery in normoxia (F). Thin arrows indicate normal mitochondria, thick arrows indicate abnormal mitochondria, asterisks indicate tortuosity, and red arrowhead indicates degradative or lysosome-like vacuoles. Scale bars: 0.5 µm. **(G–J)** Summaries of mitochondrial area (G, *n* = 29, 36, 31, and 42 technical replicates for normoxia (N: clear bars), 1 and 4 h of hypoxia (light and dark blue bars, and H1 and H4, respectively), and 4 h hypoxia with recovery (HR: grey bars), respectively, from 4 independent animals for each condition) and average max length (H, *n* = 22, 33, 29, and 30 technical replicates for normoxia, 1 and 4 h of hypoxia, and 4 h hypoxia with recovery, respectively, from 4 independent animals for each condition), and cristae length (I, *n* = 24, 26, 24, and 29 technical replicates for normoxia, 1 and 4 h of hypoxia, and 4 h hypoxia with recovery, respectively, from 4 independent animals for each condition) and number (J, *n* = 24, 29, 26, and 34 technical replicates for normoxia, 1 and 4 h of hypoxia, and 4 h hypoxia with recovery, respectively, from 4 independent animals for each condition) from NMRs treated as per (C–F). Data are mean ± SEM. Asterisks indicate significant difference from normoxic controls; letters indicate significant difference (one-way ANOVA with Dunnett's multiple comparisons test; $F_{2,15} = 3.98$, $p = 0.0428$ for TOM20; $F_{3,110} = 19.01$, $p < 0.0001$ for mitochondrial area, $F_{3,104} = 23.5_{3,}$ $p < 0.0001$ for cristae length, and $F_{3,109} = 14.20$, $p < 0.0001$ for cristae number; $p = 0.5155$ for mitochondrial length).

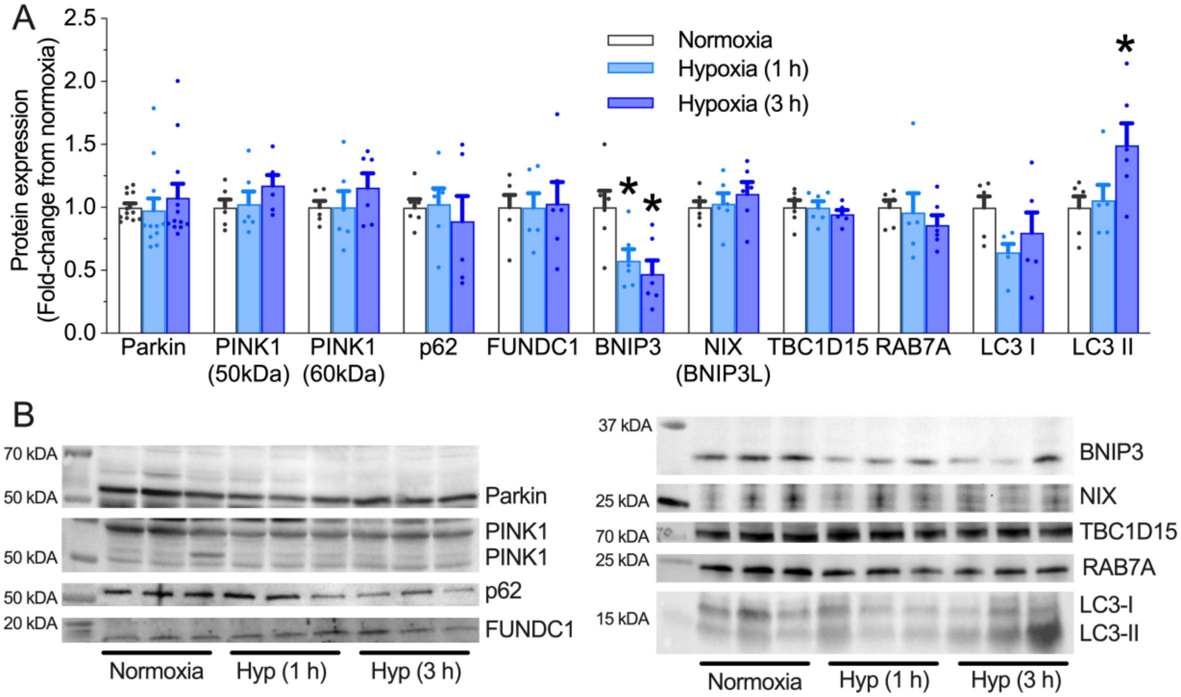

Figure 2.7 Hypoxia does not alter the expression of key mediators of ubiquitin- or receptor-mediated mitophagy.

(A) Summary of changes in receptor-mediated mitophagy-related protein expression in interscapular BAT (iBAT) homogenates from NMRs held at 30 °C in normoxia (21% O_2, clear bars) or after 1 or 3 hrs of hypoxia (7% O_2, light and dark blue bars, respectively; $n = 12$ biologically independent samples for Parkin and 6 biologically independent samples for all other proteins). **(B)** Western blot images of protein bands from (A). Data are mean ± SEM. Asterisks indicate significant difference from normoxic controls (one-way ANOVA with Tukey multiple comparisons test; $F_{2,15} = 6.16$, $p = 0.0111$ for Bcl-2 adenovirus E1B 19 kDa-interacting protein 3 (BNIP3); $F_{2,12} = 4.14$, $p = 0.0441$ for light chain 3 II (LC3II); $p > 0.05$ for FUN14 domain containing 1 (FUNDC1), sequestosome 1 (p62), phosphatase and tensin homolog (PTEN)-induced kinase 1 (PINK1), ras-related protein 7A (RAB7A), and TBC1 domain family member 15 (TBC1D15)). Additional abbreviations: N – normoxia, H1 – 1 hr hypoxia, H3 – 3 hrs hypoxia.

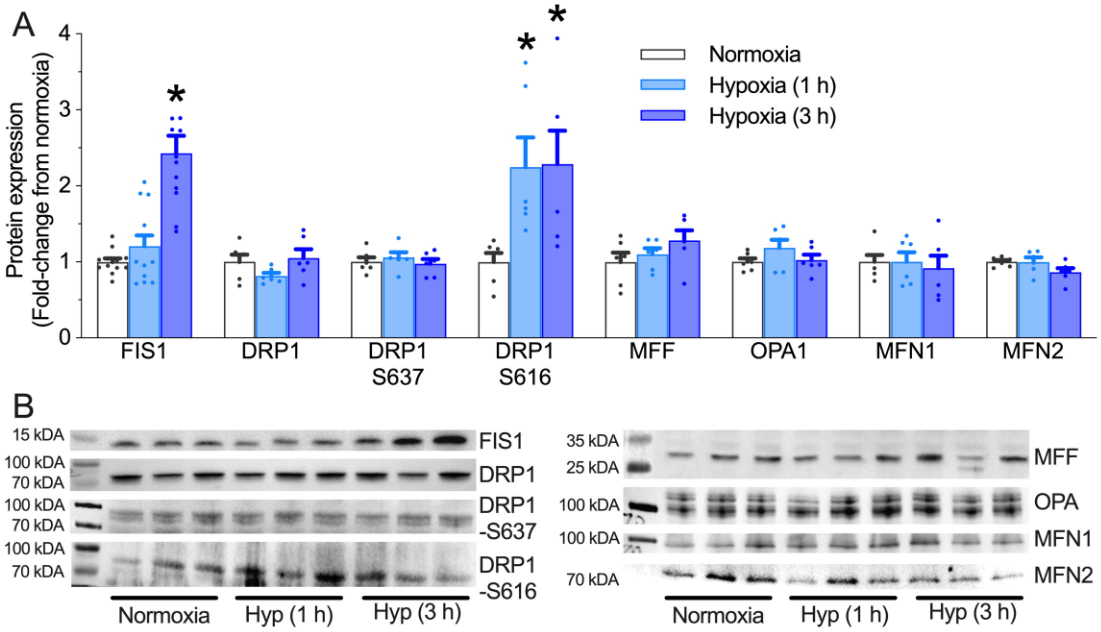

Figure 2.8 Hypoxia activates mitochondrial fission, but not mitochondrial fusion.

(A) Summary of the expression of mitochondrial fission proteins in iBAT homogenates from NMRs held at 30 °C in normoxia (21% O_2, clear bars) or after 1 or 3 hrs of hypoxia (7% O_2, light and dark blue bars, respectively; $n = 12$ biologically independent samples for FIS1 and 6 biologically independent samples for all other proteins). **(B)** Western blot images of protein bands from (A). Data are mean ± SEM. Asterisks indicate significant difference from normoxic controls (one-way ANOVA with Tukey multiple comparisons test; $F_{2,33} = 23.83$, $p < 0.0001$ for fission protein 1 (FIS1); $F_{2,15} = 4.49_{2,}$ $p = 0.0296$ for dynamin-related protein 1-S616 (DRP1-S616); $p > 0.05$ for mitochondrial fission factor (MFF), mitofusin 1 and 2 (MFN1 or 2), and optic atrophy 1 (OPA1)).

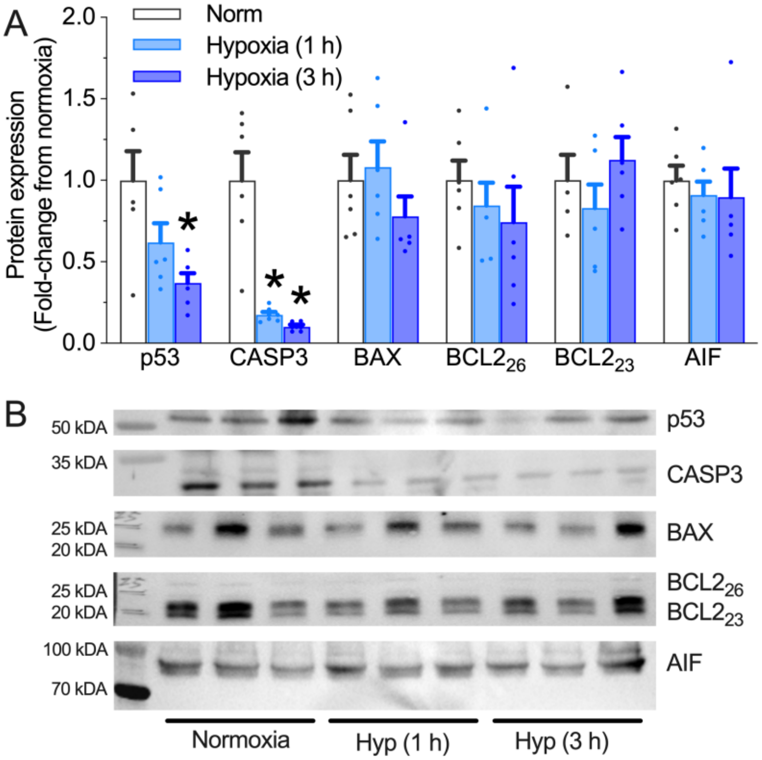

Figure 2.9 Apoptosis is not activated during hypoxia.

(A) Summary of the expression of apoptosis regulatory proteins in iBAT homogenates from NMRs held at 30 °C in normoxia (21% O_2, clear bars; $n = 6$ biologically independent samples) or after 1 or 3 hrs of hypoxia (7% O_2, light and dark blue bars, respectively; $n = 6$ biologically independent samples). **(B)** Western blot images of protein bands from (A). Data are mean ± SEM. Asterisks indicate significant difference from normoxic controls (one-way ANOVA with Tukey multiple comparisons test; $F_{2,15} = 6.087, p = 0.0116$ for p53; $F_{2,15} = 24.64, p < 0.0001$ for caspase 3 (Casp3); $p > 0.05$ apoptosis inducing factor (AIF), Bcl-2-associated X (BAX), and B-cell lymphoma 2 (Bcl-2)).

Table 2.4 Raw values of iBAT mitochondrial respiratory function analysis

Substrate	21% O_2		5% O_2 4 h		Reduction
	mean	SEM	mean	SEM	
O_2 consumption (nmol/(min*mg protein))					
PM	70.78	5.81	28.18	6.68	60.18%
GDP	22.52	1.65	7.29	1.13	67.62%
D	116.58	6.38	60.25	6.86	48.32%
MOct	91.76	7.31	31.56	6.32	65.60%
GDP	35.45	2.43	11.11	1.63	68.65%
D	141.71	7.45	77.18	8.09	45.53%
P	143.18	7.51	79.34	8.56	44.59%
G	141.53	7.13	79.76	8.59	43.65%
S	179.4	8.72	106.75	11.01	40.50%
U	1012.18	56.57	698.86	86.98	30.95%
S	135.16	9.63	69.96	11.51	48.24%
GDP	65.17	2.82	19.15	2.89	70.62%
R	58.36	3.18	17.27	3.22	70.40%
D	172.21	12.59	89.59	11.06	47.98%
AA	13.11	0.67	7.16	0.75	45.38%
TMPD	429.69	24.9	290.42	26.94	32.41%
H_2O_2 efflux (nmol/(min*mg protein))					
PM	0.25	0.03	0.13	0.01	45.63%
GDP	0.24	0.03	0.13	0.01	45.34%
D	0.22	0.03	0.1	0.01	54.35%
MOtc	0.32	0.03	0.18	0.01	44.53%
GDP	0.34	0.04	0.17	0.01	49.04%
D	0.28	0.03	0.13	0.01	52.43%
P	0.27	0.04	0.15	0.01	44.50%
G	0.27	0.03	0.15	0.01	46.67%
S	0.31	0.04	0.16	0.01	46.21%
S	0.46	0.06	0.56	0.08	-22.12%
GDP	2.02	0.15	0.44	0.08	78.27%
R	0.35	0.02	0.21	0.03	38.67%
D	0.41	0.04	0.23	0.06	43.90%

Table 2.4 Raw values of iBAT mitochondrial respiratory functions - continued

Substrate	21% O_2		5% O_2 4 h		Reduction
	mean	SEM	mean	SEM	
			H_2O_2 / O_2 (%)		
PM	0.35	0.03	0.59	0.15	-66.78%
GDP	1.08	0.09	2.01	0.33	-85.43%
D	0.19	0.02	0.18	0.02	7.76%
MOtc	0.37	0.06	0.62	0.08	-70.43%
GDP	0.98	0.15	1.62	0.15	-65.34%
D	0.2	0.03	0.18	0.01	12.36%
P	0.19	0.03	0.19	0.01	-0.86%
G	0.2	0.03	0.19	0.02	3.37%
S	0.17	0.03	0.16	0.02	8.35%
S	0.35	0.06	0.87	0.18	-144.87%
GDP	3.12	0.27	2.28	0.31	27.15%
R	0.61	0.06	1.34	0.22	-120.88%
D	0.25	0.03	0.25	0.04	-2.45%
			RCR		
PM	5.18	0.47	8.26	1.21	-59.65%
MOct	4.11	0.19	6.98	0.77	-73.80%
SR	2.95	0.04	5.19	0.54	-75.82%

Data are mean ± SEM, from *n* = 5 independent biological experiment., statistical analysis were indicated in Fig 2.1& 2.3. Abbreviations: P, pyruvate; M, malate; GDP, guanosine diphosphate; D, ADP; Oct, octanoylcarnitine; G, glutamate; S, succinate; R, rotenone; AA, Antimycin A; TMPD, ascorbate + N,N,N,N-tetramethyl-p-phenylenediamine; U, carbonyl cyanide *m*-chlorophenyl hydrazine; OXPHOS, oxidative phosphorylation; RCR, respiratory control ratio calculated as the ratio of OXPHOS capacity/leak respiration with GDP; “-” represent increasing change.

2.5 Supplementary information

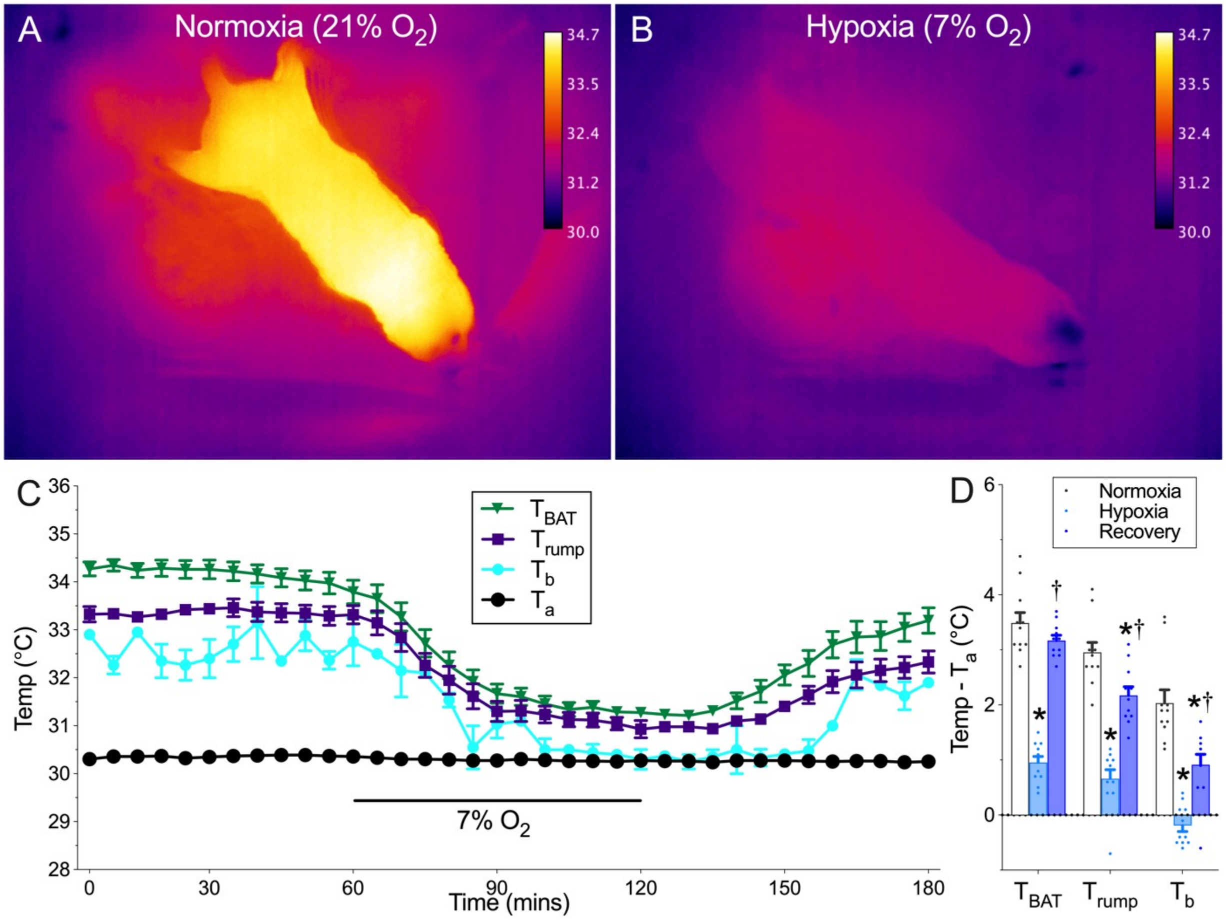

SF 2.1 Thermogenesis ceases in acute hypoxia and T_b drops to ambient levels.

(A, B) FLIR thermal images of an NMR following 60 min of exposure to normoxia (A, 21% O_2) or hypoxia (B, 7% O_2). **(C)** Summaries of T_a (black circles), core T_b (teal circles), iBAT temperature (T_{BAT}, green triangles), and dorsal skin surface temperature (T_{rump}, blue squares) from NMRs exposed to a normoxia → hypoxia → recovery protocol in 30 °C ($n = 11$ independent animals). **(D)** Summaries of temperature difference between physiological temperatures and T_a in the final 10 min of each treatment period from (C). Data are mean ± SEM. Asterisks indicate significant difference from normoxic controls; daggers indicate significant difference from hypoxia (repeated measures ANOVA with Tukey post-test; $F_{2,30} = 136.0$, $p < 0.0001$).

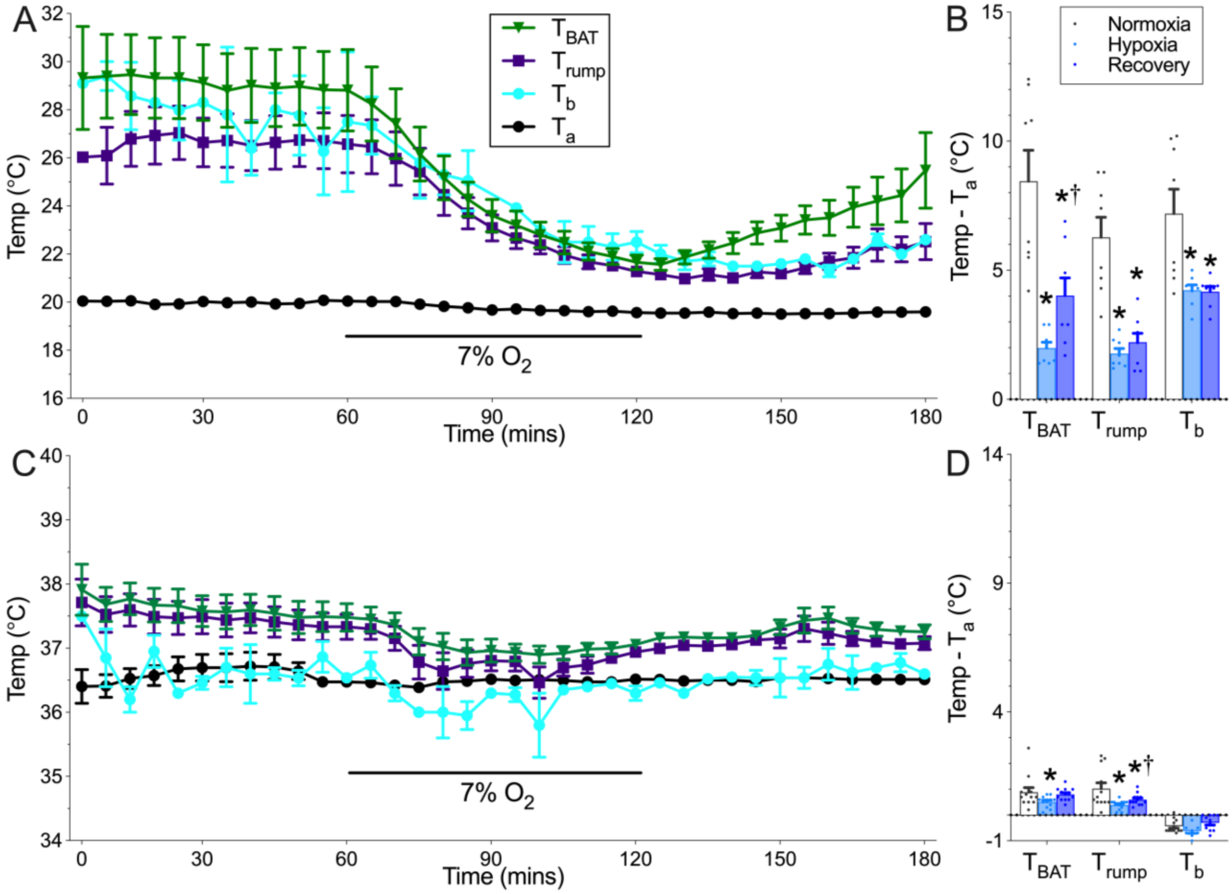

SF 2.2 NMRs actively thermoregulate in cold, but not hot temperatures.

(**A, C**) Summaries of T_a (black circles), core T_b (teal circles), iBAT temperature (T_{BAT}, green triangles), and dorsal skin surface temperature (T_{rump}, blue squares) from NMRs exposed to a normoxia → hypoxia → recovery protocol in 20 °C (A, $n = 8$ independent animals), or 36 °C (C, $n = 12$ independent animals). **(B, D)** Summaries of temperature difference between physiological temperatures and T_a at 20 °C (B) or 36 °C (D) from data presented in (A) and (C), respectively. Data are mean ± SEM. Asterisks indicate a significant difference from normoxic controls; daggers indicate significant difference from hypoxia (repeated measures ANOVA with Tukey post-test; $F_{2,15} = 29.89$, $p < 0.0001$ for 20 °C, $F_{2,22} = 6.63$, $p = 0.0113$ for 30 °C).

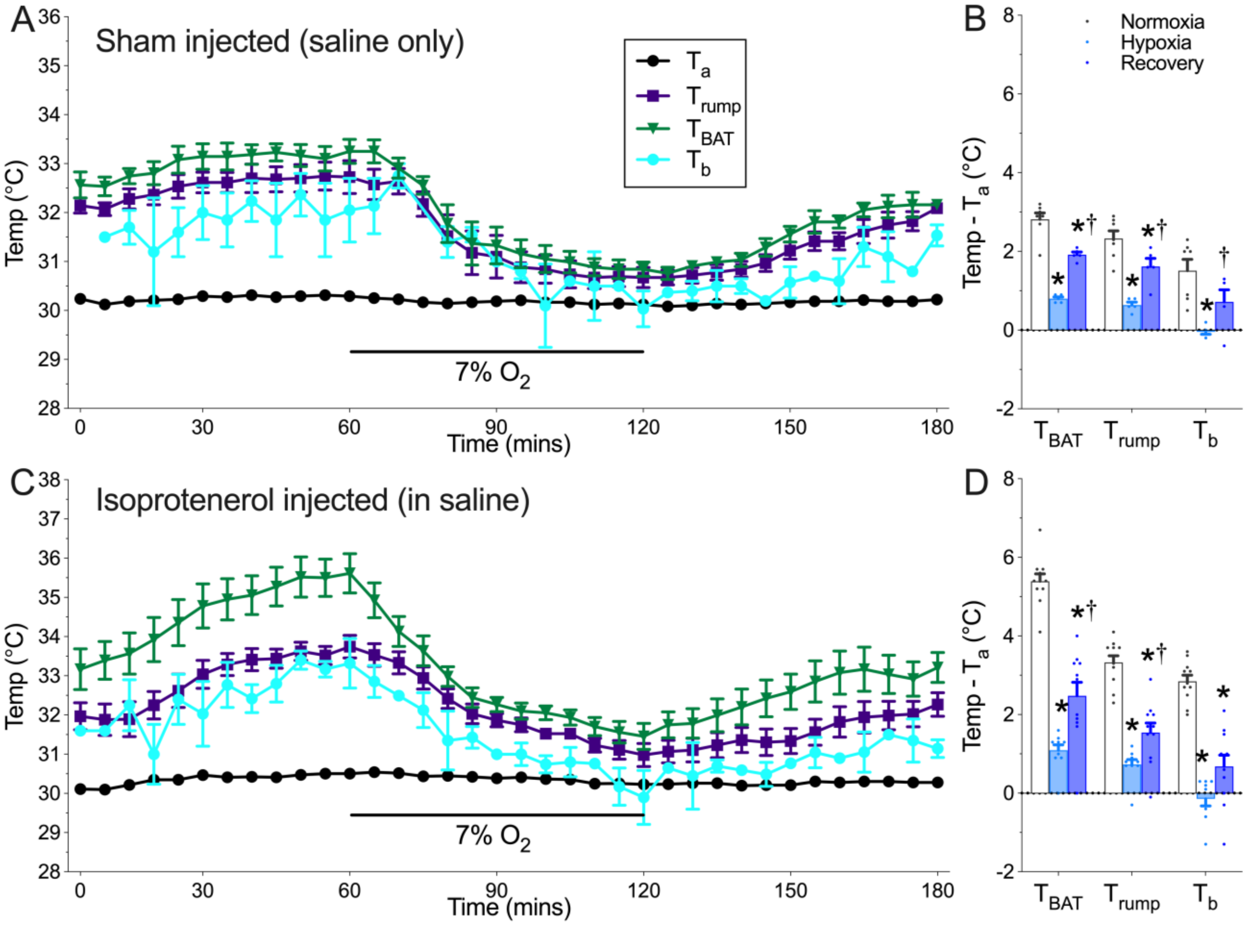

SF 2.3 Adrenergic stimulation enhances non-shivering thermogenesis in normoxia, but not in hypoxia.

(A, C) Summaries of T_a (black circles), core T_b (teal circles), iBAT temperature (T_{BAT}, green triangles), and dorsal skin surface temperature (T_{rump}, blue squares) from NMRs exposed to a normoxia → hypoxia → recovery protocol in 30 °C following injection of saline (A, $n = 5$ independent animals), or isoproterenol (C, $n = 11$ independent animals). (**B**, **D)** Summaries of temperature difference between physiological temperatures and T_a for the same animals as in (A, C). Data are mean ± SEM. Asterisks indicate significant difference from normoxic controls; daggers indicate a significant difference from hypoxia (repeated measures ANOVA with Tukey post-test; $F_{4,9} = 0.5272$, $p < 0.7190$ for shams, $F_{2,30} = 41.2$, $p < 0.0001$ for isoproterenol)

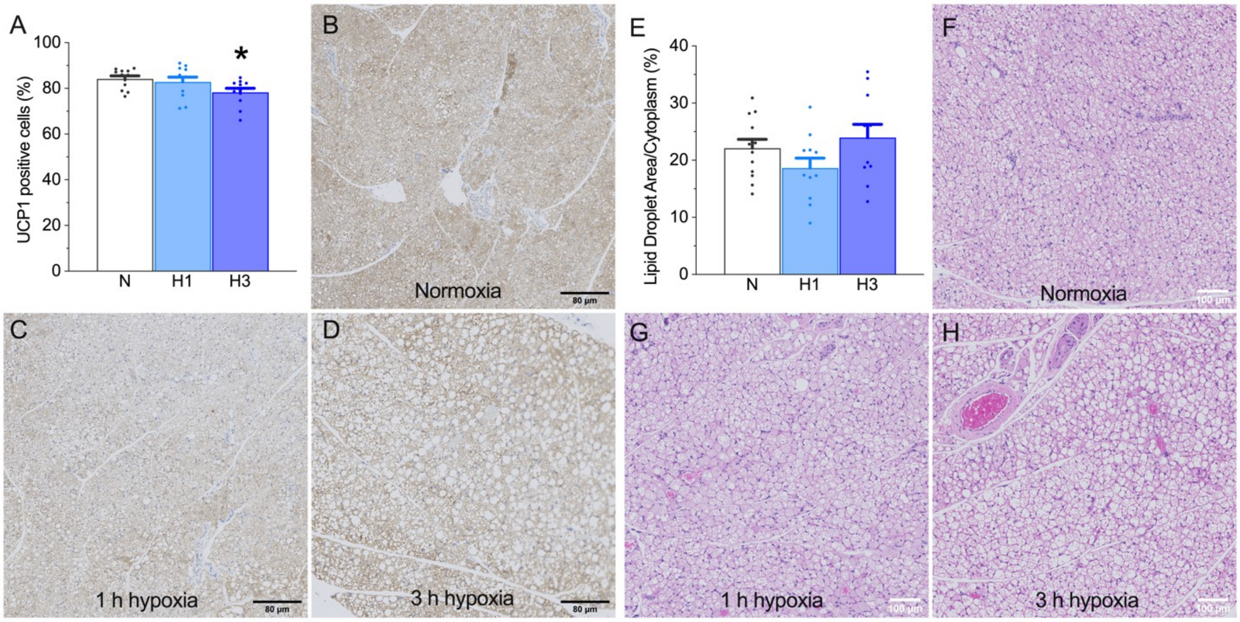

SF 2.4 Immunohistochemistry analysis of UCP1 and lipid droplets.

UCP1-positive cell number and lipid droplet area do not change markedly with acute hypoxia in NMR iBAT. (A) Summary of UCP1-positive cells in interscapular BAT from NMRs treated in normoxia (21% O$_2$; red bars; n = 12), or 1 or 3 h of hypoxia (7% O$_2$; light and dark blue bars, respectively; n = 11 each). (B-D) Representative images of UCP1 staining in BAT cells from NMRs treated as in A. (E) Summary of LD area relative to total cytoplasmic area in interscapular BAT from NMRs treated in normoxia (21% O$_2$; n = 12), or 1 or 3 h of hypoxia (7% O$_2$; n = 11 each). (F-H) Representative images of hematoxylin and eosin (H&E) staining in BAT from NMRs treated as in E. Data are mean ± SEM. Asterisks indicate significant difference from normoxic controls (One- sided Welch's ANOVA test with Dunnett's post-test; $F_{2,34} = 1.915$, $p = 0.1734$ for LD, $F_{2,34} = 3.684$, $p = 0.0442$ for UCP1). Abbreviations: N – normoxia, H1 – 1hr hypoxia, H3 – 3 h hypoxia.

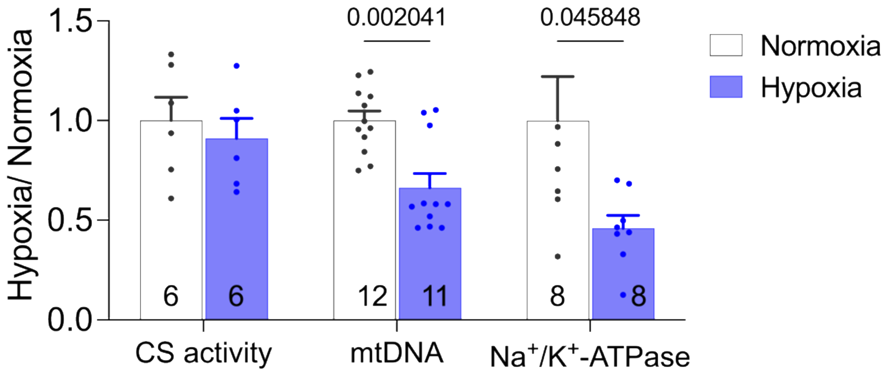

SF 2.5 Changes of CS activity, mitochondrial DNA copy number, and Na$^+$/K$^+$-ATPase activity in hypoxic iBAT.

(A) CS activity (per mg soluble protein), **(B)** mitochondrial DNA copy number (per nuclear DNA), and **(C)** Na$^+$/K$^+$-ATPase activity (per mg soluble protein) were analyzed in NMR iBAT following either normoxia (white bars), or hypoxia (7% O_2 for 4 h, blue bars). Data are presented as means ± SEM, n is indicated. Significant differences ($p < 0.05$ normoxia *vs.* hypoxia) were determined using unpaired multiple t-tests with two-stage step-up (Benjamini, Krieger, and Yekutieli) calculations.

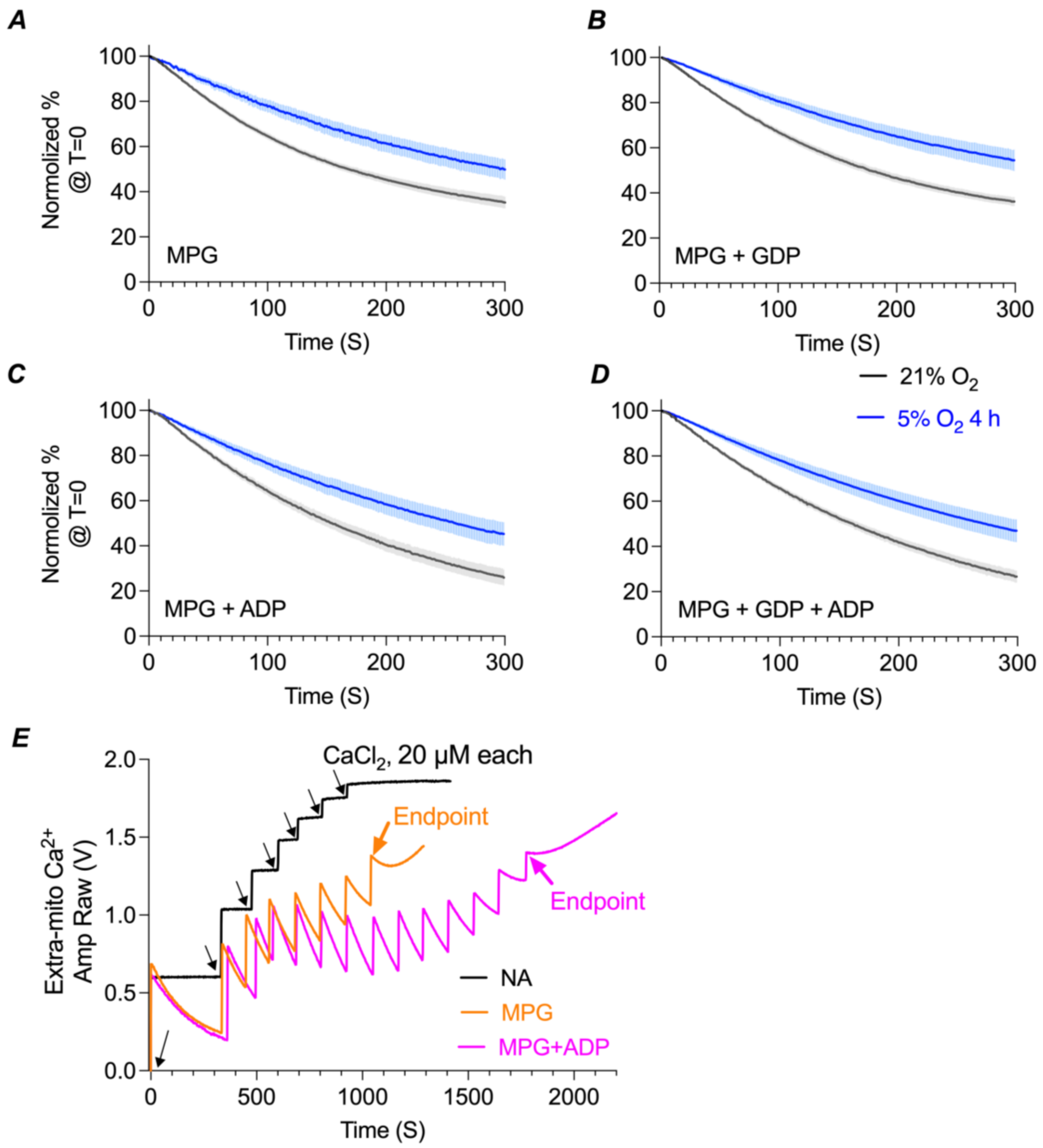

SF 2.6 Ca^{2+} titration of isolated mitochondria in iBAT.

(A-D) Normalized extra-mitochondrial Ca^{2+} followed by a bolus $CaCl_2$ addition in the first five minutes, substrates indicated in each panel, Data are presented as means ± SEM, n = 5; **(E)** examples of traces of Ca^{2+} titration in mitochondria without substrates (black), with MPG (orange), and with MPG+ADP (magenta), black arrows indicated $CaCl_2$ injections, 20 μM each time, orange and magenta arrow indicated endpoint (mPTP opening). Abbreviations: MPG, malate/pyruvate/glutamate; NA, no substrate.

2.6 Discussion

In pilot studies in the Pamenter lab, we previously demonstrated that acute hypoxia (1 h of 7% O_2 exposure) diminishes interscapular thermogenesis in NMRs, consistent with observations of substantial hypoxia-mediated suppression of whole-body metabolic rate and T_b in this species (Ilacqua et al., 2017; Kirby et al., 2018). Specifically, hypoxic NMR: (1) decrease interscapular thermogenesis at temperatures near or below thermoneutrality, and (2) exhibit a significant reduction in iBAT UCP1 and OXPHOS protein expression.

In this chapter, we build upon these early findings and describe a potential mechanism by which mitochondrial respiratory function, and changes in thermogenic and metabolic proteins in iBAT may be downregulated during hypoxia. Specifically, our study provides evidence that BAT function decreases in hypoxia, and that this is tightly associated with a rapid reduction of mitochondrial proteins, which might be mediated by a canonical mitochondrial fission pathway, the activation of which is accompanied by changes in mitochondrial content and cristae ultrastructure. Taken together, our results demonstrate that hypoxia depresses iBAT thermogenesis in NMRs via unique mechanisms that are mediated, at least in part, by targeted reductions in mitochondrial content and of the protein that is essential for non-shivering thermogenesis, UCP1. Consistent with UCP1 and OXPHOS protein degradation, mitochondrial membrane dynamics, diminished interscapular thermogenesis, and suppressed whole animal O_2 consumption, we also reported that isolated iBAT mitochondria largely reduce coupled (~45%) and uncoupled (~70%) respiration, suppress H_2O_2 emission on a per protein basis, and reduce *in vitro* Ca^{2+} uptake rates, while maintaining external Ca^{2+} resistance.

iBAT mitochondrial respiratory complexes might be involved in ETC suppression. Multiple mechanisms are involved in regulating iBAT mitochondria respiration and structure remodelling (de Meis et al., 2010; Snyder et al., 2021). We report for the first time a significant suppression of electron transport function in iBAT mitochondria from NMRs exposed to acute hypoxic. It is possible that degradation of UCP1 triggers the overall degradation of ETC proteins (Sebaa & Harper, 2020), which in turn results in suppression of mitochondrial O_2 consumption. Indeed, there is evidence that deletion of UCP1 in mouse BAT mitochondria leads to overall complex I activity reductions (Dlasková et al., 2021), which directly results in reduced complex I protein density (Riley & Mills, 2020). Our results also suggest that mitochondria may be depolarized following hypoxia treatment, because both uncoupling and coupling respiration are suppressed relative to maximal electron transport capacity and complex IV capacity (Fig. 2.7). This could be a result of inner-mitochondrial membrane remodelling, or perhaps due to a mild increase of outer-mitochondrial membrane damage (Fig. 2.8C). The relatively larger suppression of leak respiration (with GDP, ~70% reduction, Fig. 2.6A-C) than of OXPHOS (~45% reduction, Fig. 2.6A-C) results in an elevation of RCRs in hypoxic iBAT mitochondria (Fig. 2.8 A), and this relationship warrants further study.

Note that, we also noticed a reduction of Na^+/K^+-ATPase activity (SF 2.5), which is one of the mitochondrial sources of heat generation (Clarke et al., 2013; de Meis, 2003; Rothwell et al., 1982). The decrease in activity of this pump may contribute to diminishing heat production form hypoxic iBAT independent of UCP1 regulation. However, this pump is normally regulated by catecholamines and thyroid hormones (Rothwell et al., 1982). Thus, further studies of the regulation of ATPase-dependent heat production in hypoxia may provide more details on energy preservation in hypoxic NMR BAT.

Overall, these results suggest that iBAT mitochondria become less leaky to protons under hypoxic stress. Taken together with our findings regarding hypoxic iBAT mitochondrial membrane dynamics, we suggest that NMRs might remodel iBAT mitochondria through membrane and related protein changes resulting in an overall reduction in the O_2 cost to retain functional mitochondria in iBAT.

Altered mitochondrial succinate metabolism in NMR iBAT. In mouse BAT, UCP1-mediated uncoupling becomes more sensitive to GDP when the redox state is more reduced (Mailloux et al., 2012). Similarly, we report lower GDP-inhibited uncoupling respiration in hypoxic NMR iBAT mitochondria (Fig. 2.6 A-C), which may be associated with lower H_2O_2 efflux in this tissue (Fig. 2.6 D-F). Moreover, we found that complex II has higher sensitivity to GDP-inhibited uncoupling respiration than complex I. Specifically, UCP1-mediated uncoupling is more sensitive to GDP during succinate-induced respiration than when fueled by pyruvate or octanoylcarnitine (Fig. 2.8 B). Conversely, the inhibitory impact of GDP on UCP1-mediated uncoupling with succinate is minimal in mouse and rat BAT mitochondria (De Meis et al., 2012; Oelkrug et al., 2010; Shabalina et al., 2013; Shabalina et al., 2014). This result may be due to the reduction of electron leakage (H_2O_2/O_2), which was inhibited in succinate/GDP respiration but enhanced with other substrates in hypoxic iBAT mitochondria in NMRs (Fig. 2.6 G-I). Thus, our results indicate that mitochondrial complex II and/or succinate-related electron transport pathways play critical roles in hypoxia adaptation in NMR iBAT.

Is Ca^{2+} overload an initiator or an effect of iBAT mitochondrial respiratory changes in hypoxia? We report that the rate of Ca^{2+} uptake by NMR iBAT mitochondria is reduced by ~ 50% in hypoxia but that there are no defects regarding extra-mitochondrial Ca^{2+} resistance (Fig. 2.8). It is possible that the suppression of uncoupling and coupling respiration reduces the Ca^{2+} uptake rate, since isolated mitochondria cannot take up relatively high amounts of Ca^{2+} without any substrates (SF. 2.6E). These results also indicate that NMRs maintain mitochondrial inner-membrane integrity during hypoxia.

Reducing BAT mitochondrial O_2 consumption diminishes interscapular thermogenesis in hypoxic NMRs. Hypoxia reduces thermogenesis in other mammalian models of hypoxia-tolerance, including hibernators and neonates (Mortola & Dotta, 1992; Rohlicek et al., 1998), and in some hypoxia-intolerant adult rodents; however, the mechanisms underlying these decreases are varied and do not involve changes in non-shivering thermogenesis, or if they do, are not mediated by changes in thermogenic protein expression. For example, many mammals utilize a variety of behavioral and physiological strategies (*e.g.*, reduced huddling, moving to a cooler environment, etc.) to lower T_b and reduce thermogenic energy consumption, and thus conserve O_2 in hypoxia (Gordon & Fogelson, 1991; Levesque & Tattersall, 2009; Mortola & Feher, 1998). Others decrease shivering thermogenesis in hypoxia (Barros et al., 2001; Gautier et al., 1987; Tattersall & Milsom, 2003). Conversely, while non-shivering thermogenesis is also reduced in hypoxia in other small mammals (Gautier & Bonora, 1994; Gautier et al., 1991), this response seems to be largely dependent on a reset of the hypothalamic thermogenic threshold and thus of the neural activation of iBAT activity (Cannon & Nedergaard, 2004; Oelkrug et al., 2015; Tattersall & Milsom, 2009) rather than a downregulation of thermogenic effectors.

In most small mammals, BAT thermogenesis is an energy-intensive process that can drastically impact whole-body energy homeostasis (Cannon & Nedergaard, 2004; Oelkrug et al., 2015). Previous studies indicate the existence of functional iBAT in NMRs (Oiwa et al., 2020; Withers & Jarvis, 1980; Woodley & Buffenstein, 2002). Furthermore, activation of BAT in NMRs greatly increases whole-animal O_2 consumption, and this increase explains most of the increases in whole-body O_2 consumption in NMRs under these conditions (Goldman et al., 1999; Hislop & Buffenstein, 1994; Woodley & Buffenstein, 2002). Our study confirms this knowledge: we show that NMRs actively thermoregulate and engage BAT thermogenesis at temperatures near or below thermoneutrality or following treatment with an adrenergic agonist (SF 2.2&2.3). Beyond normoxic conditions, our work demonstrates that hypoxia rapidly decreases BAT thermogenesis in NMRs. Notably, we observe a hypoxia-induced decrease in BAT thermogenesis in animals that have received injections of either saline or isoproterenol (SF 2.3), and in environmental temperatures near or well below the thermoneutral zone of this species (SF 2.2). Consistently, isolated iBAT mitochondria exhibit dramatic reductions of O_2 consumption capacity, including of both UCP1-induced uncoupling and OXPHOS (Fig. 2.6 A-C). These results indicate that the hypoxia-mediated decrease in BAT thermogenesis in NMRs is a result of the degree to which BAT mitochondrial respiration is reduced in hypoxia. But how are these changes regulated?

Reducing heat production by iBAT through mitochondrial UCP1 degradation. UCP1 is essential for BAT thermogenesis (Enerback et al., 1997; Himms-Hagen, 1985; Nicholls, 2006), is expressed in mitochondria from classical BAT, and is located in the mitochondrial inner membrane (Argyropoulos & Harper, 2002; Nedergaard et al., 2001). It is estimated that UCP1 comprises approximately 10% of BAT mitochondrial protein content (Busiello et al., 2015), and it is well established that defects in the activity of UCP1 resulting from post-translation modifications or the absence of UCP1 can impact BAT thermogenesis (Chouchani et al., 2016a; Enerback et al., 1997; Sebaa et al., 2019); mice lacking UCP1 are cold intolerant (Enerback et al., 1997). Given this essential role for UCP1 in BAT thermogenesis, we examined the effect of acute hypoxia on UCP1 protein levels in iBAT and found significant decreases following only 1 hr of *in vivo* hypoxia, and that these decreases are sustained after 3 hrs. This change is likely primarily due to reduced, but not eliminated expression of UCP1 in iBAT cells as immunohistochemistry analysis reveals that the number of UCP1-positive cells decreases only mildly relative to the more robust change in a quantitative measure of total iBAT UCP1 expression (i.e., western blot data). Conversely, UCP3, which also plays a role in thermogenesis (Silvestri et al., 2020), did not change significantly with progressive hypoxia.

In other rodent species, changes in UCP1 expression require longer-term hypoxic exposure to manifest. For example, exposure of cultured and immortalized mouse SV40T fetal brown inguinal adipocytes to short-term hypoxia (1, 12, or 24 h in 1% O_2) has no impact on UCP1 protein expression (Wree et al., 2012). Conversely, longer-term hypoxia alters UCP1 function in some mammals. For example, (i) 4–6 days of chronic hypoxia results in significant decreases in UCP1 protein expression in neonatal and adult BAT in rats (Mortola & Naso, 1997, 1998), (ii) 4 weeks of chronic hypoxia increases UCP1 mRNA, but not UCP1 protein expression in mice (Beaudry & McClelland, 2010), and (iii) in a mouse model of sleep apnea, 37 days of daily 8 h periods of intermittent hypoxia decreases UCP1 mRNA expression and UCP1-positive cells in iBAT (Fiori et al., 2014). While this sparse experimental evidence indicates that hypoxia can downregulate UCP1 expression in hypoxia-intolerant species, the time required for this process ranges from several days to several weeks. This is likely because a relatively long time is required to turn over UCP1 in most mammals, the rate of which depends on the metabolic status of BAT: in mouse brown adipocytes, UCP1 turnover takes 3.7 ± 0.4 days in basal conditions and 8.4 ± 0.9 days with chronic adrenergic stimulation (Moazed & Desautels, 2002), with a half-life of ~ 30 h in basal conditions (Puigserver et al., 1992; Rousset et al., 2007). Thus, the downregulation in UCP1 expression in NMR iBAT after 1 hr of hypoxia is remarkably rapid compared to other small rodent species.

Mitochondrial fission but not mitophagy or apoptosis is involved in thermogenic protein reduction. The rapid degradation of thermogenic proteins in iBAT of NMRs could be mediated by several well-known and -characterized mechanisms, including the UPS, mitophagy, or mitochondrial fission/fusion events. In UPS-dependent pathways, targeted proteins are ligated with ubiquitin and then degraded by proteasomes. Importantly, protein ubiquitination is a post-translational modification that leads to the degradation of protein not only through proteolysis but also through mitophagy. These mechanisms are activated by hypoxia in some models (Fuhrmann et al., 2013), and NMRs have a very high rate of autophagy compared to other rodents (Zhao et al., 2014). However, although it was a global increase in ubiquitination in NMR iBAT after 1 hr of hypoxia and a general increase in LC3II activation at 3 hrs of hypoxia, we did not detect co-immunoprecipitation of ubiquitin with UCP1, nor changes in any UPS- or mitophagy-related proteins (Parkin, PINK1, p62, FUNDC1, BNIP3, Nix, or TBCD15). Taken together, these results suggest that the UPS or mitophagy mechanisms are not mediating the downregulation of UCP1 in iBAT.

In addition to UCP1, hypoxia also decreases the levels of mitochondrial OXPHOS proteins in NMR iBAT. The rate of turnover of proteins in these complexes in mice can vary depending on the tissue or treatments that cause metabolic changes in mitochondria (Karunadharma et al., 2015), but are in general considerably slower than the rate that we observe in NMR iBAT. Given the rapid decreases in UCP1 and these mitochondrial metabolic proteins in iBAT during hypoxia, and the absence of ubiquitin-binding to NMR iBAT UCP1, we considered changes in mitochondrial structure and ultrastructure, which can be potent regulators of thermogenic potential (Wikstrom et al., 2014).

Fission is a complex process in mitochondrial regulation and plays key roles in mitochondrial division and in the initiation and spatial organization of mitophagy (Liesa & Shirihai, 2013). Mitochondrial fission is mediated by Drp1, with phosphorylation at site S616 associated with translocation of Drp1 to the mitochondrial membrane and activation of fission, and dephosphorylation at site 637 associated with deactivation of Drp1 (Cereghetti et al., 2008; Shirakabe et al., 2016; Xie et al., 2020). Despite significant research attention, the mechanism of mitochondrial fission remains poorly understood. Using super-resolution microscopy, a recent study identified two spatially distinct modes of mitochondrial fission, both of which are mediated by Drp1(Kleele et al., 2021). Midzone division is associated with fission and reorganization of healthy mitochondria, whereas peripheral division is associated with the budding-off of damaged portions of mitochondria. Importantly, both forms of fission are associated with Drp1 accumulation, but are regulated by association with different cellular factors. Specifically, fission of healthy mitochondria is regulated by contact with the ER, whereas fission of damaged mitochondria is associated with Fis1 upregulation. Downstream of Drp1/Fis1-mediated fission, damaged mitochondrial segments undergo mitophagy, mediated by interactions with Parkin/PINK1(Lin et al., 2020; Ni et al., 2015; Pendin et al., 2017), and thus whole segments of mitochondria become ubiquitylated and tagged for lysosomal degradation.

Our observations indicate that Drp1 is phosphorylated at site S616 but not S637 at both 1 and 3 hrs of hypoxia, and that mitochondria exhibit rapid and reversible changes in ultrastructure and cristae morphology on the same timeline, indicate that fission is activated by hypoxia in NMR iBAT. Furthermore, the absence of any change in Fis1 expression at 1 hr suggests that fission of healthy mitochondria occurs rapidly during acute hypoxia (Kleele et al., 2021). The mitochondrial inner membrane is folded to form cristae, and this is where UCP1 and OXPHOS proteins are located. Therefore, fission of healthy mitochondria may mediate the decrease in thermogenic proteins from the IMM and facilitate the rapid decrease in iBAT thermogenesis during acute hypoxia. Notably, we observe a marked increase in Fis1 following 3 hrs of acute hypoxia, suggesting that mitochondrial degradation occurs with longer-term hypoxia and that peripheral fission of damaged portions of mitochondria occurs with prolonged hypoxia. Presumably with longer-term experiments, we would observe an upregulation in the Parkin/PINK1 mitophagy pathway, and indeed we see a weak, but insignificant trend towards such activation in the expression of both Parkin and the two components of PINK1, along with a significant increase in LC3-II at 3 hrs of hypoxia. However, in their natural environments, NMRs typically do not spend more than a few hours in the nest chamber at a time before moving about the colony to perform various tasks, and burrows are not expected to be hypoxic outside of these crowded nest chambers (Buffenstein et al., 2021), thus animals would likely not experience such prolonged durations of acute and severe hypoxia in nature.

Limitations. There is a critical question that has not been fully answered in this chapter, which is how our target mitochondrial proteins were degraded in hypoxic iBAT. Although we show that mitochondrial fission might be engaged, we have not reported any molecular mechanisms that directly link fission to this protein degradation. We did not see significant reduction of TOM20, or elevation of mitophagy proteins in hypoxic iBAT. Therefore, further study of mechanisms of protein degradation within iBAT mitochondria during hypoxia may be warranted (Bota & Davies, 2001; Kaser & Langer, 2000; Langer & Neupert, 1996).

Overall conclusion. Our results support the general conclusion that NMRs respond to acute hypoxia by diminishing iBAT thermogenesis and that, in NMRs, this is partially achieved by acutely decreasing the levels of thermogenic proteins and altering mitochondrial ultrastructure, which presumably results in the suppression of mitochondrial O_2 consumption. In addition, we provide a plausible mechanism via which fission of healthy mitochondria may mediate this process. Importantly, the absence of mitophagy and apoptosis, and the reversibility of the suppression of iBAT thermogenesis and mitochondrial morphological changes following reoxygenation, indicate that this process occurs in healthy mitochondria and is not deleterious to mitochondrial function. In addition, our results suggest that management of mitochondrial $O_2^{\cdot-}$ and Ca^{2+} may be involved in hypoxic iBAT mitochondrial homeostasis in NMRs. Further work to elucidate adaptive mechanisms in iBAT regulation in NMRs will lead to a better understanding of potentially unique mechanisms within this tissue that allow these interesting animals to survive in extreme conditions. It is likely that decreases in iBAT activity (and associated thermogenesis) occur as part of a larger suite of adaptive mechanisms during hypoxia, along with many other means of energy (and thus O_2) conservation; however, given the high metabolic cost of thermoregulation in small rodents, the mechanism we identify is likely of significant importance to the hypoxia-tolerance of NMRs.

3 Hypoxia-tolerance in NMR brain mitochondria: Ca^{2+} management, micro-architecture, redox state management, and mitochondrial quality control

This chapter includes material from the following article:

Cheng, H., Qin, Y. A., Dhillon, R., Dowell, J., Denu, J. M., & Pamenter, M. E. (2022). Metabolomic Analysis of Carbohydrate and Amino Acid Changes Induced by Hypoxia in Naked Mole-Rat Brain and Liver. Metabolites, 12(1), 56. https://doi.org/10.3390/metabo12010056

Matthew Pamenter, Rashpal Dhillon, and John M Denu designed the study, Matthew Pamenter treated animals and collected tissues. Yiming Amy Qin, Rashpal Dhillon, James Dowell performed mass spectroscopy experiments. Yiming Amy Qin and I performed the analysis. Matthew Pamenter and I wrote the manuscript.

Cheng, H., Perkins, G. A., Ju, S., Kim, K., Ellisman, M. H., and Pamenter, M. E. Enhanced mitochondrial buffering prevents Ca^{2+} overload in naked mole-rat brain. in submission.

Saeyeon Ju, Keunyoung Kim, Guy Perkins and Mark Ellisman imaged and analyzed electron microscope data at National Center for Microscopy and Imaging Research, UC San Diego.

Bivaz Jaffer (under my supervision) conducted the experiments for SF. 3.4 as her undergraduate honours thesis project.

Matthew Pamenter and I conceived of all other studies, and I conducted all other experiments.

3.1 Introduction

Brain function depends profoundly on ATP supply, which is generated by mitochondrial OXPHOS; thus, brain is one of the most O_2-dependent organs (Hall et al., 2012; Nicholls & Budd, 2000; Siesjö, 1978). Cellular Ca^{2+} is a key regulator of mitochondrial bioenergetics. Ca^{2+} accumulation in the mitochondrial matrix both stimulates aerobic metabolism (oxidative phosphorylation: OXPHOS; through the modulation of tricarboxylic acid (TCA) cycle and other enzymes) (Gellerich et al., 2010; Griffiths & Rutter, 2009), and activates and/or amplifies numerous cellular cascades that impact mitochondrial bioenergetics through the regulation of mitochondrial ultrastructure via fission, fusion, mitochondrial biogenesis, and/or mitophagy (Pandya et al., 2013; Polster & Fiskum, 2004; Raffaello et al., 2016). As a result, tight regulation of mitochondrial and cytosolic [Ca^{2+}] is important for maintaining neuronal homeostasis. However, during periods of low O_2 stress (*e.g.*, hypoxia or ischemia), neuronal cytosolic [Ca^{2+}] becomes deleteriously elevated in hypoxia-intolerant brain, leading to overloading of mitochondria with Ca^{2+}, which in turn induces excitotoxic cell death and activates cell death pathways (Polster & Fiskum, 2004).

Deleterious Ca^{2+} overload is central to hypoxic/ischemic brain cell death. Briefly, a rapid and large elevation (from 10^{-7} to 10^{-4} mole) of neuronal cytosolic [Ca^{2+}] occurs within ~ 8 min of hypoxia or ischemia onset (Silver & Erecinska, 1990). Most of this Ca^{2+} is sequestered by mitochondria in the form of calcium phosphate (Kristian & Siesjo, 1998; Shen & Jennings, 1972), but mitochondria quickly become overloaded, which leads to deficits in ATP production, mitochondrial membrane depolarization, activation of the mPTP, and ultimately the catastrophic release of mitochondrial Ca^{2+} and other molecules from mitochondria, including cytochrome c, apoptosis-inducing factor, and serine protease HTRA2 (Htra2/Omi), which promote caspase-dependent and caspase-independent cell death pathways (Kroemer et al., 2007; Polster & Fiskum, 2004). Production of mitochondrial ROS, a “by-product” of OXPHOS from the ETC, can be increased by mitochondrial Ca^{2+} overload in multiple pathways, for example Ca^{2+} interacts with alpha-ketoglutarate dehydrogenase (α-KGDH) to induce mitochondrial ROS production (Tretter & Adam-Vizi, 2005), Ca^{2+} depolarizes $\Delta\psi_m$ as a result of reverse electron transport-induced ROS increases (Zoratti & Szabo, 1995), and excess Ca^{2+} increases the H_2O_2 release rate in succinate-fuelled mitochondria (Aldakkak et al., 2013). Taken together, an increasing body of literature suggests that the hypoxic ROS imbalance is related to mitochondrial Ca^{2+} overload and plays a key role in damage to cellular components that eventually result in cell death (Brookes et al., 2004; Popa-Wagner et al., 2013; Qu et al., 2016).

Conversely, Ca^{2+} overload is delayed or even prevented in the brains of hypoxia-tolerant species, such as NMRs. Indeed, NMR brain tolerates acute and chronic *in vivo* hypoxia and *in vitro* ischemia (Nathaniel et al., 2009; Pamenter et al., 2018), such that mitochondrial membrane integrity is preserved and the ETC remains tightly coupled (Cheng & Pamenter, 2021; Pamenter et al., 2018). *In vitro*, hypoxic NMR neurons maintain mitochondrial $O_2^{\cdot -}$ and cellular H_2O_2 homeostasis (Eaton et al., 2022) and restrict *in vivo* hypoxic oxidative damage (Hadj-Moussa et al., 2022). In addition, ATP concentration in hypoxic NMR brain does not change relative to normoxic controls (Pamenter et al., 2019a), although hypoxic NMR brain mitochondria became depolarized (Pamenter et al., 2018), which normally occurs with low ATP production (Zorova et al., 2018). This paradox may be partially due to blunted Ca^{2+} uptake by NMR neurons during hypoxia (Peterson et al., 2012a). However, most mechanisms of cellular Ca^{2+} handling have not been specifically evaluated in NMR brain, including mitochondrial Ca^{2+} handling and mitochondrial ROS management under hypoxia.

We hypothesized that, relative to hypoxia-intolerant mouse brain, 1) NMR brain mitochondria have enhanced capacity to buffer otherwise deleterious external [Ca^{2+}] changes, and 2) this enhanced capacity raises the mitochondrial matrix [Ca^{2+}] threshold for mPTP opening, preserves OXPHOS capacity and $\Delta\psi_m$, and better supports ROS management.

Furthermore, we observed enhanced mitochondrial connectivity and crista density in NMR brown fat tissue (Cheng et al., 2021b), which has also been observed in hypoxia-tolerant ground squirrel brain (Popov et al., 2005), but not in hypoxia-intolerant rodent brain (Picard et al., 2015). Greater mitochondrial connectivity and cristae density enhances mitochondrial bioenergetics and improves mitochondrial Ca^{2+} buffering capacity (Perkins et al., 2010). Moreover, mitochondrial Ca^{2+} management is tightly connected to mitochondrial dynamics in multiple tissues (Guan et al., 2019; Kazak et al., 2017). **Therefore, we further hypothesized** that the unique ultrastructure of NMR brain mitochondria underlies improved mitochondrial Ca^{2+} management during acute hypoxia in NMR brain.

To test our hypotheses, we evaluated the ability of NMR and mouse brain mitochondria to take up and retain Ca^{2+}, and the impact of exogenous Ca^{2+} addition on mitochondrial OXPHOS capacity and $\Delta\psi_m$ following *in vitro* Ca^{2+} titration. We also tested the impact of Ca^{2+} on H_2O_2 consumption in permeabilized NMR brain. Finally, we exposed NMRs and mice to *in vivo* hypoxic acclimation and examined changes in metabolites related to ROS homeostasis, and the activation of Ca^{2+}-mediated mitochondrial fission/fusion/mitophagy pathways during *in vivo* hypoxia.

3.2 Methods

3.2.1 Ethics approval

NMRs were group-housed in interconnected multi-cage systems at 30°C and 21% O_2 in 50% humidity with a 12L:12D light cycle. Animals were fed fresh tubers, vegetables, and fruit, and Pronutro cereal supplement *ad libitum*. Female CD-1 mice were obtained from Charles River and were housed at room temperature under a 12L:12D light cycle and fed rodent chow *ad libitum*. Animals were not fasted prior to experimental trials. All experimental procedures were approved by the University of Ottawa Animal Care Committee in accordance with the Animals for Research Act and by the Canadian Council on Animal Care. Non-breeding (subordinate) naked mole-rats do not undergo sexual development or express sexual hormones and thus we did not take sex into consideration when evaluating our results (Holmes et al., 2009).

3.2.2 In vivo acute hypoxia treatments

Subordinate NMRs (adult, 1-2 years old, 30°C) and mice (adult, 12-16 weeks old, 24°C) were exposed to one of four treatment conditions: normoxia (21% O_2, balance N_2), acute hypoxia (4 h or 6 h in 7% O_2, balance N_2), or hypoxia/reoxygenation (6 h in 7% O_2, followed by 24 h 21% O_2, balance N_2). Animals were not provided with food during the hypoxic treatment periods.

3.2.3 Tissue collection for molecular biology assessments

Immediately following treatment, animals were sacrificed by cervical dislocation followed by immediate decapitation. Brain was rapidly dissected on ice and snap-frozen and stored at −80 °C until it was used for western blot, qPCR, and enzymes activity analysis.

3.2.4 Brain homogenate preparation for in vitro assays

Whole experiment was performed on ice. Following cervical dislocation and decapitation, cortex (100 mg wet weight/ml) was dissected in ice-cold Tris solution containing (in mM): KCl

105, Tris-HCl 50, pH 7.1). Brain tissue (100 mg wet weight/ml) was transferred to a pre-cooled glass Potter homogenizer and homogenized with 5-10 strokes manually. Brain homogenate was used immediately for assessment of respiration and Ca^{2+} titration, remained aliquots were frozen at −80°C for subsequent enzyme assays.

3.2.5 Ca^{2+} uptake experiment

Extra-mitochondrial Ca^{2+} was estimate with the Ca^{2+} sensitive Calcium green 5-N fluorescent dye using Oroboros modified from (Spinazzi et al., 2019) at physiological temperatures (mice: 37°C; NMRs: 32°C). Ca^{2+} titration was measured in an EGTA free medium ((in mM): KCl 120, HEPES 20, KH_2PO_4 20, $MgCl_2$ 2.5, NaCl 5, and BSA 0.03, 1 µM Calcium green 5-N; pH 7.2). Substrates combinations including 10 mM glutamate, 5 mM pyruvate, 5 mM malate, 1 mM ADP, 1 mM ATP, 1 µM RU360, and CCCP (1 µM for mice and 1.5 µM for NMRs), and individual experiment was performance using different substrates combinations, including glutamate/malate/ADP/RU360 (negative control), glutamate/malate/ADP/CCCP/RU360 (negative control), ATP (mitochondria-independent ATP), glutamate/malate (membrane potential dependent), glutamate/malate/ADP (mitochondria-dependent ATP), glutamate/malate/ADP/CCCP (negative control). Following 5-10 mins equilibration, permeabilized brain tissue (2 mg/ml) were then exposed to Ca^{2+} titrations (one 50 µM Ca^{2+} injection with awaiting of 5 mins followed by multiple 20 µM Ca^{2+} injections followed by 2 mins waiting), and fluorescence reductions represented mitochondrial Ca^{2+} uptake. mPTP opening was detected as a fluorescence increase and the overall titrated Ca^{2+} represented as maximal Ca^{2+} resistance capacity. Ca^{2+} uptake rates were calculated within first 5 mins of fluorescence reducing using “One phase decay-equation” in GraphPad Prism 9 (GraphPad Prism, La Jolla, CA, USA).

3.2.6 Ca^{2+} titrations on mitochondrial respiration

Ca^{2+} effected mitochondrial respiration was measured using Oroboros at physiological temperatures (mice: 37°C; NMRs: 32°C) in an EGTA free medium ((in mM): d-sucrose 110, lactobionic acid 60, taurine 20, KH_2PO_4 10, $MgCl_2$ 2, HEPES 20, and BSA 0.015; pH 7.2). 1mg/ml brain tissue, 10mM glutamate, 5mM malate, 50 µg/ml saponin, and $CaCl_2$ (0, 0.2, 10, 20, 50, 100, and 150 µM in separate rounds) was incubated ~10 min in chamber to induce leak respiration from complex I, and then 1 mM ADP to induce OXPHOS respiration from complex I, 10 µM cytochrome c to assess outer mitochondrial membrane damage, 10 mM succinate to induce OXPHOS respiration from complexes I&II, and CCCP to induce maximal electron transport capacity from complexes I&II, in 0.5 µM steps until reaching the maximal response) was added sequentially. Saturating concentrations were determined in pilot experiments (data not shown). Preparation of all substrates were as per (Fontana-Ayoub et al., 2016).

3.2.7 Ca^{2+} titrations on mitochondrial membrane potential

The impact of Ca^{2+} on $\Delta\psi_m$ was measured using the Oroboros fluo module at physiological temperatures (mice: 37°C; NMRs: 32°C) in an EGTA free medium (in mM: KCl 120, HEPES 20, KH_2PO_4 20, $MgCl_2$ 2.5, NaCl 5, and BSA 0.03; pH 7.2). 1mg/ml brain tissue, 50 µg/ml saponin, and 2 µM Rhodamine 123 (Rh-123) was incubated ~10 min in chamber, and then 10 mM glutamate and 5 mM malate to induce $\Delta\psi_m$ through complex I, $CaCl_2$ (0, 5, 10, 20, 50, 100, and 150 µM consecutively, alternatively expressed as 0, 5, 10, 20, 50, 100 and 150 µM, respectively) and CCCP to reach the minimal membrane potential (in 0.5 µM steps until reaching the maximal response) was added sequentially.

The Linear relationship between the digital signal and Rh-123 fluorescence (ΔV/μM) was validated on a five-point curve conducted with cortical brain tissue alone and by direct addition of 0.5 μM Rh-123 four-times to the chamber.

3.2.8 Ca^{2+} inhibits H_2O_2 consumption in permeabilized NMR brain

Adult NMR brains were dissected and homogenized as described in 3.2.4, followed by shaking at 100 rpm with 50 μg/ml saponin, and then centrifugation at 500 rpm in 4°C for 5 mins 2x in homogenization solution (in mM: KCl 105, Tris-HCl 50, pH 7.1), centrifuged tissue was added to homogenization solution at 5 mg/ml and kept on ice. 150 μl of 5 mg/ml permeabilized brain tissue was incubated with and without substrates (10 mM glutamate and 2 mM malate for complex I, 10 mM succinate for complex II, 1 mM ADP for OXPHOS induced H_2O_2 consumption, 1 μM rotenone for complex II without reverse electron transport to complex I, 2 μM auranofin to block thioredoxin reductase dependent H_2O_2 consumption) and $CaCl_2$ (0, 20, 50, 100 μM) for 10 min at 32°C in 96 well plates (Thermo Scientific, cat# 237108). After 10 mins equilibrium, 50 μl of 10 μM H_2O_2 was added, and then incubated another 10 mins for H_2O_2 consumption. Immediately after H_2O_2 consumption, 50 μl quenching solution (contains AUR 1μM and HRP 1μM) was added, followed by H_2O_2 standards (15, 7.5, 3.25, 0 μM) individually, and then the signal was read at Excitation 485nm/ Emission 590/ Cut off 570nM. ΔH_2O_2 consumption was calculated as ((H_2O_2 value without substrates) - (H_2O_2 value with substrates))/wet weight tissue.

3.2.9 Metabolomics analysis

The metabolite extraction method was adopted from (Haws et al., 2020) with modifications. Specifically, tissues were pulverized prior to metabolite extraction. Pulverized tissue (~30 mg) was incubated with 1 mL of ice-cold 8:2 methanol:water solution for 5 min on dry ice after 15-s of vortexing. Tissue homogenates were centrifuged at maximum speed (21,100 g) for 5 min at

4°C and the supernatant was collected into a new tube. The remaining pellet was loosened using a pipette tip and incubated with 400 µL of ice-cold 4:2:2 methanol:acetonitrile:water solution for 5 min on ice. The tissue homogenate was centrifuged again at maximum speed for 5 min at 4°C and the supernatant was pooled with the first metabolite extraction. The 4:4:2 methanol:acetonitrile:water extraction was then repeated, and three extractions were pooled and completely dried using a SpeedVac (Thermo Fisher Savant ISS110) with nitrogen flow at room temperature. The dried metabolite samples were resuspended in water (150 µL water per 5 mg frozen tissue) and centrifuged at maximum speed for 5 min at 4°C. The supernatant was used for LC-MS metabolite profiling.

The metabolite detection method was adopted from (Latorre-Muro et al., 2018). Specifically, metabolites were separated by Thermo Fisher Vanquish UHPLC with a Waters Acquity UPLC BEH C18 column (1.7 µm, 2.1 × 100 mm; Waters Corp., Milford, MA, USA) and analyzed using a Thermo Fisher Q Exactive orbitrap mass spectrometer in negative ionization mode. LC separation was performed over a 25 min method with a 14.5 min linear gradient of mobile phase (buffer A, 97% water with 3% methanol, 10 mM tributylamine, and acetic acid-adjusted pH of 8.3) and organic phase (buffer B, 100% methanol) (0 min, 5% B; 2.5 min, 5% B; 17 min, 95%B; 19.5 min, 5% B; 20 min, 5% B; 25 min, 5% B, flow rate 0.2 mL/min). A quantity of 12 µL of each sample was injected into the system for analysis. The ESI settings were 30/10/1 for sheath/aux/sweep gas flow rates, 2.50 kV for spray voltage, 50 for S-lens RF level, 350°C for capillary temperature, and 300°C for auxiliary gas heater temperature. MS1 scans were operated at resolution = 70,000, scan range = 85–1250 *m*/*z*, automatic gain control target = 1×10^6, and 100 ms maximum IT. Metabolites were identified and quantified using El-MAVEN (v0.12.1-beta)

(Agrawal et al., 2019) with metabolite retention times empirically determined in-house. Metabolite levels were compared using the peak AreaTop metric.

3.2.10 qPCR for mitochondrial DNA quantification

Tissues were homogenized using a glass tissue grinder (PYREX, CAT# 77241) at 50 mg wet weight/ml in lysis Solution (25 mM NaOH, 0.2 mM EDTA), then incubated at 95°C for 30 min, followed by centrifugation at 10,000 rpm for 5 min at 4°C. The supernatant was then collected and mixed with an equal volume of 40 mM Tris-HCl (Truett et al., 2000). DNA concentrations ere quantified using a NanoDrop Spectrophotometer (ND-1000, Thermofisher Scientific, Napean, ON, CAN). The relative mtDNA/nDNA ratios were measured by qPCR using a Rotor-Gene Q (Qiagen Inc., Montreal, QC, CAN), with a reaction medium containing 5 µl qPCR SYBR Green Mix (A600A; Promega, Madison, WI, USA), 0.1 µM primer (Primers are listed in Table 7.1), 2 µl DNA (optimal dilutions were determined previously), and H_2O; total volume 10 µl). The copy number of mtDNA was calculated using the following formula (Quiros et al., 2017):

a) $\Delta Ct = Ct\ (nDNA\ gene) – Ct\ (mtDNA\ gene)$

b) Copies of mtDNA = $2 \times 2^{\Delta\Delta Ct}$

c) Relative mtDNA content = mtDNA treatment/mtDNA normoxic

Table 3.1 List of primers for mtDNA quantification.

Species	Target	Sequence (5' to 3')
NMR	16S mitochondrial ribosomal RNA	GTACCGCAAGGGAAAGATGAAAG
		TAGCTCGTTTGGTTTCGGGGTT
	beta 2-microglobulin	GCCAAACTACTTGAACTGCTATG
		GTCCAGTCCTTGCTGAAAGA

3.2.11 Western blot

Brain tissue was homogenized by sonication (20 times, 1s/time) at 100 mg/ml (W/V) in radio-Immunoprecipitation Assay (RIPA) buffer with protease inhibitors and phosphatase inhibitors. The homogenate was spun at 12,000*g* for 10 min at 4 °C. The supernatant was kept for protein concentration measurements using the Biuret assay and followed by SDS-PAGE. First, 10–50 µg of protein was loaded per lane onto a 12 or15% SDS-polyacrylamide gel, which in turn was run for 1–1.5 h at 130 V. The separated proteins were then transferred to a nitrocellulose membrane for 1 hr at 100 V. Successful transfer was determined by Ponceau S staining. Membranes were then incubated with 5% bovine serum albumin for 60 min to block non-specific binding sites. Levels of specific proteins were determined using the antibodies listed in Table 7.2. Quantification was performed using ImageJ software (V1.53j, NIH, Bethesda, MD).

Table 3.2 List of antibodies.

Target	Vendor	Cat #
BNIP3	Abclonal	A19593
Drp1	Abclonal	A2586
Drp1-S616	Abclonal	AP0849
Fis1	Abclonal	A19666
LC3B	Abclonal	A19665
MFN1	Abclonal	A9880
NIX	Abclonal	A6283
MFN2	Abclonal	A19678
OPA1	Abclonal	A9833
p62	Abclonal	A11483
Parkin	Abclonal	A0968
Pink1	Abclonal	A7131
Rabbit IgG (secondary)	Thermofisher	31458
Mouse IgG (secondary)	Thermofisher	A16017

Polyclonal antibodies were diluted at 1 µg/ml in 3-5% BSA, monoclonal antibodies were diluted at 0.5 µg/ml in 3-5% BSA, Secondary antibodies were diluted at 0.1 µg/ml in 3-5% BSA.

3.2.12 TEM

Mice or NMR were perfusion fixed first with a Ringer's solution at 37˚C followed by primary fixative consisting of 2% paraformaldehyde + 2.5% glutaraldehyde in 0.15 M sodium cacodylate buffer (pH 7.4) also at 37˚C. The brain was rapidly removed from the skull and placed in ice-cold primary fixative for 1 h (mouse) or shipped on ice surrounded by ice packs with overnight delivery. Using a Leica vibratome with a trough containing ice-cold 0.15 M cacodylate buffer, brains were sliced into 100 micron-thick coronal slices and those containing the hippocampus were collected. The slices were rinsed in 0.15 M cacodylate buffer and incubated in a mixture of 1% OsO_4, 0.8% potassium ferrocyanide, 3 μM calcium chloride in sodium cacodylate buffer for 1 h on ice. Then, the slices were washed 3x3 min with ice-cold double-distilled water (ddH_2O) and stained with 2% uranyl acetate for 1 h ice. The slices were next incubated in increasing ethanol solutions: 20%, 50%, 70%, 90% on ice, followed by 3 x 100% at RT, each for 10 min. Subsequently, the slices were infiltrated with a mixture of 50% dry acetone and 50% Durcupan ACM resin (Fluka) for 2 h with agitation, and then incubated 3x12 h in 100% Durcupan with agitation. Durcupan ACM resin was made by mixing 11.4 g component A, 10 g component B, 0.3 g component C and 0.1 g component D. The slices were sandwiched between 2 Mold-release slides and polymerized for 48 h at 60 C in an oven. The glass slides were removed. A hacksaw was used to cut out a block about 2 mm across and glued on a dummy block. Thin sections about 70 nm thick were cut using a Leica UCT ultramicrotome. The sections were placed on 200-mesh uncoated thin-bar copper grids. A Tecnai Spirit (FEI; Hillsboro, OR) electron microscope operated at 80 kV was used to record images with a Gatan 2Kx2K CCD camera at 2.9 nm/pixel.

For quantitative analysis, the mitochondrial profile area was measured with ImageJ (National Institutes of Health). The number of mitochondria per unit cytoplasmic area was calculated by counting the number of mitochondria in an image and dividing by the profile area of the cytoplasm measured using ImageJ. The mitochondrial volume fraction, defined as the volume occupied by mitochondria divided by the volume occupied by the cytoplasm, and the crista density, defined as the cristae surface area per mitochondrial volume, were estimated using stereology with the "grid" plug-in of ImageJ.

3.2.13 Electron microscopy Tomography

Semi-thick sections of thickness about 350 nm were cut from the blocks of tissues prepared for TEM with a Leica ultramicrotome and placed on 200-mesh uncoated thin-bar copper grids. 20-nm colloidal gold particles were deposited on each side of the grid to serve as fiducial cues. A grid was placed in a Tecnai HiBase Titan (FEI; Hillsboro, OR) electron microscope operated at 300 kV. The grid was irradiated with electrons for about 20 min to limit anisotropic specimen thinning during image collection at the magnification used to collect the tilt series before initiating a dual-axis tilt series. During data collection, the illumination was held to near parallel beam conditions and the beam intensity was kept constant. Tilt series were captured using SerialEM software (University of Colorado, Boulder, CO) at 0.81 nm/pixel. Images were recorded with a Gatan 4Kx4K CCD camera. Each dual-axis tilt series consisted of first collecting 121 images taken at 1-degree increment over a range of -60 to +60 degrees followed by rotating the grid 90 degrees and collecting another 121 images with the same tilt increment. After collecting the orthogonal tilt series, to improve the signal-to-noise ratio, 2x binning was performed on each image by averaging a 2x2 x-y pixel box into 1 pixel using the newstack command in IMOD (University of Colorado, Boulder, CO). The IMOD package (https://en.wikipedia.org/wiki/IMOD_(software)) was used for tilt-series alignment, reconstruction, and volume segmentation. R-weighted back projection was used to generate the reconstructions. Volume segmentation of mitochondrial membranes was performed using IMOD by tracing in each of the 1.62 nm-thick *x-y* planes that the object appeared that then created stacks of contours with the Drawing Tools plug-in in IMOD. The traced contours were then surface-rendered by turning contours into meshes to generate a 3D model. The surface-rendered volumes were visualized using 3DMOD. Lengths, surface areas, and volumes were extracted using the program *imodinfo.* The number of crista junctions per mitochondrial slice was measured by simply counting the number of crista junctions per mitochondrion observed in a 1.6-nm thick central slice through an EM tomography volume. Because NMR brain mitochondria were larger than mouse brain mitochondria, to normalize the crista junction parameter, we divided the number of crista junctions by the mitochondrial outer membrane length (ImageJ), being a logical choice because the junctions are next to the outer membrane. This normalization removed the mitochondrial size variability between NMR and mouse.

3.2.14 Serial Block Face Electron Tomography (SBEM)

The first part of the SBEM procedure followed identically the TEM procedure up until the following step and then proceeded as described here. The slices were incubated in 2% OsO_4/1.5% potassium ferrocyanide for 1 h on ice. Slices were then washed 3x in ice-cold ddH_2O. Samples were then incubated in 1% thiocarbohydrazide (Electron Microscopy Sciences) for 15 min RT. Next, the samples were incubated in 2% aqueous OsO_4 at RT for 1 h. After washing in ice-cold ddH_2O, the samples were then left in 1% uranyl acetate overnight at 4˚C. The next day, samples were incubated in a lead aspartate solution prepared by dissolving 0.066 g lead nitrate into 10 ml 0.03 M aspartic acid with the pH subsequently adjusted to 5.5 using 1 N KOH. This incubation took place in a 60˚C oven for 30 min. The samples were then washed and dehydrated through a series of ethanol solutions on ice (50%, 70%, 90%, 100%, 100%, 10 min each) at RT and washed in 100% anhydrous acetone for 10 min at RT. Following this, samples were infiltrated with resin by first incubating them for 2 h at RT in a solution of 50% acetone and 50% Durcupan ACM and then overnight in 100% Durcupan. The next day, samples were transferred to a freshly prepared 100% Durcupan solution and incubated at RT for 2 h. Samples were then placed in a 60°C oven for 3 days to accomplish polymerization.

The brain volumes were collected using a Gatan 3View system mounted on a GeminiSEM 450 field emission SEM (Carl Zeiss Microscopy) operated at 2.0 to 2.4 kV accelerating voltages, with a raster size of 20k×20k or 24kx24k and pixel dwell time of 0.5 -1.5 µs. The pixel size was 7.4 nm and section thickness was 60 nm. Once a volume was collected, the histograms for the Digital Micrograph files were normalized to correct for drift in image intensity during acquisition. The Digital Micrograph files were then converted to 8-bit MRC format. As with EM tomography, contours were manually traced in consecutive slices in the z dimension to determine the boundaries of neurites and mitochondria. The contours were surface-rendered and the volumes were visualized using 3DMOD. Lengths, surface areas, and volumes were extracted using the program *imodinfo.*

3.2.15 Statistical analysis

All statistical analyses were performed using GraphPad Prism 9 (GraphPad Prism, La Jolla, CA, USA). Data were analyzed using two-tailed t-tests (Fig. 3.3, SF 3.2); one-way ANOVA with Dunnett multiple comparison (Fig. 3.1&3.2, SF 3.3), or Tukey (Fig. 3.6) post-tests; two-way ANOVAs followed by with a Sidak (Fig. SF 3.4C-F), Dunnett (Fig SF 3.1, SF 3.4 A&B), or Tukey (Fig. 3.4) multiple comparisons tests. Significance was determined with a level of $p < 0.05$ unless otherwise indicated in results, and all data are expressed as the mean ± SEM.

3.3 Results

NMR brain mitochondria have higher Ca^{2+} affinity and retention capacity. To compare the uptake rate and retention capacity for Ca^{2+} by brain mitochondria from NMRs and mice, boluses of $CaCl_2$ were added in serial titrations to equal amounts of permeabilized brain tissue from each species (Fig. 3.1A). Mitochondrial Ca^{2+} uptake was monitored by measuring the decrease of Ca^{2+} in the solution using a light-excitable Ca^{2+} indicator, Calcium green-5N (Rajdev & Reynolds, 1993), such that each Ca^{2+} bolus was observed as an increase in Calcium green-5N fluorescence in the solution due to Ca^{2+}-binding. Boluses of Ca^{2+} were added until Calcium green-5N fluorescence increased, indicating activation of the MPTP and release of mitochondrial Ca^{2+}, which is a hallmark of Ca^{2+} overload in hypoxic brain. Ru360, a specific antagonist of the UCM that does not impact endoplasmic reticulum (ER) Ca^{2+} uptake or release (Baughman et al., 2011; Matlib et al., 1998), was used to confirm that mitochondria were the main source of Ca^{2+} uptake in both species and in the subsequent overload of Ca^{2+} that triggered the release of mitochondrial matrix Ca^{2+} through the MCU (Fig. 3.1A-C). Note, ATP did not have any significant effect on Ca^{2+} uptake in NMR brain but caused a small release of Ca^{2+} in mouse brain (Fig. 3.1B&C).

We observed that permeabilized NMR brain tissue has a faster rate of Ca^{2+} uptake than mouse brain during the first 5 min following the initial bolus of 50 µM Ca^{2+}, with ADP, (> 2-fold), without ADP (~ 10-fold), or following uncoupling of the mitochondrial proton gradient with carbonyl cyanide 3-chlorophenylhydrazone (CCCP; > 3-fold; Fig. 3.1B&C, $F_{1,28} = 102.8$, $p < 0.0001$; Fig. 3.1D). ADP significantly increased the rate of Ca^{2+} uptake in both NMR and mouse brain (Fig. 3.1B-D). CCCP abolished the ability of mouse brain to take up Ca^{2+} within five min (Fig. 3.1B), but only slightly inhibited the rate of Ca^{2+} uptake (Fig. 3.1C&D) and Ca^{2+} retention capacity (Table 3.3) in NMR brain. Overall, NMR brain tissue has a higher retention capacity for Ca^{2+} than mouse brain (Table 3.3).

OXPHOS is more strongly inhibited by extramitochondrial Ca^{2+} in mouse brain than NMR brain. To assess the effects of Ca^{2+} on mitochondrial OXPHOS, we exposed permeabilized brain tissues with stepwise increases in Ca^{2+} concentration and then measured glutamate/malate-stimulated mitochondrial O_2 consumption. We report that Ca^{2+} generally reduces OXPHOS capacity in a dose-dependent manner in both NMR and mouse brain ($F_{6,105} = 171.4$, $p < 0.0001$; Fig. 3.2A & $F_{6,105} = 145.1$, $p < 0.0001$; B). Additionally, significant increases of leak respiration were triggered at > 50 μM Ca^{2+} in NMR brain but not in mouse brain. Finally, RCRs, calculated as the ratio of OXPHOS capacity/leak respiration, were reduced by exogenous Ca^{2+} in a dose-dependent fashion in both species (Table 3.4, & SF. 3.1), primarily due to the reduction of OXPHOS capacity (Fig 3.2, Table 3.4, & SF. 3.1).

Importantly, the inhibitory effects of Ca^{2+} on OXPHOS were greater in mouse brain than NMR brain. Specificity, OXPHOS capacity was significantly inhibited in all Ca^{2+} concentrations in mouse brain but NMR brain was not impacted by $[Ca^{2+}] < 50$ μM (Fig. 3.2A&B). Moreover, the relative reductions of OXPHOS capacity (values normalized to 100% at 0 μM Ca^{2+}) in mouse brain were significantly lower than in NMR brain ($F_{1,42} = 98.03$, $p < 0.0001$; Fig. 3.2C). Correspondingly, we calculated the half-maximal inhibitory concentration (IC_{50}, μM) at which Ca^{2+} inhibits OXPHOS capacity, which was 34.1 ± 4.61 in mouse brain versus 81.6 ± 6.74 in NMR brain (Fig. 3.2D; $p = 0.0286$).

The effect of Ca^{2+} on mitochondrial membrane permeability and the phosphorylation system control ratio was evaluated by the cytochrome c membrane integrity test and the ratio of

OXPHOS to ETC capacity (1-P/E %), separately. The effect of cytochrome c became significant at a lower [Ca^{2+}] in mouse brain (20 μM) than in NMR brain (100 μM), and overall values were higher in mouse brain than NMR brain ($F_{1, 42} = 70.28$, $p < 0.0001$; Fig. 3.2E). Interestingly, NMR brain was elastic with regard to its Ca^{2+}-induced phosphorylation system control ratio, which increased with addition of Ca^{2+} until 50 μM (from 11.20 ± 2.73 to 17.44 ± 1.78%, $p < 0.001$), and then decreased at 150 μM Ca^{2+} (3.30 ± 0.71%, $p = 0.0014$, Fig. 3.2F). On the other hand, mouse brain did not exhibit any significant change in any [Ca^{2+}], and the values were generally lower than in NMR brain ($F_{1, 42} = 160.1$, $p < 0.0001$), except with 150 μM Ca^{2+} (Fig. 3.2F).

$\Delta\psi_m$ is hyperpolarized in NMR brain and drives Ca^{2+} buffering. The proton gradient generated across the IMM (*i.e.,* $\Delta\psi_m$), was measured in permeabilized NMR and mouse brain tissue using fluorescence quenching of Rhodamine-123 (Rh-123) (Emaus et al., 1986). The impact of Ca^{2+} on $\Delta\psi_m$ was assessed by serial additions of $CaCl_2$ (Fig. 3.3A). Glutamate/malate generated a greater signal in NMR brain than mouse brain (Fig. 3.3B), indicating a more hyperpolarized $\Delta\psi_m$ in the former (see below). Serial Ca^{2+} titrations reduced $\Delta\psi_m$ in both NMR and mouse brain, but a greater change was observed in NMR brain than mouse at each Ca^{2+} concentration (Fig. 3.3B). To compare the extent of this Ca^{2+}-mediated depolarization in NMR vs. mouse brain mitochondria, we normalized the Rh-123 signal to 100% at 0 μM Ca^{2+} (Fig. 3.3C). In this analysis, we calculated that a greater proportion of $\Delta\psi_m$ was retained in NMR than mouse brain following each Ca^{2+} addition (Fig. 3.3C). Additionally, we calculated the half-maximal inhibitory concentration (IC_{50}, μM) of Ca^{2+} on $\Delta\psi_m$, which was 8.25 ± 0.18 in mouse brain versus 36.11 ± 0.38 in NMR brain ($p < 0.05$; Fig. 3.3D).

NMR brain mitochondria are larger, occupy more of the cytoplasmic volume, and have increased crista density relative to mouse brain. Mitochondrial structure is associated with Ca^{2+} sequestration capacity (Favaro et al., 2019; Hoitzing et al., 2015); therefore, we compared the ultrastructure of NMR and mouse brain mitochondria using TEM and electron microscope (EM) tomography. NMR mitochondria were distinct from mouse mitochondria in the neuronal somas (Fig. 3.4). Generally, normoxic NMR brain mitochondria were larger ($F_{1, 196} = 51.68$, $p < 0.0001$; 0.35 ± 0.03 vs. 0.22 ± 0.02 μm^2, $p = 0.0180$, Fig. 3.4I), and also had more densely packed cristae ($F_{1, 76} = 18.85$, $p < 0.0001$; 13.00 ± 1.30 vs. 8.70 ± 1.40 $\mu m^2/\mu m^3$, $p = 0.0246$, Fig. 3.4L), and more crista junctions per mitochondrion (9.00 ± 0.69 vs. 2.47 ± 1.19 per mitochondrion, $p < 0.0005$, SF. 3.2). There was no significant difference in the number of mitochondria per unit cytoplasmic area ($F_{1, 36} = 0.4754$, $p < 0.4949$; Fig. 3.4J); however, the mitochondrial volume fraction was larger in NMR brain than mouse brain ($F_{1, 36} = 9.972$, $p <$ 0.0.0032; 17.00 ± 3.40 vs. 9.90 ± 1.20%, $p = 0.0239$, Fig. 3.4K). Tethering and zippering of adjacent mitochondria was commonly observed in NMR brain but not in mouse brain (Fig. 3.4C-H). Mitochondrial nanotunnels were commonly observed in serial block face electron microscopy (SBEM) volumes of NMR and mouse brains (Fig. 3.5) and were detectable in the smaller (yet higher resolution) EM tomography volumes (Fig. 3.4E&F). Interestingly, mouse cristae were more often networked, and sometimes highly so (Fig. 3.4G&H).

NMR brain mitochondria expand in size yet shrink in number and volume fraction during hypoxia while mouse brain mitochondria build nanotunnels. Mitochondrial dynamics are critical to hypoxic/ischemic cell survival, and mitochondrial dynamics are altered by hypoxic/ischemic stress (Dong et al., 2016; Zhang et al., 2020). Therefore, we next examined structural changes of brain mitochondria during *in vivo* hypoxia (7% O_2, 4 h) in mouse and NMR brain (Fig. 3.5). As mentioned above, NMR brain has naturally larger mitochondria in normoxia (Fig. 3.4I), and increased in size further during hypoxia (from 0.35 ± 0.032 to 0.49 ± 0.042 μm^2, $p = 0.0049$, Fig. 3.4I). This growth was not the result of swelling or other abnormal structural alterations; the crista structure and density appeared the same under normoxic or hypoxic conditions (Fig. 3.5). Correspondingly, the number of mitochondria per cytoplasmic area was significantly lower during hypoxia in NMR brain (from 0.50 ± 0.098 μm^2 to 0.16 ± 0.012 μm^2, $p = 0.0033$, Fig. 3.4J), Furthermore, there was a significant reduction of mitochondrial volume fraction in NMR brain during hypoxia (from 17.00 ± 3.400 to 8.90 ± 1.100%, $p = 0.0249$, Fig. 3.4K), suggesting that there was loss of mitochondrial mass perhaps by disrupted mitochondrial biogenesis. In stark contrast, mouse brain mitochondria did not change in size during hypoxia (from 0.22 ± 0.020 to 0.20 ± 0.015 μm^2, $p = 0.9625$, Fig. 3.4I) nor did they change their number (Fig. 3.4J) or mitochondrial volume fraction (Fig. 3.4K). Not only were NMR mitochondria larger in size, but they also had a relatively greater crista density compared with mouse mitochondria under both normoxia and hypoxia (~13.00 vs. ~8.70 $\mu m^2/\mu m^3$, $p < 0.05$, Fig. 3.4L). Finally, the proportion of mitochondria connected in a nanotunnel network, and the length of these networks had increased with hypoxia in mouse brain but not NMR brain (Fig. 3.4M&N).

***Mitophagy is initiated in mouse but not NMR brain following acute* in vivo *hypoxia*.** Next, to examine mechanisms underlying changes in mitochondrial ultrastructure during hypoxia in mouse and NMR brain, we compared the expression of proteins implicated in fission/fusion pathways (*i.e.*, MFN1&2, OPA1, Fis1, Drp1, and Drp1-S616) and mitophagy/autophagy pathways (*i.e.,* Parkin, Pink1, BNIP3, NIX (BNIP3L), p62, caspase 3, LC3B). We found that Parkin and DRP1-

S616 both increased and BNIP3 decreased in hypoxic mouse brain (**Fig. 3.6**). However, there were no significant changes in any of these proteins with hypoxia in NMR brain (**Fig. 3.6**). Similarly, we noticed a significant reduction of relative mtDNA copy number in hypoxic mouse but not NMR brain (**SF. 3.3**).

Metabolite changes in hypoxic NMR and mouse brain. Ca^{2+} and ROS homeostasis are intrinsically linked to cellular signalling pathways and changes in metabolites (Bertero & Maack, 2018). For example, glutamate is a key neurotransmitter that regulates neuronal Ca^{2+} influx in hypoxia (Siesjo et al., 1995), whereas NADPH is a key metabolite that is involved in ROS scavenging and redox homeostasis (Mazat et al., 2020). Therefore, to better understand the strategies employed by NMR brain to manage ROS and Ca^{2+} homeostasis at the signalling level in response to hypoxia, we next evaluated hypoxic changes in key signalling intermediates and metabolites. Towards this aim, we identified and analyzed hypoxia-induced differences in the metabolomic profiles of NMR and mouse brain following 4 h of *in vivo* hypoxia to reveal potential mechanisms that could explain the relatively superior tolerance of NMR brain to hypoxia.

Few metabolites were similarly impacted by hypoxia between mouse and NMR brain; however, changes in metabolites were more numerable and of greater magnitude in NMRs than in mice (*e.g.*, the number of metabolites that were significantly different between treatments was 24/64 in NMR brain vs. 15/64 in mouse brain (Fig. 3.7). There were similar trends and overlapping changes of metabolites between normoxic and hypoxic NMR and mouse brains. However, we identified more metabolites that were both down- and upregulated in hypoxic NMR brain.

We assigned all significant metabolites to KEGG pathways using MetaboAnalyst 5.0 (Pang et al., 2021). A total of 22 KEGG pathways were enriched in mouse brain, while 35 were enriched in NMR, including 19 of the 22 elevated in mice (Fig. 3.7). Furthermore, within the same pathways, a greater number of metabolites were identified as altered in NMR brain than mouse (e.g., metabolites related to aminoacyl-tRNA biosynthesis, valine leucine isoleucine biosynthesis, and arginine biosynthesis, etc.) (Fig. 3.8; note that 'biosynthesis' in this context is a general term for increased bioavailability of a given metabolite and may not be due to the actual synthesis of a given metabolite within the organism). Moreover, several pathways were altered only in NMRs with particularly low *p*-values and/or high impact factors, including nicotinate nicotinamide metabolism, glutathione metabolism, and d-glutamine/d-glutamate metabolism (Fig. 3.8). Overall, the major components of these pathways can be divided into three groups, which are amino acids, carbohydrates, and coenzymes.

Glutamate, glutamine, aspartate, arginine, ornithine, proline, threonine, isoleucine, leucine, and valine were identified as changing in both NMR and mouse brain; however, the number of significant changes was larger in hypoxic NMR brain (Fig. 3.7). Therefore, these metabolites contributed higher confidence (larger hit numbers and lower *p*-values) in arginine-related metabolism, valine, leucine, and isoleucine metabolism, and alanine, aspartate, and glutamate metabolism in NMR than mouse brain (Fig. 3.8)). Phenylalanine and tyrosine were increased in hypoxic NMR brain, but not in hypoxic mouse brain (Fig. 3.7) and were assigned to phenylalanine metabolism (Fig. 3.8).

There were also changes in a group of metabolites that were not assigned using MetaboAnalyst, including a reduction in fructose 6-phosphate and accumulations of sedoheptulose 7-phosphate and glucose 6-phosphate in hypoxic NMR brain, which participate in the pentose phosphate pathway (Fig. 3.7).

The most significant changes in hypoxic NMR brain were the glutathione metabolism and nicotinate nicotinamide metabolism pathways (Fig. 3.8), as indicated by decreased levels of ornithine, glutamate, glutathione, aspartic acid, NAD^+, and $NADP^+$, and increased NADPH (Fig. 3.7). In contrast, these pathways were unchanged in mouse brain. The accumulation of NADPH possibly results from suppression of antioxidant function (Xiao et al., 2018). Thus, we mimicked hypoxia-induced Ca^{2+} stress in permeabilized NMR brain tissue and evaluated its H_2O_2 consumption ability.

In this analysis we observed that Ca^{2+} inhibits H_2O_2 consumption in permeabilized NMR brain (SF. 3.4), which suggested that mitochondrial Ca^{2+} uptake suppressed OXPHOS function (Fig. 3.3) as well as anti-oxidative capacity (SF. 3.4). Specifically, $CaCl_2$ inhibits H_2O_2 consumption with all substrates except succinate-induced leak respiration ($F_{3,\ 114} = 92.41$, $p < 0.0001$, SF 3.4A). In addition, the mitochondrial complex II (succinate/rotenone) pathway is more sensitive to $CaCl_2$ than the complex I (glutamate/malate) pathway with regard to H_2O_2 consumption (SF 3.4A), because 20 μM $CaCl_2$ does not change H_2O_2 consumption with glutamate/malate ($p = 0.2558$) but significantly reduces H_2O_2 consumption with succinate/rotenone ($p = 0.0025$) (SF 3.4A). Although there is no statical difference in some conditions (*i.e.,* between succinate/rotenone/ADP and glutamate/malate/ADP without $CaCl_2$; $p = 0.1024$), glutamate/malate/ADP-induced respiration consumes more H_2O_2 than all other substrates in all conditions (SF 3.4B), and is largely inhibited by auranofin (a thioredoxin-reductase inhibitor; $p = 0.0002$, > 80%, SF 3.4B&F). Note that, with auranofin in 100 μM $CaCl_2$ condition, tissues produce ~40% of the H_2O_2 that could be consumed without auranofin (SF 3.4F).

Interestingly, ADP (OXPHOS) does not change H_2O_2 consumption relative to succinate-induced leak respiration (SF 3.4B; $F_{1,\ 44} = 0.0048$, $p = 0.9447$, SF 3.4C). Rotenone (which blocks reverse electron transport from complex II to I) significantly enhances ($p = 0.0012$, > 200% without $CaCl_2$; and $p = 0.0107$, > 100% with 20µM $CaCl_2$) H_2O_2 consumption during succinate-related respiration ($F_{1,\ 46} = 24.86$, $p < 0.0001$, SF 3.4B). On the other hand, ADP enhances H_2O_2 consumption during glutamate/malate-induced respiration ($F_{1,46} = 87.96$, $p < 0.0001$, SF 3.4 D).

3.4 Figures and tables

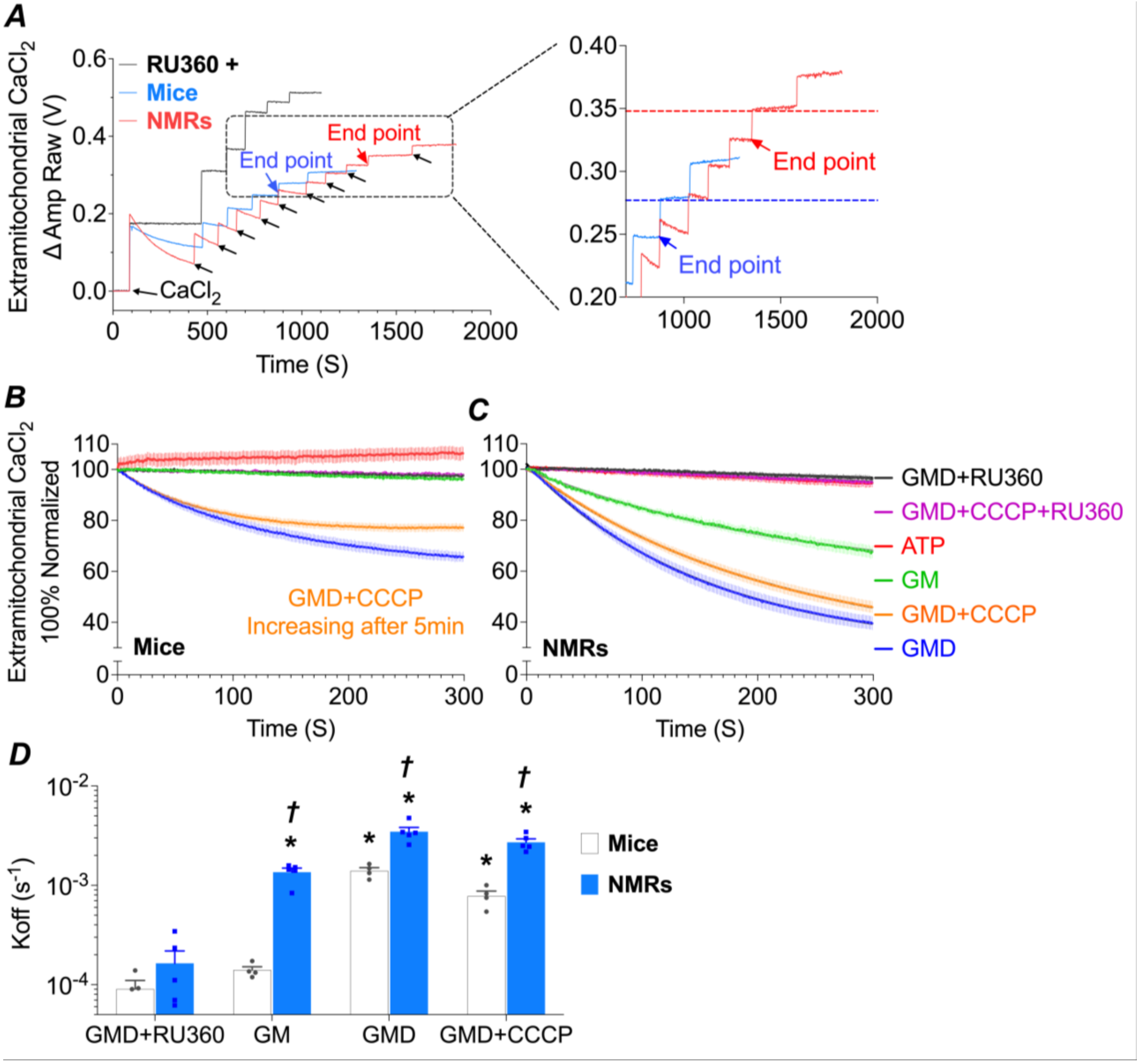

Figure 3.1 Ca^{2+} uptake by permeabilized cortical brain tissues.

(A) Fluorescent sensorgram of Ca^{2+} uptake by permeabilized cortical brain tissues from mice (blue traces), NMRs (red traces), and Ru360-treated tissue either in mouse or NMR (black traces). Black arrows indicate one 50 µM Ca^{2+} injection followed by multiple 20 µM Ca^{2+} injections in Ru360-untreated tissue. The "End point" was determined as the last dose that did not trigger and increase in the Ca^{2+} signal. **(B&C)** Fluorescent traces following 50 µM Ca^{2+} addition (100% normalized) of permeabilized cortical brain tissues from mice (B) and NMRs (C). Substrates are GMD+Ru360 (black traces), GMD+CCCP+RU360 (purple traces), ATP (red traces), GM (green traces), GMD+CCCP (orange traces), and GMD (blue traces). **(D)** The decay rate of Ca^{2+}-binding Calcium green-5N is proportional to the $[Ca^{2+}]$ that remains in the external solution calculated from (B&C). Data are presented as mean ± SEM from *n* = 4 independent biological experiment. Significant differences were determined using two-way ANOVAs followed by a Dunnett multiple comparisons test (*****, $p < 0.05$ *vs.* GMD+RU360, **D)**, or multiple unpaired t-tests with False Discovery Rate (**†**, $p < 0.05$ mice *vs.* NMR, **D)**. Abbreviations: G, glutamate; M, malate; D, ADP; CCCP, carbonyl cyanide m-chlorophenyl hydrazine; K_{off}, Ca^{2+}-binding Calcium green 5-N decay rate.

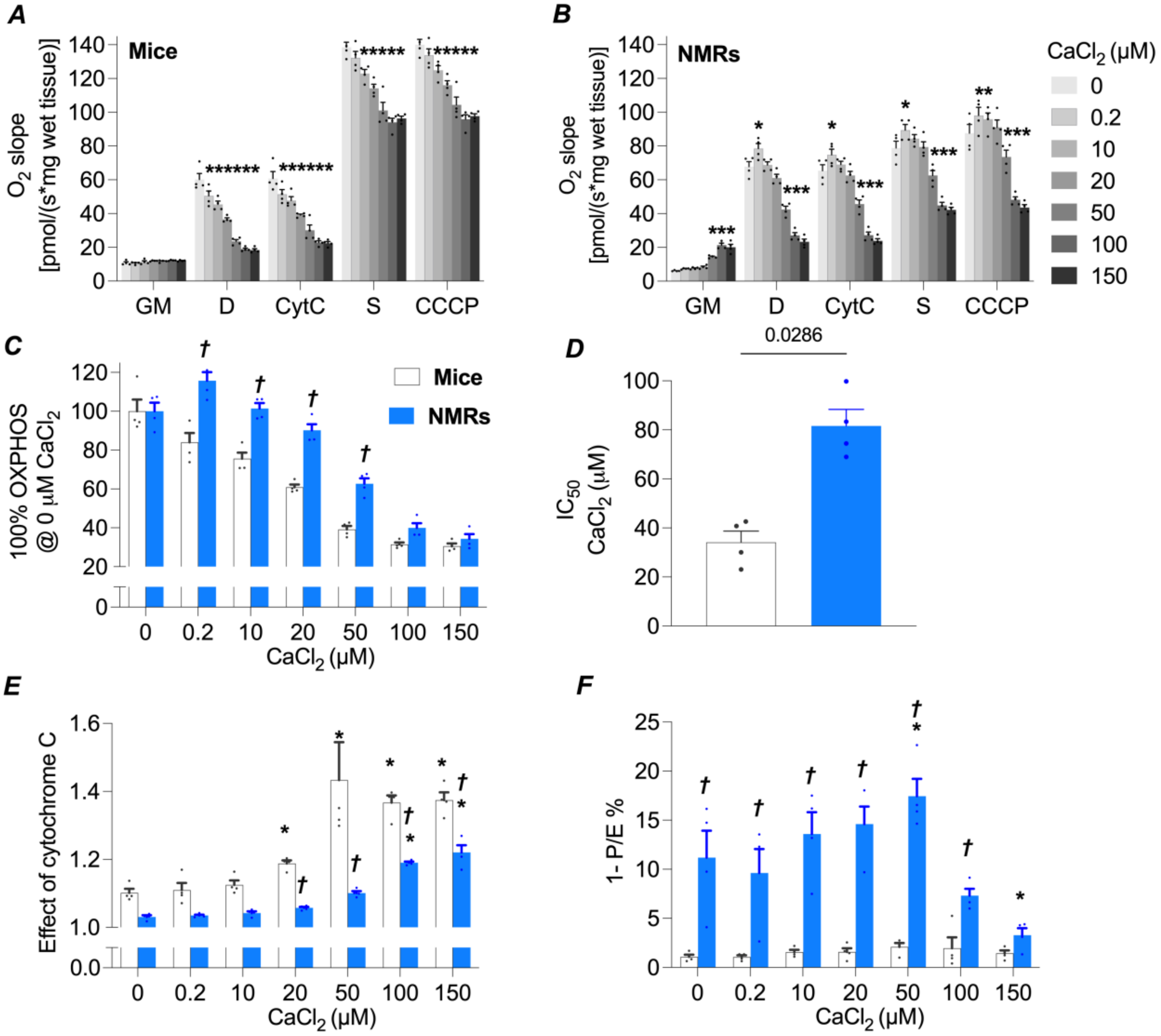

Figure 3.2 Ca^{2+} effects mitochondrial bioenergetics of permeabilized cortical brain tissues. **(A&B)** O_2 consumption by permeabilized cortical brain tissues from mice **(A)** and NMRs **(B)**. Substrates were added sequentially in the order indicated on the x-axis. **(C)** Summary of O_2 consumption in the GM-induced OXPHOS state of permeabilized cortical brain tissue normalized to 0 µM Ca^{2+}. **(D)** IC$_{50}$ of Ca^{2+} for inhibiting OXPHOS. **(E)** Effect of cytochrome c. **(F)** Phosphorylation system control ratio of complexes I-II (1-P/E %). Data are presented as mean ± SEM from $n = 4$ independent biological experiment. Significant differences were determined using two-way ANOVAs followed by a Dunnett (*****, $p < 0.05$ *vs.* 0 µM Ca^{2+}, **A&B, E&F)** or Sidak (**†**, $p < 0.05$ mice *vs.* NMR, **C, E&F)**, or unpaired T-test with two-tailed calculations **(D)**. Abbreviations: G, glutamate; M, malate; D, Cytc, Cytochrome c; ADP; S, succinate; CCCP, carbonyl cyanide m-chlorophenyl hydrazine.

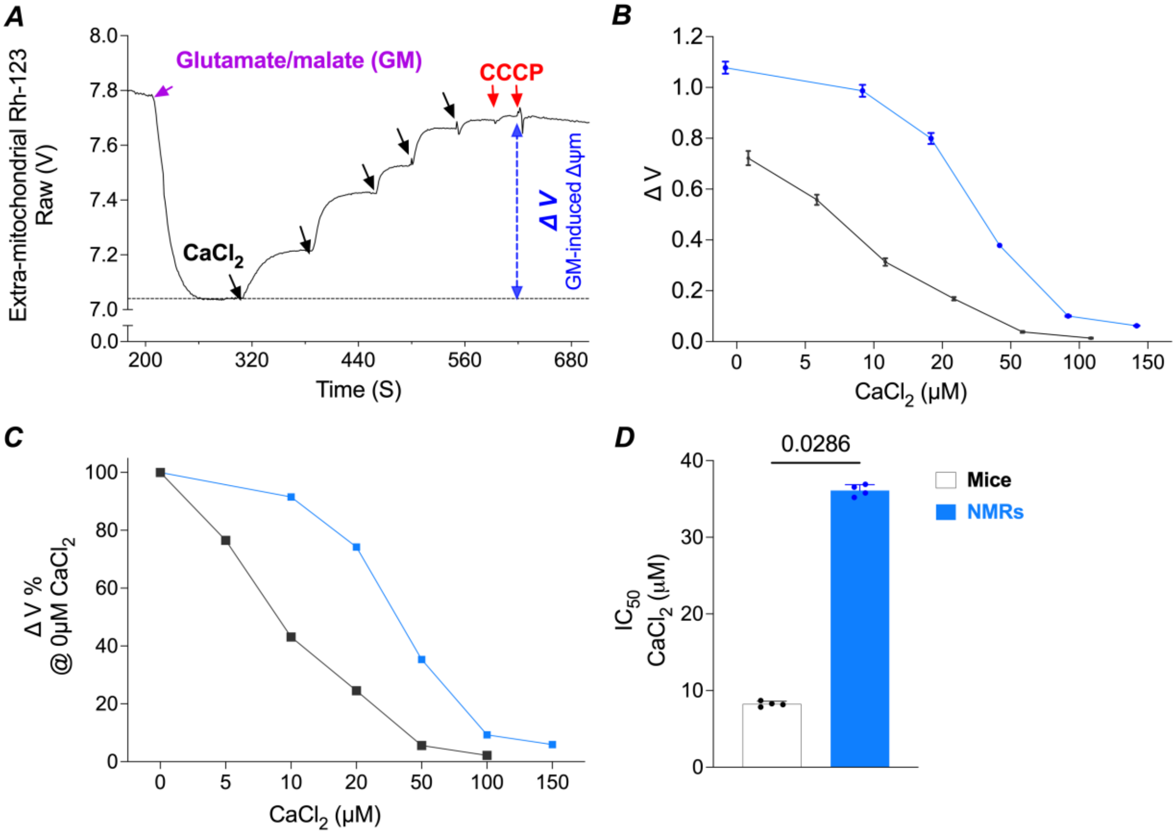

Figure 3.3 Ca^{2+} effects Δψm of permeabilized cortical brain tissues.

(A) Sensorgram of Rhodamine 123 (Rh-123) fluorescence during Ca^{2+} titration of permeabilized cortical brain tissues. **(B)** Ca^{2+} dose-dependent effects on $\Delta\psi_m$. **(C)** Ca^{2+} dose-dependent effects on $\Delta\psi_m$ normalized to 0 μM Ca^{2+}. **(D)** IC_{50} of Ca^{2+} for decreasing $\Delta\psi_m$. Data are presented as mean ± SEM from *n* = 4 independent biological experiment. Significant differences were determined using unpaired T-test with two-tailed calculations **(*p*** < 0.05 mice *vs.* NMR, **D).**

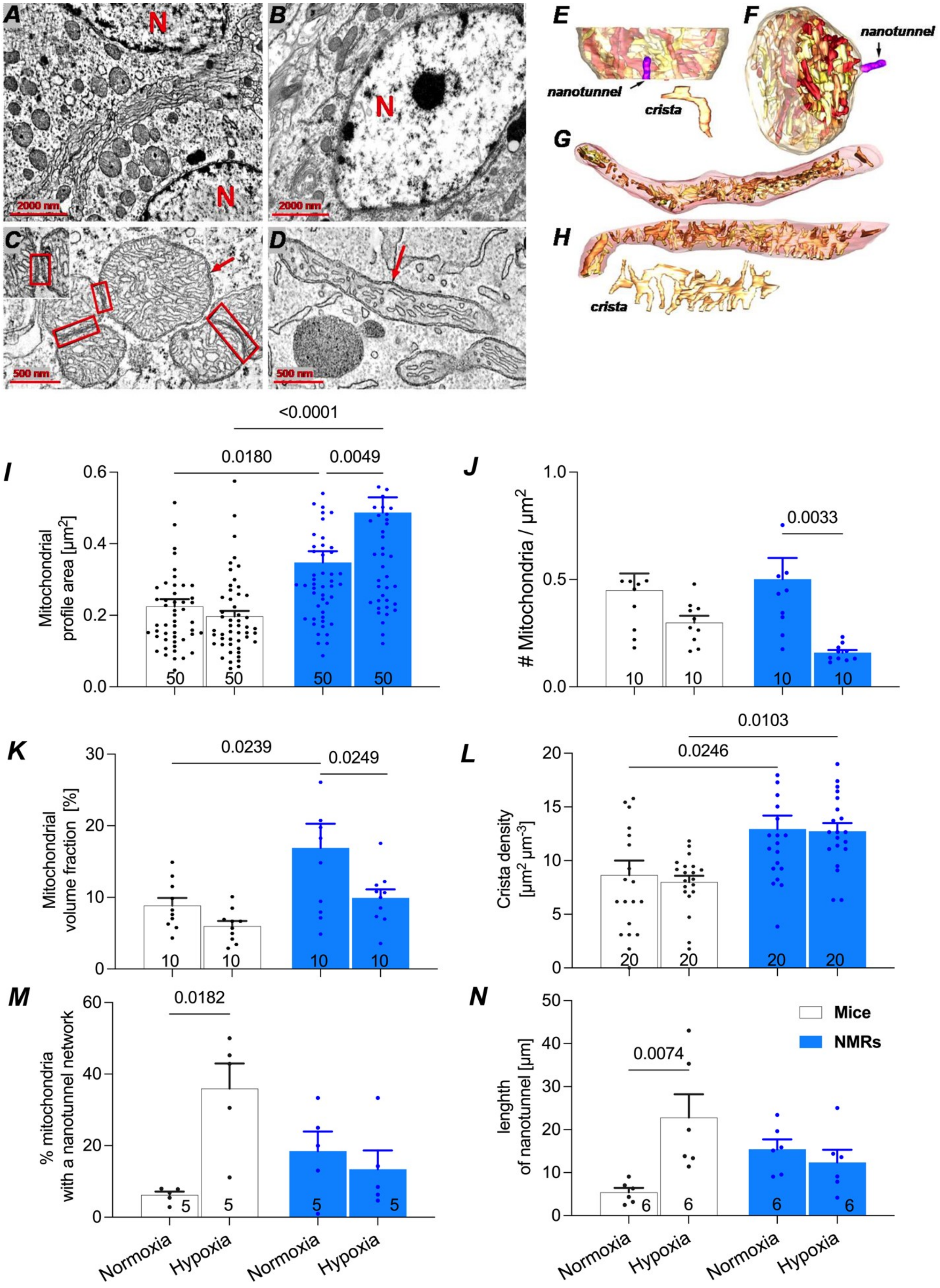

A
N
N
2000 nm
B
N
2000 nm
C
500 nm
D
500 nm
E
nanotunnel
crista
F
nanotunnel
crista
G
H
crista
I
Mitochondrial profile area [μm^2]
0.0
0.2
0.4
0.6
<0.0001
0.0180
0.0049
50
50
50
50
J
Mitochondria / μm^2
0.0
0.5
1.0
0.0033
10
10
10
10
K
Mitochondrial volume fraction [%]
0
10
20
30
0.0239
0.0249
10
10
10
10
L
Crista density [μm^2 μm^{-3}]
0
5
10
15
20
0.0103
0.0246
20
20
20
20
M
% mitochondria with a nanotunnel network
0
20
40
60
0.0182
5
5
5
5
N
lenghth of nanotunnel [μm]
0
10
20
30
40
50
0.0074
6
6
6
6
Mice
NMRs
Normoxia
Hypoxia
Normoxia
Hypoxia
Normoxia
Hypoxia
Normoxia
Hypoxia

Figure 3.4 NMR mitochondria are larger, occupy more of the cytoplasmic volume and have greater crista density than mouse mitochondria in neuronal somas of hippocampus.

(A) Low-magnification TEM showing parts of 2 NMR neuronal cell somas in hippocampus. The nuclei are marked with an "N". Scale bar is 2000 nm, also for (B). **(B)** Low-magnification TEM of a mouse neuronal cell soma in the hippocampus with smaller mitochondria. **(C)** A central slice through an EM tomography volume of NMR hippocampal neuronal soma showing large mitochondria in close proximity**.** Scale bar is 500 nm, also for (D). Tethering that connects adjacent mitochondria is observable in NMR (inset), but less so in mouse. Inside the inset red box are three clear tethers. More common in NMR are "zippered" mitochondria, with outer membranes so close together that there does not appear to be any space between them, hence the zippered look (three red boxes). However, no intermembrane junctions with cristae aligned across mitochondria were observed. **(D)** In contrast, EM tomography of mouse hippocampal neuronal soma showed mostly elongated, less densely packed mitochondria. Crista density was also lower in mouse. **(E)** The mitochondrial volume in (C, red arrow) was segmented along all its membranes and shown surface-rendered in a side view. There are 78 densely packed cristae shown in four shades of brown. The mitochondrial outer membrane was made translucent to better see the cristae. The cristae are mostly tubular. A representative example is shown below. One nanotunnel (purple) connected to the mitochondrion. **(F)** Oblique top view of the mitochondrion providing another perspective of the cristae and nanotunnel. **(G)** The mitochondrial volume (D, arrow) is shown surface-rendered in a top view. **(H)** Side view. In contrast to NMR cristae, mouse cristae were often highly networked (example shown below). **(I)** Mitochondrial profile area (size) measured from TEM images. Mouse mitochondria were significantly smaller than NMR mitochondria (blue bars) (n = 50 mitochondria). **(J)** Number of mitochondria per cytoplasmic area (n = 10 TEM images). **(K)** Mitochondrial volume fraction. Mouse is trending lower (p = 0.076, n = 10 TEM images). **(L)** Crista density (cristae surface area per mitochondrial volume) was significantly higher in NMR (n = 20 mitochondria). **(M)** Percent of the total number of mitochondria in a cell (soma and neurites) that were part of a nanotunnel network in an SBEM volume. **(N)** Mitochondrial-nanotunnel network length in an SBEM volume (n = 5 cells)**.** Data are presented as means ± SEM with data points also shown; numbers in parentheses indicate n. Significant differences ($p < 0.05$) were determined using two-way ANOVA with Tukey multiple comparisons test; significant p values shown above the bars. Unpaired T-test with two-tailed calculations.

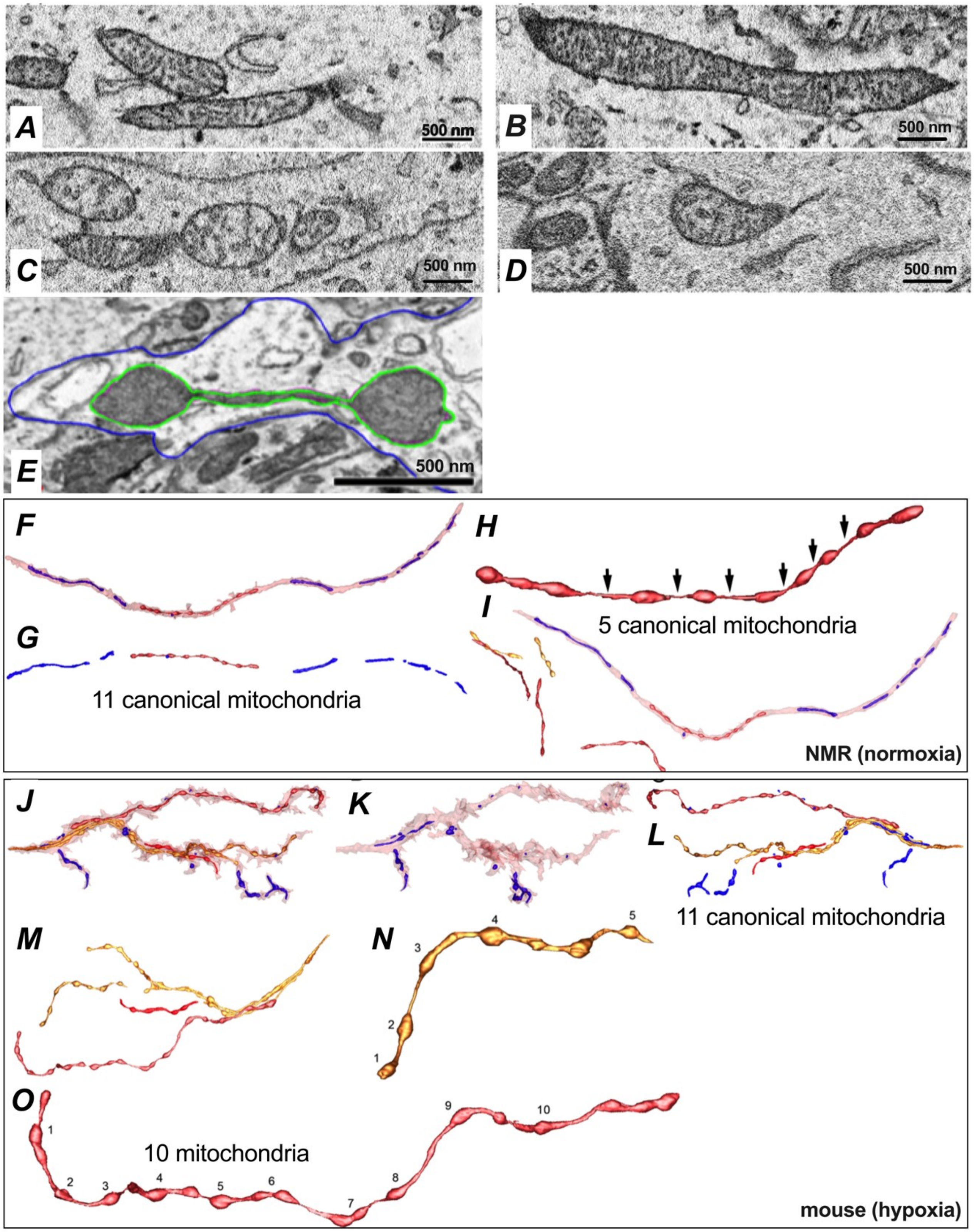

Figure 3.5 SBEM imaging of mitochondria and mitochondrial nanotunnels in NMR and mouse brain.

(A) Normoxic NMR. **(B)** Hypoxic NMR. **(C)** Normoxic mouse. **(D)** Hypoxic mouse. (A-D are slices from the SBEM volumes.) **(E)** Slice from an SBEM volume showing two mitochondria connected by a nanotunnel (traced in green) inside a dendritic process (traced in blue) near a cell soma in the CA3 region of hippocampus. Scale bar is 500 nm. **(F)** Segmentation provides surface-rendered volumes showing a mitochondrial nanotunnel network (brown) inside the neurite (translucent maroon) and the canonical mitochondria (canonical defined as mitochondria not part of a network), **(G)** Magnified view of the nanotunnel network without the cell membrane. There were six nanotunnel segments (arrows). Note that the left- and right-end mitochondria have constrictions and not true nanotunnels. Nanotunnels are distinguished from constrictions not merely by diameter, but more importantly by containing no cristae. **(H)** There were 11 canonical mitochondria (blue) extending to both sides of the nanotunnel network. **(I)** Five nearby nanotunnel networks (various shades of brown). **(J)** Three mitochondrial nanotunnel networks (different shades of brown) inside the branched neurites (translucent maroon) and the canonical mitochondria (blue). **(K)** A second orientation to help with 3D perspective. **(L)** View without the cell membrane. There were 32 canonical mitochondria of various lengths (blue). **(M)** Five nanotunnel networks in close proximity within the cell volume. **(N)** Magnified nanotunnel network. Despite appearances, there were only five (numbered) mitochondria connected by nanotunnels. There were multiple constrictions, each having cristae, which thus excluded them from being nanotunnels. **(O)** A longer nanotunnel network having 10 distinct mitochondria.

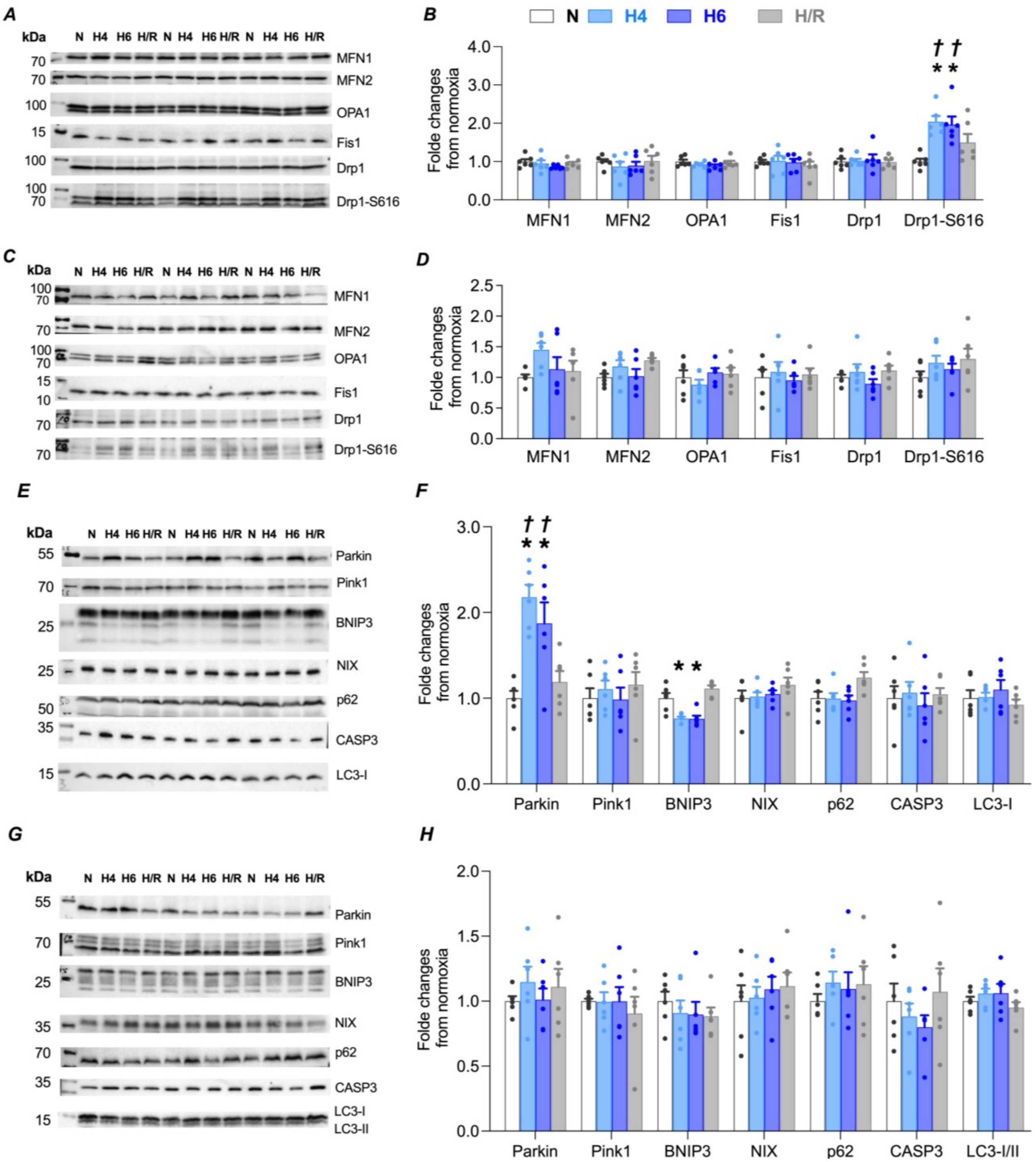

Figure 3.6 Western blot analysis of mitochondrial fission, fusion, mitophagy and autophagy proteins during normoxia, hypoxia and reoxygenation.

Representative western blot images of mouse **(A, E)** and NMR brain **(C, G)**, and relative quantification of changes in mouse **(B, F)** and NMR brain **(D, H)**. Data are presented as means ± SEM from *n* = 6. Significant differences were determined using one-way ANOVA with Tukey multiple comparisons test (*****, $p < 0.05$ *vs.* normoxia, ***†***, $p < 0.05$ *vs.* hypoxia/reoxygenation). Abbreviations: N, normoxia; H4, hypoxia 4hrs; H6, hypoxia 6hrs; H/R, hypoxia 6hrs followed by reoxygenation 24 h.

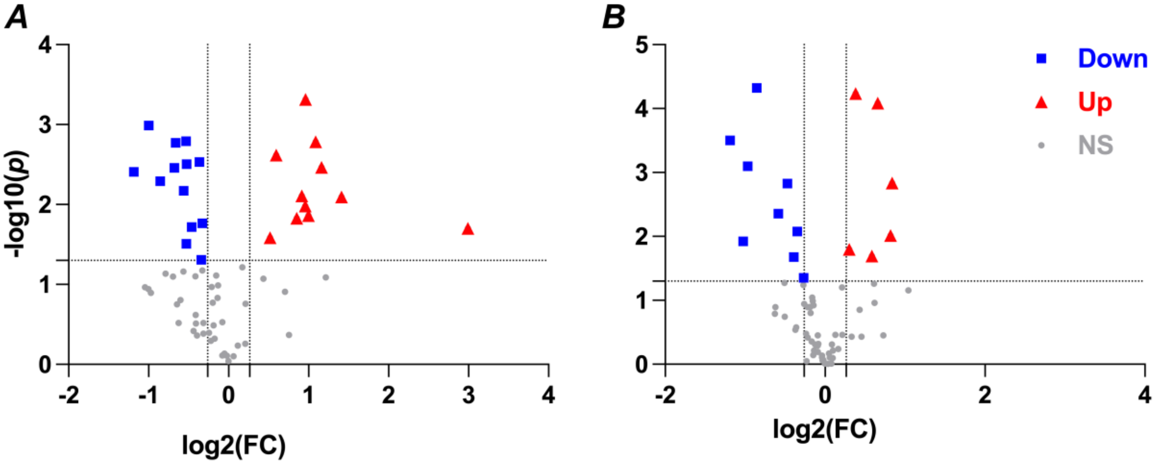

Figure 3.7 Volcano Plot of the identified metabolites illustrating a comparison between normoxia and hypoxia (7% O_2 for 4 h).

Fold change (FC) shown on x-axis: log2(FC); *p* value shown on y-axis: −log10(*p*). Downregulated (Down), upregulated (Up), and nonsignificant changes (NS) are presented with blue squares, red triangles, and grey dots, respectively, from NMR **(A)** and mouse brain **(B)**. Significantly altered metabolites were identified with a fold change > 1.2 and a *p*-value < 0.05.

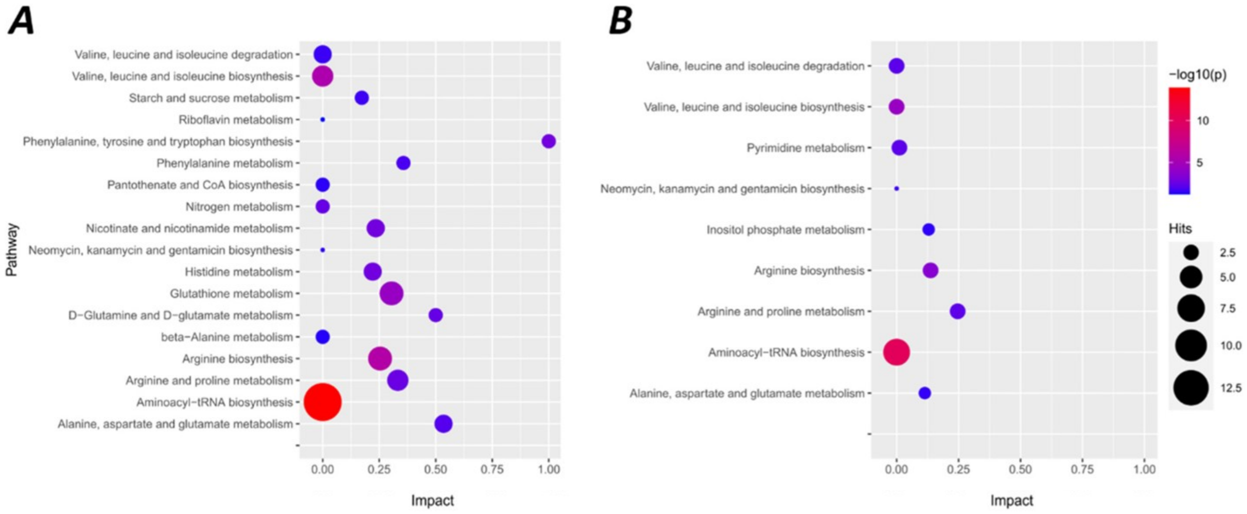

Figure 3.8 Metabolic pathways in which metabolites are altered by hypoxic treatment (7% O_2 for 4 h).

Data was shown based on the p-value (<0.05), impact factor, and Hits (number of metabolites in pathway) in NMR **(A)** and mouse brain **(B)**. The color and size of each dot are associated with the -log 10(*p*) value and hits (number of assigned metabolites), respectively.

Table 3.3 Ca^{2+} resistance of permeabilized brain tissue.

Substrates	Max Ca^{2+} resistance (µM/mg/ml wet tissue)	
	NMRs	**Mice**
GM	210	110
GMD	210	110
GMD+CCCP	150	< 50
GMD+RU360	no observed Ca^{2+} uptake	
GMD+CCCP+Ru360		

Values were determined as the amount of $CaCl_2$ given before triggering Ca^{2+} release. Data are presented as means, from *n* = 4 independent biological experiment. Abbreviations: G, glutamate; M, malate; D, ADP; CCCP, carbonyl cyanide m-chlorophenyl hydrazine.

Table 3.4 Raw values of permeabilized brain tissue respiratory functions

CaCl2 (μM)		NMR			CD1		
		GM	D	RCR	GM	D	RCR
0	mean	6.15	67.79	11.03	10.80	60.14	5.57
	SEM	0.10	2.01	0.47	0.47	2.82	0.09
0.2	mean	7.39	78.46	10.62	10.59	50.54	4.77
	SEM	0.18	2.20	0.24	0.27	2.01	0.17
10	mean	7.62	68.77	9.07	11.32	45.48	4.05
	SEM	0.21	1.47	0.42	0.65	1.43	0.08
20	mean	8.33	61.14	7.43	12.00	36.60	3.05
	SEM	0.37	1.41	0.50	0.13	0.66	0.05
50	mean	14.37	42.47	2.96	11.72	23.56	2.01
	SEM	0.33	1.55	0.09	0.42	1.07	0.07
100	mean	21.39	27.09	1.26	12.26	18.91	1.54
	SEM	0.72	1.11	0.02	0.14	0.44	0.06
150	mean	20.14	23.28	1.16	12.03	18.39	1.53
	SEM	1.12	1.08	0.03	0.19	0.55	0.05

Data are mean ± SEM, from *n* = 4 independent biological experiment. statistical analyses were indicated in Fig 3.2 & SF 3.1. Abbreviations: G, glutamate; M, malate; D, ADP; OXPHOS, oxidative phosphorylation; RCR, respiratory control ratio calculated as the ratio of OXPHOS capacity/leak respiration (D/GM).

3.5 Supplementary information

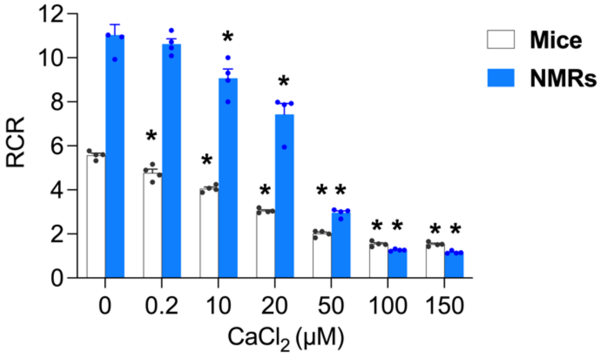

SF 3.1 RCRs of permeabilized cortical brain tissue.

Data are presented as means ± SEM from *n* = 4 independent biological experiment. Significant differences were determined using two-way ANOVAs followed by a Dunnett multiple comparisons test (*, $p < 0.05$ *vs.* 0 µM Ca^{2+}).

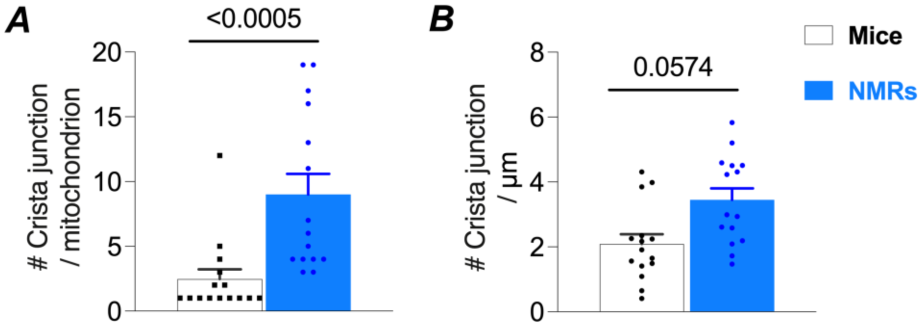

SF 3.2 Crista junction number in NMR and mouse hippocampal neuronal somas.

(A) Crista junction number per mitochondrion of NMR and mouse hippocampal neuronal somas. **(B)** Crista junction number per mitochondrial outer membrane length. Data are presented as means ± SEM from $n = 15$ mitochondria. Significant differences were determined using unpaired two-tailed t-test ($p < 0.05$ mice vs. NMR).

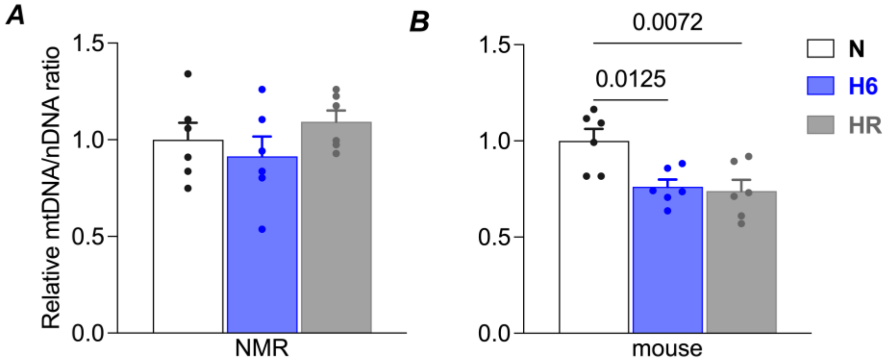

SF 3.3 Relative mitochondrial DNA/nuclear DNA (mtDNA/nDNA) ratio in hypoxic brain. Relative mtDNA quantification was evaluated in triplicates using qPCR by amplification of 16S mitochondrial ribosomal RNA gene in mtDNA and normalised to beta-2-microglobulin. Data are presented as means ± SEM from $n = 6$ each. Significant differences were determined using one-way ANOVA with Dunnett multiple comparisons test ($p < 0.05$ *vs.* normoxia). Abbreviations: N, normoxia; H6, hypoxia 6 h; H/R, hypoxia 6 h followed by reoxygenation 24 h.

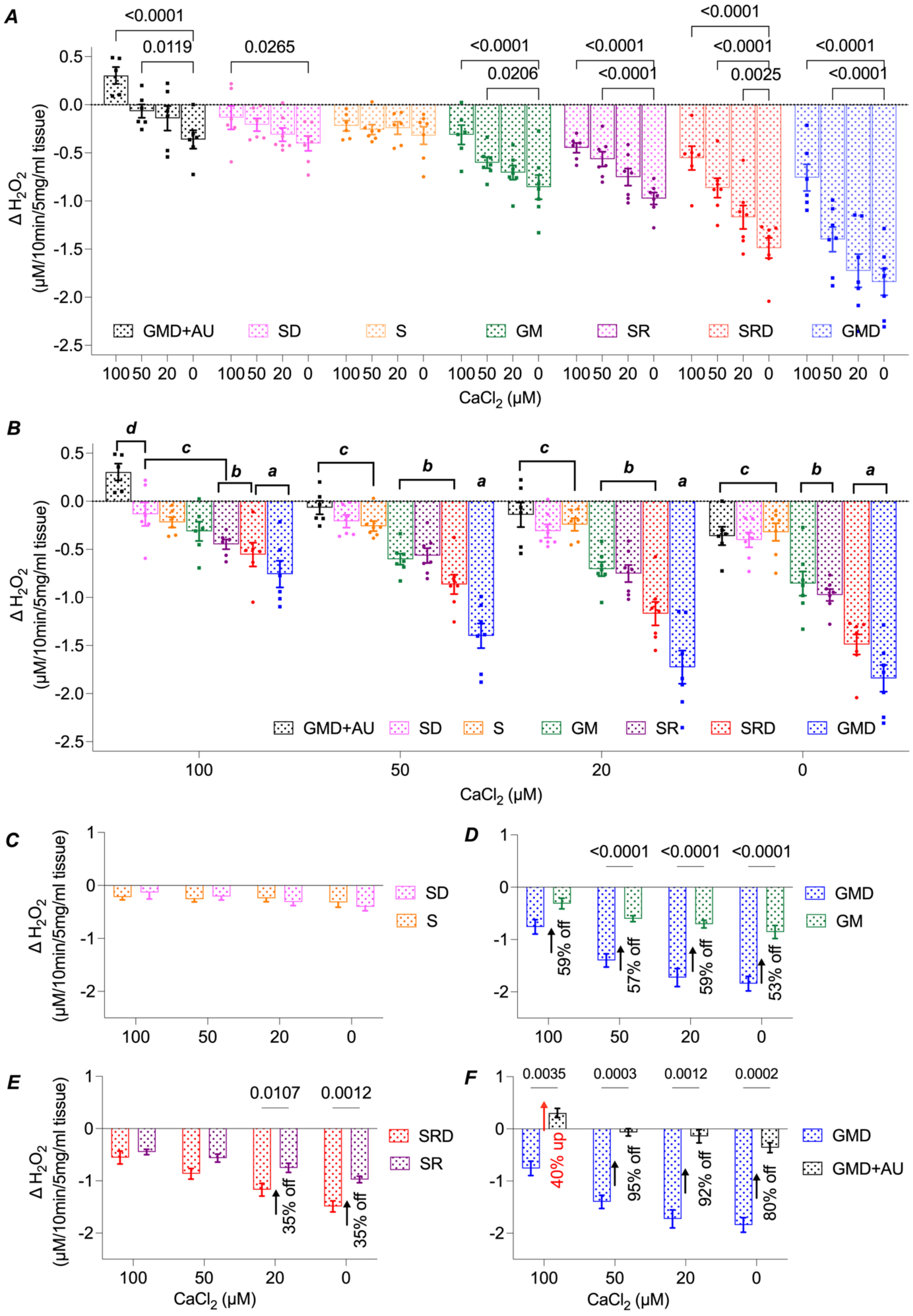
A
<0.0001
0.0119
0.0265
<0.0001
0.0206
<0.0001
<0.0001
<0.0001
<0.0001
0.0025
<0.0001
<0.0001
Δ H_2O_2 (µM/10min/5mg/ml tissue)
GMD+AU
SD
S
GM
SR
SRD
GMD
100 50 20 0
CaCl$_2$ (µM)
B
d
c
b
a
Δ H_2O_2 (µM/10min/5mg/ml tissue)
100
50
20
0
CaCl$_2$ (µM)
C
Δ H_2O_2 (µM/10min/5mg/ml tissue)
SD
S
D
<0.0001
<0.0001
<0.0001
59% off
57% off
59% off
53% off
GMD
GM
E
0.0107
0.0012
35% off
35% off
SRD
SR
F
0.0035
0.0003
0.0012
0.0002
40% up
95% off
92% off
80% off
GMD
GMD+AU
100
50
20
0
CaCl$_2$ (µM)

SF 3.4 Ca^{2+} inhibits H_2O_2 consumption in permeabilized NMR brain.

(A, B) Change (Δ) in H_2O_2 consumption (H_2O_2 consumed with substrates subtracted from consumption without substrate) in 5 mg/ml tissue incubated with 10 µM H_2O_2 for 10 min. **(C-F)** Statistical comparisons of ΔH_2O_2 consumption between **(C)** succinate and succinate/ADP, **(D)** glutamate/malate and glutamate/malate/ADP, **(E)** succinate/rotenone and succinate/rotenone/ADP, and **(F)** glutamate/malate/ADP and glutamate/malate/ADP/auranofin. Data are presented as means ± SEM from *n* = 6-8 each. Significant differences were determined using two-way ANOVA with Dunnett (A&B), and Sidak (C-F) multiple comparisons test (***p*** < 0.05 in A, and C-F; ***a, b, c, d*** in B). Abbreviations: G, glutamate; M, malate; S, succinate; D, ADP; R, rotenone; AU, auranofin; AUR, Amplex UltraRed; HRP, horseradish peroxidase.

3.6 Discussion

Mitochondria are primary regulators of cellular bioenergetics and serve as an important hub for multiple aspects of cellular signalling, including by two of the predominant cellular messengers: Ca^{2+} and ROS (Anderson et al., 2019; Giorgi et al., 2018; Szabadkai & Duchen, 2008). However, Ca^{2+} signalling is a double-edged sword as Ca^{2+} overload induces neuronal cell death in hypoxia and ischemia. In the present study we explore Ca^{2+} handling in a hypoxia-tolerant mammal brain and reveal novel adaptations at the mitochondrial level that contribute to the tolerance of NMR brain to Ca^{2+} and hypoxic stress. Specifically, we report that increasing external Ca^{2+} induces mPTP opening and the release of mitochondrial matrix Ca^{2+} in both NMR and mouse brain. However, the properties of mitochondrial Ca^{2+} handling are divergent between these species such that NMR brain mitochondria are able to take up and retain more Ca^{2+}, preserve bioenergetic, regulate redoxes state and ETC function following *in vitro* Ca^{2+} challenges, and avoid mitophagy following an *in vivo* hypoxia challenge. In relation, cellular glutamate metabolism and redox state, which are both tightly associate with mitochondrial Ca^{2+} management (Siesjo et al., 1995), are altered following *in vivo* hypoxia. These capabilities are likely mediated by ultrastructural differences between these species that precondition NMR mitochondria to tolerate severe Ca^{2+} challenges, such as occur during hypoxia in hypoxia-intolerant mammal brain. Together, the mechanisms reported in this study explain the blunted Ca^{2+} intake profile of hypoxic NMR brain *in vitro* (Peterson et al., 2012a), and contribute to hypoxia/ischemia tolerance in NMR brain *in vitro* and/or *in vivo* (Cheng & Pamenter, 2021; Nathaniel et al., 2009; Pamenter et al., 2018).

***Mitochondrial uptake is the primary mediator of Ca^{2+}-buffering in NMR brain*.** Mitochondria play major roles both as regulators of cytosolic [Ca^{2+}] and mediators of cellular Ca^{2+} signalling

(Giorgi et al., 2018). Mitochondria can accumulate large amounts of Ca^{2+}, and thereby play an essential role in maintaining cellular Ca^{2+} homeostasis, particularly when extracellular Ca^{2+} influx into the cytosolic space is increased during acute hypoxia or ischemia (Shen & Jennings, 1972). In normal conditions, the rapid mode of uptake (RaM), mitochondrial ryanodine receptor (mRyR), MCU mediate mitochondrial Ca^{2+} uptake, with the MCU being the primary conduit of Ca^{2+} uptake when RaM and mRyR are inhibited (which occurs when cytosolic $[Ca^{2+}]$ is > 40 μM) (Ryu et al., 2010). Consistent with a primarily role for the MCU in mitochondrial buffering, we report a near complete inhibitory effect on Ca^{2+} uptake with the MCU-antagonist Ru360 in both NMR and mouse (Fig. 3.1A-D). We also demonstrate that mPTP opening (increasing Ca^{2+} signal after end points), which is a necessary for the initiation of Ca^{2+}-mediated cell death in hypoxia/ischemic brain (Kroemer et al., 2007), is triggered at a much higher external $[Ca^{2+}]$ in NMR brain mitochondria than mouse (210 *vs.* 110 μM, NMR *vs.* mouse, Fig. 3.1A, Table 3.1).

In addition to having a greater capacity for Ca^{2+}, NMR brain mitochondria take up Ca^{2+} at a higher rate than mouse (Fig. 3.1B-D). The rate of mitochondrial Ca^{2+} uptake depends on multiple factors, including the energetic states of mitochondria, $\Delta\psi_m$, and external Ca^{2+} concentration (Gunter & Pfeiffer, 1990). We have previously reported that NMR brain maintains [ATP] in acute *in vivo* hypoxia (7%, 4 h) (Pamenter et al., 2019a), and this likely supports rapid uptake of higher volumes of Ca^{2+} (Fig. 3.1B-D, Table 1). Indeed, glutamate/malate-induced OXPHOS capacity is similar between NMR and mouse brain per tissue weight (Fig. 3.2A&B), but NMRs have a more tightly coupled ETC (Pamenter et al., 2018), which should result in higher O_2/ATP coupled respiration rates. In addition, the more hyperpolarized $\Delta\psi_m$ of NMR brain also contributes to faster Ca^{2+} uptake, as we report stronger glutamate/malate induced Rh-123 quenching in NMR brain than mouse (Fig. 3.3B). Note that there is a linear correlation between fluorescence quenching of

Rh-123 and $\Delta\psi_m$ (Emaus et al., 1986), which was validated in mouse and NMR brain homogenates (both (mouse and NMR) ~2.9 $\Delta V/\mu M$ Rh-123). Finally, NMR brain mitochondria have a greater volume and are endogenously more interconnected than mouse (Fig. 3.4, and see below), which should physically support a higher $\Delta\psi_m$, and provide more space in which to sequester Ca^{2+} (Gunter & Pfeiffer, 1990).

Intriguingly, the decay rate (K_{off}, Fig. 3.1D) indicates that ATP-dependent Ca^{2+} uptake is the major mechanism of Ca^{2+} uptake in mouse brain mitochondria; however, both ATP- and $\Delta\psi_m$-dependent uptake contribute to Ca^{2+} uptake in NMR brain mitochondria. Taken together, these results indicate that NMR brain mitochondria have higher sensitivity to changes in [Ca^{2+}], and greater capacity for Ca^{2+} buffering, and are also able to maintain Ca^{2+} buffering under ATP-limited situations, such as in hypoxia/ischemia.

Enhanced mitochondrial Ca^{2+} buffering supports mitochondrial bioenergetics in NMR brain. Ca^{2+} uptake by mitochondria plays an important role in regulating mitochondrial energetics (Anderson et al., 2019; Giorgi et al., 2018; Szabadkai & Duchen, 2008). Conversely, excessive mitochondrial Ca^{2+} accumulation leads to mitochondrial depolarization, mPTP opening, and release of cytochrome c due to outer mitochondrial membrane (OMM) damage (Pandya et al., 2013; Polster & Fiskum, 2004; Raffaello et al., 2016). In some hypoxia-tolerant species, mechanisms of enhanced mitochondrial Ca^{2+} management are thought to prevent excitotoxicity in hypoxic conditions. For example, turtle neurons mildly increase cytoplasmic Ca^{2+} by suppressing mitochondrial Ca^{2+} uptake (Pamenter et al., 2008) or enhance mitochondrial Ca^{2+} release (Hawrysh & Buck, 2013) to silence NMDAR activity, which is an ion channel that enables excessive influx of extracellular Ca^{2+} under hypoxia/ischemia in hypoxia-intolerant brain (Budd, 1998; Fan et al., 2014). Similar regulation of cytosolic Ca^{2+} levels by mitochondria has been reported in hypoxic goldfish retinal horizontal cells (Country & Jonz, 2021).

We report that Ca^{2+} addition triggers dose-dependent mitochondrial respiratory dysfunction in both NMR and mouse brain (Fig. 3.2A&B), in line with previous studies using isolated mouse brain mitochondria (Hamilton et al., 2018; Pandya et al., 2013). However, consistent with our finding that NMR brain mitochondria can take up more Ca^{2+} before activation of the mPTP (Table 3.1), mitochondrial OXPHOS capacity (Fig. 3.2C-D), OMM integrity (Fig. 2E), and $\Delta\psi_m$ (Fig. 3.3B-D) are all better maintained with the same Ca^{2+} challenge in NMR brain than mouse. The overall lower effect of cytochrome c and maintenance of $\Delta\psi_m$ suggests that a relatively intact mitochondrial membrane system is retained during Ca^{2+} stress, which would in return participate in Ca^{2+} resistance in NMR brain. Similar results have been reported in NMR brain during ischemic stress (Cheng & Pamenter, 2021).

Large and zippered mitochondria, greater number of mitochondria connected by nanotunnels, higher cristae density, and more crista junctions per mitochondrion help NMR brain tolerate Ca^{2+}. It is well established that biological structures determine cellular function. Furthermore, mitochondrial ultrastructural changes can occur within minutes to hours of signalling events, or even precede signalling events (Ramírez et al., 2017; Shenouda et al., 2011). Changes of mitochondrial volume are regulated by multiple factors (Kaasik et al., 2007). For example, deleterious Ca^{2+} uptake during ischemia is linked to increases in mitochondrial size, and neuroprotection can be achieved through either inhibiting the uptake of Ca^{2+}, by increasing mitochondrial fusion, or by supressing ATP demand/production (Anastacio et al., 2013; Halestrap et al., 1986). It is therefore possible that the increase in NMR brain mitochondrial size during hypoxia is a consequence of Ca^{2+} uptake during hypoxia (Pamenter et al., 2018), although no matrix swelling was observed. Indeed, Ca^{2+} uptake into the mitochondrial matrix also causes mitochondrial depolarization and related mitochondrial volume increases in neurons (Safiulina et al., 2006). Consistently, we found that Ca^{2+} uptake discharges glutamate/malate-induced $\Delta\psi_m$ in both mouse and NMR brain mitochondria (Fig. 3.3), and more depolarized mitochondria have also been reported in hypoxic NMR brain mitochondria *in vitro* (Pamenter et al., 2018). Therefore, we speculate that hypoxia-mediated increases of mitochondrial size in NMR brain (Fig. 3.4I), may be a fundamental contributor to their greater Ca^{2+} uptake capacity relative to mice (Table 3.1).

Notably, however, a higher $\Delta\psi_m$ is observed in healthy and larger mitochondria (Twig et al., 2008), whereas swollen mitochondria have lower $\Delta\psi_m$, which is due to Ca^{2+} overload (Schneider et al., 2019). We report a relatively higher $\Delta\psi_m$ (Fig. 3.3B) and larger size (Fig. 3.4I) of NMR brain mitochondria than mouse, suggesting that the larger mitochondrial size also contributes to higher $\Delta\psi_m$, which in turn induces a higher rate of Ca^{2+} uptake in NMR brain (Fig. 3.1D). Additionally, more closely packed NMR brain mitochondria (Fig. 3.4A-H), with stronger zippering, provide enhanced physical fundamentals for mitochondrial communication or transfer/exchange of molecules among NMR mitochondria, which may be beneficial, since disconnection of damaged mitochondria limits the cellular impact of local dysfunction (Glancy et al., 2018).

Crista junctions also control Ca^{2+} uptake through a constituent protein, optic atrophy type 1 (OPA1), and a stabilizing protein, mitochondrial Ca^{2+}uptake 1 (MICU1) (reviewed by Gottschalk et al., 2022). When Ca^{2+} binds to MICU1, crista junctions can open transiently by unblocking the OPA1 cap positioned over the crista junction opening. This Ca^{2+}/MICU1-mediated plasticity of the crista junction opening allows for quick Ca^{2+} uptake across the cristae membranes through the constantly active MCU, which resides on the cristae membranes. Another subpopulation of MCU resides on the mitochondrial inner boundary membrane and allows for Ca^{2+} uptake across this membrane that complements the uptake across the cristae membranes. This dual localization of MCU underlies the mechanism of biphasic mitochondrial Ca^{2+} uptake kinetics. The increased number of MICU1-regulated crista junctions in NMR brain mitochondria may help to explain how they are able to take up and retain more Ca^{2+}.

Intriguingly, we noticed enhanced connectivity between NMR brain mitochondria relative to mouse in the form of more extensive mitochondrial nanotunnel networks (Fig. 3.4). Although poorly understood from a functional perspective, structurally, mitochondrial nanotunnels are 60–200 nm wide double membranes connecting two non-adjacent mitochondria and are capable of transporting proteins and metabolic intermediates between non-adjacent mitochondria (Vincent et al., 2017). What separates a nanotunnel from a simple constriction is that nanotunnels do not contain cristae, but constrictions often do. Mitochondrial nanotunnels are more frequent in conditions of metabolic derangement than in healthy animals, including in models of mtDNA diseases (Vincent et al., 2019), aging (Morozov et al., 2017), as a result of aberrant Ca^{2+} homeostasis (Lavorato et al., 2017), and with Alzheimer’s Disease (Tyumentsev et al., 2018). In general, nanotunnels are thought to rapidly extend from immobilized mitochondria as a survival mechanism during periods of energetic stress (Lavorato et al., 2017; Morozov et al., 2017). For example, a recent report suggested that mouse brain mitochondrial nanotunnels are enhanced within as little as five min of hypoxia (Zhang et al., 2016). Consistent with this, we found that hypoxia increased the length and number of nanotunnels in mouse brain. Conversely, we did not observe significant changes to NMR brain mitochondrial nanotunnels during hypoxia, but the basal level of mitochondrial nanotunnel networks was significantly higher in NMRs than in mouse (Fig.

3.4). Based on these results, we speculate that the abundant mitochondrial nanotunnel network in NMRs represents a form of endogenous preconditioning that, along with the other ultrastructural differences outlined above, supports mitochondrial energetic homeostasis (and potentially Ca^{2+} buffering) in NMR brain during fluctuations in environmental O_2 availability.

***Short-term* in vivo *hypoxia induces fission and mitophagy in mouse but not NMR brain*.** Neuronal mitophagy is related to swelling of mitochondria and reductions of mitochondrial volume fraction, which can eventually lead to neuronal cell death (Yuan et al., 2007). We report a larger size of mitochondria and significant decrease of mitochondrial volume fraction during hypoxia in NMR brain (Fig. 3.4), however, there are no significant changes of fission/fusion, or mitophagy proteins during hypoxia (Fig. 3.6). On the other hand, several proteins that regulate mitochondrial dynamics are either accumulated (Parkin and Drp-S616) or degraded (BNIP3) during hypoxia in mouse brain (Fig. 3.6). Phosphorylation of serine 616 increases DRP1 activity, and initiates mitochondrial fission (Han et al., 2008), while increased Parkin is associated with the downstream activation of mitophagy (Ni et al., 2015; Pendin et al., 2017).

***Metabolic remodelling and redox state switching in NMR brain during acute hypoxia*.** We identified a handful of metabolites that change similarly between NMR and mouse brain following *in vivo* hypoxia, including valine, leucine, isoleucine, glucose 6-phosphate, glutamine, and arginine. Beyond these common changes, NMR brain exhibits broad metabolic reprograming during hypoxia related to (1) glutamine and glutamate metabolism, (2) phenylalanine/tyrosine-related neurotransmitter synthesis, (3) pentose phosphate pathways, and (4) coenzyme-related metabolism.

Valine, leucine, and isoleucine accumulate with hypoxia in NMR and mouse brain, which is a common response to stress in mammals, including to hypoxia (Fitzgerald et al., 2021). Interestingly, an accumulation of threonine during hypoxia is observed in NMR brain but not in mouse, the underlying mechanism is unclear.

Aspartate and glutamate metabolism are critical for maintaining energetic balance in homeostatic situations and also drive excitotoxicity in the central nervous system. We observe a decrease in glutamate and glutamine in hypoxic NMR brain but only glutamine decreases in hypoxic mouse brain. Decreases in these excitatory amino acids may be neuroprotective in NMRs, as derangements in glutamate are associated with excitotoxic cell death in hypoxia-intolerant mammalian brain (Choi & Rothman, 1990). In support of this, previous studies have reported that NMR brain is largely tolerant to hypoxic and ischemic stress *ex vivo* (Cheng & Pamenter, 2021; Nathaniel et al., 2009; Park et al., 2017), although the underlying protective mechanisms are largely unknown. It is possible that changes in the function of the aspartate–glutamate carrier, glutamic-oxaloacetic transaminase, and/or glutamate dehydrogenase occur during hypoxia in NMR brain, conferring some degree of neuroprotection. Indeed, we found that mitochondrial function is better maintained during Ca^{2+} stress *in vitro*, which could partially contribute to glutamate metabolism in NMR brain because Ca^{2+} and glutamate interact to drive excitoxic cell death in hypoxia-intolerant brain(Siesjo et al., 1995). Alternatively, the reduction in lysine in NMR brain suggests that this tissue might have increased aspartate/glutamate/glutamine demand and/or metabolism, since lysine is an important precursor in the de novo synthesis of glutamate (Papes et al., 2001). Further studies are warranted to explore the regulation of excitatory neurotransmission in NMR brain during hypoxia.

Phenylalanine and tyrosine are precursors to dopamine, which is, in turn, a precursor of epinephrine and norepinephrine (Fernstrom & Fernstrom, 2007). We observe increases in both metabolites in the hypoxic NMR brain; however, the mechanism underlying these changes in phenylalanine and tyrosine is unclear. We speculate that NMR brain may reduce the synthesis of epinephrine and norepinephrine, leading to decreases in physical activity during hypoxia, which is likely most severe in crowded nest chambers (Ilacqua et al., 2017). Additionally, limited molecular O_2 availability during hypoxia may affect the activity of dioxygenases that contribute to the metabolism of these amino acids (Parthasarathy et al., 2018).

Downregulation of fructose 6-phosphate is observed in hypoxic NMR brain, while interestingly, glucose 6-phosphate and sedoheptulose 7-phosphate are upregulated. It is thus likely that the pentose phosphate pathway is remodelled during hypoxia in NMR brain. This finding is similar to a previous report in anoxia (Park et al., 2017).

Accompanying these changes of amino acids and carbohydrates, the redox state in NMR brain changes dramatically during hypoxia. This is apparent from the very large increase in NADPH and from reductions in FAD, NAD^+, and $NADP^+$. Increased NADH levels are essential to provide electrons for mitochondrial OXPHOS (Titov et al., 2016). In this study, we report changes of nicotinate and nicotinamide metabolism in hypoxic NMR brain, which indicates that NMR brain mitochondria decrease OXPHOS function during hypoxia, as previously reported (Pamenter et al., 2018). The source of increased NADPH is unknown; however, nicotinamide nucleotide transhydrogenase is a physiologically relevant source of mitochondrial NADPH that is activated when the mitochondrial ETC is impaired, thus slowing the conversion of NADH to NAD

(Ronchi et al., 2016). This may occur during hypoxia when the efficiency of the ETC becomes limited. There are also additional enzymatic oxidative reactions that generate NADPH and may be activated here (e.g., glutamate dehydrogenase (Plaitakis et al., 2017)). During normoxic conditions, most of the cytosolic NADPH is contributed by the oxidative pentose phosphate pathway, and most NADPH is used for both reductive biosynthesis and antioxidant defence (Dringen et al., 2007). Thus, the elevation of NADPH in NMR brain might reduce biosynthesis as mentioned above, and also reduce NADPH-related antioxidant defence during hypoxia as a biproduct of the coordinated lowering of O_2 consumption and ROS production in the brain and potentially across the whole organism, since oxidative metabolism can directly contribute to the generation of ROS (Halliwell, 2001). Perhaps, decreased ROS generation in hypoxia may reduce the activity of mitochondrial thioredoxin and glutathione scavenging pathways and, thus, contribute to the accumulation of NADPH.

In support of this, we report that H_2O_2 consumption is regulated by Ca^{2+} (which may be elevated in hypoxia) in NMR brain mitochondria. As discussed above, the mitochondrial complex II (succinate/rotenone) pathway is more sensitive to $CaCl_2$ than the complex I (glutamate/malate) pathway with regard to H_2O_2 consumption (SF 3.4A). The inhibition of H_2O_2 consumption by auranofin (SF. 3.4F) indicates that the thioredoxin-dependent enzymatic pathway might be the primary contributor to antioxidative defence in NMR brain mitochondria, which is different from isolated mitochondria from NMR heart and skeletal muscle, in which the GSH pathway dominates (Munro et al., 2019). In addition, ADP (OXPHOS) does not change H_2O_2 consumption relative to succinate-induced leak respiration (SF 3.4C), possibly due to succinate-induced reverse electron transport mediated by an abundance of $O_2^{\cdot-}$, resulting in oxidative stress (Scialo et al., 2017).

Taken together, these data suggest that NMR brain may suppress mitochondrial ROS scavenging capacity when O_2 availability is limited, resulting to accumulation of NADPH.

Limitations. Mitochondria and ER are two majors intracellular Ca^{2+} stores (Giorgi et al., 2018), and ER is usually the largest store of releasable Ca^{2+} in the cell (Ashby & Tepikin, 2001). Mitochondrial Ca^{2+} uptake is a rapid response, and also involves the ER (S. Wang et al., 2022). Hypoxia-induced Ca^{2+} release from the ER is commonly reported (Gusarova et al., 2011; Shimoda et al., 2021), and is regulated by mitochondrial ROS signalling (Gusarova et al., 2011; Mungai et al., 2011; Yang et al., 2020). In return, mitochondrial respiration and membrane dynamics are associated with ER function (Kuznetsov et al., 2022; Shen et al., 2022; S. Wang et al., 2022). Due to the limits of our methodology, we did not assess Ca^{2+} signals at the cellular level. Thus, further study of intracellular Ca^{2+} signalling in whole cells would help us to better understand the role of interactions within the mitochondria-ER-Ca^{2+} network in hypoxic NMR brain.

Conclusion. Ca^{2+} overload is a hallmark initiator of catastrophic cell death during hypoxia/ischemia in brain. Remarkably, we report that NMR brain mitochondria have robust and sensitive Ca^{2+} uptake capabilities and resist mitochondrial defects following either *in vitro* Ca^{2+} challenges or *in vivo* hypoxic stress. We propose that NMR brain mitochondrial ultrastructure might support this outstanding Ca^{2+} regulation capacity, and help to maintain energetic balance, redox state, Ca^{2+} homeostasis, membrane potential, mitochondrial quality control, and metabolic regulation during *in vivo* hypoxia. These findings suggest a potential mechanism via which mitochondria contribute to hypoxia/ischemia tolerance in NMR brain. Further investigation may help provide therapeutic strategies directed to mitochondria in hypoxic/ischemic brain damage.

4 A case study: NMR brain as a hypoxia/ischemia-tolerant model for biomedical research

This chapter includes material from the following article:

Cheng, H., & Pamenter, M. E. (2021). Naked mole-rat brain mitochondria tolerate in vitro ischemia. The Journal of physiology, 599(20), 4671–4685. https://doi.org/10.1113/JP281942

4.1 Introduction

In a hypoxia-intolerant mammalian brain, defects in mitochondrial function occur during periods of low O_2 stress or ischemia, which trigger energetic depression, and eventually the formation of the mPTP, the opening of which irreversibly triggers cell death (Polster & Fiskum, 2004). More damaging than ischemia-alone are ischemia-reperfusion (I/R) events, during which mitochondrial metabolism becomes rapidly reactivated following a period of ischemia, resulting in deleterious overproduction of ROS (Chouchani et al., 2014; Jassem et al., 2002; Piantadosi & Zhang, 1996). Such mitochondrial dysfunction is a central component in the pathophysiology of ischemic stroke, which comprises 80% of stroke cases (F. Liu et al., 2018). However, some mammals avoid derangements in brain mitochondrial function during periods of *in vivo* hypoxia, and in many such species, neuroprotective mechanisms against hypoxia also confer protection against ischemia (Christian et al., 2008; Pamenter et al., 2012).

There is evidence that NMR brain is tolerant of *ex vivo* and *in vitro* hypoxic and ischemic challenges. For example, cell death does not increase in NMR brain slices during 5 h of oxygen glucose deprivation (OGD, a common *in vitro* ischemic mimic) (Nathaniel et al., 2009), and cortical neurons are resistant to acid-induced cell death (Husson & Smith, 2018) (with loss of acid-base equilibrium being a key component of ischemic cell death in the brain (von Hanwehr et al., 1986). Furthermore, neuronal Ca^{2+} influx, which is a key trigger of mPTP opening during ischemia (Halestrap, 2006), is blunted during hypoxia in NMR brain relative to mouse brain (Peterson et al., 2012a). Additionally, our study in Chapter 3 suggests that NMR brain mitochondria can resistant higher [Ca^{2+}] acclimation with rapid Ca^{2+} uptake, better maintenance of OXPHOS capacity, and less OMM damage. Little is known regarding the mechanisms that confer this neuroprotection against hypoxia/ischemia, but adult NMR brain expresses a neonatal conformation of NMDAR subunits and a unique acid-sensing ion channel, which may blunt the deleterious influx of Ca^{2+} and H^+ during ischemia, respectively (Peterson et al., 2012b; Schuhmacher et al., 2018). However, despite these findings, our understanding of neuroprotective mechanisms in the brain of this remarkably hypoxia-tolerant mammal is in its infancy.

A key question that has received minimal attention in this model is whether mitochondrial function is maintained or impaired during ischemia and following reperfusion. This is a critical question because mitochondrial dysfunction during I/R in the brain of hypoxia-intolerant mammals leads to impaired OXPHOS, ATP depletion, overproduction of ROS, Ca^{2+} overload, formation of the mPTP, and activation of apoptotic cell-death pathways (Kroemer et al., 2007; Polster & Fiskum, 2004; Yang et al., 2018). We have recently reported that NMR brain mitochondria supress ETC capacity >85% and that brain [ATP] is maintained following severe *in vivo* hypoxia (4 h in 3% O_2) (Pamenter et al., 2019a; Pamenter et al., 2018). However, ischemia is more deleterious than hypoxia (Miyamoto & Auer, 2000), and understanding if and how neuroprotective adaptations against hypoxia in NMR brain mitochondria also confer tolerance against I/R injury is of pressing interest. To address this question, we utilized NMR and CD-1 mouse brain slices to explore changes in mitochondrial ETC and OXPHOS function and ROS dynamics during and following periods of *in vitro* OGD and I/R stress (Fernandez-Lopez et al., 2005; Murata et al., 2013; Rau et al., 2012; Trumbeckaite et al., 2013).

4.2 Methods

4.2.1 Ethics approval

NMRs were group-housed in interconnected multi-cage systems at 30°C and 21% O_2 in 50% humidity with a 12L:12D light cycle. Animals were fed fresh tubers, vegetables, and fruit, and Pronutro cereal supplement *ad libitum*. CD-1 mice were obtained from Charles River and were housed at room temperature under a 12L:12D light cycle and fed rodent chow *ad libitum*. Animals were not fasted prior to experimental trials. All experimental procedures were approved by the University of Ottawa Animal Care Committee in accordance with the Animals for Research Act and by the Canadian Council on Animal Care. Non-breeding (subordinate) naked mole-rats do not undergo sexual development or express sexual hormones and thus we did not take sex into consideration when evaluating our results (Holmes et al., 2009).

4.2.2 In vitro ischemic treatment of brain slices

Adult subordinate NMRs (1-2 years old) and adult mice (14-16 weeks old) were sacrificed by cervical dislocation followed by decapitation. Brains were rapidly excised on ice and 300 μm coronal slices were sectioned with a vibratome in ice-cold oxygenated (95% O_2, 5% CO_2) sucrose-based artificial cerebral spinal fluid (aCSF) containing (in mM): sucrose 248, NaH_2PO_4 1.25, $MgSO_4$ 2, $MgCl_2$ 1, $CaCl_2$ 1, KCl 2, $NaHCO_3$ 26 and d-glucose 10; pH 7.3. Slices were then allowed to recover in an aerated beaker for 45 mins at room temperature (~25°C) in modified Hanks' Balanced Salt Solution (HBSS; containing (in mM): NaCl 140, KCl 2, NaH_2PO_4 1.25, $MgSO_4$ 2, $MgCl_2$ 1, $CaCl_2$ 1, HEPES 15 and d-glucose 10; pH 7.3), aerated with compressed air.

Following this recovery period, 4 slices from each animal were placed into one 2 ml tube, which was perforated with small holes to allow free diffusion of solution and prevent mechanical damage to the brain slices that might result from direct gas bubbling. Tubes were then placed into

50 ml tubes containing 20 ml modified HBSS held at 32 or 37°C (the normal T_b of NMRs and mice in our housing conditions, respectively), which were continuously bubbled with either compressed air or 100% N_2 gas, for 20 mins before treatments. Slices were then treated with one of four different experimental conditions: 1) 15 mins in normoxic modified HBSS (normoxic control), 2) 15 mins in oxygen–glucose deprivation (OGD, *i.e*., with glucose replaced with an equimolar amount of sucrose and bubbled with 100% N_2 gas), 3) 30 mins in OGD, or 4) 15 mins of OGD followed by 15 mins of normoxic reperfusion (with glucose restored).

Following treatment, slices were transferred into ice-cold Tris solution containing (in mM): KCl 100, Tris-HCl 50, EGTA 2, pH 7.1. Cortical regions were separated, weighed and homogenized using 200 µl pipette in a 1.5 ml tube at 100 mg wet weight of tissue per ml in Tris solution, and kept on ice for Oroboros experimentations.

4.2.3 Mitochondrial respiration and H_2O_2 emission of brain homogenate

Rates of O_2 consumption and H_2O_2 emission were monitored simultaneously using an Oroboros O2k (Oroboros, Innsbruck, Austria) equipped with a fluorescence detection module mounted with the appropriate excitation and emission filters for the fluorescent probe Amplex UltraRed (AUR), as described previously (Cheng, Munro, et al., 2021). Briefly, AUR (10 µM), SOD (10 IU/ml), horseradish peroxidase (2 IU/ml), and saponin (50 µg/ml) were added to 2 ml respiration medium containing (in mM): KCl 120, HEPES 20, KH_2PO_4 20, $MgCl_2$ 2.5, EGTA 1, and BSA 0.045; pH 7.2, followed by brain homogenate (4 mg wet weight in each chamber), and held at 32°C for NMRs and 37°C for mice. An O_2 range of 200 µM to 80 µM in the air-saturated medium was maintained during the whole measurement (Makrecka-Kuka et al., 2015).

Baseline values for O_2 consumption and H_2O_2 production were measured following addition of mitochondria to chambers without effectors. SUIT protocols were sequentially performed as below.

SUIT1 evaluated mitochondrial respiration through the pyruvate dehydrogenase complex pathway and complex I–II maximal capacity. The following components were added sequentially: pyruvate/malate to induce pyruvate dehydrogenase-dependent leak respiration from complex-I, ADP to induce OXPHOS respiration, glutamate to induce maximal OXPHOS respiration from complex I, succinate to induce maximal OXPHOS respiration from complexes I&II, and CCCP (to induce maximal electron transport capacity from complex I which was ∼1 μM for mice and ∼1.5 μM for NMRs).

SUIT2 evaluated mitochondrial respiration through the glutamate dehydrogenase pathway, and complex IV activity. The following components were added sequentially: glutamate/malate to induce glutamate dehydrogenase-dependent leak respiration from complex I, ADP to induce OXPHOS respiration, pyruvate to induce maximal OXPHOS respiration from complex I, succinate to induce maximal OXPHOS respiration from complexes I&II, antimycin A followed by ascorbate and TMPD to induce complex IV capacity.

SUIT3 evaluated mitochondrial respiration through succinate dehydrogenase and mitochondrial membrane integrity. The following components were added sequentially: succinate to induce succinate dehydrogenase-dependent leak respiration from complex II, rotenone to block complex I, ADP to induce OXPHOS respiration from complex II and cytochrome c to assess outer mitochondrial membrane damage.

Table 4.1 Substrates for mitochondrial SUIT protocols

Substrates	Abbreviation	Working concentration
Malate	M	2 mM
Glutamate	G	10 mM
Pyruvate	P	5 mM
Succinate	S	10 mM
Ascorbate	ASC	2 mM
TMPD	TMPD	0.5 mM
Cytochrome *c*	CytC	10 μM
ADP	D	1 mM
CCCP	U/CCCP	0.5 or1 μM steps to max responses
Antimycin A	AA	2.5 μM
Rotenone	R	0.5 μM

Concentrations were tested by pre-experiments. Manufacture, function, and preparation of all substrates were as per (Fontana-Ayoub et al., 2016).

In other experiments, rates of fluorescent product (resorufin) formation were converted to micromoles of H_2O_2 based on a three-point standard curve conducted with cortical brain tissue alone and by direct addition of 0.1 μM H_2O_2 twice to the chamber.

4.2.4 Statistical analysis

All statistical analyses were performed using GraphPad Prism 9 (GraphPad Prism, La Jolla, CA, USA). Data were analyzed using two-tailed t-tests (Fig. 4.7C); one-way ANOVA with Dunnett multiple comparison (Fig. 4.3 B&D) post-tests; two-way ANOVAs followed with a Sidak (Fig. 4.2, 4.6, 4.7B, Table 4.1), Dunnett (Fig. 4.1, 4.3 A&C, 4.4&4.5), or Tukey (Fig. 4.7A) multiple comparisons tests. Significance was determined with a level of $p < 0.05$ unless otherwise indicated in results, and all data are expressed as the mean ± SEM.

4.3 Results

Ischemia-induced functional defects were greater in mouse brain than NMR brain. O_2 consumption in the four experimental groups (normoxia, 15 min OGD, 30 min OGD and 15 min OGD with reperfusion) were investigated using the SUIT protocols described in the methodology section. For mitochondrial respiration, OGD treatment significantly decreased OXPHOS capacity through complexes I, II and IV in both NMR and mouse cortical brain tissue, and these effects increased with time (Fig. 4.1A-F). However, the extent of these changes was markedly different between species, with NMRs exhibiting no or smaller reductions in respiration capacity in all treatment conditions relative to mice. Specifically, complex I-linked respiration (fuelled by either pyruvate/malate or glutamate/malate) decreased ~45–76% in mice *vs*. ~28–44% in NMRs ($F_{1,14} = 45.19$, $P < 0.0001$ with pyruvate/malate, Fig. 4.2A; $F_{1,14} = 38.15$, $P < 0.0001$ with glutamate/malate, Fig. 4.2B), complex II-linked respiration (succinate/rotenone) decreased ~42–71% in mice *vs*. ~18–41% in NMRs ($F_{1,14} = 43.61$, $P < 0.0001$, Fig. 4.2C), and complex IV capacity (ascorbate/TMPD) decreased ~36–56% in mice *vs*. ~16–29% in NMRs ($F_{1,14} = 49.58$, $P < 0.0001$, Fig. 4.2D). Notably, cytochrome c-induced O_2 consumption was stable in NMRs following all treatment conditions (between 40.62 ± 2.73 and 42.19 ± 2.60 pmol/(s*mg wet tissue), $F_{3,28} = 0.4757$, $P = 0.7017$, Fig. 4.1C) but was significantly decreased in mice post-OGD (from 90.73 ± 7.92 to 67.64 ± 6.25 pmol/(s*mg wet tissue), $F_{3,28} = 11.3$, $P < 0.0001$, Fig. 4.1F)

In addition, measures of mitochondrial integrity were similarly divergent between species. In mice, RCRs (calculated individually for each experiment as OXPHOS capacity divided by leak respiration) were significantly reduced following all ischemic treatments and in all substrate conditions mainly due to the large reduction of OXPHOS respiration (from 4.66 ± 0.65 to 2.57 ± 0.43 with glutamate/malate, 4.58 ± 0.43 to 2.58 ± 0.51 with pyruvate/malate, and 2.88 ± 0.18 to

2.19 ± 0.20 with succinate/rotenone, $F_{3,84} = 64.14$, $P < 0.0001$, Fig. 4.3C & Table 4.2); conversely, a significant RCR reduction was only observed with glutamate-fuelled respiration in NMR brain (from 13.06 ± 1.44 to 9.29 ± 1.31 with glutamate/malate, $F_{3,84} = 6.601$, $P = 0.0005$, Fig. 4.3A). Additionally, the stimulatory effect of exogenous cytochrome c (i.e., exogenous cytochrome c-induced O_2 consumption divided by complex II-linked O_2 consumption) on respiration increased ~3-fold in all OGD conditions in mice (from 2.25 ± 0.21 to 6.88 ± 1.30, $F_{3,28} = 5.416$, $P = 0.0064$, Fig. 4.3D). Conversely, in NMRs, these changes were more modest than in mouse brain (between 1.50 ± 0.09 to 2.61 ± 0.20, $F_{3,28} = 1.149$, $P = 0.3468$, Fig. 4.3B)

NMR brain had lower and more stable H_2O_2 emissions post-OGD treatments than mouse. Concomitant with O_2 consumption, H_2O_2 emissions were recorded using the AUR assay in the presence of horseradish peroxidase and SOD during the three SUIT protocols (Fig. 4.4A-F). H_2O_2 emission in all conditions was similar during leak respiration driven by glutamate or pyruvate (Fig. 4.4A&B, 5.4D&E), while the overall values were slightly higher in mice than NMRs, under both normoxic and ischemic conditions. Conversely, glutamate induced significant increases in H_2O_2 emission following 30 min OGD and OGD/reperfusion, and in the presence of ADP in NMRs ($F_{3,112} = 26.58$, $P < 0.0001$, Fig. 4.4A; $F_{3,84} = 32.48$, $P < 0.0001$, Fig. 4.4B). This change was not observed in mice (Fig. 4.4D&E). Succinate-driven leak respiration was associated with higher H_2O_2 emission at rest than for other substrates, followed by significant reductions in H_2O_2 emission post-OGD and OGD/reperfusion treatments in both species ($F_{3,84} = 7.986$, $P < 0.0001$, Fig. 4.4C; $F_{3,84} = 61.95$, $P < 0.0001$, Fig. 4.4F), but with a greater magnitude of change in mice. Small but significant decreases of rotenone- and ADP-linked H_2O_2 emission were also observed in mice following 15 min OGD and OGD/reperfusion (Fig. 4.4F), while these changes were not observed in NMRs (Fig. 4.4C).

Next, we calculated the H_2O_2/O_2 flux ratio to evaluate the relative importance of H_2O_2 production in different respiratory states (Fig. 4.5A-F). Comparing with normoxic conditions, significant increases in the H_2O_2/O_2 ratio were observed for complex I-linked leak respiration in the 30 min OGD and OGD/reperfusion groups but were not observed for the OXPHOS state in NMRs ($F_{3,112} = 14.18$, $P < 0.0001$, Fig. 4.5A; $F_{3,112} = 7.852$, $P < 0.0001$, Fig. 4.5B). Conversely, H_2O_2/O_2 ratios were higher for both complex I-linked leak and OXPHOS respiration in mice following all ischemic conditions ($F_{3,112} = 111.6$, $P < 0.0001$, Fig. 4.5D; $F_{3,112} = 91.96$, $P < 0.0001$, Fig. 4.5E). Even though the trend of increasing H_2O_2/O_2 ratios for complex II-linked respiration was similar in both species post-ischemia, the magnitude was divergent (Fig. 5.5C & 5.5F).

To reveal the difference of magnitudes more clearly between NMRs and mice, we compared H_2O_2/O_2 ratios between species following each treatment (Fig. 4.6A & 5.6G). The absolute value of the H_2O_2/O_2 ratio for complex I-linked (glutamate/malate and pyruvate/malate) leak states were similar in both species (Fig. 4.6A & 5.6C). However, in the succinate-induced leak state, the H_2O_2/O_2 ratio was higher in NMRs than mice following all treatments ($F_{1,14} = 175.8$, $P < 0.0001$, Fig. 4.6E), and the higher H_2O_2/O_2 ratio was maintained in NMRs in the normoxic group when reverse electron flow was blocked by rotenone ($F_{1,14} = 2.290$, $P = 0.1525$, Fig. 4.6F). Following the addition of ADP, H_2O_2/O_2 ratios for complex II-linked OXPHOS were significantly higher in mice across all conditions ($F_{1,14} = 49.85$, $P < 0.0001$, Fig. 4.6G), and this phenomenon was also apparent for complex I-linked OXPHOS ($F_{1,14} = 88.05$, $P < 0.0001$, Fig. 4.6B; $F_{1,14} = 198.6$, $P < 0.0001$, Fig. 4.6D). Furthermore, as shown in Table 4.3, mean values of

$\Delta H_2O_2/O_2$ ratio (subtracted by the mean value of normoxic conditions) were relatively similar for succinate-induced leak, but values of the $\Delta H_2O_2/O_2$ ratio were all approximately doubled in mice relative to NMRs for complex I- and II- linked OXPHOS and complex I-linked leak states.

Substrate and electron transportation pathway preferences vary between NMR and mouse brain. Pathway control of mitochondrial function was analysed following 15 min normoxia and via normalization to complex I-II linked OXPHOS capacity (Fig. 4.7A), and complex IV activity (Fig. 4.7B). First, we found that pyruvate/malate induced a greater proportion of leak respiration in mice than NMRs, and than glutamate/malate respiration in mice ($F_{3,28} = 7.806$, $P = 0.0006$, Fig. 4.7A). Secondly, complex I-linked OXPHOS capacity was higher with glutamate/malate than pyruvate/malate in NMRs, but this relationship was reversed in mice (Fig. 4.7A). Third, the complex I pathway contributed over 82% to the total complex I-II OXPHOS capacity in NMRs, but <60% in mice (Fig. 4.7A). Similarly, this trend was also observed when complex I-II OXPHOS capacity was normalized to complex IV activity, such that there is a relatively higher ratio of complex I-II to complex IV in NMRs relative to mice ($F_{1,84} = 83.15$, $P = 0.0006$, Fig. 4.7B). Finally, the phosphorylation system control ratio of complex I-II was evaluated by examining the OXPHOS to ETC capacity ratio (1-P/E) between species. This value was ~10% in mice and ~20% in NMRs ($F_{1,14} = 5.86$, $P = 0.0326$, Fig. 4.7C).

4.4 Figures and tables

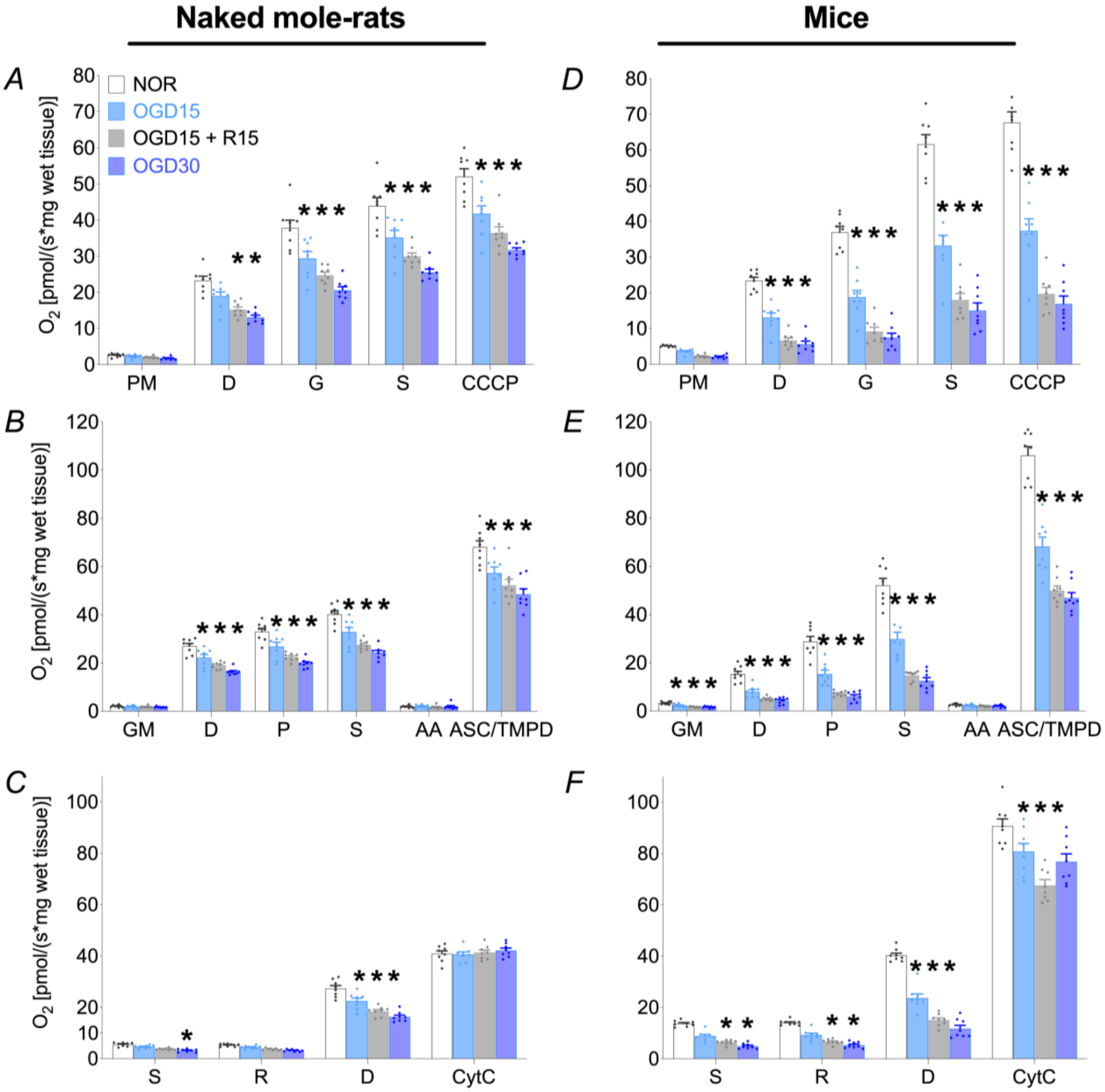

Figure 4.1 O_2 consumption of permeabilized cortical brain tissue.

Summaries of **(A, D)** pyruvate-stimulated respiration, **(B, E)** glutamate-stimulated respiration, and **(C, F)** succinate-stimulated respiration. Data are presented as means ± SEM from $n = 8$ each. Significant differences (*, $P < 0.05$ *vs*. normoxia) were determined by two-way ANOVAs followed by Dunnett's multiple comparisons test. Abbreviations: NOR, Normoxia; OGD15, oxygen glucose deprivation 15 mins; R15, reoxygenation 15 mins; OGD30, oxygen glucose deprivation 30 mins; P, pyruvate; M, malate; G, glutamate; S, succinate; D, ADP; R, rotenone; ASC, ascorbate; TMPD, N,N,N′,N′-Tetramethyl-p-phenylenediamine; CCCP, carbonyl cyanide m-chlorophenyl hydrazine; AA, antimycin A; CytC, Cytochrome c.

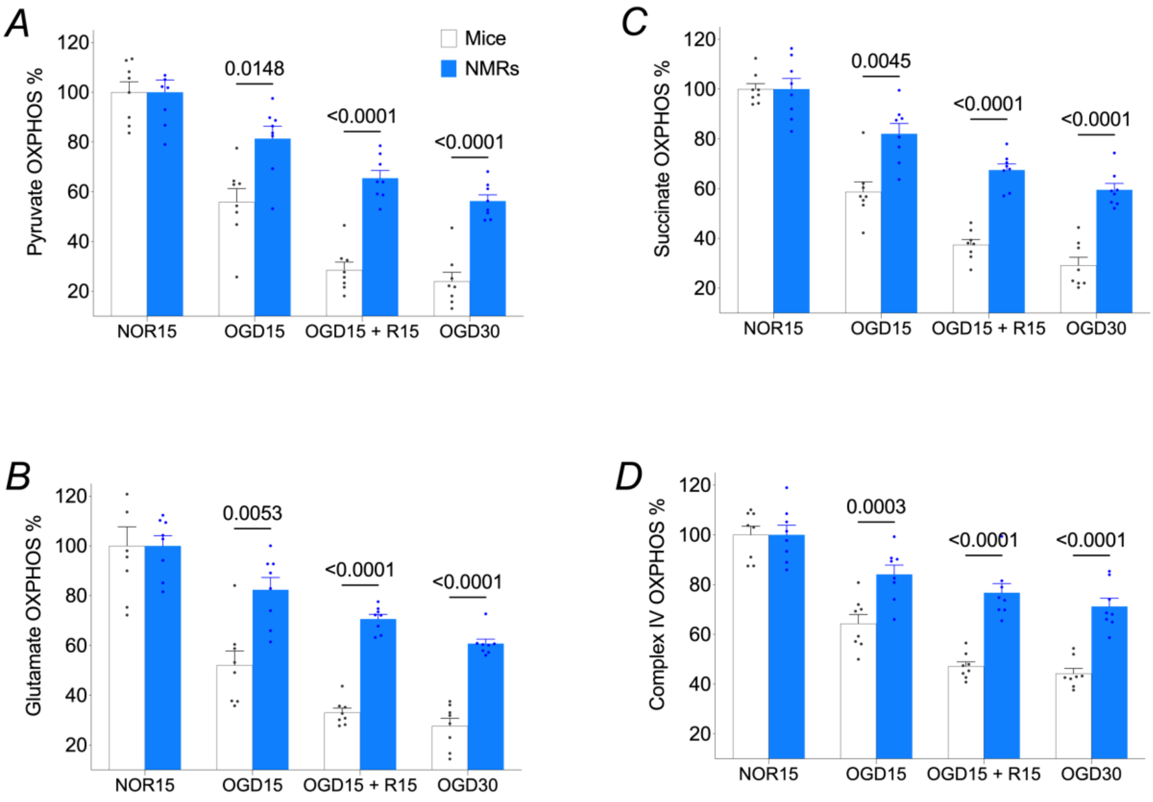

Figure 4.2 O_2 consumption at OXPHOS state of permeabilized cortical brain tissue normalized to normoxia.

Summaries of **(A)** pyruvate OXPHOS capacity, **(B)** glutamate OXPHOS capacity, **(C)** succinate OXPHOS capacity, and **(D)** complex IV activity. Data are presented as means ± SEM from $n = 8$ each. Significant differences ($P < 0.05$ *vs*. normoxia) were determined using two-way ANOVAs followed by Sidak's multiple comparisons test. Abbreviations: NOR15, Normoxia 15 mis; OGD15, oxygen glucose deprivation 15 mins; R15, reoxygenation 15 mins; OGD30, oxygen glucose deprivation 30 mins.

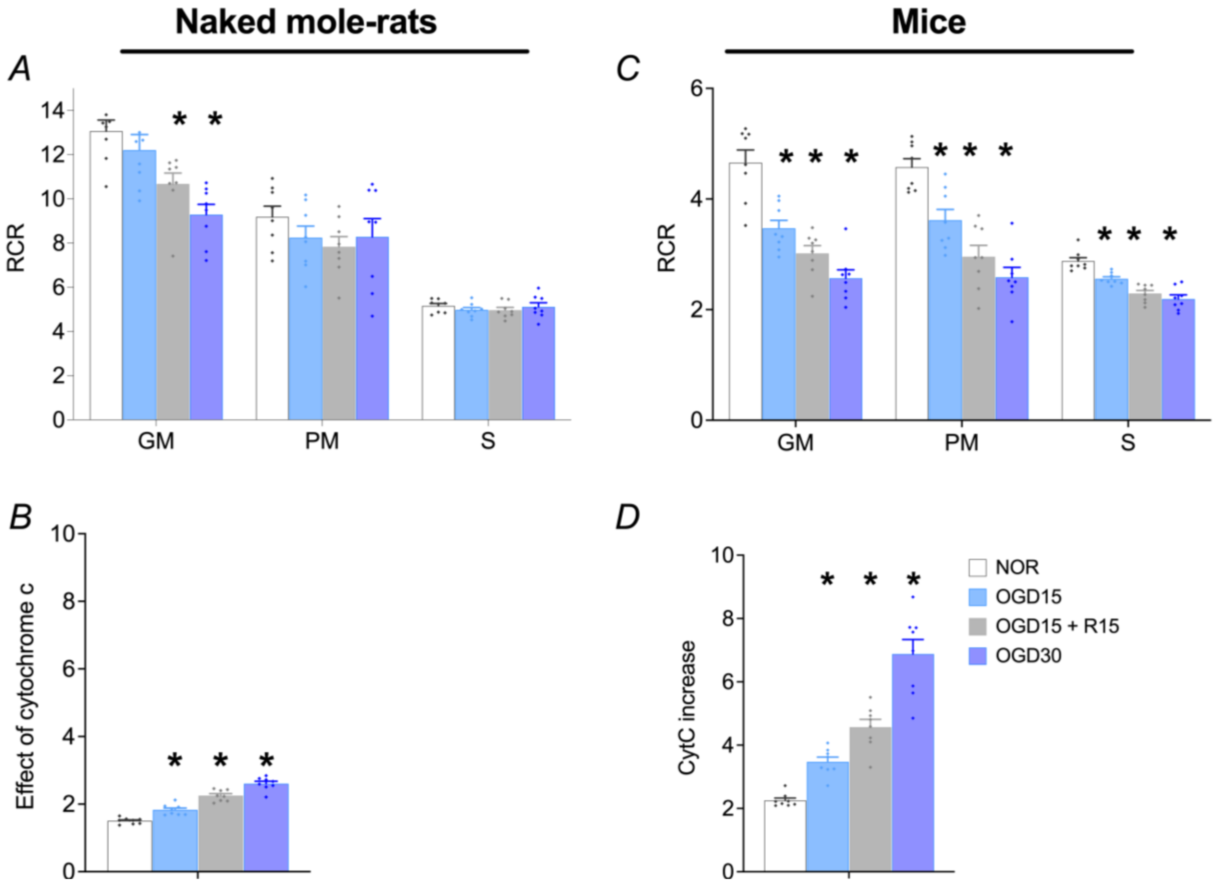

Figure 4.3 RCRs and effect of cytochrome c on permeabilized cortical brain tissue.

Summaries of **(A, C)** RCRs, and **(B, D) the** effect of cytochrome c addition. Data are presented as means ± SEM from *n* = 8 each. Significant differences (*, $P < 0.05$ *vs*. normoxia) were determined using two-way (A, C) and one-way (B, D) ANOVAs followed by Dunnett's multiple comparisons test. Abbreviations: NOR, Normoxia; OGD15, oxygen glucose deprivation 15 mins; R15, reoxygenation 15 mins; OGD30, oxygen glucose deprivation 30 mins.

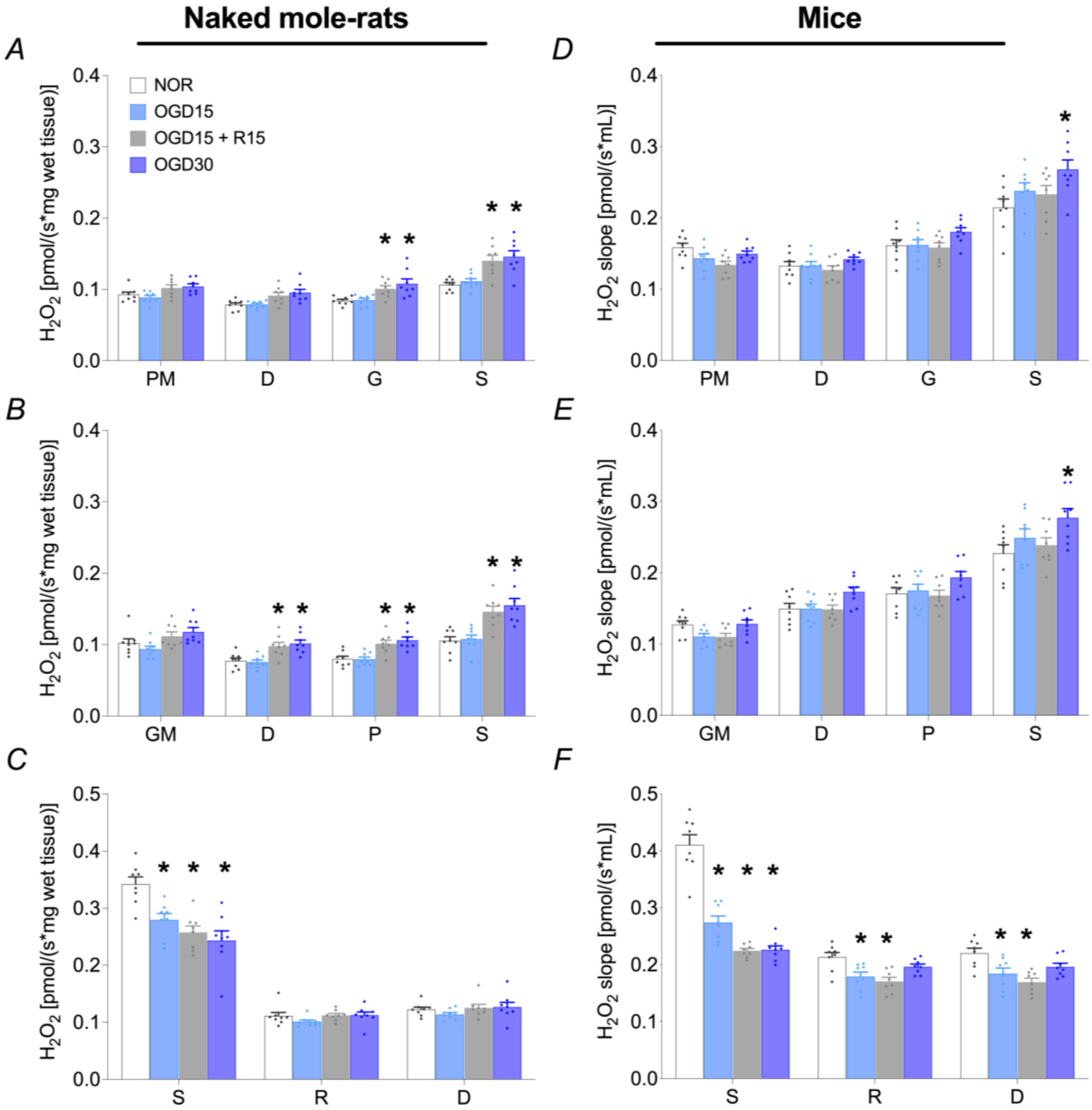

Figure 4.4 H_2O_2 efflux of permeabilized cortical brain tissue.

Summaries of **(A, D)** pyruvate-stimulated respiration, **(B, E)** glutamate-stimulated respiration, and **(C, F)** succinate-stimulated respiration. Data are presented as means ± SEM from *n* = 8 each. Significant differences (*, $P < 0.05$ *vs.* normoxia) were determined by two-way ANOVAs followed by Dunnett's multiple comparisons test. Abbreviations: NOR, Normoxia; OGD15, oxygen glucose deprivation 15 mins; R15, reoxygenation 15 mins; OGD30, oxygen glucose deprivation 30 mins; P, pyruvate; M, malate; G, glutamate; S, succinate; D, ADP; R, rotenone.

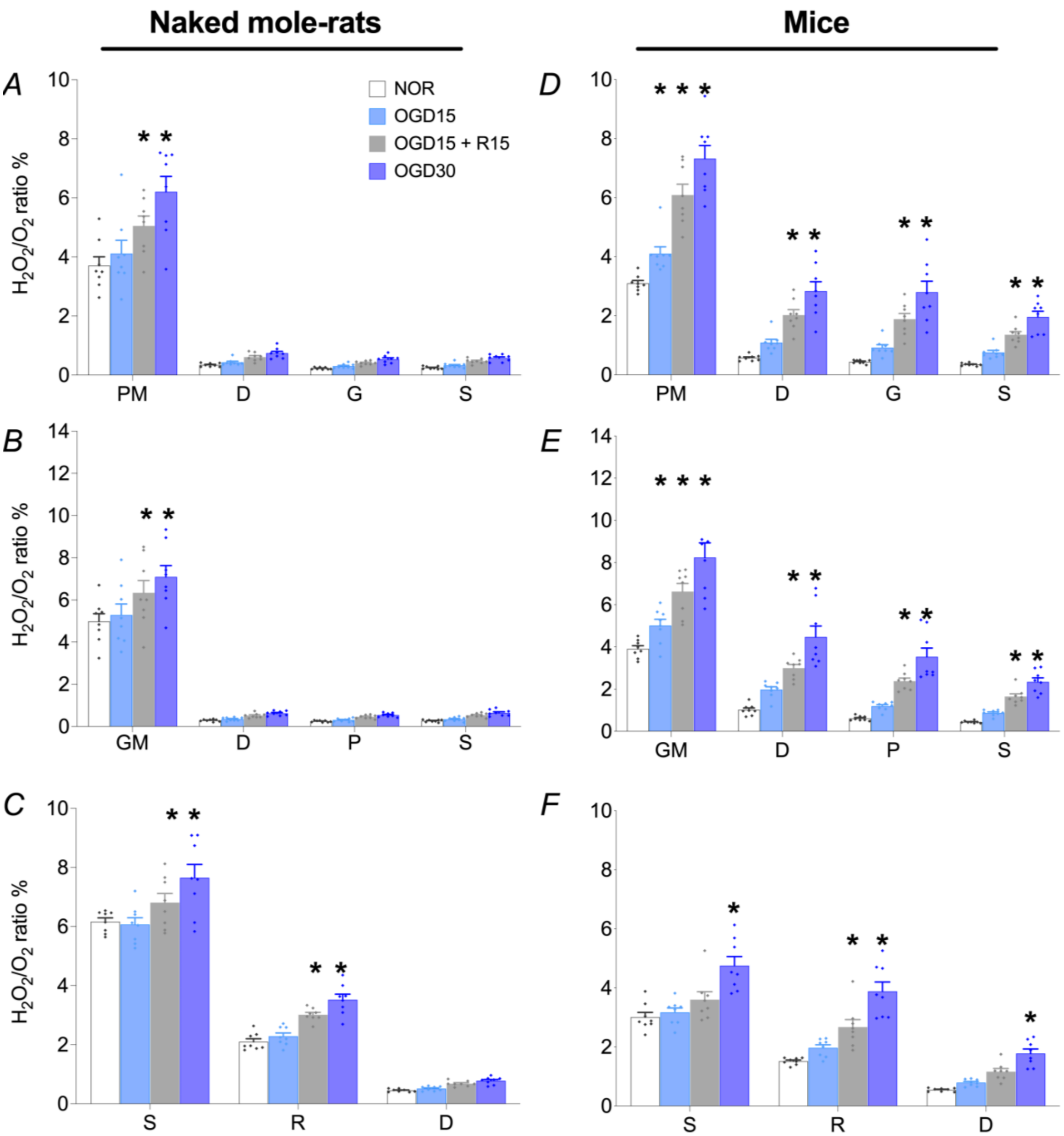

Figure 4.5 H_2O_2/O_2 ratio of permeabilized cortical brain tissue.

Summaries of **(A, D)** pyruvate stimulated respiration, **(B, E)** glutamate stimulated respiration, and **(C, F)** succinate stimulated respiration. Data are presented as means ± SEM from $n = 8$ each. Significant differences (*, $P < 0.05$ *vs*. normoxia) were determined by two-way ANOVAs followed by Dunnett's multiple comparisons test. Abbreviations: NOR, Normoxia; OGD15, oxygen glucose deprivation 15 mins; R15, reoxygenation 15 mins; OGD30, oxygen glucose deprivation 30 mins; P, pyruvate; M, malate; G, glutamate; S, succinate; D, ADP; R, rotenone.

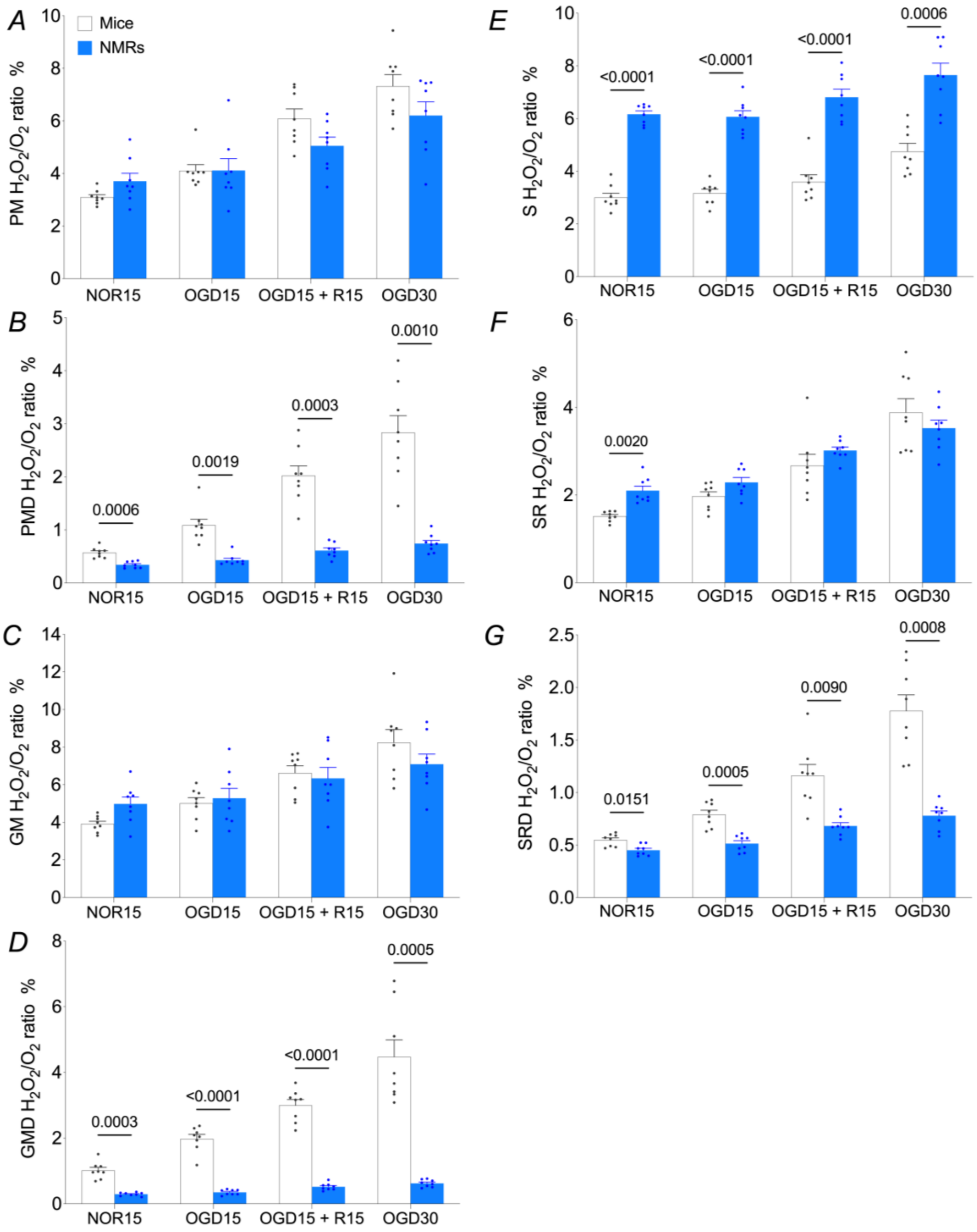

Figure 4.6 H_2O_2/O_2 ratio of permeabilized cortical brain tissue.

Summaries of **(A)** leak state with pyruvate, **(B)** OXPHOS state with pyruvate, **(C)** leak state with glutamate, **(D)** OXPHOS state with glutamate, **(E)** leak state with succinate, **(F)** leak state with succinate and rotenone, and **(G)** OXPHOS state with succinate and rotenone. Data are presented as means ± SEM from *n* = 8 each. Significant differences ($P < 0.05$ *vs*. normoxia) were determined using two-way ANOVAs followed by Sidak multiple comparisons test. Abbreviations: NOR, Normoxia; OGD15, oxygen glucose deprivation 15 mins; R15, reoxygenation 15 mins; OGD30, oxygen glucose deprivation 30 mins; P, pyruvate; M, malate; G, glutamate; S, succinate; D, ADP; R, rotenone.

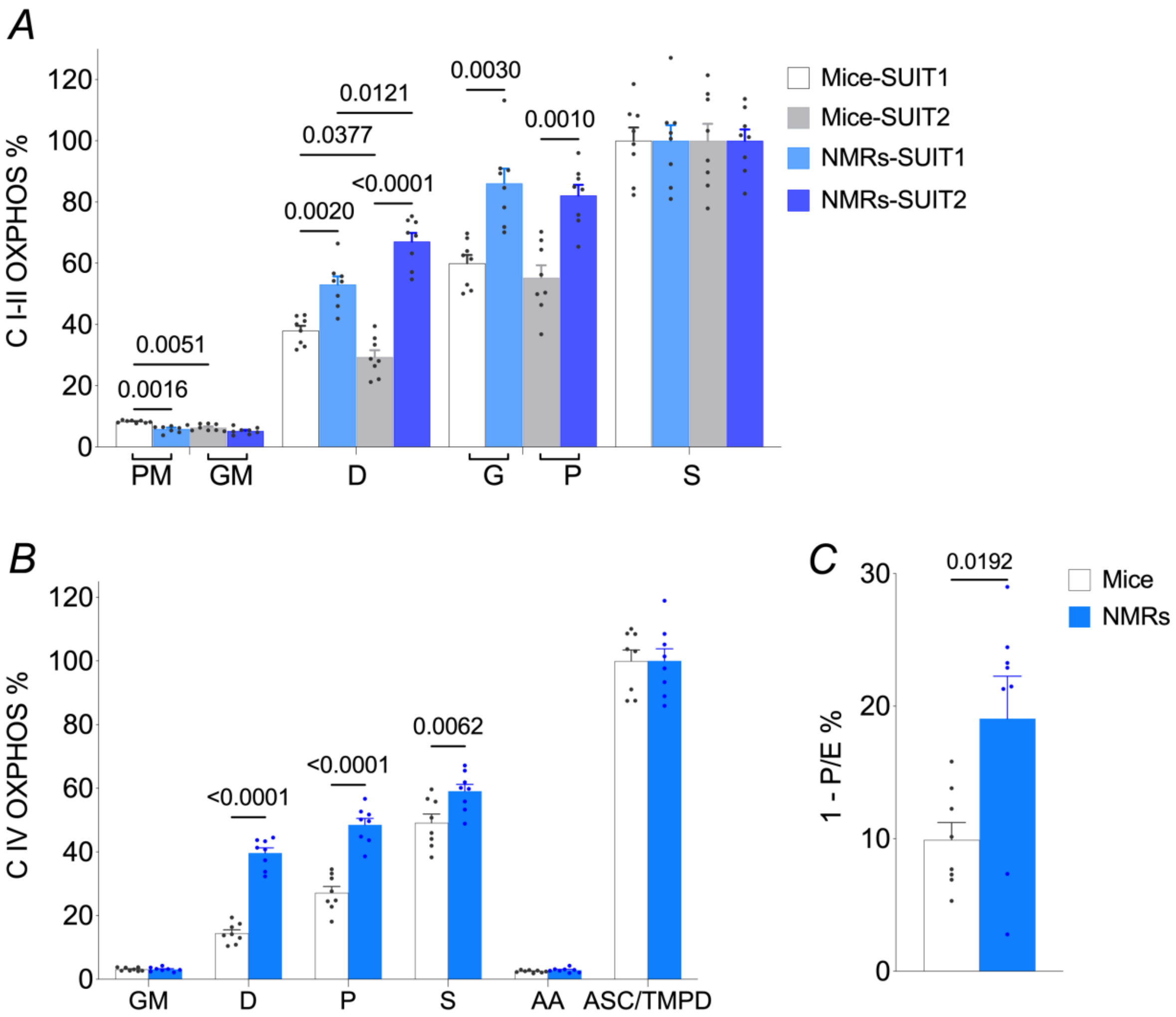

Figure 4.7 Cortical mitochondrial properties.

Summaries of **(A)** O_2 consumptions normalized to complex I-II OXPHOS capacity, **(B)** O_2 consumptions normalized to complex IV activity, and **(C)** phosphorylation system control ratio of complex I-II, (1-P/E%). Data are presented as means ± SEM from $n = 8$ each. Significant differences ($P < 0.05$ *vs*. normoxia) were determined using two-way ANOVAs followed by Tukey's multiple comparisons test (A), Sidak's multiple comparisons test (B), or t test with two-tailed calculations (C). Abbreviations: P, pyruvate; M, malate; G, glutamate; S, succinate; D, ADP; R, rotenone; AA, Antimycin A; ASC, ascorbate; TMPD, N,N,N′,N′-Tetramethyl-p-phenylenediamine.

Table 4.2 Raw values of permeabilized brain tissue respiratory functions

Species	Substrates	Leak		OXPHOS		RCR		Treatments
		mean	SEM	mean	SEM	mean	SEM	
NMRs	PM	2.59	0.18	23.33	3.28	9.18	1.39	NOR
		2.29	0.18	18.98	3.25	8.24	1.48	OGD15
		2.06	0.10	15.27	2.05	7.83	1.32	OGD15 + R15
		1.76	0.15	13.12	1.66	8.28	2.33	OGD30
	GM	2.11	0.16	27.00	3.17	13.06	1.44	NOR
		1.88	0.18	22.25	3.76	12.20	2.00	OGD15
		1.83	0.14	19.08	1.39	10.67	1.40	OGD15 + R15
		1.69	0.09	16.40	1.39	9.28	1.31	OGD30
	SR	5.31	0.20	68.12	7.42	5.15	0.29	NOR
		4.49	0.22	57.30	7.19	4.97	0.31	OGD15
		3.73	0.13	52.25	7.17	4.96	0.36	OGD15 + R15
		3.21	0.14	48.51	6.36	5.11	0.52	OGD30
Mice	PM	5.11	0.09	23.41	2.80	4.57	0.43	NOR
		3.57	0.24	13.07	3.60	3.62	0.55	OGD15
		2.24	0.14	6.69	2.07	2.96	0.58	OGD15 + R15
		2.11	0.17	5.62	2.40	2.58	0.51	OGD30
	GM	3.29	0.20	15.32	1.18	4.66	0.65	NOR
		2.29	0.21	7.98	0.88	3.47	0.42	OGD15
		1.69	0.08	5.05	0.28	3.02	0.39	OGD15 + R15
		1.62	0.13	4.23	0.47	2.57	0.43	OGD30
	SR	14.06	0.37	40.31	0.89	2.88	0.18	NOR
		8.84	0.66	23.66	1.62	2.56	0.10	OGD15
		6.39	0.33	15.09	0.85	2.29	0.16	OGD15 + R15
		4.91	0.39	11.76	1.30	2.19	0.21	OGD30

Data are presented as means ± SEM from *n* = 8 each, statistical analysis were indicated in Fig 4.1 & 4.3. Abbreviations: NOR, Normoxia; OGD15, oxygen glucose deprivation 15 mins; R15, reoxygenation 15 mins; OGD30, oxygen glucose deprivation 30 mins; P, pyruvate; M, malate; G, glutamate; S, succinate; D, ADP; R, rotenone; OXPHOS, oxidative phosphorylation; RCR, respiratory control ratio calculated as the ratio of OXPHOS /Leak.

Table 4.3 $\Delta H_2O_2/O_2$ ratios as a function of coupling and substrate post OGD conditions

Substrates	**Species**	**$\Delta H_2O_2/O_2$ ratio (%)**		
		OGD30	**OGD15+R15**	**OGD15**
PM	NMRs	2.50 ± 0.52 *	1.34 ± 0.34 *	0.41 ± 0.45
	Mice	4.23 ± 0.44	3.00 ± 0.36	1.01 ± 0.23
PMD	NMRs	0.40 ± 0.06 *	0.27 ± 0.05 *	0.09 ± 0.04
	Mice	2.26 ± 0.32	1.45 ± 0.18	0.52 ± 0.11
GM	NMRs	2.11 ± 0.54 *	1.36 ± 0.58	0.30 ± 0.52
	Mice	4.33 ± 0.69	2.72 ± 0.38	1.11 ± 0.29
GMD	NMRs	0.33 ± 0.04 *	0.23 ± 0.04 *	0.06 ± 0.03 *
	Mice	3.46 ± 0.52	1.98 ± 0.17	0.96 ± 0.13
S	NMRs	1.49 ± 0.45	0.65 ± 0.31	-0.09 ± 0.23
	Mice	1.74 ± 0.31	0.60 ± 0.26	0.16 ± 0.15
SR	NMRs	1.43 ± 0.18 *	0.92 ± 0.08	0.19 ± 0.11
	Mice	2.37 ± 0.32	1.16 ± 0.25	0.45 ± 0.11
SRD	NMRs	0.33 ± 0.04 *	0.23 ± 0.03 *	0.06 ± 0.03
	Mice	1.23 ± 0.15	0.61 ± 0.11	0.24 ± 0.04

Data are presented as means ± SEM from $n = 8$ each. Significant differences (*, $p < 0.05$ *vs.* mice) were determined using two-way ANOVAs followed by a Sidak multiple comparisons test. Abbreviations: OGD15, oxygen glucose deprivation 15 mins; R15, reoxygenation 15 mins; OGD30, oxygen glucose deprivation 30 mins; P, pyruvate; M, malate; G, glutamate; S, succinate; D, ADP; R, rotenone.

4.5 Discussion

In this chapter we report defects in cortical mitochondrial respiratory function following ischemia and I/R stresses in both NMR and mouse brain tissue. However, our results indicate that mitochondrial respiration and H_2O_2 emissions are better maintained in NMRs than mice, which may contribute to the in vitro ischemia tolerance of NMR brain slices reported previously (Nathaniel et al., 2009). Our study has several salient findings. Specifically, relative to mice and following both ischemia or I/R challenges, NMR brain mitochondria (1) exhibit reduced functional deficits in O_2 consumption, (2) better maintain respiratory control and mitochondrial membrane integrity, and (3) retain stable rates of electron leakage. Finally, (4) these functional differences in cortical mitochondrial respiratory ischemia tolerance may be partially explained by species-level differences in mitochondrial pathway control.

Ischemia-induced deficits in mitochondrial respiration are mild in NMR cortical brain tissue compared with mice. Hypoxia-intolerant species, including humans and laboratory rodents, exhibit marked deficits of mitochondrial O_2 consumption and RCRs following ischemic challenges in the brain (Nakai et al., 1997; Rojas-Morales et al., 2019; Sims et al., 1986; Sims & Pulsinelli, 1987). These defects are apparent in both *ex vivo* and *in vivo* models following I/R stress. In our study, we report significant and robust reductions in OXPHOS capacity in mouse brain (Figs 5.1 & 5.2), which agree well with these previous reports. Conversely, we report dramatically different performances of NMR cortical brain mitochondria following *in vitro* ischemic treatments. Specifically, the degree to which OXPHOS capacity is supressed in NMR brains is markedly less than in mice exposed to the same periods of OGD, and the changes in NMR brain mitochondrial function following 15 min OGD (~15–19% reduction of complexes I, II and IV function, Fig. 4.2) are sufficiently small to potentially be biologically insignificant. In addition, the relatively stable RCRs following ischemia in NMRs (Fig. 4.3A) suggest that NMR brain mitochondria are minimally damaged by ischemic stress in our experiments. Finally, cytochrome c had a significantly greater effect in mice cortical brain mitochondria (Fig. 4.3D), which is likely an indicator not only of OMM but also IMM damage following ischemia. Importantly, others have directly correlated this cytochrome c response to the degree of membrane damage using LDH leakage assays in Sprague Dawley rat brain (Bhowmick & Drew, 2017; Fernandez-Lopez et al., 2005). Thus, in NMRs, a stable cytochrome c-induced O_2 consumption response across treatment groups indicates that the IMM integrity is well-maintained, whereas the decreased capacity of complex II-linked OXPHOS might be due to slight damage to the OMM (Fig. 4.1C).

As discussed in the Introduction, previous studies suggest that NMR brain slices resist cell death when exposed to OGD *ex vitro* (Nathaniel et al., 2009), and have lower Ca^{2+} influx during hypoxia (Peterson et al., 2012a), which possibly due to enhanced Ca^{2+} buffering (Chapter 3), tolerance of acidity, and maintain evoked neuronal electrical responsiveness following anoxia/hypoxia (Larson & Park, 2009). All of these capabilities require the maintenance of cellular ion homeostasis, which is directly supported by mitochondrial respiration (Persson et al., 2016; Rizzuto et al., 2012). Our results suggest that mitochondrial respiratory function is better maintained in NMR brain after *in vitro* ischemia and I/R stresses than mouse, which likely helps NMR brain resist deleterious impacts of ischemia that may otherwise be initiated through mitochondrial dysfunction. This tolerance likely postpones and/or prevents energy failure, maintains cellular ion homeostasis, and minimizes glutamate-induced excitotoxicity and free radical-mediated damage (Yang et al., 2018).

Stable electron leakage management post-OGD in NMRs. As the major initial form of cellular ROS, $O_2^{\cdot -}$ is produced when electrons 'leak' out of the ETC and combine with O_2 to form an unstable anion radical. Studies have demonstrated that free radicals play an important role in the pathogenesis of ischemia, particularly O_2•-, which interacts with NO to form peroxynitrite (Cazevielle et al., 1993). $O_2^{\cdot -}$ also directly causes tissue damage by promoting hydroxyl radical formation through H_2O_2 (Arteaga et al., 2017).

We measured the rate of H_2O_2 emission as a representation of the net production of $O_2^{\cdot -}$ in brain tissue. Comparing with normoxic conditions, mice (Fig. 4.4F, ~0.19 pmol/(s*mg wet tissue)) have a larger reduction in the rate of succinate-induced H_2O_2 emission than NMRs (Fig. 4.4C, ~0.10 pmol/(s*mg wet tissue)) following 30 min ischemia, potentially due to structural damage to the mitochondrial respiration system (see above). Interestingly, we report that glutamate induces higher H_2O_2 emission following ischemia in NMRs (Fig. 4.4A&B) but not in mice (Fig. 4.4D&E). Glutamate dehydrogenase, which is a hexameric enzyme that is localized to the mitochondrial matrix (Aoki et al., 1987; Rothe et al., 1995), is an important site of electron leakage from the ETC, and catalyses the reversible conversion of glutamate to α-ketoglutarate and ammonia while reducing $NAD(P)^+$ to NAD(P)H (Wong et al., 2017). These results are consistent with our findings in Chapter 3, in which we report a significant reduction of glutamate and increased ratio of $NADPH/NAD^+$ in hypoxic NMR brain but not hypoxic mouse brain. The increase in H_2O_2 emission, as well as the reduction in the glutamate linked RCR, may reflect defects in mitochondrial respiration related to the GDH pathway in NMR brain (see below). Another unclear but interesting difference is significantly higher H_2O_2 emission with complex I-II fuelled respiration in NMRs following 30 min OGD and OGD/reperfusion; Fig. 4.4A&B), which is only observed in mice following 30 min OGD (Fig. 4.4D&E). In addition, cellular ROS was well maintained in brain slices under *in vitro* hypoxia and ischemia (Eaton et al., 2022). Generally, those results suggest that NMR brain have better mitochondria-related ROS management than mouse under *in vitro* hypoxia/ischemia.

To better understand the degree of electron leak between species during mitochondrial respiration, we compared H_2O_2/O_2 ratios between NMRs and mice among all substrates and conditions (Figs 5.5A-F & 5.6A-G). Based on this comparison, we suggest that NMR brain mitochondrial electron transportation function is better maintained than in mouse brain, because there is: (i) a significant increase in the H_2O_2/O_2 ratio following 15 min OGD relative to normoxia for complex I-linked leak respiration in mice (Fig. 4.5D&E) but not in NMRs (Fig. 4.5A&B), (ii) significantly higher H_2O_2/O_2 ratios in complex I-fuelled OXPHOS states in mice following 30 min OGD and OGD/reperfusion treatments (Fig. 4.5D&E), which is also not apparent in NMR brain (Fig. 4.5A&B), and (iii) a higher H_2O_2/O_2 ratio in NMRs than mice with succinate-linked leak respiration (Fig. 4.6E), which is reversed in the complex II-linked OXPHOS state (Fig. 4.6G). The relatively stable H_2O_2 emission rate and corresponding reduction of O_2 consumption may directly lead to these changes. Also, the relatively lower complex I capacity (Fig. 4.7A) in mice could partially explain the higher H_2O_2/O_2 ratio in NMRs relative to mice with succinate-linked leak respiration (Fig. 4.6E), as this reverse electron flow-induced H_2O_2 production is suppressed by the complex I inhibitor rotenone (Fig. 4.4C, 5.4F), and also by mitochondria-targeted S-nitrosothiol (MitoSNO) (Kim et al., 2018). On the other hand, complex II may be a potential regulator of ROS homeostasis in NMR brain, as we have previously found similar acute regulation of this enzyme by hypoxia in NMR skeletal muscle (Cheng et al., 2021a).

Alternatively, differences in scavenging capacity for $O_2^{\cdot -}$ between species may play a role. Previous studies report increased oxidative stress post-OGD in Albino Wistar rats (Almeida et al., 2002), as well as significantly decreased SOD and glutathione peroxidase activity compared with control subjects in human clinical trials (Demirkaya et al., 2001). In addition, genetically enhancing the mitochondrial thioredoxin system can beneficially reduce ROS level in rat hippocampus during OGD treatment (Yin et al., 2017). Notably, we have recently reported that NMR skeletal muscle and heart mitochondria have more robust and rapid $O_2^{\cdot -}$ scavenging systems than mice (Munro et al., 2019), and NMR brain may have similarly enhanced scavenging capabilities. Indeed, we reported enhanced antioxidant responses in NMR brain following acute *in vivo* hypoxia (Hadj-Moussa et al., 2022). Such an adaptation may explain the lower H_2O_2/O_2 ratios in the OXPHOS state in NMRs than mice (Fig. 4.6B, D&G), and the 2-fold increase in $\Delta H_2O_2/O_2$ ratios in mice relative to NMRs (Table 5.1).

Mitochondrial properties may contribute to divergent ischemia tolerance between NMR and mouse brain mitochondria. The contribution of leak respiration to complex I-II respiration capacity is significantly higher with pyruvate than glutamate in mice, and then either pyruvate or glutamate in NMRs (Fig. 4.7A). Correspondingly at the mitochondrial level, mice utilize a higher proportion of OXPHOS respiration with pyruvate than glutamate, whereas NMRs prefer to metabolize glutamate than pyruvate (Fig. 4.7A). It is possible that NMRs have an enhanced capacity to metabolize glutamate relative to mouse brain, which was reported through metabolomics study in Chapter 3. For example, NMR brains may express more GDH molecules per cell, or these enzymes may be more sensitive to catalytic modification by the various binding partners of GDH (e.g., ADP, ATP, GTP, etc.). Thus, differences in GDH expression/function and/or glutamate homeostasis may explain our observation of significant RCR reductions with glutamate but not pyruvate in NMR brain (Fig. 4.3A).

Alternatively, and given their critical function in regulating glutamate cycling and uptake (Sofroniew & Vinters, 2010), differences in astrocytic function between species may also explain this difference. The increase in H_2O_2 production under OGD conditions (Fig. 4.4A&B) may reflect increased OXPHOS throughput (if the ROS are produced as a natural biproduct of increased respiration) or cell/organelle damage. A potential explanation may be damage and/or remodulation of glutamate homeostasis through GDH, glutathione, etc. during OGD, which could be a deleterious consequence of ischemia, or an actively regulated neuroprotective adaptation. Regardless of the underlying mechanism, an increased ability to consume or remove glutamate may play a neuroprotective role in NMR brain. Glutamate plays important roles in bridging carbohydrate and amino acid metabolism via the tricarboxylic acid (TCA) cycle by GDH (Schousboe et al., 2014), and the amount of glutamate being oxidized through the TCA cycle increases dramatically when extracellular glutamate concentrations increase to 0.5 mM (McKenna et al., 1996). Importantly, extracellular glutamate is elevated moments after the onset of ischemia in a hypoxia-intolerant brain (Mitani & Tanaka, 2003), and this increase triggers excitotoxic cell death of neurons (Choi & Rothman, 1990). Therefore, an elevated capacity to metabolize and/or clear glutamate might support glutamate homeostasis and help avoid glutamate-mediated ecotoxicity in NMR neurons during periods of severe hypoxia or ischemia.

Finally, the contribution of complex I-linked O_2 consumption for either complex I-II capacity or complex IV activity is less in mice than in NMRs, and mice have lower coupling efficiency. These differences may be due to divergent expression of mitochondrial metabolic enzymes and proteins, such as ETC complexes, UCPs, etc. In support of this, similar patterns have been reported in Sprague Dawley rat and mouse brain between different age groups. For example, lower coupling efficiency and complex I activity are observed in older animals compared with young adults, accompanied by differences in mitochondrial protein density (Crescenzo et al., 2019; Hagl et al., 2016). Additionally, differences in respiratory complex assemblies and changes in these assemblies following ischemia may impact mitochondrial respiration and explain differences between species (Greggio et al., 2017; Lapuente-Brun et al., 2013; Lopez-Fabuel et al., 2016). Differences in these mitochondrial properties could be involved in the intrinsic tolerance of hypoxia and I/R in NMR brain.

Limitations. Ischemic stroke is a complex pathology which includes not only cell death in the ischemic core, but also in the clinically rescuable penumbral region (Baron, 2018; Ramos-Cabrer et al., 2011). Acute brain slices treated with OGD are a reasonable *in vitro* mimic model for studying ischemic core stress; however, this is not a good representation of the entirety of an ischemic challenge (Buskila et al., 2014; Kekesi & Buskila, 2020), in our study we saw a greater cytochrome c response in NMRs, which indicates outer mitochondrial membrane damage. Utilizing an organotypic brain slice culture could extend the duration of ischemia treatment to more realistically evaluate cell viability, to evaluate drug applications, and permit transgenic manipulations (Croft et al., 2019; Humpel, 2015), which would provide insight into more precise targets to assess adaptations that preserve mitochondrial function in ischemia.

Conclusions. In the present study, we comprehensively evaluate NMR brain mitochondrial function and integrity following a clinically relevant ischemic stress for the first time. We demonstrate that *in vitro* OGD impairs NMR brain mitochondrial function but that deficits are minor relative to those in similarly treated mouse brain. Specifically, and relative to mouse brain, NMR brain mitochondria better retain respiration capacity, have lower H_2O_2 emission rates and stable RCRs, and better maintain membrane integrity. These results are consistent with the findings of the previous chapter, in which we demonstrate that NMR brain mitochondria tolerate greater Ca^{2+} stress and better maintain OXPHOS capacity and redox homeostasis than mouse brain mitochondria.

Taken together, our results suggest that NMRs have more ‘robust’ brain mitochondria, which are relatively tolerant of hypoxia/ischemia, and may thus contribute to the overall hypoxia/ischemia tolerance of NMR brain. Of course, it is important to note that the conclusions that may be drawn from our results are limited by our use of a two-species comparison, which carries with it the risk of significant error, e.g. differences in their genetics, physiology, etc. (Garland & Adolph, 1994). For this reason, replication of our study in brain from other hypoxia-tolerant species, and particularly species closely related to NMRs, would be useful additions to the literature. Advancing our knowledge in this area may provide insight into novel, evolutionarily derived mechanisms of neuroprotection in a rare hypoxia-tolerant mammal, which may be translated to the brains of hypoxia-intolerant mammals and inform treatment of clinically relevant ischemic pathologies.

5 NMR skeletal muscle mitochondria are minimally responsive to hypoxia

This chapter includes material from the following article:

Cheng, H., Munro, D., Huynh, K., & Pamenter, M. E. (2021). Naked mole-rat skeletal muscle mitochondria exhibit minimal functional plasticity in acute or chronic hypoxia. *Comparative biochemistry and physiology. Part B, Biochemistry & molecular biology*, *255*, 110596. https://doi.org/10.1016/j.cbpb.2021.110596

Matthew Pamenter, Daniel Munro, and I wrote the manuscript; Daniel Munro conducted 50% of the normoxic experiments, Kenny Huynh conducted 25% of the hypoxic NMR muscle mitochondrial O_2 consumption measurements.

Marks de Chabris, N. C., Sabir, S., Perkins, G., Cheng, H., Ellisman, M. H., & Pamenter, M. E. (2022). Short communication: Acute hypoxia does not alter mitochondrial abundance in naked mole-rats. *Comparative biochemistry and physiology. Part A, Molecular & integrative physiology*, *276*, 111343. https://doi.org/10.1016/j.cbpa.2022.111343

UROP student Soulene Sabir (under my supervision) and I conducted the CS activity measurements in muscle.

Honours BSc thesis student Nathalie Marks de Chabris (under my supervision) and I conducted the mitochondrial DNA quantification in muscle.

Guy Perkins and Mark Ellisman imaged and analyzed electron microscope data at National Center for Microscopy and Imaging Research, UC San Diego from animals that I treated, perfused, and dissected.

I conducted all other experiments.

5.1 Introduction

Muscle is around 30% of total body mass in rodents, and during exercise O_2 uptake in mouse muscle can increase around four times relative to a resting state (Hoydal et al., 2007). However, the mean O_2 tension in the muscle decreases by around 90% at exercising intensities above 50% of maximal O_2 uptake (Clark & Coburn, 1975). In addition, exercise-induced local hypoxia changes redox state and results in the accumulation of lactate in skeletal muscle, which can result in oxidative damage and lactic acidosis (Sahlin et al., 1987).

There are numerous examples of plasticity (*i.e.*, an ability to change the phenotype in response to a challenge) in mitochondrial expression, function, and signalling following acclimation to low O_2 in various muscle tissues among hypoxia-tolerant species. For example, reductions in complex V activity following long-term anoxia have been reported in heart muscle from *T. scripta* (Galli et al., 2013), and skeletal muscle from the anoxia-tolerant frog (*Rana temporalis*), where this adaptation was first described in a seminal study (St-Pierre et al., 2000). High-altitude populations of deer mice acclimated to hypoxia for 6-10 weeks, skeletal muscle mitochondria exhibited reduced flux through complex IV of the ETC, higher RCRs, and reduced H_2O_2 generation (Mahalingam et al., 2017), suggesting that adaptation to these pathways may confer protection against low O_2 challenges in mammals as well.

NMRs reduce their physical activity but continue to explore their environment in hypoxia (Ilacqua et al., 2017; Pamenter et al., 2019a), and thus NMRs change their physical behaviour to adapt to hypoxia (Houlahan et al., 2018; Kirby et al., 2018). However, there is no significant elevation of oxidative damage in hypoxic skeletal muscle (Hadj-Moussa et al., 2022). Together, these studies indicate the possibility that NMR skeletal muscle mitochondrial respiratory function and ROS management may be well maintained during hypoxia. Thus, further investigation in to whether muscle mitochondrial respiration changes in hypoxia is important to understanding the hypoxia-tolerance in NMRs.

Based on previous studies, **we hypothesized that**, NMR skeletal muscle mitochondria maintain respiration capacity to support the maintenance of physical activity in hypoxia. **We predicted that** NMR skeletal mitochondria would exhibit minimal reductions in O_2 consumption capacity, but that $O_2^{\cdot -}$ management would be altered prevent oxidative damage in hypoxia and followed reoxygenation. Furthermore, it may be an innate property of life in long-term intermittent hypoxia that NMR skeletal mitochondria can maintain relatively steady respiration capacity in skeletal muscle during even chronic hypoxia.

5.2 Methods

5.2.1 Ethics approval

NMRs were group-housed in interconnected multi-cage systems at 30°C and 21% O_2 in 50% humidity with a 12L:12D light cycle. Animals were fed fresh tubers, vegetables, and fruit, and Pronutro cereal supplement *ad libitum*. CD-1 mice were obtained from Charles River and were housed at room temperature under a 12L:12D light cycle and fed rodent chow *ad libitum*. Animals were not fasted prior to experimental trials. All experimental procedures were approved by the University of Ottawa Animal Care Committee in accordance with the Animals for Research Act and by the Canadian Council on Animal Care. Non-breeding (subordinate) naked mole-rats do not undergo sexual development or express sexual hormones and thus we did not take sex into consideration when evaluating our results (Holmes et al., 2009).

5.2.2 In vivo acute hypoxia treatments

Subordinate NMRs (adult, 1-2 years old) were exposed to one of four treatment conditions: normoxia (21% O_2, balance N_2), acute hypoxia (4 h 7% O_2, balance N_2), or chronic hypoxia (4-6 weeks in 11% O_2, balance N_2). Animals were not provided with food during the acute hypoxic treatment periods and were provided food once per day during chronic hypoxia.

5.2.3 Skeletal mitochondrial isolation

Whole experiment was performance at 4°C or on ice. Isolated mitochondria were used immediately for assessment of respiration, and aliquots were frozen at −80°C for subsequent assays.

Skeletal muscles were rapidly dissected on ice and mitochondria were isolated by differential centrifugation as described (Affourtit et al., 2012). Briefly, hind leg, pectoral and dorsal skeletal muscle (~2 g) was minced using single-edged razor blades, and then digested in Chappell-Perry buffer containing 250 units/100 mL Protease Type VIII. Mitochondria were isolated in supernatant through 500 g centrifuge for 10 min, and then collected through spinning at 10,000 centrifuges for 10 min. The mitochondrial pellet was washed using Chappell-Perry buffer without Protease Type VIII and collected at 10,000 centrifuges for 10 min. The mitochondria were then resuspended in 200 µl Chappell-Perry buffer without Protease Type VIII.

5.2.4 Mitochondrial respiration and H_2O_2 emission of brain homogenates

Rates of O_2 consumption and H_2O_2 emission were monitored simultaneously using an Oroboros O2k (Oroboros, Innsbruck, Austria) equipped with a fluorescence detection module mounted with the appropriate excitation and emission filters for the fluorescent probe Amplex UltraRed (AUR), as described previously (Cheng, Munro, et al., 2021). Briefly, AUR (10 µM), SOD (10 IU/ml), and horseradish peroxidase (2 IU/ml) were added to 2 ml respiration medium containing (in mM): KCl 120, HEPES 20, KH_2PO_4 20, $MgCl_2$ 2.5, EGTA 1, and BSA 0.045; pH 7.2, followed by isolated mitochondria (~40 µg protein in each chamber), and held at 32°C. An O_2 range of 200 µM to 80 µM in the air-saturated medium was maintained during the whole measurement (Makrecka-Kuka et al., 2015).

Baseline values for O_2 consumption and H_2O_2 production were measured following addition of mitochondria to chambers without effectors. SUIT protocols were sequentially performed as indicated below.

SUIT1 evaluated mitochondrial respiration through the fatty acid oxidation pathway. The following components were added sequentially: Malate followed by palmitoylcarnitine to induce fatty acid-dependent leak respiration from complex I, ADP to induce OXPHOS, CCCP to induce acid-dependent electron transport.

SUIT2 evaluated mitochondrial respiration through the pyruvate dehydrogenase complex pathway and complex I–II maximal capacity. The following components were added sequentially: pyruvate/malate to induce carbohydrate-dependent leak respiration from complex I, ADP to induce OXPHOS, glutamate/succinate to induce maximal carbohydrate-dependent OXPHOS from complexes I&II, CCCP to induce maximal carbohydrate-dependent electron transport capacity from complexes I&II.

SUIT3 evaluated mitochondrial respiration through the succinate dehydrogenase complex pathway, and complex II maximal capacity. The following components were added sequentially: succinate to induce carbohydrate-dependent leak respiration from complex II, rotenone to block complex II, ADP to induce OXPHOS capacity, CCCP to induce maximal carbohydrate-dependent electron transport capacity from complex II.

SUIT4 evaluated mitochondrial ADP/O ratio, and complex IV maximal capacity. The following components were added sequentially: pyruvate/malate to induce carbohydrate-dependent leak respiration from complex I, ADP to induce OXPHOS and measure ADP/O ratio, ascorbate/TMPD to induce electron transport from complex-IV, CCCP to induce maximal electron transport from complexes I to IV.

Table 5.1 Substrates for mitochondrial SUIT protocols

Substrates	Abbreviation	Working concentration
Malate	M	2 mM
Pyruvate	P	5 mM
Succinate	S	10 mM
Palmitoylcarnitine	Pc	0.04 mM
Ascorbate	ASC	2 mM
TMPD	TMPD	0.5 mM
Cytochrome *c*	CytC	10 µM
ADP	D	1 mM for SUIT1-3, 200 µM for SUIT4
CCCP	U/CCCP	0.5 or1 µM steps to max responses
Antimycin A	AA	2.5 µM
Rotenone	R	0.5 µM

Saturating concentrations were determined in pilot experiments (data not shown). Preparation of all substrates were as per (Fontana-Ayoub et al., 2016).

In other experiments, rates of fluorescent product (resorufin) formation were converted to micromoles of H_2O_2 based on a three-point standard curve conducted with cortical brain tissue alone and by direct addition of 0.1 μM H_2O_2 twice to the chamber.

5.2.5 ADP/O ratio assay using Magnesium Green™

The ADP/O ratio was determined using both the traditional method (mentioned in 5.2.4, SUIT4), and a recently developed method which relies on the difference of affinity for Magnesium Green™ (MgGr) between ADP and ATP in a fluorometric method (Chinopoulos et al., 2014; Salin et al., 2016). The traditional method was performed using high-resolution respirometry (ADP 200 μM in SUIT protocol 2). In the fluorometric method, the difference in affinity (Kd) between ADP or ATP was measured by co-incubating mitochondria in 1.0 μM MgGr, followed by the ten 0.1 mM $MgCl_2$ titration steps. Once the fluorescence to $MgCl_2$ ratio was determine the same assay was continued by addition of 0.2 mM ADP/ATP titration in 25 steps to determine differences in their affinity to MgGr. The ADP/O ratio was first calibrated by injecting 10 additions of 0.2 mM $MgCl_2$, followed by 2 mM ADP, and lastly corrected by measuring mitochondrial rates residual oxidative phosphorylation and baseline fluorescence change after adding carboxylatractyloside (cATR) and rotenone. The effective ATP/O ratio for this fluorometric method was calculated as previously described (Chinopoulos et al., 2014; Salin et al., 2016), but modified to generate ATP hydrolyse (*J*ATP) and respiration (*J*O_2) values using the "Differentiate Tool" in OriginLab (Help Online - Origin Help – Differentiate (originlab.com)). Specifically, the average of the slopes between the point and its two closest neighbours was calculated as "Differentiate" for both ATP production rate (*J*ATP) and O_2 consumption rate (*J*O_2), separately. The ATP/O ratio was calculated using the equation, $ATP/O\ ratio = -JATPst3/(2 * JO2st3)$ (Salin et al., 2016).

5.2.6 TEM

Animals were anesthetized with Ketamine (200 mg/kg) + Xylazine (10 mg/kg) and then rapidly returned to their treatment condition until they had lost consciousness, to minimize reoxygenation of hypoxic animals. Animals were then perfusion-fixed *via* cardiac puncture using 2% formaldehyde and 2.5% glutaraldehyde. Following fixation, skeletal muscle was dissected and further fixed overnight at 4°C in 2.5% glutaraldehyde in 0.15 M sodium cacodylate buffer, pH 7.4, and washed three times with washing buffer. Samples were post-fixed with 1% aqueous OsO_4 + 1.5% aqueous potassium ferrocyanide for 2 h and washed three times with washing buffer. Specimens were dehydrated in a graded ethanol-dH_2O from 30, 50, 70, 80, 90 to 100% ethanol. The samples were infiltrated with a graded Epon-ethanol series (1:1, 3:1), embedded in 100% Epon and then polymerized in an oven at 60°C for 48 h. Ultra-thin sections (90–100 nm thick) were prepared from the polymerized blocks with a Diatome diamond knife using a Leica Microsystems EM UC7 ultramicrotome (Leica Biosystems, Buffalo Grove, IL, USA), transferred onto 200-mesh copper grids, and stained with 4% uranyl acetate for 6 min and Reynold's lead for 5 min. The TEM grids were imaged by a FEI Tecnai G^2 Spirit 120 kV TEM equipped with a Gatan Ultrascan 4000 CCD Camera Model 895. The proprietary Digital Micrograph 16-bit images (DM3) were converted to unsigned 8-bit TIFF images, which were analyzed to measure mitochondrial volume density.

5.2.7 Na^+/K^+-ATPase activity measurement

Frozen tissue was weighed (~50 mg hind leg skeletal muscle) and homogenized on ice with a sonicator in a 4:1 SEI:SEID buffer (SEI: 250 mM sucrose, 10 mM EDTA, 42 mM imidazole, pH

7.3; SEID: 100 mL SEI + 0.5 g sodium deoxycholate). Homogenates were then centrifuged at 10,000x *g* for 5 min at 4ºC, and the resulting supernatant was directly used in the assay.

Na^+/K^+-ATPase activity was measured using commercial Na^+/K^+-ATPase activity assay kit (Elabscience, Cat # E-BC-K539-M), ATPase activity was expressed as nmol P_i $mg^{-1}_{protein}$ min^{-1} where protein content was quantified by performing a Biuret test.

5.2.8 CS enzyme analysis

CS enzyme activity was measured using a method modified from (Farhat et al., 2020). Briefly, 50 mg of tissue (hind leg skeletal muscle) was weighed and homogenized on ice in 1 ml of extraction solution (20 mM Tris-HCl, 1 mM EDTA, and 0.1% (v/v) Triton X-100, pH 7.2). Homogenates were then centrifuged at 4°C at 10,000g for 10 min, top fat layer was discarded, and the supernatant was immediately used to assay CS activity. The CS activity was measured in assay buffer (50 mM Tris-HCl, 0.5 mM oxaloacetate, 0.1 mM acetyl CoA, 0.2 mM 5,5′-dithiobis-(2-nitrobenzoic acid) (DTNB), pH 8.1) as the increase in the slope of the absorbance at 412 nm during 5 min (Alp et al., 1976), and was determined at 32°C using a Spectra Max Plus384 Absorbance Microplate Reader (Molecular Devices, Sunnyvale, CA). Concentrations used in the assay were saturating and not inhibitory, as determined from preliminary experiments. Substrate-free controls were run simultaneously to determine background activity. Enzyme activity was normalized to total soluble protein, which was quantified with a Biuret test.

5.2.9 qPCR for mitochondrial DNA quantification

Tissues (hind leg skeletal muscle) were homogenized using a glass tissue grinder (PYREX, CAT# 77241) at 50 mg wet weight/ml in lysis Solution (25 mM NaOH, 0.2 mM EDTA), then incubated at 95°C for 30 min, followed by centrifugation at 10,000 rpm for 5 min at 4°C. Top fat layer was discarded, and the supernatant was then collected and mixed with an equal volume of

40 mM Tris-HCl (Truett et al., 2000). DNA concentrations ere quantified using a NanoDrop Spectrophotometer (ND-1000, Thermofisher Scientific, Napean, ON, CAN). The relative mtDNA/nDNA ratios were measured by qPCR using a Rotor-Gene Q (Qiagen Inc., Montreal, QC, CAN), with a reaction medium containing 5 µl qPCR SYBR Green Mix (A600A; Promega, Madison, WI, USA), 0.1 µM primer (Primers are listed in Table 7.1), 2 µl DNA (optimal dilutions were determined previously), and H_2O; total volume 10 µl). The copy number of mtDNA was calculated using the following formula (Quiros et al., 2017):

a) $\Delta Ct = Ct\ (\text{nDNA gene}) - Ct\ (\text{mtDNA gene})$

b) Copies of mtDNA = $2 \times 2^{\Delta\Delta Ct}$

c) Relative mtDNA content = mtDNA treatment/mtDNA normoxic

Table 5.2 List of primers for mtDNA quantification.

Species	Target	Sequence (5' to 3')
NMR	16S mitochondrial ribosomal RNA	GTACCGCAAGGGAAAGATGAAAG
		TAGCTCGTTTGGTTTCGGGGTT
	beta 2-microglobulin	GCCAAACTACTTGAACTGCTATG
		GTCCAGTCCTTGCTGAAAGA

5.2.10 Statistical analysis

All statistical analyses were performed using GraphPad Prism 9 (GraphPad Prism, La Jolla, CA, USA). Data were analyzed using multiple t tests followed by Welch t-test (Fig. 5.4); two-way ANOVAs followed by a Dunnett (Fig. 5.1-5.3) multiple comparisons tests. Significance was determined with a level of $p < 0.05$ unless otherwise indicated in results, and all data are expressed as the mean ± SEM.

5.3 Results

Skeletal muscle mitochondrial respiration is minimally impacted by in vivo acclimation to acute or chronic environmental hypoxia. Differential respiratory capacities between three treatment groups (normoxia, acute hypoxia, and chronic hypoxia) were investigated using four complementary SUIT protocols as described in the methodology section (Appendix 7.2.4) to reveal mitochondrial OXPHOS plasticity in response to hypoxia (Fig. 5.1A–D). Cytochrome c addition resulted in a 7.81% ± 0.18 increase in mitochondrial respiration across all treatment groups ($n = 25$ animals, data not shown), which indicates minimal damage to the mitochondrial inner membrane. There was no significant difference in cytochrome c responses between treatment groups, indicating that acute or chronic hypoxia did not have a deleterious effect on mitochondrial membrane integrity.

For palmitoylcarnitine/malate-fueled respiration, we found that total ETC capacity was significantly reduced (~15%, from 97.90 ± 4.89 to 83.81 ± 7.67 and 83.91 ± 5.11 nmol O_2 min^{-1} mg $protein^{-1}$, Fig. 5.1A) following acute and chronic hypoxia, respectively, as compared to normoxic controls. However, we did not find any significant effect of hypoxia on leak respiration or OXPHOS capacity when mitochondria were fueled with pyruvate/malate or f or following glutamate/succinate addition (Fig. 5.1B), or complex II-linked OXPHOS capacity (Fig. 5.1C). Complex IV maximal activity was significantly decreased in animals treated with acute hypoxia (~16%, from 465.53 ± 10.53 to 387.83 ± 26.37 nmol O_2 min^{-1} mg $protein^{-1}$), but this effect was absent following chronic hypoxia (Fig. 5.1D). Similarly, acute hypoxia but not chronic hypoxia decreased the uncoupled maximal activities of complexes II and IV, ~18% and ~ 13%, respectively.

The RCR varied from 9.36 to 11.06 (with palmitoylcarnitine/malate), 12.27–17.40 (with pyruvate/malate) and 5.55–7.08 (with succinate/rotenone) (Fig. 5.2A & Table 5.3). Using pyruvate/malate, we found a significant increase in RCR in response to acute hypoxia, as compared to normoxia controls, which resulted from a decrease of leak respiration, but sustained OXPHOS capacity (Fig. 5.1A & Table 5.3). This RCR difference was however not observed following chronic hypoxia. Finally, the ADP/O ratio was not different among treatment groups when measured with the traditional approach (ranging from 2.48 to 2.64) nor when measured with the fluorescent MgGr method (ranging from 3.10 to 3.45; Fig. 5.2B).

***Skeletal muscle H_2O_2 efflux was partially reduced by* in vivo *hypoxic exposure*.** Concomitant with O_2 consumption, H_2O_2 efflux was recorded using the AUR assay in the presence of horseradish peroxidase and SOD during the three SUIT protocols (Fig. 5.3A–C). We did not observe any significant changes in palmitoylcarnitine/malate or pyruvate/malate fueled H_2O_2 efflux (Fig. 5.3A–B). Conversely, during succinate respiration we report a small but significant reduction of H_2O_2 efflux following acute hypoxia in succinate-fueled mitochondria (~33%, from 4.62 ± 0.71 to 3.07 ± 0.96 nmol H_2O_2 min^{-1} mg protein^{-1}, Fig. 5.3C).

***Acute hypoxia did not change mitochondrial abundance*.** We also assessed whether acute *in vivo* hypoxia alters mitochondrial abundance. Following 3 h of *in vivo* exposure to 5% O_2, Mann-Whitney tests indicated that neither CS enzyme activity, mtDNA copy number, nor mitochondrial volume density (from 9.17 ± 0.80% in normoxia to 8.29 ± 0.82% in hypoxia) were changed in NMR skeletal muscle per wet tissue weight but decreased by ~50% when normalized to protein density (data not shown). However, this change was likely mediated by a change in protein density in hypoxic muscle tissue and not mitochondrial abundance because CS enzyme activity was not different between treatments when normalized to tissue weight (Fig. 5.4A; $U = 15$, $p = 0.699$). In support of this conclusion, the mtDNA:nDNA ratio was unchanged by acute hypoxia (Fig. 5.4 A; $p = 0.093$). To confirm this, we also conducted TEM analysis in skeletal muscle tissue and found no change in mitochondrial volume density between treatment groups (Fig. 5.4A &B; $U = 40.5$, $p = 0.489$). In addition, we did not see significant changes of Na^+/K^+-ATPase activity between conditions (Fig. 5.4A; $U = 27.00$, $p = 0.645$).

5.4 Figures and tables

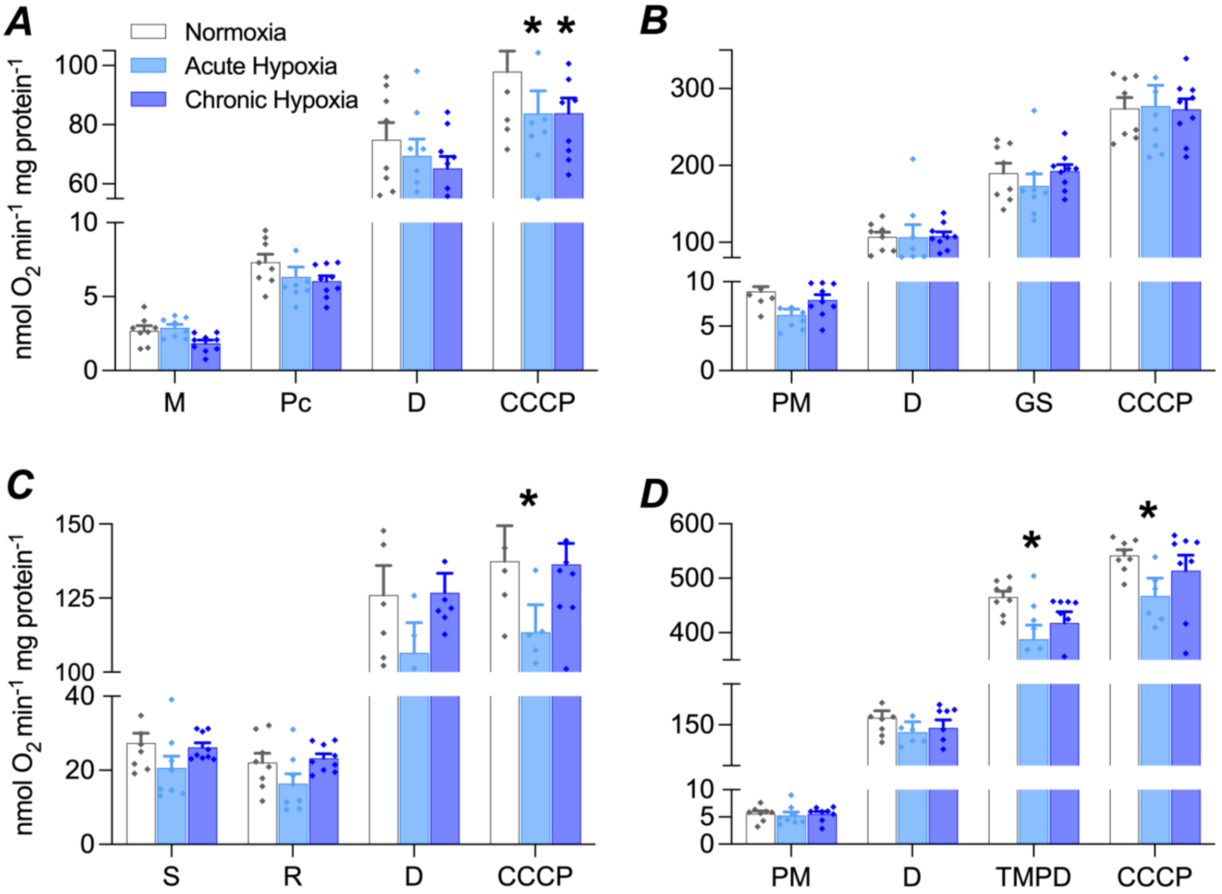

Figure 5.1 O_2 consumption by isolated NMR skeletal muscle mitochondria following in vivo treatment with normoxia, acute hypoxia (7% O_2 4 h), and chronic hypoxia (11% O_2 4-6 weeks).

Summaries of **(A)** palmitoylcarnitine stimulated respiration, **(B)** pyruvate stimulated respiration, **(C)** succinate stimulated respiration, and **(D)** TMPD (complex IV) stimulated respiration (Cytochrome C and rotenone were omitted in D). Substrates were added sequentially in the order indicated on the x-axis for each graph. Abbreviations: M, malate; Pc, palmitoylcarnitine; P, pyruvate; G, glutamate; S, succinate; D, ADP; R, rotenone; ASC, ascorbate; TMPD, *N*,*N*,*N′*,*N′*-Tetramethyl-*p*-phenylenediamine; CCCP, carbonyl cyanide *m*-chlorophenyl hydrazine, $n = 8–9$. Data are means ± SEM. Significant differences (*, $p < 0.05$ normoxia *vs.* hypoxia) were determined by two-way ANOVAs followed by with a Dunnett multiple comparisons test.

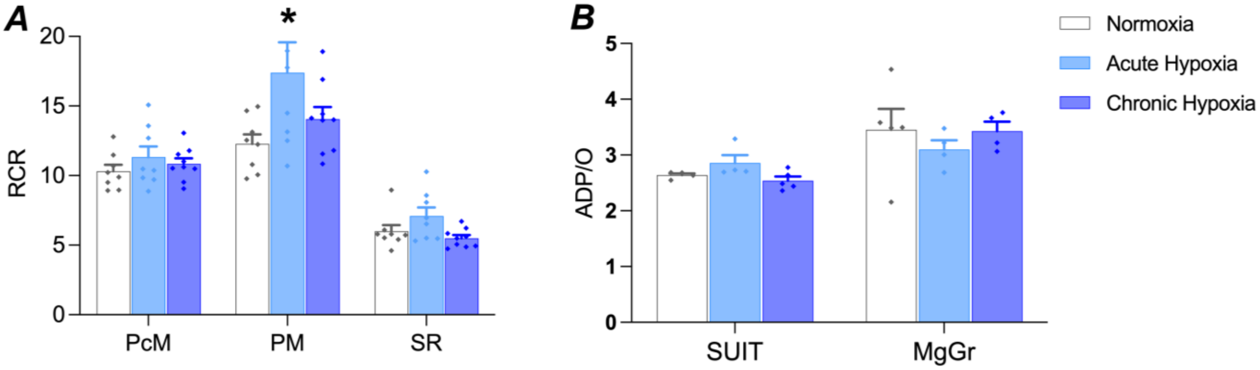

Figure 5.2 Mitochondrial coupling efficiency and respiratory coupling ratio of isolated NMR skeletal muscle mitochondria following *in vivo* treatment with normoxia, acute hypoxia (7% O_2 4 h), and chronic hypoxia (11% O_2 4-6 weeks).

(A) The RCR was evaluated as the quotient of OXPHOS capacity to leak respiration; mitochondria were stimulated with palmitoylcarnitine/malate (PcM), pyruvate/malate (PM), or succinate/rotenone (SR), $n = 8–9$. Data are mean ± SEM. **(B)** Phosphorylation efficiency (ATP/O ratio) was measured using two approaches: as the amount of O_2 consumed following a non-saturating pulse of ADP (200 µM) in the presence of pyruvate and malate (SUIT), $n = 8–9$, and a fluorometric method (using MgGr), $n = 4–5$. Significant differences ($^*p < 0.05$ normoxia *vs.* hypoxia) were determined by two-way ANOVAs followed by a Dunnett multiple comparisons test.

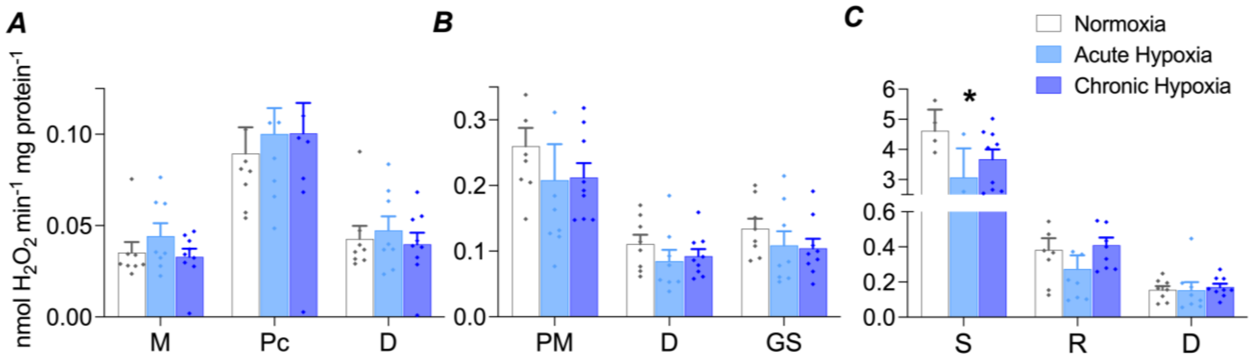

Figure 5.3 H_2O_2 efflux of isolated NMR skeletal muscle mitochondria following *in vivo* treatment with normoxia, acute hypoxia (7% O_2 4 h), and chronic hypoxia (11% O_2 4-6 weeks).

Summaries of **(A)** palmitoylcarnitine stimulated, **(B)** pyruvate stimulated, and **(C)** succinate stimulated H_2O_2 production. Substrates were added sequentially in the order indicated on the x-axis for each graph. Abbreviations: M, malate; Pc, palmitoylcarnitine; P, pyruvate; G, glutamate; S, succinate; D, ADP; R, rotenone, $n = 8–9$. Data are presented as means ± SEM. Significant differences ($*p < 0.05$ normoxia *vs.* hypoxia) were determined by two-way ANOVAs followed by with a Dunnett multiple comparisons test.

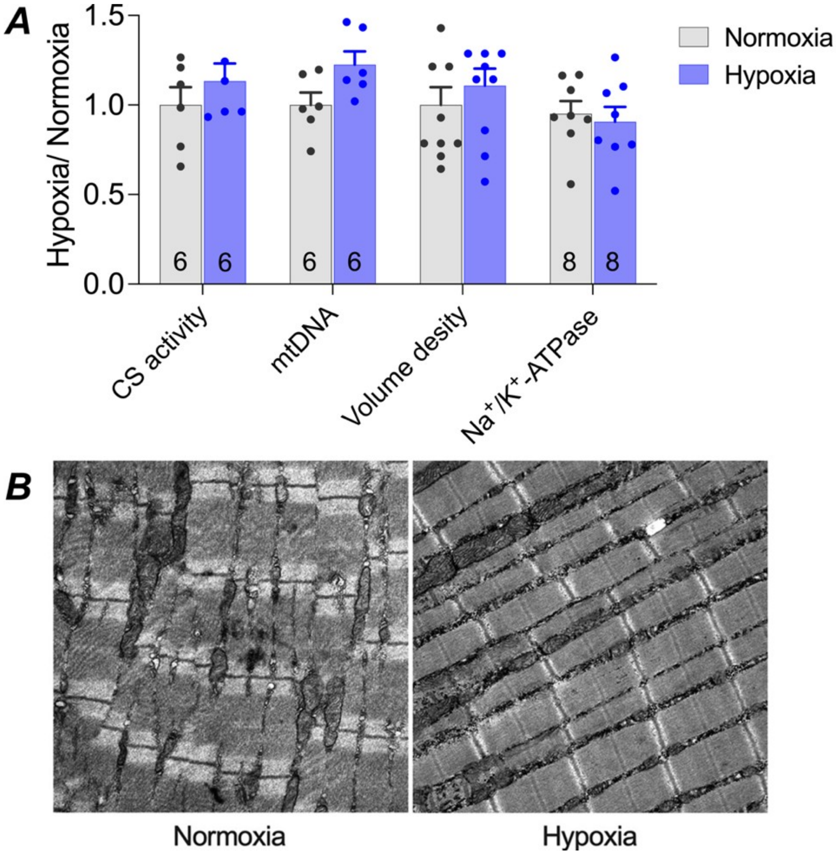

Figure 5.4 Mitochondrial abundance and Na$^+$/K$^+$-ATPase activity were not changed by acute hypoxia in skeletal muscle.

(A) Ratio of CS activity per weight tissue weight, mitochondrial (mtDNA) to nuclear (nDNA), mitochondrial volume density from, and Na$^+$/K$^+$-ATPase activity per weight tissue, raw data from (Marks de Chabris et al., 2023), and **(B)** Representative electron micrographs of hind leg skeletal muscle from NMRs treated with 3 h of normoxia (21% O$_2$) or acute hypoxia (5% O$_2$), absolute values from (Marks de Chabris et al., 2023). Data are mean ± SEM from n = 6 or 8 (A), n = 2 (B) biologically independent replicates. Mann-Whitney tests with an alpha value of 0.05 revealed no significant differences.

Table 5.3 Raw values of isolated skeletal muscle mitochondrial respiratory functions

Substrates	Respiration	Normoxia		Acute Hypoxia		Chronic Hypoxia	
		mean	SEM	mean	SEM	mean	SEM
PcM	Leak	7.32	0.55	6.34	0.66	6.05	0.36
	OXPHOS	74.91	5.85	69.50	5.61	65.18	4.11
	RCR	10.31	0.47	11.33	0.77	10.84	0.40
PM	Leak	8.89	0.56	6.27	0.66	7.94	0.61
	OXPHOS	106.86	6.50	106.46	16.30	108.06	5.52
	RCR	12.27	0.69	17.39	2.19	14.06	0.86
SR	Leak	22.06	2.53	16.36	2.68	23.22	1.24
	OXPHOS	125.97	10.05	106.56	10.18	126.81	6.53
	RCR	5.99	0.45	7.08	0.63	5.50	0.22

Data are presented as means ± SEM from *n* = 8-9 each, statistical analysis were indicated in Fig 5.1 & 5.2. Abbreviations: P, pyruvate; M, malate; Pc, palmitoylcarnitine; S, succinate; R, rotenone; OXPHOS, oxidative phosphorylation; RCR, respiratory control ratio calculated as the ratio of OXPHOS /Leak.

5.5 Discussion

In this chapter we investigated functional plasticity of NMR skeletal muscle mitochondria for OXPHOS capacity and H_2O_2 efflux in response to acute and chronic *in vivo* hypoxia. We found that mitochondrial respiration and H_2O_2 production were affected by hypoxic exposure in certain conditions; however, the magnitude of these changes is rather small. Specifically, the effects of acute and chronic hypoxia on NMR skeletal muscle are minimal relative to previous studies in both hypoxia-tolerant and hypoxia-intolerant species. This suggests that our finding of minor functional change in skeletal muscle mitochondria may not be biologically significant. This minimal level of plasticity to hypoxia in most aspects of NMR skeletal muscle mitochondrial function may prevent expensive remodelling of mitochondria in an animal that putatively moves frequently in and out of hypoxia and may therefore represent a strategy to support exercise in intermittent and highly variable levels of hypoxia.

In other species, hypoxia drives changes in ETC flux and substrate preference to reduce whole-animal metabolic demand, and/or improve mitochondrial efficiency. Many of the most hypoxia-tolerant vertebrates employ metabolic rate suppression in acute hypoxia or anoxia. For example, hypoxia/anoxia-tolerant freshwater turtles, carp, goldfish, sharks, bats, and African mole-rats, among many others, all substantially reduce their whole animal metabolic rate when O_2 is limited (Bickler & Buck, 2007; Ivy et al., 2020; Jackson & Ultsch, 1982; Nilsson & Renshaw, 2004; Regan et al., 2017; Speers-Roesch et al., 2012)

Generally, a wide variety of physiological, behavioural, and molecular adaptations contribute to metabolic rate suppression (Guppy & Withers, 1999); however, as primary consumers of metabolic O_2 and key regulators of energetically-expensive cellular processes

(Pamenter et al., 2014), alterations in mitochondrial density or function are likely to be major contributors to this adaptation. Together, these alterations act to either reduce O_2 consumption at the mitochondrial level (*i.e.*, to match the reduction at the whole-animal level), or to improve the efficiency of O_2 consumption (*i.e.*, the ADP/O ratio). Indeed, a wide range of research in a variety of hypoxia-intolerant and hypoxia-tolerant organisms has demonstrated that hypoxia alters mitochondrial function (although whether these adaptations are beneficial or deleterious is debateable).

Skeletal muscle mitochondria from many other hypoxia-tolerant and -intolerant species are plastic following hypoxia. For example, a fuel preference shift occurs following hypoxia and towards greater reliance on carbohydrates in high-altitude deer mice, and carbohydrate metabolism-related genes are also increased in skeletal muscle (Lau et al., 2017; see also Introduction and below for additional examples). Furthermore, 2 days of severe hypoxia triggers decreases in OXPHOS capacity and increases in leak respiration in both pyruvate/malate and succinate fuelled murine skeletal muscle mitochondria (Magalhaes et al., 2005), and also downregulates OXPHOS in human skeletal muscle (Horscroft & Murray, 2014). Also, in human skeletal muscle mitochondria, energetic efficiency is improved after 4 weeks in hypobaric hypoxia (Jacobs et al., 2012). Hence, we hypothesized similar mechanisms would be apparent in NMR skeletal muscle. However, our findings do not support this prediction because the observed changes are minimal, we did not find a significant fuel preference shift post hypoxia towards carbohydrates, and ADP/O ratios are not improved under any condition.

Nonetheless, we do observe a small downregulation of complex II-linked uncoupled OXPHOS capacity following acute but not chronic hypoxia exposure (Fig. 5.1C). This observation is particularly important given the emerging role for succinate metabolism in cell damage during the reoxygenation phase post-hypoxia. Specifically, succinate augmentation in hypoxic tissue, which was observed nearly half century ago (Taegtmeyer, 1978), is now widely recognized as the main source of uncontrolled ROS efflux rates. The reduction in complex II uncoupled OXPHOS capacity that we report following acute hypoxia-acclimation may be a minor evolved stress response to reduce reoxygenation-induced ROS bursts following hypoxia, while the lack of plasticity in complex I-II OXPHOS capacity may be an inherited modulation to this lifestyle and support a wider range of metabolic capabilities in skeletal muscle. Finally, although complex II function may be impaired as a result of ROS-mediated damage during hypoxia-reoxygenation, this is usually associated with increased ROS generation. Since we did not observe such an increase (see below), it is more likely that the downregulation in complex II respiration is an actively mediated and potentially adaptive change. Notably, at least two other studies have reported similar regulation of complex II in hypoxia-tolerant species: including as part of energy-conserving metabolic depression post-anoxia in epaulette shark brain (Devaux et al., 2019), and also in 13-lined ground squirrel during torpor (Staples, 2014).

A similar trend is reported for complex IV, where reduced maximal uncoupled capacity is observed following acute hypoxia (Fig. 5.1D). In this case, however, the change elicited by hypoxia would increase instead of decreasing reverse electron flux towards complex I, which is one of the main sources of ROS (De Bilbao et al., 2004). Very similar responses (downregulation of complex IV activity) have been observed post null/low O_2 in a fairly wide variety of hypoxia-tolerant species and tissues, including anoxia-tolerant turtle heart and brain following weeks of anoxia (Galli et al., 2013; Pamenter et al., 2016), and in NMR brain following 4 h under 3% O_2 (Pamenter et al., 2018), while adaptations to complex IV that reduce overall ETC flux during hypoxia have been reported in bar-headed geese, among others (Lau et al., 2017; Scott et al., 2011). These findings have been linked to a putative regulatory role for complex IV in downregulating overall ETC flux, rather than a means to regulate ROS production.

ROS production is beneficially modulated in NMR skeletal muscle under certain conditions. As discussed above, ROS are important cellular messengers but sudden uncontrolled increases in their formation rate, as seems to occur during hypoxia and/or reoxygenation, is deleterious to cellular function. In mammalian mitochondria *in vitro*, the highest rates of mitochondrial ROS formation are achieved by reverse electron flow at the level of complex I, or from complex III in the presence of its inhibitor antimycin A (Goncalves et al., 2015). Reverse electron flow is associated with the accumulation of succinate and subsequent generation of high levels of ROS, which are generally deleterious (Chouchani et al., 2014; Chouchani et al., 2016b). A key result of such a damaging ROS burst is a reduction in complex I and II function, which has been demonstrated in hypoxia-intolerant mice and humans (Gamboa & Andrade, 2010; Jacobs et al., 2012), and in hypoxia-tolerant grey carpet sharks (*Chiloscyllium punctatum*) (Devaux et al., 2019).

Based on these findings, we hypothesized that the capacity for succinate-driven oxidation should decrease during hypoxia in NMR skeletal muscle mitochondria to limit deleterious excessive ROS production. Reductions in ROS production during low O_2 exposure have been reported in mitochondria and tissues from a wide variety of hypoxia-tolerant species. For example, weeks of acute or intermittent hypoxia-exposure reduces liver mitochondrial H_2O_2 generation in estuarine killifish (*Fundulus heteroclitus*; but mitochondrial energetics are not impacted by either hypoxic protocol; (Du et al., 2016)). Similar reductions are reported in response to short-term anoxia in freshwater turtle brain (Milton et al., 2007), and in skeletal muscle from high-altitude deer mice (Mahalingam et al., 2017). In line with these previous findings, we report here that acute hypoxia-treated skeletal muscle mitochondria decrease the rate of H_2O_2 emission during succinate oxidation under non-phosphorylating conditions (Fig. 5.2C), regardless of the contribution of complexes I, II or III. However, we did not observe lower H_2O_2 emission from pyruvate/malate fueled mitochondria following chronic hypoxia, which was observed in high-altitude deer mice (Mahalingam et al., 2017).

It is important to note that ROS efflux is only a portion of the total cellular ROS equation, with free radical scavengers that detoxify ROS also playing important roles in the mitochondria and the cytosol. With respect to this overall ROS metabolism, it is interesting that many hypoxia-tolerant species express high endogenous ROS scavenging capabilities at all times compared to intolerant species, or upregulate these abilities during hypoxia. For example, NMR heart and skeletal muscle mitochondria have constitutively more active matrix scavenging capacities than is found for mice (Munro et al., 2019). Similarly, enhanced endogenous expression of ROS scavengers (or their genes), or upregulation of the same by hypoxic exposure have been reported in other organs of NMRs, and also in the blind mole-rat and carp, among others (Lewis et al., 2013; Lushchak et al., 2005; Schulke et al., 2012). Enhanced ROS scavenging capabilities may mitigate the need to suppress ROS generation during hypoxia and particularly during reoxygenation in these species.

Other potential mechanisms of suppressing O_2 consumption. We report no change in NMR skeletal mitochondrial abundance between normoxic and acute hypoxic conditions. Neither did we see Na^+/K^+-ATPase activity changes in acute hypoxic NMR skeletal muscle tissues, although the activity of this transporter consumes at most 10% of the total energy consumed by skeletal muscle (Clausen, 2013). Nonetheless, the relative stability of mitochondrial respiratory function and

Na^+/K^+-ATPase activity is consistent within skeletal muscle during hypoxia, because mitochondrial functional depression is associated with reduced Na^+/K^+-ATPase activity in several studies of muscle in rodent (Comellas et al., 2006; Green et al., 2000; Li et al., 2014; Maiti et al., 2018).

Several pathways might regulate energy conservation in hypoxic skeletal muscle. For example, NMRs might reduce glucose uptake in skeletal muscle cell regulated by AMPK (Hadj-Moussa et al., 2021a); however, we previously reported unchanged glucose levels in hypoxic muscle (Pamenter et al., 2019a). This result indicates that hypoxic NMR skeletal muscle may inhibit mitochondrial O_2 consumption by limiting carbohydrate metabolism (Hadj-Moussa et al., 2021a). On the other hand, acutely hypoxic NMR skeletal muscle also likely reduces O_2 consuming process in other aspects, for example, decrease in activity of the ribosomal protein biosynthesis through PTM (protein phosphorylation) in Akt/mTOR pathway (Al-Attar et al., 2020). Another chronic hypoxia study suggested that skeletal muscle might reduce O_2 consumption by downregulating the aerobic supply of acetyl-CoA from glycolysis and β-oxidation to the TCA cycle through alterations (mostly decreasing) of enzyme activities of energy metabolism (Farhat et al., 2020).

NMRs live in a variably hypoxic environment and likely experience severe and acute hypoxia while resting in the colony nest chamber and while digging aggressively into densely packed and poorly ventilated soils at the terminus of tunnel networks. Conversely, they likely experience relative normoxia in the majority of the burrow, and particularly in connecting tunnels with lower animal density or near burrow openings (Holtze et al., 2018). As a result, NMRs likely move in and out of hypoxia constantly while exercising and working, with hypoxic exposures being unpredictable in their duration and severity. Given this environment, it is perhaps sensible to avoid drastic changes in mitochondrial function and maintain a steady rate of ROS production.

Limitations. An important limitation of our study is the use of isolated mitochondria. Although this preparation is widely utilized and well-accepted in the field of mitochondrial research, it nonetheless always results in altered function relative to the *in vivo* cellular milieu. This largely occurs due to the disruption of the extensive mitochondrial networks during isolation (Zamponi et al., 2018), from the loss of normal cytosolic cellular signalling mechanisms that are critical in mediating mitochondrial function, and from the loss of communicating signals from the mitochondria to other cellular components (Pamenter, 2014; Picard et al., 2011). It is notable that our previous experiments demonstrating significant plasticity in NMR brain mitochondria were conducted on permeabilized brain homogenates (Pamenter et al., 2018), which would better preserve mitochondrial networks and may have preserved signalling interactions that mediated the changes we observed in that study. However, these experiments were conducted at 3% O_2 and we cannot discount the possibility of incremental inhibition of mitochondrial respiration with increasing depth of hypoxia.

It is also important to note that we did not measure $\Delta\psi_m$ or proton leak in our experiments. We have previously demonstrated adaptations to these characteristics in NMR brain that likely enhance the efficiency of energy production in that organ (Pamenter et al., 2018). Since a high proton motive force is required to produce reverse electron flow, adaptations to this aspect of mitochondrial physiology may exist in this tissue and contribute to the hypoxia-tolerance of this species. Another general parameter that has not been considered in our report is the potential effect of the magnitude and duration of hypoxia exposure. The literature on human skeletal muscle varies between studies, which is reasonable because of different altitudes and periods of hypoxia (D'Hulst & Deldicque, 2017). The exposure duration may not only influence the acute response but could also contribute to the differences of O_2 distribution in different tissues. Therefore, our report of a mild mitochondrial response in NMR skeletal muscle may also partly be a result of experimental design (magnitude, duration, and temperature). Similarly, mitochondria from different muscle groups may have varying responses to hypoxia due to mitochondrial quantity (Scott et al., 2018), O_2 affinity, and Ca^{2+} management (Fu et al., 2016). We conducted our study using a pool of skeletal muscle from hind leg, pectoral and dorsal skeletal muscles in NMRs, which represented an overall response to hypoxia in skeletal mitochondria. However, a recent study indicated that NMRs have more oxidative-glycolytic and oxidative fibres but less glycolytic fibres than the Cape dune mole-rat (*Bathyergus suillus*), which is a less hypoxia-tolerant African mole-rat species (Sahd et al., 2023). Further study of specific muscle group expression may help to better understand mechanisms of adaptation to hypoxia in NMR skeletal muscle.

Conclusions. In summary, we demonstrate that acute or chronic hypoxia exposure induces minor functional changes in OXPHOS capacity and ROS efflux in NMR skeletal muscle mitochondria. The phenotype and magnitude of these changes is, however, markedly different from observations in previous chapters, including brain and BAT. Nevertheless, the nature of the changes is in line with adaptations to reduce energy production in hypoxia and to ameliorate the deleterious ROS burst occurring upon reoxygenation because of succinate accumulation (complex IV and site I_Q regulation of O_2 consumption and oxidative stress, respectively).

6 General conclusions

Hypoxia has been implicated as a key component of multiple pathological events, including neurodegenerative disease, stroke, obesity, and muscular dystrophy, among many others (Giaccia et al., 2004; Nguyen et al., 2021; Semenza, 2011b; Trayhurn & Alomar, 2015). Mitochondria are exquisitely sensitive to O_2 availability, because mitochondrial ATP production requires molecular O_2 as the terminal electron acceptor in the OXPHOS pathway (Chandel, 2015; Gao et al., 2022; Lim et al., 2021), and because the regulation of key cellular signalling mechanisms, including ROS and Ca^{2+}, are closely tied to mitochondrial function. NMRs are mammals that can tolerant extreme hypoxic environments, including hours of 3% O_2 (Farhat et al., 2021; Pamenter et al., 2018) and even minutes of anoxia (Park et al., 2017), without any significant cell damage. A growing body of literature suggests that NMRs employ multiple mechanisms to achieve this hypoxia-tolerance and mitochondria likely play a key role in initiating and regulating these mechanisms. In this thesis, I explore the role of mitochondria in regulating cellular responses to hypoxia in three key organ systems: BAT, brain, and skeletal muscle. My results yielded numerous salient findings, including several novel mechanisms of mitochondrial adaptation to hypoxia. Importantly, this multi-tissue analysis provides important insight into the similarities and differences of mitochondrial regulation during hypoxia across different tissues within the same organism.

Common responses to hypoxia across NMR tissues: suppression of O_2 consumption and prevention of hypoxia-induced damage. NMRs suppress whole animal O_2 consumption during hypoxia, as do many other hypoxia-tolerant animals (Pamenter, 2022), and they achieve this suppression in multiple ways that are tissue specific. Like many other mammals (Frappell et al., 1992), NMRs reduce T_b to save energy during hypoxia. The primary mechanism of T_b reduction in hypoxic NMRs is a reduction of O_2-intensive non-shivering thermogenesis mediated through changes in BAT mitochondrial protein expression and membrane dynamics, which in turn suppresses mitochondrial respiration (reduced by 45-70%) without loss of mitochondrial integrity (Cheng et al., 2021b). Hypoxic NMR brain mitochondria also reduce O_2 consumption capacity during *in vitro* hypoxia (Pamenter et al., 2018), and NMR brain mitochondria exhibit no damage during *in vivo* hypoxia (Chapter 3) and reduced damage relative to mouse brain mitochondria during *in vitro* ischemia (Chapter 4). Conversely, skeletal muscle mitochondrial respiratory function is only mildly reduced during acute hypoxia, but mitochondrial damage is still avoided, possibly because other pathways are activated to limit O_2 and energy consumption, *e.g.*, reducing glucose uptake through AMPK (Hadj-Moussa et al., 2021a; Pamenter et al., 2019a), or depressing ribosomal protein biosynthesis in Akt/mTOR pathway (Al-Attar et al., 2020).

Indeed, NMRs exhibit minimal hypoxia-induced damage across our tissues of study. NMR neurons maintain synaptic transmission under *in vitro* hypoxia and can even recover from short-term anoxia (Larson & Park, 2009). Additionally, NMR brain slices avoid ischemia-induced cell death for 24 h (Nathaniel et al., 2009). Our study indicates that the maintenance of mitochondrial electron transport function (OXPHOS and ROS management) and Ca^{2+} homeostasis may play critical roles in preserving mitochondrial integrity and supporting neuronal function during hypoxia and ischemia in this tissue (Cheng & Pamenter, 2021; Eaton et al., 2022; Wang et al., 2020). Consistent with this, we observed maintenance of mitochondrial membrane integrity during hypoxia across all tissues in our study, including the absence of any change in cytochrome c-mediated respiration *in vitro* between treatments, and the prevention of mitophagy in at least iBAT and brain following *in vivo* hypoxia. We also report resistance to Ca^{2+} stress (in iBAT and brain), hypoxia stress (in all tissues), and even ischemic conditions (in brain). This tolerance may result from protection of mitochondrial membranes, hyperpolarized membrane potentials, improved electron leakage/ROS management, and an enhanced ATP-independent Ca^{2+} buffering capacity, depending on the tissue. Other pathways/regulators likely also inhibit cell death, such as miRNAs (Hadj-Moussa et al., 2021b; Logan et al., 2020), and HIF1α (Hawkins et al., 2019). Similarly, NMRs maintain physical activity under "mild" hypoxia conditions (Ilacqua et al., 2017), however, there is no significant elevation of oxidative damage in skeletal muscle (or in brain or BAT) (Hadj-Moussa et al., 2022). This may be related to the high antioxidant capacity of NMR skeletal muscle mitochondria (Munro et al., 2019), an adaptation which may be conserved in other tissues as well.

Tissue-specific responses in hypoxic NMR mitochondria. An important finding of our study is that mitochondria drive unique protective responses to hypoxia that are in some cases divergent between tissues. For example, in iBAT mitochondria these responses include a large (~45%) suppression of OXPHOS and even greater (~70%) reduction of UCP1-stimulated uncoupled O_2 consumption, as well as correspondingly reduced H_2O_2 efflux. These results are in line with the suppression of T_b in hypoxic NMRs (Pamenter et al., 2019a), which is mediated by the degradation of UCP1 and OXPHOS proteins. We also report more tightly coupled mitochondria, (*i.e.*, increased RCR in all substrates in iBAT), and further suppression of coupled and uncoupled respiration relative to electron transport capacity. These results indicate the occurrence of very rapid hypoxia-induced membrane reprograming, which is consistent with our finding of a mild reduction in mitochondrial density mediated by fission but not mitophagy or autophagy. Also, we noticed that succinate-induced H_2O_2 efflux varies between pyruvate- *vs*. octanoylcarnitine-fueled respiration in hypoxic NMR iBAT mitochondria, which is similar to BAT mitochondria from

UCP1-ablated mice (Oelkrug et al., 2010). In this mouse model, the reduction of UCP1 correlates with increasing ROS production. In another words, ROS may trigger UCP1 protein reductions (Kazak et al., 2017; Oelkrug et al., 2010). Importantly, Ca^{2+} exclusion is better maintained in hypoxic NMR iBAT, which may be related to ROS production in this UCP1 knockout mouse model (Kazak et al., 2017). Further study is warranted to explore this interaction in NMR BAT mitochondria.

It was previously reported that NMR brain mitochondria suppress electron transport in hypoxia (Pamenter et al., 2018). Building upon this finding, our research indicates that this reduction of O_2 consumption may be due to improved mitochondrial Ca^{2+} management, which is endogenously mediated by the unique architecture of NMR brain mitochondria, but is not due to membrane remodelling in acute hypoxia. Specifically, we report that NMR brain cells have relatively larger mitochondria, which may support a higher mitochondrial membrane potential, enhanced Ca^{2+} uptake, and increased capacity of the mitochondrial matrix to store Ca^{2+} (Halestrap et al., 1986). Indeed, a large number of independent mitochondrial crista correlates with increased Ca^{2+} capacity (Kushnareva et al., 2013; Strubbe-Rivera et al., 2021), which is consistent with the phenomenon we observed in NMR brain mitochondria. NMR brain mitochondria are also highly interconnected through adjacent connections and elaborate nanotunnel systems, the latter of which may support energy and Ca^{2+} homeostasis in hypometabolic conditions. Nanotunnel systems are expressed to a lesser degree in normal mouse brain mitochondria but are increased during hypoxic stress (Zhang et al., 2016). Note, the ultrastructure of NMR brain mitochondria may be shared among other NMR tissues, as we and others have observed (but have not quantified) similar structures (*e.g.*, larger mitochondrial size than mouse, and high density of mitochondrial crista)) in NMR iBAT, heart and skeletal muscle (Bakeeva et al., 2019; Vays et al., 2021).

Following *in vivo* hypoxia, mouse brain mitochondrial proteins exhibit changes that are typical of cells damaged in a hypometabolic state, including mitochondrial fission (Han et al., 2008) and the downstream activation of mitophagy (Ni et al., 2015; Pendin et al., 2017). On the other hand, hypoxic NMR brain mitochondrial proteins do not exhibit similar changes. However, NMR brain mitochondria nonetheless increase in size in acute hypoxia, which warrants further study. Conversely, and as discussed above, hypoxic NMR iBAT exhibits enhanced fission and inhibition of apoptotic processing (Chapter 2). These results suggest that brain and iBAT mitochondria maintain integrity through divergent mechanisms.

Unlike hypoxic brain and iBAT, skeletal muscle mitochondria did not exhibit the same extent of reduction of O_2 consumption capacity in hypoxia. Changes in skeletal muscle mitochondrial ultrastructure remain to be explored.

Future work. In scientific research, answering one question often raises two more interesting questions to explore. Consistent with this idea, and although the work in this thesis answers many questions regarding how mitochondria contribute to the regulation of hypoxia tolerance in NMR iBAT, brain, and skeletal muscle, our results raise many additional interesting questions that are worthy of further exploration.

One particularly promising area of future research is the regulation of succinate and/or the succinate dehydrogenase pathway in hypoxia-tolerant organisms. For example, succinate is an activator in BAT mitochondrial heat production involving mitochondrial ROS emission (Q. Li et al., 2022; Liao et al., 2022; Liu et al., 2020; Mills et al., 2018). Consistent with this, we observed a significant elevation of succinate-induced (coupled, with GDP) H_2O_2 emission in normoxic

NMR iBAT mitochondria; however, this increased H_2O_2 signal vanished in hypoxic mitochondria. This finding suggests that succinate may activate heat production from BAT in normoxia and that NMRs may have a mechanism of regulating succinate metabolism to deactivate UCP1-induced heat production in hypoxia, which may be associated with mitochondrial ROS. Similarly, succinate mediated H_2O_2 consumption is more sensitive to Ca^{2+} stress in permeabilized NMR brain tissue than that mediated by the mitochondrial complex I pathway, and succinate (with or without rotenone) did not produce H_2O_2. Consistent with this finding, a study in *in vitro* hypoxic brain slices found no changes of cellular H_2O_2 (Eaton et al., 2022). *In vitro* ischemia also inhibited succinate-induced H_2O_2 emission but not that mediated by glutamate or pyruvate (Cheng & Pamenter, 2021). Finally, in hypoxic skeletal muscle mitochondria, there is a significant reduction of H_2O_2 emission during succinate-induced leak respiration but not pyruvate and palmitoylcarnitine-induced leak respiration (Cheng et al., 2021a). Notably, a difference of succinate dehydratase activity in skeletal muscle was also reported in different groups of deer mice (Dawson & Scott, 2022). Taken together, these data suggest that mitochondrial succinate metabolism may play an important role in regulating mechanisms of hypoxia-tolerance in numerous NMR tissues, and perhaps in other hypoxia-tolerant species as well. Thus, further investigation of succinate metabolism (*e.g.*, using isotope tracing techniques (Fernandez-Garcia et al., 2020)) is warranted.

Another interesting result warranting further exploration is our observation of an inhibition of mitochondrial-dependent apoptosis in hypoxic BAT mitochondria and the lack of change of apoptotic proteins in hypoxic brain, which is consistent with antiapoptotic changes in other hypoxic tissues (Al-Attar et al., 2020; Hawkins et al., 2019). Various mechanisms of regulating antiapoptotic responses have also been described in other hypoxia-tolerant species (Larson et al., 2014; Malik et al., 2012). A comparative study of antiapoptotic pathway in both mitochondria-dependent and -independent tissues will be another critical approach to understand mechanisms limiting hypoxia-induced cell damage in NMRs.

Finally, a fundamental topic of interest that arises from this thesis is the impact of changes in mitochondrial ultrastructure on cellular viability in hypoxia. We observed a relatively high density of cristae in NMR iBAT and brain mitochondria, which has also been anecdotally observed in NMR heart and skeletal muscle mitochondria (Holtze et al., 2016; Vays et al., 2021). Another study also reported similar mitochondrial parameters in hypoxia-tolerant ground squirrel brain (Popov et al., 2005) but did not present any exploration of physiological function. We are the first to link these structures with mitochondrial physiology as it relates to hypoxia-tolerance in NMR brain. Based on the clear understanding of mitochondrial ultrastructure (Joubert & Puff, 2021; Stephan et al., 2020), there is great potential in the study of these fundamental components of mitochondrial structure in NMRs and other hypoxia-tolerance animals.

Taken together, it is obvious that considerable work remains in the journey to understand the mechanisms behind hypoxic changes in mitochondrial OXPHOS, ROS management, Ca^{2+} buffering, and membrane dynamics, and to uncover the roles of mitochondria in hypoxia-/ischemia-tolerance in NMRs.

Reference

Abramov, A. Y., Scorziello, A., & Duchen, M. R. (2007). Three distinct mechanisms generate oxygen free radicals in neurons and contribute to cell death during anoxia and reoxygenation. *J Neurosci*, *27*(5), 1129-1138. https://doi.org/10.1523/JNEUROSCI.4468-06.2007

Affourtit, C., Quinlan, C. L., & Brand, M. D. (2012). Measurement of Proton Leak and Electron Leak in Isolated Mitochondria. In *Mitochondrial Bioenergetics* (pp. 165-182). Humana Press. https://doi.org/10.1007/978-1-61779-382-0_11

Agrawal, S., Kumar, S., Sehgal, R., George, S., Gupta, R., Poddar, S., Jha, A., & Pathak, S. (2019). El-MAVEN: A Fast, Robust, and User-Friendly Mass Spectrometry Data Processing Engine for Metabolomics. *Methods Mol Biol*, *1978*, 301-321. https://doi.org/10.1007/978-1-4939-9236-2_19

Al-Anazi, A., Parhar, R., Saleh, S., Al-Hijailan, R., Inglis, A., Al-Jufan, M., Bazzi, M., Hashmi, S., Conca, W., Collison, K., & Al-Mohanna, F. (2018). Intracellular calcium and NF-kB regulate hypoxia-induced leptin, VEGF, IL-6 and adiponectin secretion in human adipocytes. *Life Sci*, *212*, 275-284. https://doi.org/10.1016/j.lfs.2018.10.014

Al-Attar, R., Childers, C. L., Nguyen, V. C., Pamenter, M. E., & Storey, K. B. (2020). Differential protein phosphorylation is responsible for hypoxia-induced regulation of the Akt/mTOR pathway in naked mole rats. *Comp Biochem Physiol A Mol Integr Physiol*, *242*, 110653. https://doi.org/10.1016/j.cbpa.2020.110653

Aldakkak, M., Stowe, D. F., Dash, R. K., & Camara, A. K. (2013). Mitochondrial handling of excess Ca2+ is substrate-dependent with implications for reactive oxygen species generation. *Free Radic Biol Med*, *56*, 193-203. https://doi.org/10.1016/j.freeradbiomed.2012.09.020

Allen, K. N., & Vazquez-Medina, J. P. (2019). Natural Tolerance to Ischemia and Hypoxemia in Diving Mammals: A Review. *Front Physiol*, *10*, 1199. https://doi.org/10.3389/fphys.2019.01199

Almeida, A., Delgado-Esteban, M., Bolanos, J. P., & Medina, J. M. (2002). Oxygen and glucose deprivation induces mitochondrial dysfunction and oxidative stress in neurones but not in astrocytes in primary culture. *J Neurochem*, *81*(2), 207-217. https://doi.org/10.1046/j.1471-4159.2002.00827.x

Alp, P. R., Newsholme, E. A., & Zammit, V. A. (1976). Activities of citrate synthase and NAD+-linked and NADP+-linked isocitrate dehydrogenase in muscle from vertebrates and invertebrates. *Biochem J*, *154*(3), 689-700. https://doi.org/10.1042/bj1540689

Altmann, R. (1890). *Die Elementarorganismen und ihre beziehungen zu den Zellen*. Veit.

Anastacio, M. M., Kanter, E. M., Makepeace, C. M., Keith, A. D., Zhang, H., Schuessler, R. B., Nichols, C. G., & Lawton, J. S. (2013). Relationship between mitochondrial matrix volume and cellular volume in response to stress and the role of ATP-sensitive potassium channel. *Circulation*, *128*(11 Suppl 1), S130-135. https://doi.org/10.1161/CIRCULATIONAHA.112.000128

Anderson, A. J., Jackson, T. D., Stroud, D. A., & Stojanovski, D. (2019). Mitochondria-hubs for regulating cellular biochemistry: emerging concepts and networks. *Open Biol*, *9*(8), 190126. https://doi.org/10.1098/rsob.190126

Andreyev, A. Y., Kushnareva, Y. E., & Starkov, A. A. (2005). Mitochondrial metabolism of reactive oxygen species. *Biochemistry (Mosc)*, *70*(2), 200-214. https://doi.org/10.1007/s10541-005-0102-7

Aoki, C., Milner, T. A., Berger, S. B., Sheu, K. F., Blass, J. P., & Pickel, V. M. (1987). Glial glutamate dehydrogenase: ultrastructural localization and regional distribution in relation to the mitochondrial enzyme, cytochrome oxidase. *J Neurosci Res*, *18*(2), 305-318. https://doi.org/10.1002/jnr.490180207

Archacka, K., Grabowska, I., Mierzejewski, B., Graffstein, J., Gorzynska, A., Krawczyk, M., Rozycka, A. M., Kalaszczynska, I., Muras, G., Streminska, W., Janczyk-Ilach, K., Walczak, P., Janowski, M., Ciemerych, M. A., & Brzoska, E. (2021). Hypoxia preconditioned bone marrow-derived mesenchymal stromal/stem cells enhance myoblast fusion and skeletal muscle regeneration. *Stem Cell Res Ther*, *12*(1), 448. https://doi.org/10.1186/s13287-021-02530-3

Argyropoulos, G., & Harper, M. E. (2002). Uncoupling proteins and thermoregulation. *J Appl Physiol (1985)*, *92*(5), 2187-2198. https://doi.org/10.1152/japplphysiol.00994.2001

Arnold, J. T., Bailey, S. J., Hodder, S. G., Fujii, N., & Lloyd, A. B. (2021). Independent and combined impact of hypoxia and acute inorganic nitrate ingestion on thermoregulatory responses to the cold. *Eur J Appl Physiol*, *121*(4), 1207-1218. https://doi.org/10.1007/s00421-021-04602-x

Arteaga, O., Alvarez, A., Revuelta, M., Santaolalla, F., Urtasun, A., & Hilario, E. (2017). Role of Antioxidants in Neonatal Hypoxic-Ischemic Brain Injury: New Therapeutic Approaches. *Int J Mol Sci*, *18*(2), Article 265. https://doi.org/10.3390/ijms18020265

Ashby, M. C., & Tepikin, A. V. (2001). ER calcium and the functions of intracellular organelles. *Semin Cell Dev Biol*, *12*(1), 11-17. https://doi.org/10.1006/scdb.2000.0212

Bailey, D. M., Davies, B., & Baker, J. (2000). Training in hypoxia: modulation of metabolic and cardiovascular risk factors in men. *Med Sci Sports Exerc*, *32*(6), 1058-1066. https://doi.org/10.1097/00005768-200006000-00004

Bailey, D. M., Young, I. S., McEneny, J., Lawrenson, L., Kim, J., Barden, J., & Richardson, R. S. (2004). Regulation of free radical outflow from an isolated muscle bed in exercising humans. *Am J Physiol Heart Circ Physiol*, *287*(4), H1689-1699. https://doi.org/10.1152/ajpheart.00148.2004

Bakeeva, L., Vays, V., Vangeli, I., Eldarov, C., Holtze, S., Hildebrandt, T., & Skulachev, V. (2019). Delayed Onset of Age-Dependent Changes in Ultrastructure of Myocardial Mitochondria as One of the Neotenic Features in Naked Mole Rats (Heterocephalus glaber). *Int J Mol Sci*, *20*(3), 566. https://doi.org/10.3390/ijms20030566

Ballinger, M. A., & Andrews, M. T. (2018). Nature's fat-burning machine: brown adipose tissue in a hibernating mammal. *J Exp Biol*, *221*(Pt Suppl 1). https://doi.org/10.1242/jeb.162586

Bangsbo, J. (2000). Muscle oxygen uptake in humans at onset of and during intense exercise. *Acta Physiol Scand*, *168*(4), 457-464. https://doi.org/10.1046/j.1365-201x.2000.00697.x

Bangsbo, J., & Hellsten, Y. (1998). Muscle blood flow and oxygen uptake in recovery from exercise. *Acta Physiol Scand*, *162*(3), 305-312. https://doi.org/10.1046/j.1365-201X.1998.0331e.x

Baracca, A., Chiaradonna, F., Sgarbi, G., Solaini, G., Alberghina, L., & Lenaz, G. (2010). Mitochondrial Complex I decrease is responsible for bioenergetic dysfunction in K-ras transformed cells. *Biochim Biophys Acta*, *1797*(2), 314-323. https://doi.org/10.1016/j.bbabio.2009.11.006

Baracca, A., Sgarbi, G., Mattiazzi, M., Casalena, G., Pagnotta, E., Valentino, M. L., Moggio, M., Lenaz, G., Carelli, V., & Solaini, G. (2007). Biochemical phenotypes associated with the mitochondrial ATP6 gene mutations at nt8993. *Biochim Biophys Acta*, *1767*(7), 913-919. https://doi.org/10.1016/j.bbabio.2007.05.005

Barger, J. L., Barnes, B. M., & Boyer, B. B. (2006). Regulation of UCP1 and UCP3 in arctic ground squirrels and relation with mitochondrial proton leak. *J Appl Physiol (1985)*, *101*(1), 339-347. https://doi.org/10.1152/japplphysiol.01260.2005

Baron, J. C. (2018). Protecting the ischaemic penumbra as an adjunct to thrombectomy for acute stroke. *Nat Rev Neurol*, *14*(6), 325-337. https://doi.org/10.1038/s41582-018-0002-2

Barros, R. C., Zimmer, M. E., Branco, L. G., & Milsom, W. K. (2001). Hypoxic metabolic response of the golden-mantled ground squirrel. *J Appl Physiol (1985)*, *91*(2), 603-612. https://doi.org/10.1152/jappl.2001.91.2.603

Basse, A. L., Isidor, M. S., Winther, S., Skjoldborg, N. B., Murholm, M., Andersen, E. S., Pedersen, S. B., Wolfrum, C., Quistorff, B., & Hansen, J. B. (2017). Regulation of glycolysis in brown adipocytes by HIF-1alpha. *Sci Rep*, *7*(1), 4052. https://doi.org/10.1038/s41598-017-04246-y

Baughman, J. M., Perocchi, F., Girgis, H. S., Plovanich, M., Belcher-Timme, C. A., Sancak, Y., Bao, X. R., Strittmatter, L., Goldberger, O., Bogorad, R. L., Koteliansky, V., & Mootha, V. K. (2011). Integrative genomics identifies MCU as an essential component of the mitochondrial calcium uniporter. *Nature*, *476*(7360), 341-345. https://doi.org/10.1038/nature10234

Beaudry, J. L., & McClelland, G. B. (2010). Thermogenesis in CD-1 mice after combined chronic hypoxia and cold acclimation. *Comp Biochem Physiol B Biochem Mol Biol*, *157*(3), 301-309. https://doi.org/10.1016/j.cbpb.2010.07.004

Benda, C. (1898). Weitere Mitteilungen über die Mitochondria. *Verh Dtsch Physiol Ges*, 376-383.

Bennett, C. F., Latorre-Muro, P., & Puigserver, P. (2022). Mechanisms of mitochondrial respiratory adaptation. *Nat Rev Mol Cell Biol*. https://doi.org/10.1038/s41580-022-00506-6

Benzi, G., Pastoris, O., & Dossena, M. (1982). Relationships between gamma-aminobutyrate and succinate cycles during and after cerebral ischemia. *J Neurosci Res*, *7*(2), 193-201. https://doi.org/10.1002/jnr.490070210

Bernardi, P., & Petronilli, V. (1996). The permeability transition pore as a mitochondrial calcium release channel: a critical appraisal. *J Bioenerg Biomembr*, *28*(2), 131-138. https://doi.org/10.1007/BF02110643

Bertero, E., & Maack, C. (2018). Calcium Signaling and Reactive Oxygen Species in Mitochondria. *Circ Res*, *122*(10), 1460-1478. https://doi.org/10.1161/CIRCRESAHA.118.310082

Bertholet, A. M., & Kirichok, Y. (2022). Mitochondrial H(+) Leak and Thermogenesis. *Annu Rev Physiol*, *84*, 381-407. https://doi.org/10.1146/annurev-physiol-021119-034405

Bhowmick, S., & Drew, K. L. (2017). Arctic ground squirrel resist peroxynitrite-mediated cell death in response to oxygen glucose deprivation. *Free Radic Biol Med*, *113*, 203-211. https://doi.org/10.1016/j.freeradbiomed.2017.09.024

Bickler, P. E., & Buck, L. T. (2007). Hypoxia tolerance in reptiles, amphibians, and fishes: life with variable oxygen availability. *Annu Rev Physiol*, *69*, 145-170. https://doi.org/10.1146/annurev.physiol.69.031905.162529

Bota, D. A., & Davies, K. J. (2001). Protein degradation in mitochondria: implications for oxidative stress, aging and disease: a novel etiological classification of mitochondrial proteolytic disorders. *Mitochondrion*, *1*(1), 33-49. https://doi.org/10.1016/s1567-7249(01)00005-8

Boveris, A., & Chance, B. (1973). The mitochondrial generation of hydrogen peroxide. General properties and effect of hyperbaric oxygen. *Biochem J*, *134*(3), 707-716. https://doi.org/10.1042/bj1340707

Breen, E., Tang, K., Olfert, M., Knapp, A., & Wagner, P. (2008). Skeletal muscle capillarity during hypoxia: VEGF and its activation. *High Alt Med Biol*, *9*(2), 158-166. https://doi.org/10.1089/ham.2008.1010

Brookes, P. S., Yoon, Y., Robotham, J. L., Anders, M. W., & Sheu, S. S. (2004). Calcium, ATP, and ROS: a mitochondrial love-hate triangle. *Am J Physiol Cell Physiol*, *287*(4), C817-833. https://doi.org/10.1152/ajpcell.00139.2004

Bruick, R. K. (2003). Oxygen sensing in the hypoxic response pathway: regulation of the hypoxia-inducible transcription factor. *Genes Dev*, *17*(21), 2614-2623. https://doi.org/10.1101/gad.1145503

Bryan, R. M., Jr., & Jones, D. R. (1980). Cerebral energy metabolism in diving and non-diving birds during hypoxia and apnoeic asphyxia. *J Physiol*, *299*, 323-336. https://doi.org/10.1113/jphysiol.1980.sp013127

Budd, S. L. (1998). Mechanisms of Neuronal Damage in Brain Hypoxia/Ischemia. *Pharmacology & therapeutics*, *80*(2), 203-229. https://doi.org/10.1016/s0163-7258(98)00029-1

Buffenstein, R., Amoroso, V., Andziak, B., Avdieiev, S., Azpurua, J., Barker, A. J., Bennett, N. C., Brieno-Enriquez, M. A., Bronner, G. N., Coen, C., Delaney, M. A., Dengler-Crish, C. M., Edrey, Y. H., Faulkes, C. G., Frankel, D., Friedlander, G., Gibney, P. A., Gorbunova, V., Hine, C., . . . Smith, E. S. J. (2021). The naked truth: a comprehensive clarification and classification of current 'myths' in naked mole-rat biology. *Biol Rev Camb Philos Soc*. https://doi.org/10.1111/brv.12791

Buffenstein, R., Amoroso, V., Andziak, B., Avdieiev, S., Azpurua, J., Barker, A. J., Bennett, N. C., Brieno-Enriquez, M. A., Bronner, G. N., Coen, C., Delaney, M. A., Dengler-Crish, C. M., Edrey, Y. H., Faulkes, C. G., Frankel, D., Friedlander, G., Gibney, P. A., Gorbunova, V., Hine, C., . . . Smith, E. S. J. (2022). The naked truth: a comprehensive clarification and classification of current 'myths' in naked mole-rat biology. *Biol Rev Camb Philos Soc*, *97*(1), 115-140. https://doi.org/10.1111/brv.12791

Buffenstein, R., & Yahav, S. (1991). Is the naked mole-rat Hererocephalus glaber an endothermic yet poikilothermic mammal? *Journal of Thermal Biology*, *16*(4), 227-232. https://doi.org/10.1016/0306-4565(91)90030-6

Burtscher, J., Mallet, R. T., Burtscher, M., & Millet, G. P. (2021). Hypoxia and brain aging: Neurodegeneration or neuroprotection? *Ageing research reviews*, *68*, 101343. https://doi.org/10.1016/j.arr.2021.101343

Busiello, R. A., Savarese, S., & Lombardi, A. (2015). Mitochondrial uncoupling proteins and energy metabolism. *Front Physiol*, *6*, 36. https://doi.org/10.3389/fphys.2015.00036

Buskila, Y., Breen, P. P., Tapson, J., van Schaik, A., Barton, M., & Morley, J. W. (2014). Extending the viability of acute brain slices. *Sci Rep*, *4*, 5309. https://doi.org/10.1038/srep05309

Butler, P. J., & Stephenson, R. (1988). Chemoreceptor control of heart rate and behaviour during diving in the tufted duck (Aythya fuligula). *J Physiol*, *397*, 63-80. https://doi.org/10.1113/jphysiol.1988.sp016988

Cabanac, A. J., Messelt, E. B., Folkow, L. P., & Blix, A. S. (1999). The structure and blood-storing function of the spleen of the hooded seal (Cystophora cristata). *Journal of Zoology*, *248*(1), 75-81. https://doi.org/10.1111/j.1469-7998.1999.tb01024.x

Campian, J. L., Qian, M., Gao, X., & Eaton, J. W. (2004). Oxygen tolerance and coupling of mitochondrial electron transport. *J Biol Chem*, *279*(45), 46580-46587. https://doi.org/10.1074/jbc.M406685200

Cannon, B., & Nedergaard, J. (2004). Brown adipose tissue: function and physiological significance. *Physiol Rev*, *84*(1), 277-359. https://doi.org/10.1152/physrev.00015.2003

Carafoli, E., Gamble, R. L., & Lehninger, A. L. (1966). Rebounds and oscillations in respiration-linked movements of Ca++ and H+ in rat liver mitochondria. *J Biol Chem*, *241*(11), 2644-2652. https://doi.org/10.1016/S0021-9258(18)96588-9

Carreau, A., Hafny-Rahbi, B. E., Matejuk, A., Grillon, C., & Kieda, C. (2011). Why is the partial oxygen pressure of human tissues a crucial parameter? Small molecules and hypoxia. *Journal of Cellular and Molecular Medicine*, *15*(6), 1239-1253. https://doi.org/10.1111/j.1582-4934.2011.01258.x

Cazevielle, C., Muller, A., Meynier, F., & Bonne, C. (1993). Superoxide and nitric oxide cooperation in hypoxia/ reoxygenation-induced neuron injury. *Free Radical Biology and Medicine*, *14*(4), 389-395. https://doi.org/10.1016/0891-5849(93)90088-c

Cereghetti, G. M., Stangherlin, A., Martins de Brito, O., Chang, C. R., Blackstone, C., Bernardi, P., & Scorrano, L. (2008). Dephosphorylation by calcineurin regulates translocation of Drp1 to mitochondria. *Proc Natl Acad Sci U S A*, *105*(41), 15803-15808. https://doi.org/10.1073/pnas.0808249105

Chaillou, T. (2018). Skeletal Muscle Fiber Type in Hypoxia: Adaptation to High-Altitude Exposure and Under Conditions of Pathological Hypoxia. *Front Physiol*, *9*, 1450. https://doi.org/10.3389/fphys.2018.01450

Chance, B., & Williams, G. R. (1955). A method for the localization of sites for oxidative phosphorylation. *Nature*, *176*(4475), 250-254. https://doi.org/10.1038/176250a0

Chandel, N. S. (2015). Evolution of Mitochondria as Signaling Organelles. *Cell Metab*, *22*(2), 204-206. https://doi.org/10.1016/j.cmet.2015.05.013

Chao, D., & Xia, Y. (2010). Ionic storm in hypoxic/ischemic stress: can opioid receptors subside it? *Prog Neurobiol*, *90*(4), 439-470. https://doi.org/10.1016/j.pneurobio.2009.12.007

Cheng, H., Munro, D., Huynh, K., & Pamenter, M. E. (2021a). Naked mole-rat skeletal muscle mitochondria exhibit minimal functional plasticity in acute or chronic hypoxia. *Comp Biochem Physiol B Biochem Mol Biol*, *255*, 110596. https://doi.org/10.1016/j.cbpb.2021.110596

Cheng, H., & Pamenter, M. E. (2021). Naked mole-rat brain mitochondria tolerate in vitro ischaemia. *J Physiol*, *599*(20), 4671-4685. https://doi.org/10.1113/JP281942

Cheng, H., Sebaa, R., Malholtra, N., Lacoste, B., El Hankouri, Z., Kirby, A., Bennett, N. C., van Jaarsveld, B., Hart, D. W., Tattersall, G. J., Harper, M. E., & Pamenter, M. E. (2021b). Naked mole-rat brown fat thermogenesis is diminished during hypoxia through a rapid decrease in UCP1. *Nat Commun*, *12*(1), 6801. https://doi.org/10.1038/s41467-021-27170-2

Chinopoulos, C., Kiss, G., Kawamata, H., & Starkov, A. A. (2014). Measurement of ADP-ATP exchange in relation to mitochondrial transmembrane potential and oxygen consumption. *Methods Enzymol*, *542*, 333-348. https://doi.org/10.1016/B978-0-12-416618-9.00017-0

Chipurupalli, S., Kannan, E., Tergaonkar, V., D'Andrea, R., & Robinson, N. (2019). Hypoxia Induced ER Stress Response as an Adaptive Mechanism in Cancer. *Int J Mol Sci*, *20*(3), 749. https://doi.org/10.3390/ijms20030749

Chiu, D. K.-C., Pui-Wah Tse, A., Law, C. T., Ming-Jing Xu, I., Lee, D., Chen, M., Kit-Ho Lai, R., Wai-Hin Yuen, V., Wing-Sum Cheu, J., Wai-Hung Ho, D., Wong, C. M., Zhang, H., Oi-Lin Ng, I., & Chak-Lui Wong, C. (2019). Hypoxia regulates the mitochondrial activity of hepatocellular carcinoma cells through HIF/HEY1/PINK1 pathway. *Cell Death Dis*, *10*(12), 934. https://doi.org/10.1038/s41419-019-2155-3

Choi, D. W., & Rothman, S. M. (1990). The role of glutamate neurotoxicity in hypoxic-ischemic neuronal death. *Annu Rev Neurosci*, *13*, 171-182. https://doi.org/10.1146/annurev.ne.13.030190.001131

Chouchani, E. T., Kazak, L., Jedrychowski, M. P., Lu, G. Z., Erickson, B. K., Szpyt, J., Pierce, K. A., Laznik-Bogoslavski, D., Vetrivelan, R., Clish, C. B., Robinson, A. J., Gygi, S. P., & Spiegelman, B. M. (2016a). Mitochondrial ROS regulate thermogenic energy expenditure and sulfenylation of UCP1. *Nature*, *532*(7597), 112-116. https://doi.org/10.1038/nature17399

Chouchani, E. T., Pell, V. R., Gaude, E., Aksentijevic, D., Sundier, S. Y., Robb, E. L., Logan, A., Nadtochiy, S. M., Ord, E. N. J., Smith, A. C., Eyassu, F., Shirley, R., Hu, C. H., Dare, A. J., James, A. M., Rogatti, S., Hartley, R. C., Eaton, S., Costa, A. S. H., . . . Murphy, M. P. (2014). Ischaemic accumulation of succinate controls reperfusion injury through mitochondrial ROS. *Nature*, *515*(7527), 431-435. https://doi.org/10.1038/nature13909

Chouchani, E. T., Pell, V. R., James, A. M., Work, L. M., Saeb-Parsy, K., Frezza, C., Krieg, T., & Murphy, M. P. (2016b). A Unifying Mechanism for Mitochondrial Superoxide Production during Ischemia-Reperfusion Injury. *Cell Metab*, *23*(2), 254-263. https://doi.org/10.1016/j.cmet.2015.12.009

Christian, S. L., Ross, A. P., Zhao, H. W., Kristenson, H. J., Zhan, X., Rasley, B. T., Bickler, P. E., & Drew, K. L. (2008). Arctic ground squirrel (Spermophilus parryii) hippocampal neurons tolerate prolonged oxygen-glucose deprivation and maintain baseline ERK1/2 and JNK activation despite drastic ATP loss. *J Cereb Blood Flow Metab*, *28*(7), 1307-1319. https://doi.org/10.1038/jcbfm.2008.20

Chung, D., Dzal, Y. A., Seow, A., Milsom, W. K., & Pamenter, M. E. (2016). Naked mole rats exhibit metabolic but not ventilatory plasticity following chronic sustained hypoxia. *Proc Biol Sci*, *283*(1827), 20160216. https://doi.org/10.1098/rspb.2016.0216

Cinti, S. (2006). The role of brown adipose tissue in human obesity. *Nutr Metab Cardiovasc Dis*, *16*(8), 569-574. https://doi.org/10.1016/j.numecd.2006.07.009

Clanton, T. L. (2007). Hypoxia-induced reactive oxygen species formation in skeletal muscle. *J Appl Physiol (1985)*, *102*(6), 2379-2388. https://doi.org/10.1152/japplphysiol.01298.2006

Clark, B. J., & Coburn, R. F. (1975). Mean myoglobin oxygen tension during exercise at maximal oxygen uptake. *J Appl Physiol*, *39*(1), 135-144. https://doi.org/10.1152/jappl.1975.39.1.135

Clarke, R. J., Catauro, M., Rasmussen, H. H., & Apell, H. J. (2013). Quantitative calculation of the role of the Na(+),K(+)-ATPase in thermogenesis. *Biochim Biophys Acta*, *1827*(10), 1205-1212. https://doi.org/10.1016/j.bbabio.2013.06.010

Clausen, T. (2013). Quantification of Na+,K+ pumps and their transport rate in skeletal muscle: functional significance. *J Gen Physiol*, *142*(4), 327-345. https://doi.org/10.1085/jgp.201310980

Comellas, A. P., Dada, L. A., Lecuona, E., Pesce, L. M., Chandel, N. S., Quesada, N., Budinger, G. R., Strous, G. J., Ciechanover, A., & Sznajder, J. I. (2006). Hypoxia-mediated degradation of Na,K-ATPase via mitochondrial reactive oxygen species and the ubiquitin-conjugating system. *Circ Res*, *98*(10), 1314-1322. https://doi.org/10.1161/01.RES.0000222418.99976.1d

Connolly, E., & Nedergaard, J. (1988). Beta-adrenergic modulation of Ca2+ uptake by isolated brown adipocytes. Possible involvement of mitochondria. *J Biol Chem*, *263*(22), 10574-10582. https://www.ncbi.nlm.nih.gov/pubmed/2839496

Country, M. W., & Jonz, M. G. (2021). Mitochondrial KATP channels stabilize intracellular Ca2+ during hypoxia in retinal horizontal cells of goldfish (Carassius auratus). *J Exp Biol*, *224*(18). https://doi.org/10.1242/jeb.242634

Crescenzo, R., Spagnuolo, M. S., Cancelliere, R., Iannotta, L., Mazzoli, A., Gatto, C., Iossa, S., & Cigliano, L. (2019). Effect of Initial Aging and High-Fat/High-Fructose Diet on Mitochondrial Bioenergetics and Oxidative Status in Rat Brain. *Mol Neurobiol*, *56*(11), 7651-7663. https://doi.org/10.1007/s12035-019-1617-z

Croft, C. L., Futch, H. S., Moore, B. D., & Golde, T. E. (2019). Organotypic brain slice cultures to model neurodegenerative proteinopathies. *Mol Neurodegener*, *14*(1), 45. https://doi.org/10.1186/s13024-019-0346-0

D'Alecy, L. G., Lundy, E. F., Kluger, M. J., Harker, C. T., LeMay, D. R., & Shlafer, M. (1990). Beta-hydroxybutyrate and response to hypoxia in the ground squirrel, Spermophilus tridecimlineatus. *Comp Biochem Physiol B*, *96*(1), 189-193. https://doi.org/10.1016/0305-0491(90)90361-v

D'Hulst, G., & Deldicque, L. (2017). Human skeletal muscle wasting in hypoxia: a matter of hypoxic dose? *J Appl Physiol (1985)*, *122*(2), 406-408. https://doi.org/10.1152/japplphysiol.00264.2016

Daly, T. J., Williams, L. A., & Buffenstein, R. (1997). Catecholaminergic innervation of interscapular brown adipose tissue in the naked mole-rat (Heterocephalus glaber). *J Anat*, *190 (Pt 3)*(Pt 3), 321-326. https://doi.org/10.1046/j.1469-7580.1997.19030321.x

Dang, K., & Myers, K. A. (2015). The role of hypoxia-induced miR-210 in cancer progression. *Int J Mol Sci*, *16*(3), 6353-6372. https://doi.org/10.3390/ijms16036353

Dave, K. R., Prado, R., Raval, A. P., Drew, K. L., & Perez-Pinzon, M. A. (2006). The arctic ground squirrel brain is resistant to injury from cardiac arrest during euthermia. *Stroke*, *37*(5), 1261-1265. https://doi.org/10.1161/01.STR.0000217409.60731.38

Dawson, N. J., Lyons, S. A., Henry, D. A., & Scott, G. R. (2018). Effects of chronic hypoxia on diaphragm function in deer mice native to high altitude. *Acta Physiol (Oxf)*, *223*(1), e13030. https://doi.org/10.1111/apha.13030

Dawson, N. J., & Scott, G. R. (2022). Adaptive increases in respiratory capacity and O(2) affinity of subsarcolemmal mitochondria from skeletal muscle of high-altitude deer mice. *Faseb J*, *36*(7), e22391. https://doi.org/10.1096/fj.202200219R

de Meis, L. (2003). Brown adipose tissue Ca2+-ATPase: uncoupled ATP hydrolysis and thermogenic activity. *J Biol Chem*, *278*(43), 41856-41861. https://doi.org/10.1074/jbc.M308280200

De Meis, L., Ketzer, L. A., Camacho-Pereira, J., & Galina, A. (2012). Brown adipose tissue mitochondria: modulation by GDP and fatty acids depends on the respiratory substrates. *Biosci Rep*, *32*(1), 53-59. https://doi.org/10.1042/BSR20100144 de Meis, L., Ketzer, L. A., da Costa, R. M., de Andrade, I. R., & Benchimol, M. (2010). Fusion of the endoplasmic reticulum and mitochondrial outer membrane in rats brown adipose tissue: activation of thermogenesis by Ca2+. *PLoS One*, *5*(3), e9439. https://doi.org/10.1371/journal.pone.0009439

Deguil, J., Ravasi, L., Lanteaume, L., Lamberty, Y., & Bordet, R. (2016). Translational Challenge Models in Support of Efficacy Studies: Effect of Cerebral Hypoxia on Cognitive Performances in Rodents. *CNS Neurol Disord Drug Targets*, *15*(7), 765-776. https://doi.org/10.2174/1871527315666160518124926

Demirkaya, S., Topcuoglu, M. A., Aydin, A., Ulas, U. H., Isimer, A. I., & Vural, O. (2001). Malondialdehyde, glutathione peroxidase and superoxide dismutase in peripheral blood erythrocytes of patients with acute cerebral ischemia. *Eur J Neurol*, *8*(1), 43-51. https://doi.org/10.1046/j.1468-1331.2001.00166.x

Devaux, J. B. L., Hickey, A. J. R., & Renshaw, G. M. C. (2019). Mitochondrial plasticity in the cerebellum of two anoxia-tolerant sharks: contrasting responses to anoxia/re-oxygenation. *J Exp Biol*, *222*(Pt 6). https://doi.org/10.1242/jeb.191353

Dingledine, R., Borges, K., Bowie, D., & Traynelis, S. F. (1999). The glutamate receptor ion channels. *Pharmacol Rev*, *51*(1), 7-61. https://www.ncbi.nlm.nih.gov/pubmed/10049997

Dlasková, A., Clarke, K. J., Rooney, M. F., & Porter, R. K. (2021). The Use of Reactive Oxygen Species Production by Succinate-Driven Reverse Electron Flow as an Index of Complex 1 Activity in Isolated Brown Adipose Tissue Mitochondria. In *Methods in Molecular Biology* (pp. 247-258). Springer US. https://doi.org/10.1007/978-1-0716-1433-4_13

Dong, G., Chen, T., Ren, X., Zhang, Z., Huang, W., Liu, L., Luo, P., & Zhou, H. (2016). Rg1 prevents myocardial hypoxia/reoxygenation injury by regulating mitochondrial dynamics imbalance via modulation of glutamate dehydrogenase and mitofusin 2. *Mitochondrion*, *26*, 7-18. https://doi.org/10.1016/j.mito.2015.11.003

Dringen, R., Hoepken, H. H., Minich, T., & Ruedig, C. (2007). 1.3 Pentose Phosphate Pathway and NADPH Metabolism. In *Handbook of Neurochemistry and Molecular Neurobiology* (pp. 41-62). https://doi.org/10.1007/978-0-387-30411-3_3

Droge, W. (2002). Free radicals in the physiological control of cell function. *Physiol Rev*, *82*(1), 47-95. https://doi.org/10.1152/physrev.00018.2001

Du, S. N., Mahalingam, S., Borowiec, B. G., & Scott, G. R. (2016). Mitochondrial physiology and reactive oxygen species production are altered by hypoxia acclimation in killifish (Fundulus heteroclitus). *J Exp Biol*, *219*(Pt 8), 1130-1138. https://doi.org/10.1242/jeb.132860

Eaton, L., Wang, T., Roy, M., & Pamenter, M. E. (2022). Naked Mole-Rat Cortex Maintains Reactive Oxygen Species Homeostasis During in vitro Hypoxia or Ischemia and Reperfusion. *Curr Neuropharmacol*. https://doi.org/10.2174/1570159X20666220327220929

Eisner, V., Picard, M., & Hajnoczky, G. (2018). Mitochondrial dynamics in adaptive and maladaptive cellular stress responses. *Nat Cell Biol*, *20*(7), 755-765. https://doi.org/10.1038/s41556-018-0133-0

Emaus, R. K., Grunwald, R., & Lemasters, J. J. (1986). Rhodamine 123 as a probe of transmembrane potential in isolated rat-liver mitochondria: spectral and metabolic properties. *Biochimica et Biophysica Acta (BBA) - Bioenergetics*, *850*(3), 436-448. https://doi.org/10.1016/0005-2728(86)90112-x

Enerback, S., Jacobsson, A., Simpson, E. M., Guerra, C., Yamashita, H., Harper, M. E., & Kozak, L. P. (1997). Mice lacking mitochondrial uncoupling protein are cold-sensitive but not obese. *Nature*, *387*(6628), 90-94. https://doi.org/10.1038/387090a0

Fan, X., Jin, W. Y., & Wang, Y. T. (2014). The NMDA receptor complex: a multifunctional machine at the glutamatergic synapse. *Front Cell Neurosci*, *8*, 160. https://doi.org/10.3389/fncel.2014.00160

Farhat, E., Devereaux, M. E. M., Cheng, H., Weber, J. M., & Pamenter, M. E. (2021). Na(+)/K(+)-ATPase activity is regionally regulated by acute hypoxia in naked mole-rat brain. *Neurosci Lett*, *764*, 136244. https://doi.org/10.1016/j.neulet.2021.136244

Farhat, E., Devereaux, M. E. M., Pamenter, M. E., & Weber, J. M. (2020). Naked mole-rats suppress energy metabolism and modulate membrane cholesterol in chronic hypoxia. *Am J Physiol Regul Integr Comp Physiol*, *319*(2), R148-R155. https://doi.org/10.1152/ajpregu.00057.2020

Favaro, G., Romanello, V., Varanita, T., Andrea Desbats, M., Morbidoni, V., Tezze, C., Albiero, M., Canato, M., Gherardi, G., De Stefani, D., Mammucari, C., Blaauw, B., Boncompagni, S., Protasi, F., Reggiani, C., Scorrano, L., Salviati, L., & Sandri, M. (2019). DRP1-mediated mitochondrial shape controls calcium homeostasis and muscle mass. *Nat Commun*, *10*(1), 2576. https://doi.org/10.1038/s41467-019-10226-9

Ferdinand, P., & Roffe, C. (2016). Hypoxia after stroke: a review of experimental and clinical evidence. *Experimental & translational stroke medicine*, *8*(1), 9-9. https://doi.org/10.1186/s13231-016-0023-0

Fernandez-Garcia, J., Altea-Manzano, P., Pranzini, E., & Fendt, S. M. (2020). Stable Isotopes for Tracing Mammalian-Cell Metabolism In Vivo. *Trends Biochem Sci*, *45*(3), 185-201. https://doi.org/10.1016/j.tibs.2019.12.002

Fernandez-Lopez, D., Martinez-Orgado, J., Casanova, I., Bonet, B., Leza, J. C., Lorenzo, P., Moro, M. A., & Lizasoain, I. (2005). Immature rat brain slices exposed to oxygen-glucose deprivation as an in vitro model of neonatal hypoxic-ischemic encephalopathy. *J Neurosci Methods*, *145*(1-2), 205-212. https://doi.org/10.1016/j.jneumeth.2005.01.005

Fernstrom, J. D., & Fernstrom, M. H. (2007). Tyrosine, phenylalanine, and catecholamine synthesis and function in the brain. *J Nutr*, *137*(6 Suppl 1), 1539S-1547S; discussion 1548S. https://doi.org/10.1093/jn/137.6.1539S

Ferri, K. F., & Kroemer, G. (2001). Organelle-specific initiation of cell death pathways. *Nat Cell Biol*, *3*(11), E255-263. https://doi.org/10.1038/ncb1101-e255

Finkel, T. (2012). Signal transduction by mitochondrial oxidants. *J Biol Chem*, *287*(7), 4434-4440. https://doi.org/10.1074/jbc.R111.271999

Fiori, C. Z., Martinez, D., Baronio, D., da Rosa, D. P., Kretzmann, N. A., Forgiarini, L. F., Montanari, C. C., Marroni, N. P., & Carissimi, A. (2014). Downregulation of uncoupling protein-1 mRNA expression and hypoadiponectinemia in a mouse model of sleep apnea. *Sleep Breath*, *18*(3), 541-548. https://doi.org/10.1007/s11325-013-0916-2

Fitzgerald, E., Roberts, J., Tennant, D. A., Boardman, J. P., & Drake, A. J. (2021). Metabolic adaptations to hypoxia in the neonatal mouse forebrain can occur independently of the transporters SLC7A5 and SLC3A2. *Sci Rep*, *11*(1), 9092. https://doi.org/10.1038/s41598-021-88757-9

Fontana-Ayoub, M., Fasching, M., & Gnaiger, E. (2016). Selected media and chemicals for respirometry with mitochondrial preparations. In *Mitochondr Physiol Network* (pp. 1-10). https://wiki.oroboros.at/index.php/MiPNet03.02_Chemicals-Media

Foster, D. O., & Frydman, M. L. (1978). Nonshivering thermogenesis in the rat. II. Measurements of blood flow with microspheres point to brown adipose tissue as the dominant site of the calorigenesis induced by noradrenaline. *Can J Physiol Pharmacol*, *56*(1), 110-122. https://doi.org/10.1139/y78-015

Frappell, P., Lanthier, C., Baudinette, R. V., & Mortola, J. P. (1992). Metabolism and ventilation in acute hypoxia: a comparative analysis in small mammalian species. *Am J Physiol*, *262*(6 Pt 2), R1040-1046. https://doi.org/10.1152/ajpregu.1992.262.6.R1040

Friedman, J. R., & Nunnari, J. (2014). Mitochondrial form and function. *Nature*, *505*(7483), 335-343. https://doi.org/10.1038/nature12985

Fu, W., Hu, H., Dang, K., Chang, H., Du, B., Wu, X., & Gao, Y. (2016). Remarkable preservation of Ca(2+) homeostasis and inhibition of apoptosis contribute to anti-muscle atrophy effect in hibernating Daurian ground squirrels. *Sci Rep*, *6*, 27020. https://doi.org/10.1038/srep27020

Fuhrmann, D. C., & Brune, B. (2017). Mitochondrial composition and function under the control of hypoxia. *Redox Biol*, *12*, 208-215. https://doi.org/10.1016/j.redox.2017.02.012

Fuhrmann, D. C., Wittig, I., Heide, H., Dehne, N., & Brune, B. (2013). Chronic hypoxia alters mitochondrial composition in human macrophages. *Biochim Biophys Acta*, *1834*(12), 2750-2760. https://doi.org/10.1016/j.bbapap.2013.09.023

Galli, G. L., Lau, G. Y., & Richards, J. G. (2013). Beating oxygen: chronic anoxia exposure reduces mitochondrial F1FO-ATPase activity in turtle (Trachemys scripta) heart. *J Exp Biol*, *216*(Pt 17), 3283-3293. https://doi.org/10.1242/jeb.087155

Galluzzi, L., Kepp, O., & Kroemer, G. (2012). Mitochondria: master regulators of danger signalling. *Nat Rev Mol Cell Biol*, *13*(12), 780-788. https://doi.org/10.1038/nrm3479

Gamboa, J. L., & Andrade, F. H. (2010). Mitochondrial content and distribution changes specific to mouse diaphragm after chronic normobaric hypoxia. *Am J Physiol Regul Integr Comp Physiol*, *298*(3), R575-583. https://doi.org/10.1152/ajpregu.00320.2009

Gao, L., Ortega-Saenz, P., Moreno-Dominguez, A., & Lopez-Barneo, J. (2022). Mitochondrial Redox Signaling in O2-Sensing Chemoreceptor Cells. *Antioxid Redox Signal*, *37*(4-6), 274-289. https://doi.org/10.1089/ars.2021.0255

Garcia-Martin, R., Alexaki, V. I., Qin, N., Rubin de Celis, M. F., Economopoulou, M., Ziogas, A., Gercken, B., Kotlabova, K., Phieler, J., Ehrhart-Bornstein, M., Bornstein, S. R., Eisenhofer, G., Breier, G., Bluher, M., Hampe, J., El-Armouche, A., Chatzigeorgiou, A., Chung, K. J., & Chavakis, T. (2016). Adipocyte-Specific Hypoxia-Inducible Factor 2alpha Deficiency Exacerbates Obesity-Induced Brown Adipose Tissue Dysfunction and Metabolic Dysregulation. *Mol Cell Biol*, *36*(3), 376-393. https://doi.org/10.1128/MCB.00430-15

Garland, T., & Adolph, S. C. (1994). Why Not to Do Two-Species Comparative Studies: Limitations on Inferring Adaptation. *Physiological Zoology*, *67*(4), 797-828. https://doi.org/10.1086/physzool.67.4.30163866

Gautier, H., & Bonora, M. (1994). Ventilatory and metabolic responses to cold and CO-induced hypoxia in awake rats. *Respir Physiol*, *97*(1), 79-91. https://doi.org/10.1016/0034-5687(94)90013-2

Gautier, H., Bonora, M., M'Barek, S. B., & Sinclair, J. D. (1991). Effects of hypoxia and cold acclimation on thermoregulation in the rat. *J Appl Physiol (1985)*, *71*(4), 1355-1363. https://doi.org/10.1152/jappl.1991.71.4.1355

Gautier, H., Bonora, M., Schultz, S. A., & Remmers, J. E. (1987). Hypoxia-induced changes in shivering and body temperature. *J Appl Physiol (1985)*, *62*(6), 2477-2484. https://doi.org/10.1152/jappl.1987.62.6.2477

Gellerich, F. N., Gizatullina, Z., Trumbeckaite, S., Nguyen, H. P., Pallas, T., Arandarcikaite, O., Vielhaber, S., Seppet, E., & Striggow, F. (2010). The regulation of OXPHOS by extramitochondrial calcium. *Biochim Biophys Acta*, *1797*(6-7), 1018-1027. https://doi.org/10.1016/j.bbabio.2010.02.005

Giaccia, A. J., Simon, M. C., & Johnson, R. (2004). The biology of hypoxia: the role of oxygen sensing in development, normal function, and disease. *Genes Dev*, *18*(18), 2183-2194. https://doi.org/10.1101/gad.1243304

Giacomello, M., Pyakurel, A., Glytsou, C., & Scorrano, L. (2020). The cell biology of mitochondrial membrane dynamics. *Nature Reviews Molecular Cell Biology*, *21*(4), 204-224. https://doi.org/10.1038/s41580-020-0210-7

Giorgi, C., Marchi, S., & Pinton, P. (2018). The machineries, regulation and cellular functions of mitochondrial calcium. *Nat Rev Mol Cell Biol*, *19*(11), 713-730. https://doi.org/10.1038/s41580-018-0052-8

Glancy, B., Hartnell, L. M., Combs, C. A., Femnou, A., Sun, J., Murphy, E., Subramaniam, S., & Balaban, R. S. (2018). Power Grid Protection of the Muscle Mitochondrial Reticulum. *Cell Rep*, *23*(9), 2832. https://doi.org/10.1016/j.celrep.2018.05.055

Goldman, B. D., Goldman, S. L., Lanz, T., Magaurin, A., & Maurice, A. (1999). Factors influencing metabolic rate in naked mole-rats (Heterocephalus glaber). *Physiol Behav*, *66*(3), 447-459. https://doi.org/S0031-9384(98)00306-0 [pii]

Goncalves, R. L., Quinlan, C. L., Perevoshchikova, I. V., Hey-Mogensen, M., & Brand, M. D. (2015). Sites of superoxide and hydrogen peroxide production by muscle mitochondria assessed ex vivo under conditions mimicking rest and exercise. *J Biol Chem*, *290*(1), 209-227. https://doi.org/10.1074/jbc.M114.619072

Gordon, C. J., & Fogelson, L. (1991). Comparative Effects of Hypoxia on Behavioral Thermoregulation in Rats, Hamsters, and Mice. *American Journal of Physiology*, *260*(1), R120-R125. https://doi.org/10.1152/ajpregu.1991.260.1.R120

Gorlach, A., Bertram, K., Hudecova, S., & Krizanova, O. (2015). Calcium and ROS: A mutual interplay. *Redox Biol*, *6*, 260-271. https://doi.org/10.1016/j.redox.2015.08.010

Gottschalk, B., Madreiter-Sokolowski, C. T., & Graier, W. F. (2022). Cristae junction as a fundamental switchboard for mitochondrial ion signaling and bioenergetics. *Cell Calcium*, *101*, 102517. https://doi.org/10.1016/j.ceca.2021.102517

Green, H., Roy, B., Grant, S., Burnett, M., Tupling, R., Otto, C., Pipe, A., & McKenzie, D. (2000). Downregulation in muscle Na(+)-K(+)-ATPase following a 21-day expedition to 6,194 m. *J Appl Physiol (1985)*, *88*(2), 634-640. https://doi.org/10.1152/jappl.2000.88.2.634

Greenberg, R., Cadena, V., Danner, R. M., & Tattersall, G. J. (2012). Heat loss may explain bill size differences between birds occupying different habitats. *PLoS One*, *7*(7), e40933. https://doi.org/10.1371/journal.pone.0040933

Greggio, C., Jha, P., Kulkarni, S. S., Lagarrigue, S., Broskey, N. T., Boutant, M., Wang, X., Conde Alonso, S., Ofori, E., Auwerx, J., Canto, C., & Amati, F. (2017). Enhanced Respiratory Chain Supercomplex Formation in Response to Exercise in Human Skeletal Muscle. *Cell Metab*, *25*(2), 301-311. https://doi.org/10.1016/j.cmet.2016.11.004

Griffiths, E. J., & Rutter, G. A. (2009). Mitochondrial calcium as a key regulator of mitochondrial ATP production in mammalian cells. *Biochim Biophys Acta*, *1787*(11), 1324-1333. https://doi.org/10.1016/j.bbabio.2009.01.019

Grivennikova, V. G., & Vinogradov, A. D. (2006). Generation of superoxide by the mitochondrial Complex I. *Biochim Biophys Acta*, *1757*(5-6), 553-561. https://doi.org/10.1016/j.bbabio.2006.03.013

Guan, L., Che, Z., Meng, X., Yu, Y., Li, M., Yu, Z., Shi, H., Yang, D., & Yu, M. (2019). MCU Up-regulation contributes to myocardial ischemia-reperfusion Injury through calpain/OPA-1-mediated mitochondrial fusion/mitophagy Inhibition. *J Cell Mol Med*, *23*(11), 7830-7843. https://doi.org/10.1111/jcmm.14662

Gunter, T. E., Gunter, K. K., Sheu, S. S., & Gavin, C. E. (1994). Mitochondrial calcium transport: physiological and pathological relevance. *Am J Physiol*, *267*(2 Pt 1), C313-339. https://doi.org/10.1152/ajpcell.1994.267.2.C313

Gunter, T. E., & Pfeiffer, D. R. (1990). Mechanisms by which mitochondria transport calcium. *Am J Physiol*, *258*(5 Pt 1), C755-786. https://doi.org/10.1152/ajpcell.1990.258.5.C755

Guo, R., Gu, J., Zong, S., Wu, M., & Yang, M. (2018). Structure and mechanism of mitochondrial electron transport chain. *Biomed J*, *41*(1), 9-20. https://doi.org/10.1016/j.bj.2017.12.001

Guppy, M., & Withers, P. (1999). Metabolic depression in animals: physiological perspectives and biochemical generalizations. *Biol Rev Camb Philos Soc*, *74*(1), 1-40. https://doi.org/10.1017/s0006323198005258

Gusarova, G. A., Trejo, H. E., Dada, L. A., Briva, A., Welch, L. C., Hamanaka, R. B., Mutlu, G. M., Chandel, N. S., Prakriya, M., & Sznajder, J. I. (2011). Hypoxia leads to Na,K-ATPase downregulation via Ca(2+) release-activated Ca(2+) channels and AMPK activation. *Mol Cell Biol*, *31*(17), 3546-3556. https://doi.org/10.1128/MCB.05114-11

Hadj-Moussa, H., Chiasson, S., Cheng, H., Eaton, L., Storey, K. B., & Pamenter, M. E. (2021a). MicroRNA-mediated inhibition of AMPK coordinates tissue-specific downregulation of skeletal muscle metabolism in hypoxic naked mole-rats. *J Exp Biol*, *224*(15). https://doi.org/10.1242/jeb.242968

Hadj-Moussa, H., Eaton, L., Cheng, H., Pamenter, M. E., & Storey, K. B. (2022). Naked mole-rats resist the accumulation of hypoxia-induced oxidative damage. *Comp Biochem Physiol A Mol Integr Physiol*, *273*, 111282. https://doi.org/10.1016/j.cbpa.2022.111282

Hadj-Moussa, H., Pamenter, M. E., & Storey, K. B. (2021b). Hypoxic naked mole-rat brains use microRNA to coordinate hypometabolic fuels and neuroprotective defenses. *J Cell Physiol*, *236*(7), 5080-5097. https://doi.org/10.1002/jcp.30216

Hagl, S., Asseburg, H., Heinrich, M., Sus, N., Blumrich, E. M., Dringen, R., Frank, J., & Eckert, G. P. (2016). Effects of Long-Term Rice Bran Extract Supplementation on Survival, Cognition and Brain Mitochondrial Function in Aged NMRI Mice. *Neuromolecular Med*, *18*(3), 347-363. https://doi.org/10.1007/s12017-016-8420-z

Halestrap, A. P. (2006). Calcium, mitochondria and reperfusion injury: a pore way to die. *Biochem Soc Trans*, *34*(Pt 2), 232-237. https://doi.org/10.1042/BST20060232

Halestrap, A. P., Quinlan, P. T., Whipps, D. E., & Armston, A. E. (1986). Regulation of the mitochondrial matrix volume in vivo and in vitro. The role of calcium. *Biochem J*, *236*(3), 779-787. https://doi.org/10.1042/bj2360779

Haley, M. J., Mullard, G., Hollywood, K. A., Cooper, G. J., Dunn, W. B., & Lawrence, C. B. (2017). Adipose tissue and metabolic and inflammatory responses to stroke are altered in obese mice. *Dis Model Mech*, *10*(10), 1229-1243. https://doi.org/10.1242/dmm.030411

Hall, C. N., Klein-Flugge, M. C., Howarth, C., & Attwell, D. (2012). Oxidative phosphorylation, not glycolysis, powers presynaptic and postsynaptic mechanisms underlying brain information processing. *J Neurosci*, *32*(26), 8940-8951. https://doi.org/10.1523/JNEUROSCI.0026-12.2012

Halliwell, B. (2001). Role of free radicals in the neurodegenerative diseases: therapeutic implications for antioxidant treatment. *Drugs Aging*, *18*(9), 685-716. https://doi.org/10.2165/00002512-200118090-00004

Hamanaka, R. B., & Chandel, N. S. (2010). Mitochondrial reactive oxygen species regulate cellular signaling and dictate biological outcomes. *Trends Biochem Sci*, *35*(9), 505-513. https://doi.org/10.1016/j.tibs.2010.04.002

Hamilton, J., Brustovetsky, T., Rysted, J. E., Lin, Z., Usachev, Y. M., & Brustovetsky, N. (2018). Deletion of mitochondrial calcium uniporter incompletely inhibits calcium uptake and induction of the permeability transition pore in brain mitochondria. *J Biol Chem*, *293*(40), 15652-15663. https://doi.org/10.1074/jbc.RA118.002926

Han, X. J., Lu, Y. F., Li, S. A., Kaitsuka, T., Sato, Y., Tomizawa, K., Nairn, A. C., Takei, K., Matsui, H., & Matsushita, M. (2008). CaM kinase I alpha-induced phosphorylation of Drp1 regulates mitochondrial morphology. *J Cell Biol*, *182*(3), 573-585. https://doi.org/10.1083/jcb.200802164

Han, Y., Kim, B., Cho, U., Park, I. S., Kim, S. I., Dhanasekaran, D. N., Tsang, B. K., & Song, Y. S. (2019). Mitochondrial fission causes cisplatin resistance under hypoxic conditions via ROS in ovarian cancer cells. *Oncogene*, *38*(45), 7089-7105. https://doi.org/10.1038/s41388-019-0949-5

Hartung, J., & Cottrell, J. E. (1987). Nitrous oxide reduces thiopental-induced prolongation of survival in hypoxic and anoxic mice. *Anesth Analg*, *66*(1), 47-52. https://www.ncbi.nlm.nih.gov/pubmed/3800018

Hawkins, L. J., Hadj-Moussa, H., Nguyen, V. C., Pamenter, M. E., & Storey, K. B. (2019). Naked mole rats activate neuroprotective proteins during hypoxia. *J Exp Zool A Ecol Integr Physiol*, *331*(10), 571-576. https://doi.org/10.1002/jez.2321

Hawrysh, P. J., & Buck, L. T. (2013). Anoxia-mediated calcium release through the mitochondrial permeability transition pore silences NMDA receptor currents in turtle neurons. *J Exp Biol*, *216*(Pt 23), 4375-4387. https://doi.org/10.1242/jeb.092650

Haws, S. A., Yu, D., Ye, C., Wille, C. K., Nguyen, L. C., Krautkramer, K. A., Tomasiewicz, J. L., Yang, S. E., Miller, B. R., Liu, W. H., Igarashi, K., Sridharan, R., Tu, B. P., Cryns, V. L., Lamming, D. W., & Denu, J. M. (2020). Methyl-Metabolite Depletion Elicits Adaptive Responses to Support Heterochromatin Stability and Epigenetic Persistence. *Mol Cell*, *78*(2), 210-223 e218. https://doi.org/10.1016/j.molcel.2020.03.004

Herbers, E., Kekalainen, N. J., Hangas, A., Pohjoismaki, J. L., & Goffart, S. (2019). Tissue specific differences in mitochondrial DNA maintenance and expression. *Mitochondrion*, *44*, 85-92. https://doi.org/10.1016/j.mito.2018.01.004

Himms-Hagen, J. (1985). Brown adipose tissue metabolism and thermogenesis. *Annu Rev Nutr*, *5*, 69-94. https://doi.org/10.1146/annurev.nu.05.070185.000441

Hislop, M. S., & Buffenstein, R. (1994). Noradrenaline induces nonshivering thermogenesis in both the naked mole-rat (Heterocephalus glaber) and the Damara mole-rat (Cryptomys damarensis) despite very different modes of thermoregulation. *Journal of Thermal Biology*, *19*(1), 25-32. https://doi.org/10.1016/0306-4565(94)90006-x

Hochachka, P. W. (2000). Pinniped diving response mechanism and evolution: a window on the paradigm of comparative biochemistry and physiology. *Comp Biochem Physiol A Mol Integr Physiol*, *126*(4), 435-458. https://doi.org/10.1016/s1095-6433(00)00231-2

Hoitzing, H., Johnston, I. G., & Jones, N. S. (2015). What is the function of mitochondrial networks? A theoretical assessment of hypotheses and proposal for future research. *BioEssays*, *37*(6), 687-700. https://doi.org/10.1002/bies.201400188

Holmes, M. M., Goldman, B. D., Goldman, S. L., Seney, M. L., & Forger, N. G. (2009). Neuroendocrinology and sexual differentiation in eusocial mammals. *Front Neuroendocrinol*, *30*(4), 519-533. https://doi.org/10.1016/j.yfrne.2009.04.010

Holmstrom, M. H., Iglesias-Gutierrez, E., Zierath, J. R., & Garcia-Roves, P. M. (2012). Tissue-specific control of mitochondrial respiration in obesity-related insulin resistance and diabetes. *Am J Physiol Endocrinol Metab*, *302*(6), E731-739. https://doi.org/10.1152/ajpendo.00159.2011

Holtze, S., Braude, S., Lemma, A., Koch, R., Morhart, M., Szafranski, K., Platzer, M., Alemayehu, F., Goeritz, F., & Hildebrandt, T. B. (2018). The microenvironment of naked mole-rat burrows in East Africa. *African Journal of Ecology*, *56*(2), 279-289. https://doi.org/10.1111/aje.12448

Holtze, S., Eldarov, C. M., Vays, V. B., Vangeli, I. M., Vysokikh, M. Y., Bakeeva, L. E., Skulachev, V. P., & Hildebrandt, T. B. (2016). Study of Age-Dependent Structural and Functional Changes of Mitochondria in Skeletal Muscles and Heart of Naked Mole Rats (Heterocephalus glaber). *Biochemistry (Mosc)*, *81*(12), 1429-1437. https://doi.org/10.1134/S000629791612004X

Hoppeler, H., Kleinert, E., Schlegel, C., Claassen, H., Howald, H., Kayar, S. R., & Cerretelli, P. (1990). Morphological adaptations of human skeletal muscle to chronic hypoxia. *Int J Sports Med*, *11 Suppl 1*, S3-9. https://doi.org/10.1055/s-2007-1024846

Hoppeler, H., & Vogt, M. (2001). Muscle tissue adaptations to hypoxia. *J Exp Biol*, *204*(Pt 18), 3133-3139. https://doi.org/10.1242/jeb.204.18.3133

Hoppeler, H., Vogt, M., Weibel, E. R., & Fluck, M. (2003). Response of skeletal muscle mitochondria to hypoxia. *Exp Physiol*, *88*(1), 109-119. https://doi.org/10.1113/eph8802513

Hornbein, T. F., Townes, B. D., Schoene, R. B., Sutton, J. R., & Houston, C. S. (1989). The cost to the central nervous system of climbing to extremely high altitude. *N Engl J Med*, *321*(25), 1714-1719. https://doi.org/10.1056/NEJM198912213212505

Horscroft, J. A., & Murray, A. J. (2014). Skeletal muscle energy metabolism in environmental hypoxia: climbing towards consensus. *Extrem Physiol Med*, *3*(1), 19. https://doi.org/10.1186/2046-7648-3-19

Houlahan, C. R., Kirby, A. M., Dzal, Y. A., Fairman, G. D., & Pamenter, M. E. (2018). Divergent behavioural responses to acute hypoxia between individuals and groups of naked mole rats. *Comp Biochem Physiol B Biochem Mol Biol*, *224*, 38-44. https://doi.org/10.1016/j.cbpb.2018.01.004

Hoydal, M. A., Wisloff, U., Kemi, O. J., & Ellingsen, O. (2007). Running speed and maximal oxygen uptake in rats and mice: practical implications for exercise training. *Eur J Cardiovasc Prev Rehabil*, *14*(6), 753-760. https://doi.org/10.1097/HJR.0b013e3281eacef1

Humpel, C. (2015). Organotypic brain slice cultures: A review. *Neuroscience*, *305*, 86-98. https://doi.org/10.1016/j.neuroscience.2015.07.086

Husson, Z., & Smith, E. S. J. (2018). Naked mole-rat cortical neurons are resistant to acid-induced cell death. *Mol Brain*, *11*(1), 26. https://doi.org/10.1186/s13041-018-0369-4

Ikeda, K., & Yamada, T. (2020). UCP1 Dependent and Independent Thermogenesis in Brown and Beige Adipocytes. *Front Endocrinol (Lausanne)*, *11*, 498. https://doi.org/10.3389/fendo.2020.00498

Ilacqua, A. N., Kirby, A. M., & Pamenter, M. E. (2017). Behavioural responses of naked mole rats to acute hypoxia and anoxia. *Biol Lett*, *13*(12). https://doi.org/10.1098/rsbl.2017.0545

Ivy, C. M., Sprenger, R. J., Bennett, N. C., van Jaarsveld, B., Hart, D. W., Kirby, A. M., Yaghoubi, D., Storey, K. B., Milsom, W. K., & Pamenter, M. E. (2020). The hypoxia tolerance of eight related African mole-rat species rivals that of naked mole-rats, despite divergent ventilatory and metabolic strategies in severe hypoxia. *Acta Physiol (Oxf)*, *228*(4), e13436. https://doi.org/10.1111/apha.13436

Jackson, C. G., Sillau, A. H., & Banchero, N. (1987). Fiber composition and capillarity in growing guinea pigs acclimated to cold and cold plus hypoxia. *Proc Soc Exp Biol Med*, *185*(1), 101-106. https://doi.org/10.3181/00379727-185-42524

Jackson, D. C., & Ultsch, G. R. (1982). Long-Term Submergence at 3 °C of the Turtle, Chrysemys Picta Bellii, in Normoxic And Severely Hypoxic Water: II. Extracellular Ionic Responses to Extreme Lactic Acidosis. *Journal of Experimental Biology*, *96*(1), 29-43. https://doi.org/10.1242/jeb.96.1.29

Jacobs, R. A., Siebenmann, C., Hug, M., Toigo, M., Meinild, A. K., & Lundby, C. (2012). Twenty-eight days at 3454-m altitude diminishes respiratory capacity but enhances efficiency in human skeletal muscle mitochondria. *Faseb Journal*, *26*(12), 5192-5200. https://doi.org/10.1096/fj.12-218206

Jassem, W., Fuggle, S. V., Rela, M., Koo, D. D., & Heaton, N. D. (2002). The role of mitochondria in ischemia/reperfusion injury. *Transplantation*, *73*(4), 493-499. https://doi.org/10.1097/00007890-200202270-00001

Johansen, K., Lykkeboe, G., Weber, R. E., & Maloiy, G. M. (1976). Blood respiratory properties in the naked mole rat Heterocephalus glaber, a mammal of low body temperature. *Respir Physiol*, *28*(3), 303-314. https://doi.org/10.1016/0034-5687(76)90025-6

Joubert, F., & Puff, N. (2021). Mitochondrial Cristae Architecture and Functions: Lessons from Minimal Model Systems. *Membranes (Basel)*, *11*(7). https://doi.org/10.3390/membranes11070465

Joyner, M. J., & Casey, D. P. (2015). Regulation of increased blood flow (hyperemia) to muscles during exercise: a hierarchy of competing physiological needs. *Physiol Rev*, *95*(2), 549-601. https://doi.org/10.1152/physrev.00035.2013

Joza, N., Susin, S. A., Daugas, E., Stanford, W. L., Cho, S. K., Li, C. Y., Sasaki, T., Elia, A. J., Cheng, H. Y., Ravagnan, L., Ferri, K. F., Zamzami, N., Wakeham, A., Hakem, R., Yoshida, H., Kong, Y. Y., Mak, T. W., Zuniga-Pflucker, J. C., Kroemer, G., & Penninger, J. M. (2001). Essential role of the mitochondrial apoptosis-inducing factor in programmed cell death. *Nature*, *410*(6828), 549-554. https://doi.org/10.1038/35069004

Kaasik, A., Safiulina, D., Zharkovsky, A., & Veksler, V. (2007). Regulation of mitochondrial matrix volume. *Am J Physiol Cell Physiol*, *292*(1), C157-163. https://doi.org/10.1152/ajpcell.00272.2006

Kalback, W., Esh, C., Castano, E. M., Rahman, A., Kokjohn, T., Luehrs, D. C., Sue, L., Cisneros, R., Gerber, F., Richardson, C., Bohrmann, B., Walker, D. G., Beach, T. G., & Roher, A. E. (2004). Atherosclerosis, vascular amyloidosis and brain hypoperfusion in the pathogenesis of sporadic Alzheimer's disease. *Neurol Res*, *26*(5), 525-539. https://doi.org/10.1179/016164104225017668

Kallio, P. J., Pongratz, I., Gradin, K., McGuire, J., & Poellinger, L. (1997). Activation of hypoxia-inducible factor 1alpha: posttranscriptional regulation and conformational change by recruitment of the Arnt transcription factor. *Proc Natl Acad Sci U S A*, *94*(11), 5667-5672. https://doi.org/10.1073/pnas.94.11.5667

Kappler, L., Hoene, M., Hu, C., von Toerne, C., Li, J., Bleher, D., Hoffmann, C., Bohm, A., Kollipara, L., Zischka, H., Konigsrainer, A., Haring, H. U., Peter, A., Xu, G., Sickmann, A., Hauck, S. M., Weigert, C., & Lehmann, R. (2019). Linking bioenergetic function of mitochondria to tissue-specific molecular fingerprints. *Am J Physiol Endocrinol Metab*, *317*(2), E374-E387. https://doi.org/10.1152/ajpendo.00088.2019

Karahalil, B., Hogue, B. A., de Souza-Pinto, N. C., & Bohr, V. A. (2002). Base excision repair capacity in mitochondria and nuclei: tissue-specific variations. *Faseb J*, *16*(14), 1895-1902. https://doi.org/10.1096/fj.02-0463com

Karunadharma, P. P., Basisty, N., Chiao, Y. A., Dai, D. F., Drake, R., Levy, N., Koh, W. J., Emond, M. J., Kruse, S., Marcinek, D., Maccoss, M. J., & Rabinovitch, P. S. (2015). Respiratory chain protein turnover rates in mice are highly heterogeneous but strikingly conserved across tissues, ages, and treatments. *Faseb J*, *29*(8), 3582-3592. https://doi.org/10.1096/fj.15-272666

Kaser, M., & Langer, T. (2000). Protein degradation in mitochondria. *Semin Cell Dev Biol*, *11*(3), 181-190. https://doi.org/10.1006/scdb.2000.0166

Katsura, K., Kristian, T., & Siesjo, B. K. (1994). Energy metabolism, ion homeostasis, and cell damage in the brain. *Biochem Soc Trans*, *22*(4), 991-996. https://doi.org/10.1042/bst0220991

Kayser, B. (1992). Nutrition and high altitude exposure. *Int J Sports Med*, *13 Suppl 1*, S129-132. https://doi.org/10.1055/s-2007-1024616

Kazak, L., Chouchani, E. T., Stavrovskaya, I. G., Lu, G. Z., Jedrychowski, M. P., Egan, D. F., Kumari, M., Kong, X., Erickson, B. K., Szpyt, J., Rosen, E. D., Murphy, M. P., Kristal, B. S., Gygi, S. P., & Spiegelman, B. M. (2017). UCP1 deficiency causes brown fat respiratory chain depletion and sensitizes mitochondria to calcium overload-induced dysfunction. *Proc Natl Acad Sci U S A*, *114*(30), 7981-7986. https://doi.org/10.1073/pnas.1705406114

Kekesi, O., & Buskila, Y. (2020). Method for Prolonged Incubation of Brain Slices. *Bio Protoc*, *10*(14), e3683. https://doi.org/10.21769/BioProtoc.3683

Kerksick, C. M., & Zuhl, M. (2015). Mechanisms of Oxidative Damage and Their Impact on Contracting Muscle. In M. Lamprecht (Ed.), *Antioxidants in Sport Nutrition*. https://www.ncbi.nlm.nih.gov/pubmed/26065093

Khaspekov, L., Friberg, H., Halestrap, A., Viktorov, I., & Wieloch, T. (1999). Cyclosporin A and its nonimmunosuppressive analogue N-Me-Val-4-cyclosporin A mitigate glucose/oxygen deprivation-induced damage to rat cultured hippocampal neurons. *Eur J Neurosci*, *11*(9), 3194-3198. https://doi.org/10.1046/j.1460-9568.1999.00743.x

Kietzmann, T., & Gorlach, A. (2005). Reactive oxygen species in the control of hypoxia-inducible factor-mediated gene expression. *Semin Cell Dev Biol*, *16*(4-5), 474-486. https://doi.org/10.1016/j.semcdb.2005.03.010

Kim, M., Stepanova, A., Niatsetskaya, Z., Sosunov, S., Arndt, S., Murphy, M. P., Galkin, A., & Ten, V. S. (2018). Attenuation of oxidative damage by targeting mitochondrial complex I in neonatal hypoxic-ischemic brain injury. *Free Radic Biol Med*, *124*, 517-524. https://doi.org/10.1016/j.freeradbiomed.2018.06.040

Kingsbury, B. F. (1912). Cytoplasmic fixation. *The Anatomical record*, *6*(2), 39-52. https://doi.org/10.1002/ar.1090060202

Kinnally, K. W., Peixoto, P. M., Ryu, S. Y., & Dejean, L. M. (2011). Is mPTP the gatekeeper for necrosis, apoptosis, or both? *Biochim Biophys Acta*, *1813*(4), 616-622. https://doi.org/10.1016/j.bbamcr.2010.09.013

Kirby, A. M., Fairman, G. D., & Pamenter, M. E. (2018). Atypical behavioural, metabolic and thermoregulatory responses to hypoxia in the naked mole rat (Heterocephalus glaber). *Journal of Zoology*, *305*(2), 106-115. https://doi.org/10.1111/jzo.12542

Kissova, I., Deffieu, M., Manon, S., & Camougrand, N. (2004). Uth1p is involved in the autophagic degradation of mitochondria. *J Biol Chem*, *279*(37), 39068-39074. https://doi.org/10.1074/jbc.M406960200

Kleele, T., Rey, T., Winter, J., Zaganelli, S., Mahecic, D., Perreten Lambert, H., Ruberto, F. P., Nemir, M., Wai, T., Pedrazzini, T., & Manley, S. (2021). Distinct fission signatures predict mitochondrial degradation or biogenesis. *Nature*. https://doi.org/10.1038/s41586-021-03510-6

Knickerbocker, D. L., & Lutz, P. L. (2001). Slow ATP loss and the defense of ion homeostasis in the anoxic frog brain. *Journal of Experimental Biology*, *204*(20), 3547-3551. https://doi.org/10.1242/jeb.204.20.3547

Ko, M. S., Yun, J. Y., Baek, I. J., Jang, J. E., Hwang, J. J., Lee, S. E., Heo, S. H., Bader, D. A., Lee, C. H., Han, J., Moon, J. S., Lee, J. M., Hong, E. G., Lee, I. K., Kim, S. W., Park, J. Y., Hartig, S. M., Kang, U. J., Moore, D. D., . . . Lee, K. U. (2021). Mitophagy deficiency increases NLRP3 to induce brown fat dysfunction in mice. *Autophagy*, *17*(5), 1205-1221. https://doi.org/10.1080/15548627.2020.1753002

Kohlgruber, S., Upadhye, A., Dyballa-Rukes, N., McNamara, C. A., & Altschmied, J. (2017). Regulation of Transcription Factors by Reactive Oxygen Species and Nitric Oxide in Vascular Physiology and Pathology. *Antioxid Redox Signal*, *26*(13), 679-699. https://doi.org/10.1089/ars.2016.6946

Konishi, H., Yamauchi, E., Taniguchi, H., Yamamoto, T., Matsuzaki, H., Takemura, Y., Ohmae, K., Kikkawa, U., & Nishizuka, Y. (2001). Phosphorylation sites of protein kinase C delta in H2O2-treated cells and its activation by tyrosine kinase in vitro. *Proc Natl Acad Sci U S A*, *98*(12), 6587-6592. https://doi.org/10.1073/pnas.111158798

Kottke, F. J., Phalen, J. S., & et al. (1948). Effect of hypoxia upon temperature regulation of mice, dogs, and man. *Am J Physiol*, *153*(1), 10-15. https://doi.org/10.1152/ajplegacy.1948.153.1.10

Kozlov, A. V., Bahrami, S., Calzia, E., Dungel, P., Gille, L., Kuznetsov, A. V., & Troppmair, J. (2011). Mitochondrial dysfunction and biogenesis: do ICU patients die from mitochondrial failure? *Ann Intensive Care*, *1*(1), 41. https://doi.org/10.1186/2110-5820-1-41

Kristian, T., & Siesjo, B. K. (1998). Calcium in ischemic cell death. *Stroke*, *29*(3), 705-718. https://doi.org/10.1161/01.str.29.3.705

Kroemer, G., Galluzzi, L., & Brenner, C. (2007). Mitochondrial membrane permeabilization in cell death. *Physiol Rev*, *87*(1), 99-163. https://doi.org/10.1152/physrev.00013.2006

Kuhlbrandt, W. (2015). Structure and function of mitochondrial membrane protein complexes. *BMC Biol*, *13*, 89. https://doi.org/10.1186/s12915-015-0201-x

Kushnareva, Y., Murphy, A. N., & Andreyev, A. (2002). Complex I-mediated reactive oxygen species generation: modulation by cytochrome c and NAD(P)+ oxidation-reduction state. *Biochem J*, *368*(Pt 2), 545-553. https://doi.org/10.1042/BJ20021121

Kushnareva, Y. E., Gerencser, A. A., Bossy, B., Ju, W. K., White, A. D., Waggoner, J., Ellisman, M. H., Perkins, G., & Bossy-Wetzel, E. (2013). Loss of OPA1 disturbs cellular calcium homeostasis and sensitizes for excitotoxicity. *Cell Death Differ*, *20*(2), 353-365. https://doi.org/10.1038/cdd.2012.128

Kuznetsov, A. V., Margreiter, R., Ausserlechner, M. J., & Hagenbuchner, J. (2022). The Complex Interplay between Mitochondria, ROS and Entire Cellular Metabolism. *Antioxidants (Basel)*, *11*(10). https://doi.org/10.3390/antiox11101995

Lahiri, S., Buerk, D. G., Chugh, D., Osanai, S., & Mokashi, A. (1995). Reciprocal photolabile O2 consumption and chemoreceptor excitation by carbon monoxide in the cat carotid body : evidence for cytochrome a3 as the primary O2 sensor. *Brain research*, *684*(2), 194-200. https://doi.org/10.1016/0006-8993(95)00420-U

Lahiri, S., Roy, A., Baby, S. M., Hoshi, T., Semenza, G. L., & Prabhakar, N. R. (2006). Oxygen sensing in the body. *Prog Biophys Mol Biol*, *91*(3), 249-286. https://doi.org/10.1016/j.pbiomolbio.2005.07.001

Lai, T. W., Zhang, S., & Wang, Y. T. (2014). Excitotoxicity and stroke: identifying novel targets for neuroprotection. *Prog Neurobiol*, *115*, 157-188. https://doi.org/10.1016/j.pneurobio.2013.11.006

Langer, T., & Neupert, W. (1996). Regulated protein degradation in mitochondria. *Experientia*, *52*(12), 1069-1076. https://doi.org/10.1007/BF01952104

Lapuente-Brun, E., Moreno-Loshuertos, R., Acin-Perez, R., Latorre-Pellicer, A., Colas, C., Balsa, E., Perales-Clemente, E., Quiros, P. M., Calvo, E., Rodriguez-Hernandez, M. A., Navas, P., Cruz, R., Carracedo, A., Lopez-Otin, C., Perez-Martos, A., Fernandez-Silva, P., Fernandez-Vizarra, E., & Enriquez, J. A. (2013). Supercomplex assembly determines electron flux in the mitochondrial electron transport chain. *Science*, *340*(6140), 1567-1570. https://doi.org/10.1126/science.1230381

Larson, J., Drew, K. L., Folkow, L. P., Milton, S. L., & Park, T. J. (2014). No oxygen? No problem! Intrinsic brain tolerance to hypoxia in vertebrates. *J Exp Biol*, *217*(Pt 7), 1024-1039. https://doi.org/10.1242/jeb.085381

Larson, J., & Park, T. J. (2009). Extreme hypoxia tolerance of naked mole-rat brain. *Neuroreport*, *20*(18), 1634-1637. https://doi.org/10.1097/WNR.0b013e32833370cf

Latorre-Muro, P., Baeza, J., Armstrong, E. A., Hurtado-Guerrero, R., Corzana, F., Wu, L. E., Sinclair, D. A., Lopez-Buesa, P., Carrodeguas, J. A., & Denu, J. M. (2018). Dynamic Acetylation of Phosphoenolpyruvate Carboxykinase Toggles Enzyme Activity between Gluconeogenic and Anaplerotic Reactions. *Mol Cell*, *71*(5), 718-732 e719. https://doi.org/10.1016/j.molcel.2018.07.031

Lau, D. S., Connaty, A. D., Mahalingam, S., Wall, N., Cheviron, Z. A., Storz, J. F., Scott, G. R., & McClelland, G. B. (2017). Acclimation to hypoxia increases carbohydrate use during exercise in high-altitude deer mice. *American Journal of Physiology-Regulatory Integrative and Comparative Physiology*, *312*(3), R400-R411. https://doi.org/10.1152/ajpregu.00365.2016

Lauren, J. C. a. L. S. K. a. C. A. C. a. F. E. M. (1995). in Twelve Tolerance of East African Hypoxia Species for Low Oxygen in Cichlids : Potential Refugia. *Conservation Biology*, *9*, 1274-1287.

Lavorato, M., Iyer, V. R., Dewight, W., Cupo, R. R., Debattisti, V., Gomez, L., De la Fuente, S., Zhao, Y. T., Valdivia, H. H., Hajnoczky, G., & Franzini-Armstrong, C. (2017). Increased mitochondrial nanotunneling activity, induced by calcium imbalance, affects intermitochondrial matrix exchanges. *Proc Natl Acad Sci U S A*, *114*(5), E849-E858. https://doi.org/10.1073/pnas.1617788113

Lemasters, J. J. (2005). Selective mitochondrial autophagy, or mitophagy, as a targeted defense against oxidative stress, mitochondrial dysfunction, and aging. *Rejuvenation Res*, *8*(1), 3-5. https://doi.org/10.1089/rej.2005.8.3

Lenaz, G., & Genova, M. L. (2010). Structure and organization of mitochondrial respiratory complexes: a new understanding of an old subject. *Antioxid Redox Signal*, *12*(8), 961-1008. https://doi.org/10.1089/ars.2009.2704

Lenfant, C., Johansen, K., & Torrance, J. D. (1970). Gas transport and oxygen storage capacity in some pinnipeds and the sea otter. *Respir Physiol*, *9*(2), 277-286. https://doi.org/10.1016/0034-5687(70)90076-9

Letts, J. A., & Sazanov, L. A. (2017). Clarifying the supercomplex: the higher-order organization of the mitochondrial electron transport chain. *Nat Struct Mol Biol*, *24*(10), 800-808. https://doi.org/10.1038/nsmb.3460

Levesque, D. L., & Tattersall, G. J. (2009). Seasonal changes in thermoregulatory responses to hypoxia in the Eastern chipmunk (Tamias striatus). *J Exp Biol*, *212*(Pt 12), 1801-1810. https://doi.org/10.1242/jeb.027094

Lewis, K. N., Andziak, B., Yang, T., & Buffenstein, R. (2013). The Naked Mole-Rat Response to Oxidative Stress: Just Deal with It. *Antioxidants & Redox Signaling*, *19*(12), 1388-1399. https://doi.org/10.1089/ars.2012.4911

Lewis, M. R., & Lewis, W. H. (1915). Mitochondria (and other cytoplasmic structures) in tissue cultures. *American journal of anatomy*, *17*(3), 339-401. https://doi.org/10.1002/aja.1000170304

Li, Q., Pogwizd, S. M., Prabhu, S. D., & Zhou, L. (2014). Inhibiting Na+/K+ ATPase can impair mitochondrial energetics and induce abnormal Ca2+ cycling and automaticity in guinea pig cardiomyocytes. *PLoS One*, *9*(4), e93928. https://doi.org/10.1371/journal.pone.0093928

Li, Q., Wang, L., Liu, H., Ren, W., Zhang, Z., & Xia, B. (2022). Roles of miR-124-3p/Scd1 in urolithin A-induced brown adipocyte differentiation and succinate-dependent regulation of mitochondrial complex II. *Biochem Biophys Res Commun*, *606*, 174-181. https://doi.org/10.1016/j.bbrc.2022.03.112

Li, W., Dong, Y., Dong, Q., Sun, H., Zhang, Y., & Wang, Z. (2021). The remarkable hypoxia tolerance in Brandt's voles (Lasiopodomys brandtii). *Eur J Neurosci*, *53*(5), 1652-1660. https://doi.org/10.1111/ejn.15012

Li, X. J., Qiao, C. C., Chen, B. J., Li, M. Y., Chen, P., Huang, M. L., Chen, C. X., Liu, Y., Cheng, H., Jiang, M. W., Shi, L. Y., & Wang, Z. L. (2022). Fuel source shift or cost reduction: Context-dependent adaptation strategies in closely related Neodon fuscus and Lasiopodomys brandtii against hypoxia. *Zool Res*, *43*(4), 497-513. https://doi.org/10.24272/j.issn.2095-8137.2022.011

Liao, F. H., Yao, C. N., Chen, S. P., Wu, T. H., & Lin, S. Y. (2022). Transdermal Delivery of Succinate Accelerates Energy Dissipation of Brown Adipocytes to Reduce Remote Fat Accumulation. *Mol Pharm*, *19*(11), 4299-4310. https://doi.org/10.1021/acs.molpharmaceut.2c00628

Liesa, M., & Shirihai, O. S. (2013). Mitochondrial dynamics in the regulation of nutrient utilization and energy expenditure. *Cell Metab*, *17*(4), 491-506. https://doi.org/10.1016/j.cmet.2013.03.002

Lim, D., Dematteis, G., Tapella, L., Genazzani, A. A., Cali, T., Brini, M., & Verkhratsky, A. (2021). Ca(2+) handling at the mitochondria-ER contact sites in neurodegeneration. *Cell Calcium*, *98*, 102453. https://doi.org/10.1016/j.ceca.2021.102453

Lin, X. H., Qiu, B. Q., Ma, M., Zhang, R., Hsu, S. J., Liu, H. H., Chen, J., Gao, D. M., Cui, J. F., Ren, Z. G., & Chen, R. X. (2020). Suppressing DRP1-mediated mitochondrial fission and mitophagy increases mitochondrial apoptosis of hepatocellular carcinoma cells in the setting of hypoxia. *Oncogenesis*, *9*(7), 67. https://doi.org/10.1038/s41389-020-00251-5

Liu, B., Zhu, X., Chen, C. L., Hu, K., Swartz, H. M., Chen, Y. R., & He, G. (2010). Opening of the mitoKATP channel and decoupling of mitochondrial complex II and III contribute to the suppression of myocardial reperfusion hyperoxygenation. *Mol Cell Biochem*, *337*(1-2), 25-38. https://doi.org/10.1007/s11010-009-0283-2

Liu, F., Lu, J., Manaenko, A., Tang, J., & Hu, Q. (2018). Mitochondria in Ischemic Stroke: New Insight and Implications. *Aging Dis*, *9*(5), 924-937. https://doi.org/10.14336/AD.2017.1126

Liu, K., Lin, L., Li, Q., Xue, Y., Zheng, F., Wang, G., Zheng, C., Du, L., Hu, M., Huang, Y., Shao, C., Kong, X., Melino, G., Shi, Y., & Wang, Y. (2020). Scd1 controls de novo beige fat biogenesis through succinate-dependent regulation of mitochondrial complex II. *Proc Natl Acad Sci U S A*, *117*(5), 2462-2472. https://doi.org/10.1073/pnas.1914553117

Liu, Y., Fiskum, G., & Schubert, D. (2002). Generation of reactive oxygen species by the mitochondrial electron transport chain. *J Neurochem*, *80*(5), 780-787. https://doi.org/10.1046/j.0022-3042.2002.00744.x

Liu, Z., Ren, Z., Zhang, J., Chuang, C. C., Kandaswamy, E., Zhou, T., & Zuo, L. (2018). Role of ROS and Nutritional Antioxidants in Human Diseases. *Front Physiol*, *9*, 477. https://doi.org/10.3389/fphys.2018.00477

Logan, S. M., Szereszewski, K. E., Bennett, N. C., Hart, D. W., van Jaarsveld, B., Pamenter, M. E., & Storey, K. B. (2020). The brains of six African mole-rat species show divergent responses to hypoxia. *J Exp Biol*, *223*(Pt 9). https://doi.org/10.1242/jeb.215905

Long, Y. C., & Zierath, J. R. (2006). AMP-activated protein kinase signaling in metabolic regulation. *J Clin Invest*, *116*(7), 1776-1783. https://doi.org/10.1172/JCI29044

Lopez-Fabuel, I., Le Douce, J., Logan, A., James, A. M., Bonvento, G., Murphy, M. P., Almeida, A., & Bolanos, J. P. (2016). Complex I assembly into supercomplexes determines differential mitochondrial ROS production in neurons and astrocytes. *Proc Natl Acad Sci U S A*, *113*(46), 13063-13068. https://doi.org/10.1073/pnas.1613701113

Loschen, G., Flohe, L., & Chance, B. (1971). Respiratory chain linked H(2)O(2) production in pigeon heart mitochondria. *FEBS Lett*, *18*(2), 261-264. https://doi.org/10.1016/0014-5793(71)80459-3

Lu, Y., Fujioka, H., Joshi, D., Li, Q., Sangwung, P., Hsieh, P., Zhu, J., Torio, J., Sweet, D., Wang, L., Chiu, S. Y., Croniger, C., Liao, X., & Jain, M. K. (2018). Mitophagy is required for brown adipose tissue mitochondrial homeostasis during cold challenge. *Sci Rep*, *8*(1), 8251. https://doi.org/10.1038/s41598-018-26394-5

Lubos, E., Handy, D. E., & Loscalzo, J. (2008). Role of oxidative stress and nitric oxide in atherothrombosis. *Front Biosci*, *13*, 5323-5344. https://doi.org/10.2741/3084

Lui, M. A., Mahalingam, S., Patel, P., Connaty, A. D., Ivy, C. M., Cheviron, Z. A., Storz, J. F., McClelland, G. B., & Scott, G. R. (2015). High-altitude ancestry and hypoxia acclimation have distinct effects on exercise capacity and muscle phenotype in deer mice. *Am J Physiol Regul Integr Comp Physiol*, *308*(9), R779-791. https://doi.org/10.1152/ajpregu.00362.2014

Lundby, C., Calbet, J. A., & Robach, P. (2009). The response of human skeletal muscle tissue to hypoxia. *Cell Mol Life Sci*, *66*(22), 3615-3623. https://doi.org/10.1007/s00018-009-0146-8

Lushchak, V. I., Bagnyukova, T. V., Lushchak, O. V., Storey, J. M., & Storey, K. B. (2005). Hypoxia and recovery perturb free radical processes and antioxidant potential in common carp (Cyprinus carpio) tissues. *International Journal of Biochemistry & Cell Biology*, *37*(6), 1319-1330. https://doi.org/10.1016/j.biocel.2005.01.006

Ma, Y., Wu, S., Rasley, B., & Duffy, L. (2009). Adaptive response of brain tissue oxygenation to environmental hypoxia in non-sedated, non-anesthetized arctic ground squirrels. *Comp Biochem Physiol A Mol Integr Physiol*, *154*(3), 315-322. https://doi.org/10.1016/j.cbpa.2009.06.016

Ma, Y. L., Zhu, X., Rivera, P. M., Toien, O., Barnes, B. M., LaManna, J. C., Smith, M. A., & Drew, K. L. (2005). Absence of cellular stress in brain after hypoxia induced by arousal from hibernation in Arctic ground squirrels. *Am J Physiol Regul Integr Comp Physiol*, *289*(5), R1297-1306. https://doi.org/10.1152/ajpregu.00260.2005

MacDougall, J. D., Green, H. J., Sutton, J. R., Coates, G., Cymerman, A., Young, P., & Houston, C. S. (1991). Operation Everest II: structural adaptations in skeletal muscle in response to extreme simulated altitude. *Acta Physiol Scand*, *142*(3), 421-427. https://doi.org/10.1111/j.1748-1716.1991.tb09176.x

Madden, C. J., & Morrison, S. F. (2005). Hypoxic activation of arterial chemoreceptors inhibits sympathetic outflow to brown adipose tissue in rats. *J Physiol*, *566*(Pt 2), 559-573. https://doi.org/10.1113/jphysiol.2005.086322

Magalhaes, J., Ascensao, A., Soares, J. M., Ferreira, R., Neuparth, M. J., Marques, F., & Duarte, J. A. (2005). Acute and severe hypobaric hypoxia increases oxidative stress and impairs mitochondrial function in mouse skeletal muscle. *J Appl Physiol (1985)*, *99*(4), 1247-1253. https://doi.org/10.1152/japplphysiol.01324.2004

Mahalingam, S., McClelland, G. B., & Scott, G. R. (2017). Evolved changes in the intracellular distribution and physiology of muscle mitochondria in high-altitude native deer mice. *J Physiol*, *595*(14), 4785-4801. https://doi.org/10.1113/JP274130

Mailloux, R. J., Adjeitey, C. N., Xuan, J. Y., & Harper, M. E. (2012). Crucial yet divergent roles of mitochondrial redox state in skeletal muscle vs. brown adipose tissue energetics. *Faseb J*, *26*(1), 363-375. https://doi.org/10.1096/fj.11-189639

Maiti, A. K., Saha, N. C., Paul, G., & Dhara, K. (2018). Mitochondrial respiratory chain inhibition and Na(+)K(+)ATPase dysfunction are determinant factors modulating the toxicity of nickel in the brain of indian catfish Clarias batrachus L. *Interdiscip Toxicol*, *11*(4), 306-315. https://doi.org/10.2478/intox-2018-0030

Maklashina, E., Sher, Y., Zhou, H. Z., Gray, M. O., Karliner, J. S., & Cecchini, G. (2002). Effect of anoxia/reperfusion on the reversible active/de-active transition of NADH-ubiquinone oxidoreductase (complex I) in rat heart. *Biochim Biophys Acta*, *1556*(1), 6-12. https://doi.org/10.1016/s0005-2728(02)00280-3

Makrecka-Kuka, M., Krumschnabel, G., & Gnaiger, E. (2015). High-Resolution Respirometry for Simultaneous Measurement of Oxygen and Hydrogen Peroxide Fluxes in Permeabilized Cells, Tissue Homogenate and Isolated Mitochondria. *Biomolecules*, *5*(3), 1319-1338. https://doi.org/10.3390/biom5031319

Malik, A., Korol, A., Weber, M., Hankeln, T., Avivi, A., & Band, M. (2012). Transcriptome analysis of the spalax hypoxia survival response includes suppression of apoptosis and tight control of angiogenesis. *BMC Genomics*, *13*, 615. https://doi.org/10.1186/1471-2164-13-615

Malinska, D., Kulawiak, B., Kudin, A. P., Kovacs, R., Huchzermeyer, C., Kann, O., Szewczyk, A., & Kunz, W. S. (2010). Complex III-dependent superoxide production of brain mitochondria contributes to seizure-related ROS formation. *Biochim Biophys Acta*, *1797*(6-7), 1163-1170. https://doi.org/10.1016/j.bbabio.2010.03.001

Marks de Chabris, N. C., Sabir, S., Perkins, G., Cheng, H., Ellisman, M. H., & Pamenter, M. E. (2023). Short communication: Acute hypoxia does not alter mitochondrial abundance in naked mole-rats. *Comp Biochem Physiol A Mol Integr Physiol*, *276*, 111343. https://doi.org/10.1016/j.cbpa.2022.111343

Martinez, D., Fiori, C. Z., Baronio, D., Carissimi, A., Kaminski, R. S., Kim, L. J., Rosa, D. P., & Bos, A. (2010). Brown adipose tissue: is it affected by intermittent hypoxia? *Lipids Health Dis*, *9*, 121. https://doi.org/10.1186/1476-511X-9-121

Martinez, D., Vasconcellos, L. F., de Oliveira, P. G., & Konrad, S. P. (2008). Weight loss and brown adipose tissue reduction in rat model of sleep apnea. *Lipids Health Dis*, *7*, 26. https://doi.org/10.1186/1476-511X-7-26

Marutani, E., Morita, M., Hirai, S., Kai, S., Grange, R. M. H., Miyazaki, Y., Nagashima, F., Traeger, L., Magliocca, A., Ida, T., Matsunaga, T., Flicker, D. R., Corman, B., Mori, N., Yamazaki, Y., Batten, A., Li, R., Tanaka, T., Ikeda, T., . . . Ichinose, F. (2021). Sulfide catabolism ameliorates hypoxic brain injury. *Nat Commun*, *12*(1), 3108. https://doi.org/10.1038/s41467-021-23363-x

Masuda, K., Okazaki, K., Kuno, S., Asano, K., Shimojo, H., & Katsuta, S. (2001). Endurance training under 2500-m hypoxia does not increase myoglobin content in human skeletal muscle. *Eur J Appl Physiol*, *85*(5), 486-490. https://doi.org/10.1007/s004210100471

Matlib, M. A., Zhou, Z., Knight, S., Ahmed, S., Choi, K. M., Krause-Bauer, J., Phillips, R., Altschuld, R., Katsube, Y., Sperelakis, N., & Bers, D. M. (1998). Oxygen-bridged dinuclear ruthenium amine complex specifically inhibits Ca2+ uptake into mitochondria in vitro and in situ in single cardiac myocytes. *J Biol Chem*, *273*(17), 10223-10231. https://doi.org/10.1074/jbc.273.17.10223

Matsumoto, S., Friberg, H., Ferrand-Drake, M., & Wieloch, T. (1999). Blockade of the mitochondrial permeability transition pore diminishes infarct size in the rat after transient middle cerebral artery occlusion. *J Cereb Blood Flow Metab*, *19*(7), 736-741. https://doi.org/10.1097/00004647-199907000-00002

Mazat, J. P., Devin, A., & Ransac, S. (2020). Modelling mitochondrial ROS production by the respiratory chain. *Cell Mol Life Sci*, *77*(3), 455-465. https://doi.org/10.1007/s00018-019-03381-1

McCafferty, D. J., Gilbert, C., Thierry, A. M., Currie, J., Le Maho, Y., & Ancel, A. (2013). Emperor penguin body surfaces cool below air temperature. *Biol Lett*, *9*(3), 20121192. https://doi.org/10.1098/rsbl.2012.1192

McFarlane, S. V., Mathers, K. E., & Staples, J. F. (2017). Reversible temperature-dependent differences in brown adipose tissue respiration during torpor in a mammalian hibernator. *Am J Physiol Regul Integr Comp Physiol*, *312*(3), R434-R442. https://doi.org/10.1152/ajpregu.00316.2016

McKenna, M. C., Sonnewald, U., Huang, X., Stevenson, J., & Zielke, H. R. (1996). Exogenous glutamate concentration regulates the metabolic fate of glutamate in astrocytes. *J Neurochem*, *66*(1), 386-393. https://doi.org/10.1046/j.1471-4159.1996.66010386.x

Mcnab, B. K. (1966). The Metabolism of Fossorial Rodents: A Study of Convergence. *Ecology*, *47*(5), 712-733. https://doi.org/10.2307/1934259

Mekahli, D., Bultynck, G., Parys, J. B., De Smedt, H., & Missiaen, L. (2011). Endoplasmic-reticulum calcium depletion and disease. *Cold Spring Harb Perspect Biol*, *3*(6), a004317-a004317. https://doi.org/10.1101/cshperspect.a004317

Melissa, L., MacDougall, J. D., Tarnopolsky, M. A., Cipriano, N., & Green, H. J. (1997). Skeletal muscle adaptations to training under normobaric hypoxic versus normoxic conditions. *Med Sci Sports Exerc*, *29*(2), 238-243. https://doi.org/10.1097/00005768-199702000-00012

Mills, E. L., Pierce, K. A., Jedrychowski, M. P., Garrity, R., Winther, S., Vidoni, S., Yoneshiro, T., Spinelli, J. B., Lu, G. Z., Kazak, L., Banks, A. S., Haigis, M. C., Kajimura, S., Murphy, M. P., Gygi, S. P., Clish, C. B., & Chouchani, E. T. (2018). Accumulation of succinate controls activation of adipose tissue thermogenesis. *Nature*, *560*(7716), 102-106. https://doi.org/10.1038/s41586-018-0353-2

Milner, R. E., Wang, L. C., & Trayhurn, P. (1989). Brown fat thermogenesis during hibernation and arousal in Richardson's ground squirrel. *Am J Physiol*, *256*(1 Pt 2), R42-48. https://doi.org/10.1152/ajpregu.1989.256.1.R42

Milton, S. L., Nayak, G., Kesaraju, S., Kara, L., & Prentice, H. M. (2007). Suppression of reactive oxygen species production enhances neuronal survival in vitro and in vivo in the anoxia-tolerant turtle Trachemys scripta. *J Neurochem*, *101*(4), 993-1001. https://doi.org/10.1111/j.1471-4159.2007.04466.x

Mishra, P., & Chan, D. C. (2016). Metabolic regulation of mitochondrial dynamics. *J Cell Biol*, *212*(4), 379-387. https://doi.org/10.1083/jcb.201511036

Mitani, A., & Tanaka, K. (2003). Functional Changes of Glial Glutamate Transporter GLT-1 during Ischemia: An In Vivo Study in the Hippocampal CA1 of Normal Mice and Mutant Mice Lacking GLT-1. *The Journal of Neuroscience*, *23*(18), 7176-7182. https://doi.org/10.1523/jneurosci.23-18-07176.2003

Miyamoto, O., & Auer, R. N. (2000). Hypoxia, hyperoxia, ischemia, and brain necrosis. *Neurology*, *54*(2), 362-371. https://doi.org/10.1212/wnl.54.2.362

Moazed, B., & Desautels, M. (2002). Differentiation-dependent expression of cathepsin D and importance of lysosomal proteolysis in the degradation of UCP1 in brown adipocytes. *Can J Physiol Pharmacol*, *80*(6), 515-525. https://doi.org/10.1139/y02-067

Moore, T. M., Cheng, L., Wolf, D. M., Ngo, J., Segawa, M., Zhu, X., Strumwasser, A. R., Cao, Y., Clifford, B. L., Ma, A., Scumpia, P., Shirihai, O. S., Vallim, T. Q. A., Laakso, M., Lusis, A. J., Hevener, A. L., & Zhou, Z. (2022). Parkin regulates adiposity by coordinating mitophagy with mitochondrial biogenesis in white adipocytes. *Nat Commun*, *13*(1), 6661. https://doi.org/10.1038/s41467-022-34468-2

Morozov, Y. M., Datta, D., Paspalas, C. D., & Arnsten, A. F. T. (2017). Ultrastructural evidence for impaired mitochondrial fission in the aged rhesus monkey dorsolateral prefrontal cortex. *Neurobiol Aging*, *51*, 9-18. https://doi.org/10.1016/j.neurobiolaging.2016.12.001

Mortola, J. P. (1993). Hypoxic Hypometabolism in Mammals. *Physiology*, *8*(2), 79-82. https://doi.org/10.1152/physiologyonline.1993.8.2.79

Mortola, J. P., & Dotta, A. (1992). Effects of hypoxia and ambient temperature on gaseous metabolism of newborn rats. *Am J Physiol*, *263*(2 Pt 2), R267-272. https://doi.org/10.1152/ajpregu.1992.263.2.R267

Mortola, J. P., & Feher, C. (1998). Hypoxia inhibits cold-induced huddling in rat pups. *Respir Physiol*, *113*(3), 213-222. https://doi.org/10.1016/s0034-5687(98)00056-5

Mortola, J. P., Merazzi, D., & Naso, L. (1999). Blood flow to the brown adipose tissue of conscious young rabbits during hypoxia in cold and warm conditions. *Pflugers Arch*, *437*(2), 255-260. https://doi.org/10.1007/s004240050777

Mortola, J. P., & Naso, L. (1997). Brown adipose tissue and its uncoupling protein in chronically hypoxic rats. *Clin Sci (Lond)*, *93*(4), 349-354. https://doi.org/10.1042/cs0930349

Mortola, J. P., & Naso, L. (1998). Thermogenesis in newborn rats after prenatal or postnatal hypoxia. *J Appl Physiol (1985)*, *85*(1), 84-90. https://doi.org/10.1152/jappl.1998.85.1.84

Muller, F. L., Liu, Y., Abdul-Ghani, M. A., Lustgarten, M. S., Bhattacharya, A., Jang, Y. C., & Van Remmen, H. (2008). High rates of superoxide production in skeletal-muscle mitochondria respiring on both complex I- and complex II-linked substrates. *Biochem J*, *409*(2), 491-499. https://doi.org/10.1042/BJ20071162

Mungai, P. T., Waypa, G. B., Jairaman, A., Prakriya, M., Dokic, D., Ball, M. K., & Schumacker, P. T. (2011). Hypoxia triggers AMPK activation through reactive oxygen species-mediated activation of calcium release-activated calcium channels. *Mol Cell Biol*, *31*(17), 3531-3545. https://doi.org/10.1128/MCB.05124-11

Munro, D., Baldy, C., Pamenter, M. E., & Treberg, J. R. (2019). The exceptional longevity of the naked mole-rat may be explained by mitochondrial antioxidant defenses. *Aging Cell*, *18*(3), e12916. https://doi.org/10.1111/acel.12916

Murata, A., Agematsu, K., Korotcova, L., Gallo, V., Jonas, R. A., & Ishibashi, N. (2013). Rodent brain slice model for the study of white matter injury. *J Thorac Cardiovasc Surg*, *146*(6), 1526-1533 e1521. https://doi.org/10.1016/j.jtcvs.2013.02.071

Nakai, A., Kuroda, S., Kristian, T., & Siesjo, B. K. (1997). The immunosuppressant drug FK506 ameliorates secondary mitochondrial dysfunction following transient focal cerebral ischemia in the rat. *Neurobiol Dis*, *4*(3-4), 288-300. https://doi.org/10.1006/nbdi.1997.0146

Nathaniel, T. I., Saras, A., Umesiri, F. E., & Olajuyigbe, F. (2009). Tolerance to oxygen nutrient deprivation in the hippocampal slices of the naked mole rats. *J Integr Neurosci*, *8*(2), 123-136. https://doi.org/10.1142/s0219635209002149

Nedergaard, J., & Cannon, B. (2018). Brown adipose tissue as a heat-producing thermoeffector. *Handb Clin Neurol*, *156*, 137-152. https://doi.org/10.1016/B978-0-444-63912-7.00009-6

Nedergaard, J., Golozoubova, V., Matthias, A., Asadi, A., Jacobsson, A., & Cannon, B. (2001). UCP1: the only protein able to mediate adaptive non-shivering thermogenesis and metabolic inefficiency. *Biochim Biophys Acta*, *1504*(1), 82-106. https://doi.org/10.1016/s0005-2728(00)00247-4

Nguyen, T. H., Conotte, S., Belayew, A., Decleves, A. E., Legrand, A., & Tassin, A. (2021). Hypoxia and Hypoxia-Inducible Factor Signaling in Muscular Dystrophies: Cause and Consequences. *Int J Mol Sci*, *22*(13). https://doi.org/10.3390/ijms22137220

Nguyen, V. C., Deck, C. A., & Pamenter, M. E. (2019). Naked mole-rats reduce the expression of ATP-dependent but not ATP-independent heat shock proteins in acute hypoxia. *J Exp Biol*, *222*(Pt 22). https://doi.org/10.1242/jeb.211243

Ni, H. M., Williams, J. A., & Ding, W. X. (2015). Mitochondrial dynamics and mitochondrial quality control. *Redox Biol*, *4*, 6-13. https://doi.org/10.1016/j.redox.2014.11.006

Nicholls, D. G. (1976). Hamster brown-adipose-tissue mitochondria. Purine nucleotide control of the ion conductance of the inner membrane, the nature of the nucleotide binding site. *Eur J Biochem*, *62*(2), 223-228. https://doi.org/10.1111/j.1432-1033.1976.tb10151.x

Nicholls, D. G. (2006). The physiological regulation of uncoupling proteins. *Biochim Biophys Acta*, *1757*(5-6), 459-466. https://doi.org/10.1016/j.bbabio.2006.02.005

Nicholls, D. G., & Budd, S. L. (2000). Mitochondria and neuronal survival. *Physiol Rev*, *80*(1), 315-360. https://doi.org/10.1152/physrev.2000.80.1.315

Nikel, K. E., Shanishchara, N. K., Ivy, C. M., Dawson, N. J., & Scott, G. R. (2018). Effects of hypoxia at different life stages on locomotory muscle phenotype in deer mice native to high altitudes. *Comp Biochem Physiol B Biochem Mol Biol*, *224*, 98-104. https://doi.org/10.1016/j.cbpb.2017.11.009

Nilsson, G. E., & Renshaw, G. M. (2004). Hypoxic survival strategies in two fishes: extreme anoxia tolerance in the North European crucian carp and natural hypoxic preconditioning in a coral-reef shark. *J Exp Biol*, *207*(Pt 18), 3131-3139. https://doi.org/10.1242/jeb.00979

O'Brien, P. J., Shen, H., McCutcheon, L. J., O'Grady, M., Byrne, P. J., Ferguson, H. W., Mirsalimi, M. S., Julian, R. J., Sargeant, J. M., Tremblay, R. R., & et al. (1992). Rapid, simple and sensitive microassay for skeletal and cardiac muscle myoglobin and hemoglobin: use in various animals indicates functional role of myohemoproteins. *Mol Cell Biochem*, *112*(1), 45-52. https://doi.org/10.1007/BF00229642

O'Connor, T. P., Lee, A., Jarvis, J. U., & Buffenstein, R. (2002). Prolonged longevity in naked mole-rats: age-related changes in metabolism, body composition and gastrointestinal function. *Comp Biochem Physiol A Mol Integr Physiol*, *133*(3), 835-842. https://doi.org/10.1016/s1095-6433(02)00198-8

Oelkrug, R., Kutschke, M., Meyer, C. W., Heldmaier, G., & Jastroch, M. (2010). Uncoupling protein 1 decreases superoxide production in brown adipose tissue mitochondria. *J Biol Chem*, *285*(29), 21961-21968. https://doi.org/10.1074/jbc.M110.122861

Oelkrug, R., Polymeropoulos, E. T., & Jastroch, M. (2015). Brown adipose tissue: physiological function and evolutionary significance. *J Comp Physiol B*, *185*(6), 587-606. https://doi.org/10.1007/s00360-015-0907-7

Oiwa, Y., Oka, K., Yasui, H., Higashikawa, K., Bono, H., Kawamura, Y., Miyawaki, S., Watarai, A., Kikusui, T., Shimizu, A., Okano, H., Kuge, Y., Kimura, K., Okamatsu-Ogura, Y., & Miura, K. (2020). Characterization of brown adipose tissue thermogenesis in the naked mole-rat (Heterocephalus glaber), a heterothermic mammal. *Sci Rep*, *10*(1), 19488. https://doi.org/10.1038/s41598-020-74929-6

Ong, S. B., Subrayan, S., Lim, S. Y., Yellon, D. M., Davidson, S. M., & Hausenloy, D. J. (2010). Inhibiting mitochondrial fission protects the heart against ischemia/reperfusion injury. *Circulation*, *121*(18), 2012-2022. https://doi.org/10.1161/CIRCULATIONAHA.109.906610

Onodera, H., Okabe, S., Kikuchi, Y., Tsuda, T., & Itoyama, Y. (2000). Impaired chemosensitivity and perception of dyspnoea in Parkinson's disease. *Lancet*, *356*(9231), 739-740. https://doi.org/10.1016/S0140-6736(00)02638-6

Orava, J., Nuutila, P., Lidell, M. E., Oikonen, V., Noponen, T., Viljanen, T., Scheinin, M., Taittonen, M., Niemi, T., Enerback, S., & Virtanen, K. A. (2011). Different metabolic responses of human brown adipose tissue to activation by cold and insulin. *Cell Metab*, *14*(2), 272-279. https://doi.org/10.1016/j.cmet.2011.06.012

Pacheu-Grau, D., Rucktaschel, R., & Deckers, M. (2018). Mitochondrial dysfunction and its role in tissue-specific cellular stress. *Cell Stress*, *2*(8), 184-199. https://doi.org/10.15698/cst2018.07.147

Palma, F. R., He, C., Danes, J. M., Paviani, V., Coelho, D. R., Gantner, B. N., & Bonini, M. G. (2020). Mitochondrial Superoxide Dismutase: What the Established, the Intriguing, and the Novel Reveal About a Key Cellular Redox Switch. *Antioxid Redox Signal*, *32*(10), 701-714. https://doi.org/10.1089/ars.2019.7962

Pamenter, M., Dzal, Y., & Milsom, W. (2014). Profound metabolic depression in the hypoxia‐tolerant naked mole rat (879.2). *The FASEB Journal*, *28*(S1), 879.872 , publisher = John Wiley & Sons, Ltd. https://doi.org/10.1096/fasebj.28.1_supplement.879.2

Pamenter, M. E. (2014). Mitochondria: a multimodal hub of hypoxia tolerance. *Canadian Journal of Zoology*, *92*(7), 569-589. https://doi.org/10.1139/cjz-2013-0247

Pamenter, M. E. (2022). Adaptations to a hypoxic lifestyle in naked mole-rats. *J Exp Biol*, *225*(4). https://doi.org/10.1242/jeb.196725

Pamenter, M. E., Dzal, Y. A., Thompson, W. A., & Milsom, W. K. (2019a). Do naked mole rats accumulate a metabolic acidosis or an oxygen debt in severe hypoxia? *J Exp Biol*, *222*(Pt 3). https://doi.org/10.1242/jeb.191197

Pamenter, M. E., Hogg, D. W., Gu, X. Q., Buck, L. T., & Haddad, G. G. (2012). Painted turtle cortex is resistant to an in vitro mimic of the ischemic mammalian penumbra. *J Cereb Blood Flow Metab*, *32*(11), 2033-2043. https://doi.org/10.1038/jcbfm.2012.103

Pamenter, M. E., Lau, G. Y., Richards, J. G., & Milsom, W. K. (2018). Naked mole rat brain mitochondria electron transport system flux and H(+) leak are reduced during acute hypoxia. *J Exp Biol*, *221*(Pt 4). https://doi.org/10.1242/jeb.171397

Pamenter, M. E., Shin, D. S., Cooray, M., & Buck, L. T. (2008). Mitochondrial ATP-sensitive K+ channels regulate NMDAR activity in the cortex of the anoxic western painted turtle. *J Physiol*, *586*(4), 1043-1058. https://doi.org/10.1113/jphysiol.2007.142380

Pamenter, M. E., Uysal-Onganer, P., Huynh, K. W., Kraev, I., & Lange, S. (2019b). Post-Translational Deimination of Immunological and Metabolic Protein Markers in Plasma and Extracellular Vesicles of Naked Mole-Rat (Heterocephalus glaber). *Int J Mol Sci*, *20*(21). https://doi.org/10.3390/ijms20215378

Pan, Y., Mansfield, K. D., Bertozzi, C. C., Rudenko, V., Chan, D. A., Giaccia, A. J., & Simon, M. C. (2007). Multiple factors affecting cellular redox status and energy metabolism modulate hypoxia-inducible factor prolyl hydroxylase activity in vivo and in vitro. *Mol Cell Biol*, *27*(3), 912-925. https://doi.org/10.1128/MCB.01223-06

Pandya, J. D., Nukala, V. N., & Sullivan, P. G. (2013). Concentration dependent effect of calcium on brain mitochondrial bioenergetics and oxidative stress parameters. *Front Neuroenergetics*, *5*, 10. https://doi.org/10.3389/fnene.2013.00010

Pang, Z., Chong, J., Zhou, G., de Lima Morais, D. A., Chang, L., Barrette, M., Gauthier, C., Jacques, P. E., Li, S., & Xia, J. (2021). MetaboAnalyst 5.0: narrowing the gap between raw spectra and functional insights. *Nucleic Acids Res*, *49*(W1), W388-W396. https://doi.org/10.1093/nar/gkab382

Panov, A., Dikalov, S., Shalbuyeva, N., Hemendinger, R., Greenamyre, J. T., & Rosenfeld, J. (2007). Species- and tissue-specific relationships between mitochondrial permeability transition and generation of ROS in brain and liver mitochondria of rats and mice. *Am J Physiol Cell Physiol*, *292*(2), C708-718. https://doi.org/10.1152/ajpcell.00202.2006

Papes, F., Surpili, M. J., Langone, F., Trigo, J. R., & Arruda, P. (2001). The essential amino acid lysine acts as precursor of glutamate in the mammalian central nervous system. *FEBS letters*, *488*(1-2), 34-38. https://doi.org/10.1016/s0014-5793(00)02401-7

Park, T. J., Reznick, J., Peterson, B. L., Blass, G., Omerbasic, D., Bennett, N. C., Kuich, P., Zasada, C., Browe, B. M., Hamann, W., Applegate, D. T., Radke, M. H., Kosten, T., Lutermann, H., Gavaghan, V., Eigenbrod, O., Begay, V., Amoroso, V. G., Govind, V., . . . Lewin, G. R. (2017). Fructose-driven glycolysis supports anoxia resistance in the naked mole-rat. *Science*, *356*(6335), 307-311. https://doi.org/10.1126/science.aab3896

Parlee, S. D., Lentz, S. I., Mori, H., & MacDougald, O. A. (2014). Quantifying size and number of adipocytes in adipose tissue. *Methods Enzymol*, *537*, 93-122. https://doi.org/10.1016/B978-0-12-411619-1.00006-9

Parra, V., Bravo-Sagua, R., Norambuena-Soto, I., Hernandez-Fuentes, C. P., Gomez-Contreras, A. G., Verdejo, H. E., Mellado, R., Chiong, M., Lavandero, S., & Castro, P. F. (2017). Inhibition of mitochondrial fission prevents hypoxia-induced metabolic shift and cellular proliferation of pulmonary arterial smooth muscle cells. *Biochim Biophys Acta Mol Basis Dis*, *1863*(11), 2891-2903. https://doi.org/10.1016/j.bbadis.2017.07.018

Parthasarathy, A., Cross, P. J., Dobson, R. C. J., Adams, L. E., Savka, M. A., & Hudson, A. O. (2018). A Three-Ring Circus: Metabolism of the Three Proteogenic Aromatic Amino Acids and Their Role in the Health of Plants and Animals. *Front Mol Biosci*, *5*, 29. https://doi.org/10.3389/fmolb.2018.00029

Patron, M., Granatiero, V., Espino, J., Rizzuto, R., & De Stefani, D. (2019). MICU3 is a tissue-specific enhancer of mitochondrial calcium uptake. *Cell Death Differ*, *26*(1), 179-195. https://doi.org/10.1038/s41418-018-0113-8

Payne, F. (1909). The Chondriosomes as Bearers of the Hereditary Qualities. *The American naturalist*, *43*(507), 190-192. https://doi.org/10.1086/279046

Pedersen, B. K. (2013). Muscle as a secretory organ. *Compr Physiol*, *3*(3), 1337-1362. https://doi.org/10.1002/cphy.c120033

Peers, C., Dallas, M. L., Boycott, H. E., Scragg, J. L., Pearson, H. A., & Boyle, J. P. (2009). Hypoxia and neurodegeneration. *Ann N Y Acad Sci*, *1177*, 169-177. https://doi.org/10.1111/j.1749-6632.2009.05026.x

Peeters-Scholte, C., Koster, J., Veldhuis, W., van den Tweel, E., Zhu, C., Kops, N., Blomgren, K., Bar, D., van Buul-Offers, S., Hagberg, H., Nicolay, K., van Bel, F., & Groenendaal, F. (2002). Neuroprotection by selective nitric oxide synthase inhibition at 24 hours after perinatal hypoxia-ischemia. *Stroke*, *33*(9), 2304-2310. https://doi.org/10.1161/01.str.0000028343.25901.09

Pekkurnaz, G., & Wang, X. (2022). Mitochondrial heterogeneity and homeostasis through the lens of a neuron. *Nat Metab*, *4*(7), 802-812. https://doi.org/10.1038/s42255-022-00594-w

Pendin, D., Filadi, R., & Pizzo, P. (2017). The Concerted Action of Mitochondrial Dynamics and Positioning: New Characters in Cancer Onset and Progression. *Front Oncol*, *7*, 102. https://doi.org/10.3389/fonc.2017.00102

Perez-Pinzon, M. A., Stetler, R. A., & Fiskum, G. (2012). Novel mitochondrial targets for neuroprotection. *J Cereb Blood Flow Metab*, *32*(7), 1362-1376. https://doi.org/10.1038/jcbfm.2012.32

Perkins, G. A., Tjong, J., Brown, J. M., Poquiz, P. H., Scott, R. T., Kolson, D. R., Ellisman, M. H., & Spirou, G. A. (2010). The micro-architecture of mitochondria at active zones: electron tomography reveals novel anchoring scaffolds and cristae structured for high-rate metabolism. *J Neurosci*, *30*(3), 1015-1026. https://doi.org/10.1523/JNEUROSCI.1517-09.2010

Perry, T. L., Godin, D. V., & Hansen, S. (1982). Parkinson's disease: a disorder due to nigral glutathione deficiency? *Neurosci Lett*, *33*(3), 305-310. https://doi.org/10.1016/0304-3940(82)90390-1

Persson, A. K., Hoeijmakers, J. G. J., Estacion, M., Black, J. A., & Waxman, S. G. (2016). Sodium Channels, Mitochondria, and Axonal Degeneration in Peripheral Neuropathy. *Trends Mol Med*, *22*(5), 377-390. https://doi.org/10.1016/j.molmed.2016.03.008

Peterson, B. L., Larson, J., Buffenstein, R., Park, T. J., & Fall, C. P. (2012a). Blunted neuronal calcium response to hypoxia in naked mole-rat hippocampus. *PLoS One*, *7*(2), e31568. https://doi.org/10.1371/journal.pone.0031568

Peterson, B. L., Park, T. J., & Larson, J. (2012b). Adult naked mole-rat brain retains the NMDA receptor subunit GluN2D associated with hypoxia tolerance in neonatal mammals. *Neurosci Lett*, *506*(2), 342-345. https://doi.org/10.1016/j.neulet.2011.11.042

Piantadosi, C. A., & Zhang, J. (1996). Mitochondrial generation of reactive oxygen species after brain ischemia in the rat. *Stroke*, *27*(2), 327-331; discussion 332. https://doi.org/10.1161/01.str.27.2.327

Picard, M., McManus, M. J., Csordas, G., Varnai, P., Dorn, G. W., 2nd, Williams, D., Hajnoczky, G., & Wallace, D. C. (2015). Trans-mitochondrial coordination of cristae at regulated membrane junctions. *Nat Commun*, *6*(1), 6259. https://doi.org/10.1038/ncomms7259

Picard, M., Taivassalo, T., Gouspillou, G., & Hepple, R. T. (2011). Mitochondria: isolation, structure and function. *J Physiol*, *589*(Pt 18), 4413-4421. https://doi.org/10.1113/jphysiol.2011.212712

Pickles, S., Vigie, P., & Youle, R. J. (2018). Mitophagy and Quality Control Mechanisms in Mitochondrial Maintenance. *Curr Biol*, *28*(4), R170-R185. https://doi.org/10.1016/j.cub.2018.01.004

Plaitakis, A., Kalef-Ezra, E., Kotzamani, D., Zaganas, I., & Spanaki, C. (2017). The Glutamate Dehydrogenase Pathway and Its Roles in Cell and Tissue Biology in Health and Disease. *Biology (Basel)*, *6*(1). https://doi.org/10.3390/biology6010011

Polasek, L. K., & Davis, R. W. (2001). Heterogeneity of myoglobin distribution in the locomotory muscles of five cetacean species. *J Exp Biol*, *204*(Pt 2), 209-215. https://doi.org/10.1242/jeb.204.2.209

Polster, B. M., & Fiskum, G. (2004). Mitochondrial mechanisms of neural cell apoptosis. *J Neurochem*, *90*(6), 1281-1289. https://doi.org/10.1111/j.1471-4159.2004.02572.x

Ponsot, E., Dufour, S. P., Zoll, J., Doutrelau, S., N'Guessan, B., Geny, B., Hoppeler, H., Lampert, E., Mettauer, B., Ventura-Clapier, R., & Richard, R. (2006). Exercise training in normobaric hypoxia in endurance runners. II. Improvement of mitochondrial properties in skeletal muscle. *J Appl Physiol (1985)*, *100*(4), 1249-1257. https://doi.org/10.1152/japplphysiol.00361.2005

Popa-Wagner, A., Mitran, S., Sivanesan, S., Chang, E., & Buga, A. M. (2013). ROS and brain diseases: the good, the bad, and the ugly. *Oxid Med Cell Longev*, *2013*, 963520. https://doi.org/10.1155/2013/963520

Popov, V., Medvedev, N. I., Davies, H. A., & Stewart, M. G. (2005). Mitochondria form a filamentous reticular network in hippocampal dendrites but are present as discrete bodies in axons: a three-dimensional ultrastructural study. *J Comp Neurol*, *492*(1), 50-65. https://doi.org/10.1002/cne.20682

Powers, W. J. (2020). Acute Ischemic Stroke. *N Engl J Med*, *383*(3), 252-260. https://doi.org/10.1056/NEJMcp1917030

Prabhakar, N. R., & Overholt, J. L. (2000). Cellular mechanisms of oxygen sensing at the carotid body: heme proteins and ion channels. *Respiration physiology*, *122*(2-3), 209-221. https://doi.org/10.1016/s0034-5687(00)00160-2

Puigserver, P., Herron, D., Gianotti, M., Palou, A., Cannon, B., & Nedergaard, J. (1992). Induction and degradation of the uncoupling protein thermogenin in brown adipocytes in vitro and in vivo. Evidence for a rapidly degradable pool. *Biochem J*, *284 (Pt 2)*, 393-398. https://doi.org/10.1042/bj2840393

Qu, J., Chen, W., Hu, R., & Feng, H. (2016). The Injury and Therapy of Reactive Oxygen Species in Intracerebral Hemorrhage Looking at Mitochondria. *Oxid Med Cell Longev*, *2016*, 2592935. https://doi.org/10.1155/2016/2592935

Quiros, P. M., Goyal, A., Jha, P., & Auwerx, J. (2017). Analysis of mtDNA/nDNA Ratio in Mice. *Curr Protoc Mouse Biol*, *7*(1), 47-54. https://doi.org/10.1002/cpmo.21

Raffaello, A., Mammucari, C., Gherardi, G., & Rizzuto, R. (2016). Calcium at the Center of Cell Signaling: Interplay between Endoplasmic Reticulum, Mitochondria, and Lysosomes. *Trends Biochem Sci*, *41*(12), 1035-1049. https://doi.org/10.1016/j.tibs.2016.09.001

Raha, S., & Robinson, B. H. (2001). Mitochondria, oxygen free radicals, and apoptosis. *Am J Med Genet*, *106*(1), 62-70. https://doi.org/10.1002/ajmg.1398

Rajdev, S., & Reynolds, I. J. (1993). Calcium green-5N, a novel fluorescent probe for monitoring high intracellular free Ca2+ concentrations associated with glutamate excitotoxicity in cultured rat brain neurons. *Neuroscience Letters*, *162*(1-2), 149-152. https://doi.org/10.1016/0304-3940(93)90582-6

Raley-Susman, K. M., Kass, I. S., Cottrell, J. E., Newman, R. B., Chambers, G., & Wang, J. (2001). Sodium influx blockade and hypoxic damage to CA1 pyramidal neurons in rat hippocampal slices. *J Neurophysiol*, *86*(6), 2715-2726. https://doi.org/10.1152/jn.2001.86.6.2715

Rambold, A. S., Kostelecky, B., Elia, N., & Lippincott-Schwartz, J. (2011). Tubular network formation protects mitochondria from autophagosomal degradation during nutrient starvation. *Proc Natl Acad Sci U S A*, *108*(25), 10190-10195. https://doi.org/10.1073/pnas.1107402108

Ramírez, S., Gómez-Valadés, A. G., Schneeberger, M., Varela, L., Haddad-Tóvolli, R., Altirriba, J., Noguera, E., Drougard, A., Flores-Martínez, Á., Imbernón, M., Chivite, I., Pozo, M., Vidal-Itriago, A., Garcia, A., Cervantes, S., Gasa, R., Nogueiras, R., Gama-Pérez, P., Garcia-Roves, P. M., . . . Claret, M. (2017). Mitochondrial Dynamics Mediated by Mitofusin 1 Is Required for POMC Neuron Glucose-Sensing and Insulin Release Control. *Cell Metabolism*, *25*(6), 1390-1399.e1396. https://doi.org/10.1016/j.cmet.2017.05.010

Ramming, T., Hansen, H. G., Nagata, K., Ellgaard, L., & Appenzeller-Herzog, C. (2014). GPx8 peroxidase prevents leakage of H2O2 from the endoplasmic reticulum. *Free Radic Biol Med*, *70*, 106-116. https://doi.org/10.1016/j.freeradbiomed.2014.01.018

Ramos-Cabrer, P., Campos, F., Sobrino, T., & Castillo, J. (2011). Targeting the ischemic penumbra. *Stroke*, *42*(1 Suppl), S7-11. https://doi.org/10.1161/STROKEAHA.110.596684

Rau, T. F., Lu, Q., Sharma, S., Sun, X., Leary, G., Beckman, M. L., Hou, Y., Wainwright, M. S., Kavanaugh, M., Poulsen, D. J., & Black, S. M. (2012). Oxygen glucose deprivation in rat hippocampal slice cultures results in alterations in carnitine homeostasis and mitochondrial dysfunction. *PLoS One*, *7*(9), e40881, Article e40881. https://doi.org/10.1371/journal.pone.0040881

Regan, M. D., Gill, I. S., & Richards, J. G. (2017). Calorespirometry reveals that goldfish prioritize aerobic metabolism over metabolic rate depression in all but near-anoxic environments. *J Exp Biol*, *220*(Pt 4), 564-572. https://doi.org/10.1242/jeb.145169

Reynafarje, B. (1962). Myoglobin content and enzymatic activity of muscle and altitude adaptation. *J Appl Physiol*, *17*, 301-305. https://doi.org/10.1152/jappl.1962.17.2.301

Rhee, S. G., Chae, H. Z., & Kim, K. (2005). Peroxiredoxins: a historical overview and speculative preview of novel mechanisms and emerging concepts in cell signaling. *Free Radic Biol Med*, *38*(12), 1543-1552. https://doi.org/10.1016/j.freeradbiomed.2005.02.026

Richardson, R. S., Noyszewski, E. A., Kendrick, K. F., Leigh, J. S., & Wagner, P. D. (1995). Myoglobin O2 desaturation during exercise. Evidence of limited O2 transport. *J Clin Invest*, *96*(4), 1916-1926. https://doi.org/10.1172/JCI118237

Ridnour, L. A., Thomas, D. D., Mancardi, D., Espey, M. G., Miranda, K. M., Paolocci, N., Feelisch, M., Fukuto, J., & Wink, D. A. (2004). The chemistry of nitrosative stress induced by nitric oxide and reactive nitrogen oxide species. Putting perspective on stressful biological situations. *Biol Chem*, *385*(1), 1-10. https://doi.org/10.1515/BC.2004.001

Riley, C. L., & Mills, E. M. (2020). *The role of UCP3 in brown adipose tissue mitochondrial bioenergetics is complementary to that of UCP1*. Cold Spring Harbor Laboratory.

Rizzuto, R., De Stefani, D., Raffaello, A., & Mammucari, C. (2012). Mitochondria as sensors and regulators of calcium signalling. *Nat Rev Mol Cell Biol*, *13*(9), 566-578. https://doi.org/10.1038/nrm3412

Rohlicek, C. V., Saiki, C., Matsuoka, T., & Mortola, J. P. (1998). Oxygen transport in conscious newborn dogs during hypoxic hypometabolism. *J Appl Physiol (1985)*, *84*(3), 763-768. https://doi.org/10.1152/jappl.1998.84.3.763

Rojas-Morales, P., Leon-Contreras, J. C., Aparicio-Trejo, O. E., Reyes-Ocampo, J. G., Medina-Campos, O. N., Jimenez-Osorio, A. S., Gonzalez-Reyes, S., Marquina-Castillo, B., Hernandez-Pando, R., Barrera-Oviedo, D., Sanchez-Lozada, L. G., Pedraza-Chaverri, J., & Tapia, E. (2019). Fasting reduces oxidative stress, mitochondrial dysfunction and fibrosis induced by renal ischemia-reperfusion injury. *Free Radic Biol Med*, *135*, 60-67. https://doi.org/10.1016/j.freeradbiomed.2019.02.018

Ronchi, J. A., Francisco, A., Passos, L. A., Figueira, T. R., & Castilho, R. F. (2016). The Contribution of Nicotinamide Nucleotide Transhydrogenase to Peroxide Detoxification Is Dependent on the Respiratory State and Counterbalanced by Other Sources of NADPH in Liver Mitochondria. *J Biol Chem*, *291*(38), 20173-20187. https://doi.org/10.1074/jbc.M116.730473

Roper, T. J., Bennett, N. C., Conradt, L., & Molteno, A. J. (2001). Environmental conditions in burrows of two species of African mole-rat, *Georhychus capensis* and *Cryptomys* *damarensis*. *Journal of Zoology*, *254*, 101-107. https://doi.org/Doi 10.1017/S0952836901000590

Rothe, F., Brosz, M., & Storm-Mathisen, J. (1995). Quantitative ultrastructural localization of glutamate dehydrogenase in the rat cerebellar cortex. *Neuroscience*, *64*(4), iii-xvi. https://doi.org/10.1016/0306-4522(94)e0200-n

Rothwell, N. J., Saville, M. E., Stock, M. J., & Wyllie, M. G. (1982). Catecholamine and thyroid hormone influence on brown fat Na+, K+-ATPase activity and thermogenesis in the rat. *Horm Metab Res*, *14*(5), 261-265. https://doi.org/10.1055/s-2007-1018987

Rousset, S., Mozo, J., Dujardin, G., Emre, Y., Masscheleyn, S., Ricquier, D., & Cassard-Doulcier, A. M. (2007). UCP2 is a mitochondrial transporter with an unusual very short half-life. *FEBS Lett*, *581*(3), 479-482. https://doi.org/10.1016/j.febslet.2007.01.010

Ryu, S. Y., Beutner, G., Dirksen, R. T., Kinnally, K. W., & Sheu, S. S. (2010). Mitochondrial ryanodine receptors and other mitochondrial Ca2+ permeable channels. *FEBS Lett*, *584*(10), 1948-1955. https://doi.org/10.1016/j.febslet.2010.01.032

Safiulina, D., Veksler, V., Zharkovsky, A., & Kaasik, A. (2006). Loss of mitochondrial membrane potential is associated with increase in mitochondrial volume: physiological role in neurones. *J Cell Physiol*, *206*(2), 347-353. https://doi.org/10.1002/jcp.20476

Sahd, L., Doubell, N., Bennett, N. C., & Kotze, S. H. (2023). Muscle architecture and muscle fibre type composition in the forelimb of two African mole-rat species, Bathyergus suillus and Heterocephalus glaber. *J Morphol*, *284*(3), e21557. https://doi.org/10.1002/jmor.21557

Sahlin, K., Katz, A., & Henriksson, J. (1987). Redox state and lactate accumulation in human skeletal muscle during dynamic exercise. *Biochem J*, *245*(2), 551-556. https://doi.org/10.1042/bj2450551

Sakushima, K., Yoshikawa, M., Osaki, T., Miyamoto, N., & Hashimoto, T. (2020). Moderate hypoxia promotes skeletal muscle cell growth and hypertrophy in C2C12 cells. *Biochem Biophys Res Commun*, *525*(4), 921-927. https://doi.org/10.1016/j.bbrc.2020.02.152

Salin, K., Villasevil, E. M., Auer, S. K., Anderson, G. J., Selman, C., Metcalfe, N. B., & Chinopoulos, C. (2016). Simultaneous measurement of mitochondrial respiration and ATP production in tissue homogenates and calculation of effective P/O ratios. *Physiol Rep*, *4*(20). https://doi.org/10.14814/phy2.13007

Salvi, M., Battaglia, V., Brunati, A. M., La Rocca, N., Tibaldi, E., Pietrangeli, P., Marcocci, L., Mondovi, B., Rossi, C. A., & Toninello, A. (2007). Catalase takes part in rat liver mitochondria oxidative stress defense. *J Biol Chem*, *282*(33), 24407-24415. https://doi.org/10.1074/jbc.M701589200

Schneider, A., Kurz, S., Manske, K., Janas, M., Heikenwalder, M., Misgeld, T., Aichler, M., Weissmann, S. F., Zischka, H., Knolle, P., & Wohlleber, D. (2019). Single organelle analysis to characterize mitochondrial function and crosstalk during viral infection. *Sci Rep*, *9*(1), 8492. https://doi.org/10.1038/s41598-019-44922-9

Schousboe, A., Scafidi, S., Bak, L. K., Waagepetersen, H. S., & McKenna, M. C. (2014). Glutamate metabolism in the brain focusing on astrocytes. *Adv Neurobiol*, *11*, 13-30. https://doi.org/10.1007/978-3-319-08894-5_2

Schuhmacher, L. N., Callejo, G., Srivats, S., & Smith, E. S. J. (2018). Naked mole-rat acid-sensing ion channel 3 forms nonfunctional homomers, but functional heteromers. *J Biol Chem*, *293*(5), 1756-1766. https://doi.org/10.1074/jbc.M117.807859

Schulke, S., Dreidax, D., Malik, A., Burmester, T., Nevo, E., Band, M., Avivi, A., & Hankeln, T. (2012). Living with stress: regulation of antioxidant defense genes in the subterranean, hypoxia-tolerant mole rat, Spalax. *Gene*, *500*(2), 199-206. https://doi.org/10.1016/j.gene.2012.03.019

Scialo, F., Fernandez-Ayala, D. J., & Sanz, A. (2017). Role of Mitochondrial Reverse Electron Transport in ROS Signaling: Potential Roles in Health and Disease. *Front Physiol*, *8*, 428. https://doi.org/10.3389/fphys.2017.00428

Scott, G. R., Guo, K. H., & Dawson, N. J. (2018). The Mitochondrial Basis for Adaptive Variation in Aerobic Performance in High-Altitude Deer Mice. *Integr Comp Biol*, *58*(3), 506-518. https://doi.org/10.1093/icb/icy056

Sebaa, R., & Harper, M.-E. (2020). *New Advances in Our Understanding of the Control and Functions of Brown Adipose Tissue Thermogenesis* Thesis (Ph.D.)--University of Ottawa, 2020.].

Sebaa, R., Johnson, J., Pileggi, C., Norgren, M., Xuan, J., Sai, Y., Tong, Q., Krystkowiak, I., Bondy-Chorney, E., Davey, N. E., Krogan, N., Downey, M., & Harper, M. E. (2019). SIRT3 controls brown fat thermogenesis by deacetylation regulation of pathways upstream of UCP1. *Mol Metab*, *25*, 35-49. https://doi.org/10.1016/j.molmet.2019.04.008

Sekerdag, E., Solaroglu, I., & Gursoy-Ozdemir, Y. (2018). Cell Death Mechanisms in Stroke and Novel Molecular and Cellular Treatment Options. *Curr Neuropharmacol*, *16*(9), 1396-1415. https://doi.org/10.2174/1570159X16666180302115544

Semenza, G. L. (2001). HIF-1 and mechanisms of hypoxia sensing. *Curr Opin Cell Biol*, *13*(2), 167-171. https://doi.org/10.1016/s0955-0674(00)00194-0

Semenza, G. L. (2007a). Life with oxygen. *Science*, *318*(5847), 62-64. https://doi.org/10.1126/science.1147949

Semenza, G. L. (2007b). Oxygen-dependent regulation of mitochondrial respiration by hypoxia-inducible factor 1. *Biochem J*, *405*(1), 1-9. https://doi.org/10.1042/BJ20070389

Semenza, G. L. (2011a). Hypoxia-inducible factor 1: regulator of mitochondrial metabolism and mediator of ischemic preconditioning. *Biochim Biophys Acta*, *1813*(7), 1263-1268. https://doi.org/10.1016/j.bbamcr.2010.08.006

Semenza, G. L. (2011b). Oxygen sensing, homeostasis, and disease. *N Engl J Med*, *365*(6), 537-547. https://doi.org/10.1056/NEJMra1011165

Shabalina, I. G., Jacobsson, A., Cannon, B., & Nedergaard, J. (2004). Native UCP1 displays simple competitive kinetics between the regulators purine nucleotides and fatty acids. *J Biol Chem*, *279*(37), 38236-38248. https://doi.org/10.1074/jbc.M402375200

Shabalina, I. G., Petrovic, N., de Jong, J. M., Kalinovich, A. V., Cannon, B., & Nedergaard, J. (2013). UCP1 in brite/beige adipose tissue mitochondria is functionally thermogenic. *Cell Rep*, *5*(5), 1196-1203. https://doi.org/10.1016/j.celrep.2013.10.044

Shabalina, I. G., Vrbacky, M., Pecinova, A., Kalinovich, A. V., Drahota, Z., Houstek, J., Mracek, T., Cannon, B., & Nedergaard, J. (2014). ROS production in brown adipose tissue mitochondria: the question of UCP1-dependence. *Biochim Biophys Acta*, *1837*(12), 2017-2030. https://doi.org/10.1016/j.bbabio.2014.04.005

Shams, I., Avivi, A., & Nevo, E. (2005). Oxygen and carbon dioxide fluctuations in burrows of subterranean blind mole rats indicate tolerance to hypoxic-hypercapnic stresses. *Comp Biochem Physiol A Mol Integr Physiol*, *142*(3), 376-382. https://doi.org/10.1016/j.cbpa.2005.09.003

Shen, A. C., & Jennings, R. B. (1972). Myocardial calcium and magnesium in acute ischemic injury. *Am J Pathol*, *67*(3), 417-440. https://www.ncbi.nlm.nih.gov/pubmed/5033257

Shen, K., Pender, C. L., Bar-Ziv, R., Zhang, H., Wickham, K., Willey, E., Durieux, J., Ahmad, Q., & Dillin, A. (2022). Mitochondria as Cellular and Organismal Signaling Hubs. *Annu Rev Cell Dev Biol*, *38*, 179-218. https://doi.org/10.1146/annurev-cellbio-120420-015303

Shenouda, S. M., Widlansky, M. E., Chen, K., Xu, G., Holbrook, M., Tabit, C. E., Hamburg, N. M., Frame, A. A., Caiano, T. L., Kluge, M. A., Duess, M. A., Levit, A., Kim, B., Hartman, M. L., Joseph, L., Shirihai, O. S., & Vita, J. A. (2011). Altered mitochondrial dynamics contributes to endothelial dysfunction in diabetes mellitus. *Circulation*, *124*(4), 444-453. https://doi.org/10.1161/CIRCULATIONAHA.110.014506

Shi, L., Chen, B., Wang, X., Huang, M., Qiao, C., Wang, J., & Wang, Z. (2022). Antioxidant response to severe hypoxia in Brandt's vole Lasiopodomys brandtii. *Integr Zool*, *17*(4), 581-595. https://doi.org/10.1111/1749-4877.12602

Shimoda, L. A., & Polak, J. (2011). Hypoxia. 4. Hypoxia and ion channel function. *Am J Physiol Cell Physiol*, *300*(5), C951-967. https://doi.org/10.1152/ajpcell.00512.2010

Shimoda, L. A., Suresh, K., Undem, C., Jiang, H., Yun, X., Sylvester, J. T., & Swenson, E. R. (2021). Acetazolamide prevents hypoxia-induced reactive oxygen species generation and calcium release in pulmonary arterial smooth muscle. *Pulm Circ*, *11*(4), 20458940211049948. https://doi.org/10.1177/20458940211049948

Shirakabe, A., Zhai, P., Ikeda, Y., Saito, T., Maejima, Y., Hsu, C. P., Nomura, M., Egashira, K., Levine, B., & Sadoshima, J. (2016). Drp1-Dependent Mitochondrial Autophagy Plays a Protective Role Against Pressure Overload-Induced Mitochondrial Dysfunction and Heart Failure. *Circulation*, *133*(13), 1249-1263. https://doi.org/10.1161/CIRCULATIONAHA.115.020502

Shortt, C. M., Fredsted, A., Bradford, A., & O'Halloran, K. D. (2013). Diaphragm muscle remodeling in a rat model of chronic intermittent hypoxia. *J Histochem Cytochem*, *61*(7), 487-499. https://doi.org/10.1369/0022155413490947

Siesjö, B. K. (1978). *Brain energy metabolism*. John Wiley & Sons. https://doi.org/10.1002/ana.410050318

Siesjo, B. K., Zhao, Q., Pahlmark, K., Siesjo, P., Katsura, K., & Folbergrova, J. (1995). Glutamate, calcium, and free radicals as mediators of ischemic brain damage. *Ann Thorac Surg*, *59*(5), 1316-1320. https://doi.org/10.1016/0003-4975(95)00077-x

Silver, I., & Erecinska, M. (1998). Oxygen and ion concentrations in normoxic and hypoxic brain cells. *Adv Exp Med Biol*, *454*, 7-16. https://doi.org/10.1007/978-1-4615-4863-8_2

Silver, I. A., & Erecinska, M. (1990). Intracellular and extracellular changes of [Ca2+] in hypoxia and ischemia in rat brain in vivo. *J Gen Physiol*, *95*(5), 837-866. https://doi.org/10.1085/jgp.95.5.837

Silverman, H. S. (1993). Mitochondrial free calcium regulation in hypoxia and reoxygenation: relation to cellular injury. *Basic Res Cardiol*, *88*(5), 483-494. https://doi.org/10.1007/BF00795414

Silvestri, E., Senese, R., De Matteis, R., Cioffi, F., Moreno, M., Lanni, A., Gentile, A., Busiello, R. A., Salzano, A. M., Scaloni, A., de Lange, P., Goglia, F., & Lombardi, A. (2020). Absence of uncoupling protein 3 at thermoneutrality influences brown adipose tissue mitochondrial functionality in mice. *Faseb J*, *34*(11), 15146-15163. https://doi.org/10.1096/fj.202000995R

Sims, N. R., Finegan, J. M., & Blass, J. P. (1986). Effects of postdecapitative ischemia on mitochondrial respiration in brain tissue homogenates. *J Neurochem*, *47*(2), 506-511. https://doi.org/10.1111/j.1471-4159.1986.tb04530.x

Sims, N. R., & Pulsinelli, W. A. (1987). Altered mitochondrial respiration in selectively vulnerable brain subregions following transient forebrain ischemia in the rat. *J Neurochem*, *49*(5), 1367-1374. https://doi.org/10.1111/j.1471-4159.1987.tb01001.x

Skoog, I., & Gustafson, D. (2006). Update on hypertension and Alzheimer's disease. *Neurol Res*, *28*(6), 605-611. https://doi.org/10.1179/016164106X130506

Slot, I. G., Schols, A. M., de Theije, C. C., Snepvangers, F. J., & Gosker, H. R. (2016). Alterations in Skeletal Muscle Oxidative Phenotype in Mice Exposed to 3 Weeks of Normobaric Hypoxia. *J Cell Physiol*, *231*(2), 377-392. https://doi.org/10.1002/jcp.25083

Smeitink, J., van den Heuvel, L., & DiMauro, S. (2001). The genetics and pathology of oxidative phosphorylation. *Nat Rev Genet*, *2*(5), 342-352. https://doi.org/10.1038/35072063

Snyder, G. K. (1983). Respiratory adaptations in diving mammals. *Respir Physiol*, *54*(3), 269-294. https://doi.org/10.1016/0034-5687(83)90072-5

Snyder, M. M., Yue, F., Zhang, L., Shang, R., Qiu, J., Chen, J., Kim, K. H., Peng, Y., Oprescu, S. N., Donkin, S. S., Bi, P., & Kuang, S. (2021). LETMD1 is required for mitochondrial structure and thermogenic function of brown adipocytes. *Faseb J*, *35*(11), e21965. https://doi.org/10.1096/fj.202100597R

Sofroniew, M. V., & Vinters, H. V. (2010). Astrocytes: biology and pathology. *Acta Neuropathol*, *119*(1), 7-35. https://doi.org/10.1007/s00401-009-0619-8

Sokolova, I. M., Sokolov, E. P., & Haider, F. (2019). Mitochondrial Mechanisms Underlying Tolerance to Fluctuating Oxygen Conditions: Lessons from Hypoxia-Tolerant Organisms. *Integr Comp Biol*, *59*(4), 938-952. https://doi.org/10.1093/icb/icz047

Speers-Roesch, B., Brauner, C. J., Farrell, A. P., Hickey, A. J., Renshaw, G. M., Wang, Y. S., & Richards, J. G. (2012). Hypoxia tolerance in elasmobranchs. II. Cardiovascular function and tissue metabolic responses during progressive and relative hypoxia exposures. *J Exp Biol*, *215*(Pt 1), 103-114. https://doi.org/10.1242/jeb.059667

Spinazzi, M., Radaelli, E., Horre, K., Arranz, A. M., Gounko, N. V., Agostinis, P., Maia, T. M., Impens, F., Morais, V. A., Lopez-Lluch, G., Serneels, L., Navas, P., & De Strooper, B. (2019). PARL deficiency in mouse causes Complex III defects, coenzyme Q depletion, and Leigh-like syndrome. *Proc Natl Acad Sci U S A*, *116*(1), 277-286. https://doi.org/10.1073/pnas.1811938116

St-Pierre, J., Brand, M. D., & Boutilier, R. G. (2000). Mitochondria as ATP consumers: cellular treason in anoxia. *Proc Natl Acad Sci U S A*, *97*(15), 8670-8674. https://doi.org/10.1073/pnas.140093597

Staples, J. F. (2014). Metabolic suppression in mammalian hibernation: the role of mitochondria. *J Exp Biol*, *217*(Pt 12), 2032-2036. https://doi.org/10.1242/jeb.092973

Steinbacher, P., & Eckl, P. (2015). Impact of oxidative stress on exercising skeletal muscle. *Biomolecules*, *5*(2), 356-377. https://doi.org/10.3390/biom5020356

Steiner, A. A., & Branco, L. G. (2002). Hypoxia-induced anapyrexia: implications and putative mediators. *Annu Rev Physiol*, *64*, 263-288. https://doi.org/10.1146/annurev.physiol.64.081501.155856

Stephan, T., Bruser, C., Deckers, M., Steyer, A. M., Balzarotti, F., Barbot, M., Behr, T. S., Heim, G., Hubner, W., Ilgen, P., Lange, F., Pacheu-Grau, D., Pape, J. K., Stoldt, S., Huser, T., Hell, S. W., Mobius, W., Rehling, P., Riedel, D., & Jakobs, S. (2020). MICOS assembly controls mitochondrial inner membrane remodeling and crista junction redistribution to mediate cristae formation. *EMBO J*, *39*(14), e104105. https://doi.org/10.15252/embj.2019104105

Stocks, J. M., Taylor, N. A., Tipton, M. J., & Greenleaf, J. E. (2004). Human physiological responses to cold exposure. *Aviat Space Environ Med*, *75*(5), 444-457. https://www.ncbi.nlm.nih.gov/pubmed/15152898

Storz, J. F., Cheviron, Z. A., McClelland, G. B., & Scott, G. R. (2019). Evolution of physiological performance capacities and environmental adaptation: insights from high-elevation deer mice (Peromyscus maniculatus). *J Mammal*, *100*(3), 910-922. https://doi.org/10.1093/jmammal/gyy173

Strubbe-Rivera, J. O., Chen, J., West, B. A., Parent, K. N., Wei, G. W., & Bazil, J. N. (2021). Modeling the Effects of Calcium Overload on Mitochondrial Ultrastructural Remodeling. *Appl Sci (Basel)*, *11*(5), 2071. https://doi.org/10.3390/app11052071

Šumbera, R., Chitaukali, W. N., Elichová, M., Kubová, J., & Burda, H. (2006). Microclimatic stability in burrows of an Afrotropical solitary bathyergid rodent, the silvery mole‐rat (
Heliophobius argenteocinereus
). *Journal of Zoology*, *263*(4), 409-416. https://doi.org/10.1017/s095283690400545x

Szabadkai, G., & Duchen, M. R. (2008). Mitochondria: the hub of cellular Ca2+ signaling. *Physiology (Bethesda)*, *23*(2), 84-94. https://doi.org/10.1152/physiol.00046.2007

Taegtmeyer, H. (1978). Metabolic responses to cardiac hypoxia. Increased production of succinate by rabbit papillary muscles. *Circ Res*, *43*(5), 808-815. https://doi.org/10.1161/01.res.43.5.808

Tattersall, G. J., Blank, J. L., & Wood, S. C. (2002). Ventilatory and metabolic responses to hypoxia in the smallest simian primate, the pygmy marmoset. *J Appl Physiol (1985)*, *92*(1), 202-210. https://doi.org/10.1152/japplphysiol.00500.2001

Tattersall, G. J., & Milsom, W. K. (2003). Transient peripheral warming accompanies the hypoxic metabolic response in the golden-mantled ground squirrel. *J Exp Biol*, *206*(Pt 1), 33-42. https://doi.org/10.1242/jeb.00057

Tattersall, G. J., & Milsom, W. K. (2009). Hypoxia reduces the hypothalamic thermogenic threshold and thermosensitivity. *J Physiol*, *587*(Pt 21), 5259-5274. https://doi.org/jphysiol.2009.175828 [pii]
10.1113/jphysiol.2009.175828

Tenney, S. M., & Remmers, J. E. (1963). Comparative quantitative morphology of the mammalian lung: diffusing area. *Nature*, *197*, 54-56. https://doi.org/10.1038/197054a0

Terrados, N., Jansson, E., Sylven, C., & Kaijser, L. (1990). Is hypoxia a stimulus for synthesis of oxidative enzymes and myoglobin? *J Appl Physiol (1985)*, *68*(6), 2369-2372. https://doi.org/10.1152/jappl.1990.68.6.2369

Thornton, C., Leaw, B., Mallard, C., Nair, S., Jinnai, M., & Hagberg, H. (2017). Cell Death in the Developing Brain after Hypoxia-Ischemia. *Front Cell Neurosci*, *11*, 248. https://doi.org/10.3389/fncel.2017.00248

Tilokani, L., Nagashima, S., Paupe, V., & Prudent, J. (2018). Mitochondrial dynamics: overview of molecular mechanisms. *Essays Biochem*, *62*(3), 341-360. https://doi.org/10.1042/EBC20170104

Titov, D. V., Cracan, V., Goodman, R. P., Peng, J., Grabarek, Z., & Mootha, V. K. (2016). Complementation of mitochondrial electron transport chain by manipulation of the NAD+/NADH ratio. *Science*, *352*(6282), 231-235. https://doi.org/10.1126/science.aad4017

Trayhurn, P., & Alomar, S. Y. (2015). Oxygen deprivation and the cellular response to hypoxia in adipocytes - perspectives on white and brown adipose tissues in obesity. *Front Endocrinol (Lausanne)*, *6*, 19. https://doi.org/10.3389/fendo.2015.00019

Trayhurn, P., Wang, B., & Wood, I. S. (2008). Hypoxia and the endocrine and signalling role of white adipose tissue. *Arch Physiol Biochem*, *114*(4), 267-276. https://doi.org/10.1080/13813450802306602

Tretter, L., & Adam-Vizi, V. (2005). Alpha-ketoglutarate dehydrogenase: a target and generator of oxidative stress. *Philos Trans R Soc Lond B Biol Sci*, *360*(1464), 2335-2345. https://doi.org/10.1098/rstb.2005.1764

Truett, G. E., Heeger, P., Mynatt, R. L., Truett, A. A., Walker, J. A., & Warman, M. L. (2000). Preparation of PCR-quality mouse genomic DNA with hot sodium hydroxide and tris (HotSHOT). *BioTechniques*, *29*(1), 52, 54. https://doi.org/10.2144/00291bm09

Trumbeckaite, S., Gizatullina, Z., Arandarcikaite, O., Rohnert, P., Vielhaber, S., Malesevic, M., Fischer, G., Seppet, E., Striggow, F., & Gellerich, F. N. (2013). Oxygen glucose deprivation causes mitochondrial dysfunction in cultivated rat hippocampal slices: protective effects of CsA, its immunosuppressive congener [D-Ser](8)CsA, the novel non-immunosuppressive cyclosporin derivative Cs9, and the NMDA receptor antagonist MK 801. *Mitochondrion*, *13*(5), 539-547. https://doi.org/10.1016/j.mito.2012.07.110

Turner, C. E., Barker-Collo, S. L., Connell, C. J., & Gant, N. (2015). Acute hypoxic gas breathing severely impairs cognition and task learning in humans. *Physiol Behav*, *142*, 104-110. https://doi.org/10.1016/j.physbeh.2015.02.006

Twig, G., Elorza, A., Molina, A. J., Mohamed, H., Wikstrom, J. D., Walzer, G., Stiles, L., Haigh, S. E., Katz, S., Las, G., Alroy, J., Wu, M., Py, B. F., Yuan, J., Deeney, J. T., Corkey, B. E., & Shirihai, O. S. (2008). Fission and selective fusion govern mitochondrial segregation and elimination by autophagy. *EMBO J*, *27*(2), 433-446. https://doi.org/10.1038/sj.emboj.7601963

Tyumentsev, M. A., Stefanova, N. A., Muraleva, N. A., Rumyantseva, Y. V., Kiseleva, E., Vavilin, V. A., & Kolosova, N. G. (2018). Mitochondrial Dysfunction as a Predictor and Driver of Alzheimer's Disease-Like Pathology in OXYS Rats. *J Alzheimers Dis*, *63*(3), 1075-1088. https://doi.org/10.3233/JAD-180065

Vandewint, A. L., Zhu-Pawlowsky, A. J., Kirby, A., Tattersall, G. J., & Pamenter, M. E. (2019). Evaporative cooling and vasodilation mediate thermoregulation in naked mole-rats during normoxia but not hypoxia. *J Therm Biol*, *84*, 228-235. https://doi.org/10.1016/j.jtherbio.2019.07.011

Vays, V., Vangely, I., Eldarov, C., Holtze, S., Hildebrandt, T., Bakeeva, L., & Skulachev, V. (2021). Progressive reorganization of mitochondrial apparatus in aging skeletal muscle of naked mole rats (Heterocephalus glaber) as revealed by electron microscopy: potential role in continual maintenance of muscle activity. *Aging (Albany NY)*, *13*(22), 24524-24541. https://doi.org/10.18632/aging.203720

Vincent, A. E., Turnbull, D. M., Eisner, V., Hajnoczky, G., & Picard, M. (2017). Mitochondrial Nanotunnels. *Trends Cell Biol*, *27*(11), 787-799. https://doi.org/10.1016/j.tcb.2017.08.009

Vincent, A. E., White, K., Davey, T., Philips, J., Ogden, R. T., Lawless, C., Warren, C., Hall, M. G., Ng, Y. S., Falkous, G., Holden, T., Deehan, D., Taylor, R. W., Turnbull, D. M., & Picard, M. (2019). Quantitative 3D Mapping of the Human Skeletal Muscle Mitochondrial Network. *Cell Rep*, *27*(1), 321. https://doi.org/10.1016/j.celrep.2019.03.051

Virani, S. S., Alonso, A., Benjamin, E. J., Bittencourt, M. S., Callaway, C. W., Carson, A. P., Chamberlain, A. M., Chang, A. R., Cheng, S., Delling, F. N., Djousse, L., Elkind, M. S. V., Ferguson, J. F., Fornage, M., Khan, S. S., Kissela, B. M., Knutson, K. L., Kwan, T. W., Lackland, D. T., . . . Stroke Statistics, S. (2020). Heart Disease and Stroke Statistics-2020 Update: A Report From the American Heart Association. *Circulation*, *141*(9), e139-e596. https://doi.org/10.1161/CIR.0000000000000757

Vogt, M., Puntschart, A., Geiser, J., Zuleger, C., Billeter, R., & Hoppeler, H. (2001). Molecular adaptations in human skeletal muscle to endurance training under simulated hypoxic conditions. *J Appl Physiol (1985)*, *91*(1), 173-182. https://doi.org/10.1152/jappl.2001.91.1.173

von Hanwehr, R., Smith, M. L., & Siesjo, B. K. (1986). Extra- and intracellular pH during near-complete forebrain ischemia in the rat. *J Neurochem*, *46*(2), 331-339. https://doi.org/10.1111/j.1471-4159.1986.tb12973.x

Wang, C., & Youle, R. J. (2009). The role of mitochondria in apoptosis*. *Annu Rev Genet*, *43*, 95-118. https://doi.org/10.1146/annurev-genet-102108-134850

Wang, S., Tan, J., Miao, Y., & Zhang, Q. (2022). Mitochondrial Dynamics, Mitophagy, and Mitochondria-Endoplasmic Reticulum Contact Sites Crosstalk Under Hypoxia. *Front Cell Dev Biol*, *10*, 848214. https://doi.org/10.3389/fcell.2022.848214

Wang, T. H., Eaton, L., & Pamenter, M. E. (2020). Nitric oxide homeostasis is maintained during acute in vitro hypoxia and following reoxygenation in naked mole-rat but not mouse cortical neurons. *Comp Biochem Physiol A Mol Integr Physiol*, *250*, 110792. https://doi.org/10.1016/j.cbpa.2020.110792

Wang, X., Cui, L., & Ji, X. (2022). Cognitive impairment caused by hypoxia: from clinical evidences to molecular mechanisms. *Metab Brain Dis*, *37*(1), 51-66. https://doi.org/10.1007/s11011-021-00796-3

Wardman, P., & Candeias, L. P. (1996). Fenton chemistry: an introduction. *Radiat Res*, *145*(5), 523-531. https://www.ncbi.nlm.nih.gov/pubmed/8619017

Waypa, G. B., & Schumacker, P. T. (2010). Hypoxia-induced changes in pulmonary and systemic vascular resistance: where is the O2 sensor? *Respir Physiol Neurobiol*, *174*(3), 201-211. https://doi.org/10.1016/j.resp.2010.08.007

Widmer, H. R., Hoppeler, H., Nevo, E., Taylor, C. R., & Weibel, E. R. (1997). Working underground: respiratory adaptations in the blind mole rat. *Proc Natl Acad Sci U S A*, *94*(5), 2062-2067. https://doi.org/10.1073/pnas.94.5.2062

Wiesner, R. J., Rosen, P., & Grieshaber, M. K. (1988). Pathways of succinate formation and their contribution to improvement of cardiac function in the hypoxic rat heart. *Biochem Med Metab Biol*, *40*(1), 19-34. https://doi.org/10.1016/0885-4505(88)90100-4

Wikstrom, J. D., Mahdaviani, K., Liesa, M., Sereda, S. B., Si, Y., Las, G., Twig, G., Petrovic, N., Zingaretti, C., Graham, A., Cinti, S., Corkey, B. E., Cannon, B., Nedergaard, J., & Shirihai, O. S. (2014). Hormone-induced mitochondrial fission is utilized by brown adipocytes as an amplification pathway for energy expenditure. *EMBO J*, *33*(5), 418-436. https://doi.org/10.1002/embj.201385014

Withers, P. C., & Jarvis, J. U. M. (1980). The effect of huddling on thermoregulation and oxygen consumption for the naked mole-rat. *Comparative Biochemistry and Physiology Part A: Physiology*, *66*(2), 215-219. https://doi.org/10.1016/0300-9629(80)90154-1

Wong, H. S., Dighe, P. A., Mezera, V., Monternier, P. A., & Brand, M. D. (2017). Production of superoxide and hydrogen peroxide from specific mitochondrial sites under different bioenergetic conditions. *J Biol Chem*, *292*(41), 16804-16809. https://doi.org/10.1074/jbc.R117.789271

Woodley, R., & Buffenstein, R. (2002). Thermogenic changes with chronic cold exposure in the naked mole-rat (Heterocephalus glaber). *Comp Biochem Physiol A Mol Integr Physiol*, *133*(3), 827-834. https://doi.org/S109564330200199X [pii]

Wree, A., Mayer, A., Westphal, S., Beilfuss, A., Canbay, A., Schick, R. R., Gerken, G., & Vaupel, P. (2012). Adipokine expression in brown and white adipocytes in response to hypoxia. *J Endocrinol Invest*, *35*(5), 522-527. https://doi.org/10.3275/7964

Xiao, W., Wang, R. S., Handy, D. E., & Loscalzo, J. (2018). NAD(H) and NADP(H) Redox Couples and Cellular Energy Metabolism. *Antioxid Redox Signal*, *28*(3), 251-272. https://doi.org/10.1089/ars.2017.7216

Xie, L., Shi, F., Li, Y., Li, W., Yu, X., Zhao, L., Zhou, M., Hu, J., Luo, X., Tang, M., Fan, J., Zhou, J., Gao, Q., Wu, W., Zhang, X., Liao, W., Bode, A. M., & Cao, Y. (2020). Drp1-dependent remodeling of mitochondrial morphology triggered by EBV-LMP1 increases cisplatin resistance. *Signal Transduct Target Ther*, *5*(1), 56. https://doi.org/10.1038/s41392-020-0151-9

Xie, T. R., Liu, C. F., & Kang, J. S. (2017). Sympathetic transmitters control thermogenic efficacy of brown adipocytes by modulating mitochondrial complex V. *Signal Transduct Target Ther*, *2*, 17060. https://doi.org/10.1038/sigtrans.2017.60

Yahav, S., & Buffenstein, R. (1991). The effect of temperature on caecal fermentation processes in a poikilothermic mammal, Heterocephalus glaber. *Journal of Thermal Biology*, *16*(6), 345-349. https://doi.org/10.1016/0306-4565(91)90061-6

Yahav, S., & Buffenstein, R. (1991). Huddling behavior facilitates homeothermy in the naked mole rat Heterocephalus glaber. *Physiological Zoology*, *64*(3), 871-884.

Yang, J. L., Mukda, S., & Chen, S. D. (2018). Diverse roles of mitochondria in ischemic stroke. *Redox Biol*, *16*, 263-275. https://doi.org/10.1016/j.redox.2018.03.002

Yang, Z., Song, T., Truong, L., Reyes-Garcia, J., Wang, L., Zheng, Y. M., & Wang, Y. X. (2020). Important Role of Sarcoplasmic Reticulum Ca(2+) Release via Ryanodine Receptor-2 Channel in Hypoxia-Induced Rieske Iron-Sulfur Protein-Mediated Mitochondrial Reactive Oxygen Species Generation in Pulmonary Artery Smooth Muscle Cells. *Antioxid Redox Signal*, *32*(7), 447-462. https://doi.org/10.1089/ars.2018.7652

Ye, J. (2009). Emerging role of adipose tissue hypoxia in obesity and insulin resistance. *Int J Obes (Lond)*, *33*(1), 54-66. https://doi.org/10.1038/ijo.2008.229

Yin, B., Barrionuevo, G., Batinic-Haberle, I., Sandberg, M., & Weber, S. G. (2017). Differences in Reperfusion-Induced Mitochondrial Oxidative Stress and Cell Death Between Hippocampal CA1 and CA3 Subfields Are Due to the Mitochondrial Thioredoxin System. *Antioxid Redox Signal*, *27*(9), 534-549. https://doi.org/10.1089/ars.2016.6706

Yuan, H., Gerencser, A. A., Liot, G., Lipton, S. A., Ellisman, M., Perkins, G. A., & Bossy-Wetzel, E. (2007). Mitochondrial fission is an upstream and required event for bax foci formation in response to nitric oxide in cortical neurons. *Cell Death Differ*, *14*(3), 462-471. https://doi.org/10.1038/sj.cdd.4402046

Zamponi, N., Zamponi, E., Cannas, S. A., Billoni, O. V., Helguera, P. R., & Chialvo, D. R. (2018). Mitochondrial network complexity emerges from fission/fusion dynamics. *Sci Rep*, *8*(1), 363. https://doi.org/10.1038/s41598-017-18351-5

Zarruk, J. G., Greenhalgh, A. D., & David, S. (2018). Microglia and macrophages differ in their inflammatory profile after permanent brain ischemia. *Exp Neurol*, *301*(Pt B), 120-132. https://doi.org/10.1016/j.expneurol.2017.08.011

Zhang, C., Wang, J., Zhu, J., Chen, Y., & Han, X. (2020). Microcystin-leucine-arginine induced neurotoxicity by initiating mitochondrial fission in hippocampal neurons. *Sci Total Environ*, *703*, 134702. https://doi.org/10.1016/j.scitotenv.2019.134702

Zhang, D., Liu, Y., Tang, Y., Wang, X., Li, Z., Li, R., Ti, Z., Gao, W., Bai, J., & Lv, Y. (2018). Increased mitochondrial fission is critical for hypoxia-induced pancreatic beta cell death. *PLoS One*, *13*(5), e0197266. https://doi.org/10.1371/journal.pone.0197266

Zhang, H., Bosch-Marce, M., Shimoda, L. A., Tan, Y. S., Baek, J. H., Wesley, J. B., Gonzalez, F. J., & Semenza, G. L. (2008). Mitochondrial autophagy is an HIF-1-dependent adaptive metabolic response to hypoxia. *J Biol Chem*, *283*(16), 10892-10903. https://doi.org/10.1074/jbc.M800102200

Zhang, J., & Ney, P. A. (2009). Role of BNIP3 and NIX in cell death, autophagy, and mitophagy. *Cell Death Differ*, *16*(7), 939-946. https://doi.org/10.1038/cdd.2009.16

Zhang, L., Ebenezer, P. J., Dasuri, K., Fernandez-Kim, S. O., Francis, J., Mariappan, N., Gao, Z., Ye, J., Bruce-Keller, A. J., & Keller, J. N. (2011). Aging is associated with hypoxia and oxidative stress in adipose tissue: implications for adipose function. *Am J Physiol Endocrinol Metab*, *301*(4), E599-607. https://doi.org/10.1152/ajpendo.00059.2011

Zhang, L., Trushin, S., Christensen, T. A., Bachmeier, B. V., Gateno, B., Schroeder, A., Yao, J., Itoh, K., Sesaki, H., Poon, W. W., Gylys, K. H., Patterson, E. R., Parisi, J. E., Diaz Brinton, R., Salisbury, J. L., & Trushina, E. (2016). Altered brain energetics induces mitochondrial fission arrest in Alzheimer's Disease. *Sci Rep*, *6*, 18725. https://doi.org/10.1038/srep18725

Zhao, S., Lin, L., Kan, G., Xu, C., Tang, Q., Yu, C., Sun, W., Cai, L., Xu, C., & Cui, S. (2014). High autophagy in the naked mole rat may play a significant role in maintaining good health. *Cell Physiol Biochem*, *33*(2), 321-332. https://doi.org/10.1159/000356672

Zick, M., Rabl, R., & Reichert, A. S. (2009). Cristae formation-linking ultrastructure and function of mitochondria. *Biochim Biophys Acta*, *1793*(1), 5-19. https://doi.org/10.1016/j.bbamcr.2008.06.013

Zoratti, M., & Szabo, I. (1995). The mitochondrial permeability transition. *Biochim Biophys Acta*, *1241*(2), 139-176. https://doi.org/10.1016/0304-4157(95)00003-a

Zorov, D. B., Juhaszova, M., & Sollott, S. J. (2014). Mitochondrial reactive oxygen species (ROS) and ROS-induced ROS release. *Physiol Rev*, *94*(3), 909-950. https://doi.org/10.1152/physrev.00026.2013

Zorova, L. D., Popkov, V. A., Plotnikov, E. Y., Silachev, D. N., Pevzner, I. B., Jankauskas, S. S., Babenko, V. A., Zorov, S. D., Balakireva, A. V., Juhaszova, M., Sollott, S. J., & Zorov, D. B. (2018). Mitochondrial membrane potential. *Anal Biochem*, *552*, 50-59. https://doi.org/10.1016/j.ab.2017.07.009